การคำนวณบนฐานทฤษฎีจลน์ของอุทกพลศาสตร์และการถ่ายโอนมวลในฟลูอิไดซ์เบด

นาย เบญจพล เฉลิมสินสุวรรณ

KINETIC THEORY BASED COMPUTATION OF HYDRODYNAMICS AND

MASS TRANSFER IN FLUIDIZED BEDS
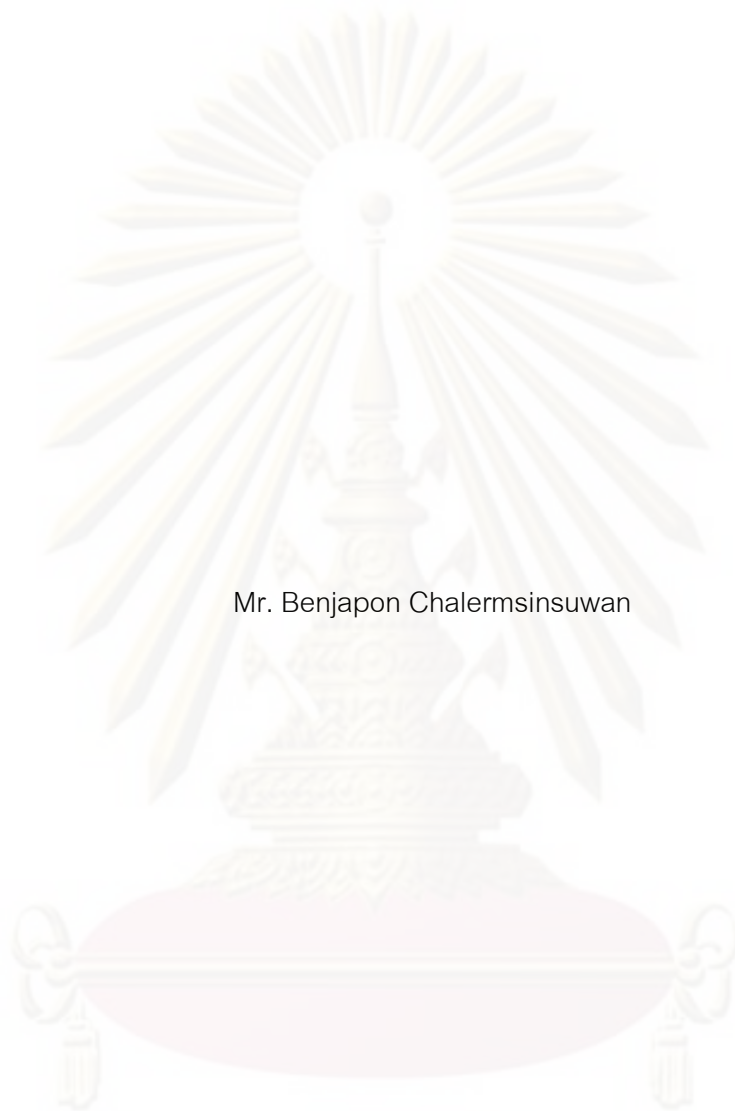
Mr. Benjapon Chalermsinsuwan

A Dissertation Submitted in Partial Fulfillment of the Requirements

for the Degree of Doctor of Philosophy Program in Chemical Technology

Department of Chemical Technology
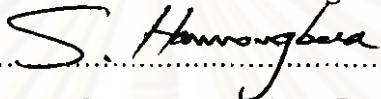
Faculty of Science

Chulalongkorn University

Academic year 2009

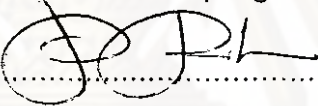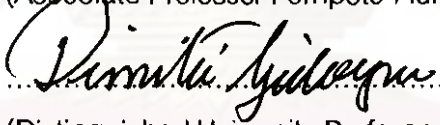|	
Thesis Title	KINETIC THEORY BASED COMPUTATION OF
	HYDRODYNAMICS AND MASS TRANSFER IN FLUIDIZED BEDS
By	Mr. Benjapon Chalermsinsuwan
Field of Study	Chemical Technology
Thesis Advisor	Associate Professor Pornpote Piumsomboon, Ph.D.
Thesis Co-Advisor	Distinguished University Professor Dimitri Gidaspow, Ph.D.
Thesis Co-Advisor	Assistant Professor Prapan Kuchonthara, Ph.D.

Accepted by the Faculty of Science, Chulalongkorn University in Partial Fulfillment of the Requirements for the Doctoral Degree

.... Dean of the Faculty of Science

(Professor Supot Hannongbua, Dr.rer.nat.)

THESIS COMMITTEE

.... Chairman

(Associate Professor Tharapong Vitidsant, Dr.Ing.)

.... Thesis Advisor

(Associate Professor Pornpote Piumsomboon, Ph.D.)

.... Thesis Co-Advisor

(Distinguished University Professor Dimitri Gidaspow, Ph.D.)

.... Thesis Co-Advisor

(Assistant Professor Prapan Kuchonthara, Ph.D.)

.... Examiner

(Professor Somsak Damronglerd, Dr.Ing.)

.... Examiner

(Associate Professor Lursuang Mekasut, Dr.Ing.)

.... External Examiner

(Associate Professor Sunun Limtrakul, D.Sc.)

เบญจพล เฉลิมสินสุวรรณ : การคำนวณบนฐานทฤษฎีจลน์ของอุทกพลศาสตร์และการ
ถ่ายโอนมวลในฟลูอิไดซ์เบด. (KINETIC THEORY BASED COMPUTATION OF
HYDRODYNAMICS AND MASS TRANSFER IN FLUIDIZED BEDS) อ.ที่ปรึกษา
วิทยานิพนธ์หลัก : รศ.ดร. พรพจน์ เปี่ยมสมบูรณ์, อ.ที่ปรึกษาวิทยานิพนธ์ร่วม :
Distinguished University Prof. Dimitri Gidaspow, ผศ.ดร. ประพันธ์ คูชลธารา,
300 หน้า.

ระบบเครื่องปฏิกรณ์แบบฟลูอิไดซ์เบดได้ถูกจำลองด้วยวิธีการคำนวณของไหลเชิงพลวัติ
ร่วมกับทฤษฎีจลน์การไหลของของแข็ง แบบจำลองทางคณิตศาสตร์ที่ได้เสนอขึ้นในงานวิจัยนี้
ให้ผลการเปรียบเทียบกับผลการทดลองจริงที่ดีกว่าแบบจำลองทางคณิตศาสตร์จากงานวิจัยที่
ผ่านมา ดังนั้น แบบจำลองที่ได้เสนอขึ้นจึงเหมาะสมสำหรับการนำไปวิเคราะห์ข้อมูลเพิ่มเติม
เกี่ยวกับกลุ่มอนุภาคและพารามิเตอร์เชิงลึกต่างๆ ที่สามารถอธิบายถึงอุทกพลศาสตร์และการถ่าย
โอนมวล โดยความรู้ที่ได้รับจะเป็นประโยชน์อย่างยิ่งต่อการออกแบบระบบเครื่องปฏิกรณ์ชนิดนี้ให้
มีประสิทธิภาพ เส้นผ่านศูนย์กลางของกลุ่มอนุภาคที่คำนวณได้จากทฤษฎีจลน์การไหลของ
ของแข็งและความเข้มข้นของกลุ่มอนุภาคที่คำนวณได้จากวิธีการทางสถิติให้ผลที่สอดคล้องกับ
สหสัมพันธ์เชิงประสบการณ์จากงานวิจัยที่ผ่านมา แบบจำลองที่เสนอขึ้นได้ถูกใช้ในการคำนวณ
ค่าอุณหภูมิแกรนูลาร์และค่าสัมประสิทธิ์การกระจายตัวอย่างแม่นยำ จากนั้น ค่าสัมประสิทธิ์การ
ถ่ายโอนมวลและค่าตัวเลขไร้หน่วยเชอร์วูดได้ถูกประมาณขึ้นจากเส้นผ่านศูนย์กลางของกลุ่ม
อนุภาคด้วยวิธีการลดส่วนและได้ถูกคำนวณขึ้นจากปฏิกิริยาเคมีด้วยวิธีการรวมความต้านทาน
ของระบบ ในงานวิจัยนี้ ผลของการออกแบบรูปทรงระบบใหม่ยังได้ถูกทำการศึกษา ผลทั้งหมดที่
ได้นำไปสู่แนวทางในการเลือกรูปทรงระบบกับลักษณะของปฏิกิริยาเคมีที่แตกต่างกัน รูปทรง
ระบบหรือท่อไรเซอร์แบบลู่เข้าและลู่ออกจะเหมาะกับปฏิกิริยาเคมีที่มีอัตราการเกิดปฏิกิริยาเร็ว
และช้า ตามลำดับ นอกจากนี้ พารามิเตอร์เชิงลึกทางด้านอุทกพลศาสตร์บางตัวได้ถูกคำนวณขึ้น
จากการทดลองจริงในระบบเครื่องปฏิกรณ์แบบฟลูอิไดซ์เบด

ภาควิชา เคมีเทคนิค	ลายมือชื่อนิสิต เบญจพล เฉลิมสินสุวรรณ	
สาขาวิชา เคมีเทคนิค	ลายมือชื่ออ.ที่ปรึกษาวิทยานิพนธ์หลัก	
ปีการศึกษา 2552	ลายมือชื่ออ.ที่ปรึกษาวิทยานิพนธ์ร่วม	
	ลายมือชื่ออ.ที่ปรึกษาวิทยานิพนธ์ร่วม	

487 39007 23   : MAJOR CHEMICAL TECHNOLOGY

KEYWORDS : FLUIDIZED BEDS / HYDRODYNAMICS / MASS TRANSFER / KINETIC THEORY OF GRANULAR FLOW / COMPUTATIONAL FLUID DYNAMICS

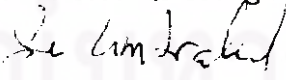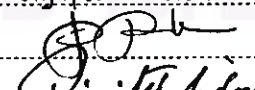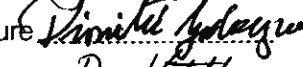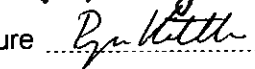BENJAPON   CHALERMSINSUWAN   :   KINETIC   THEORY   BASED COMPUTATION OF HYDRODYNAMICS AND MASS TRANSFER IN FLUIDIZED BEDS. THESIS ADVISOR : ASSOC. PROF. PORNPOTE PIUMSOMBOON, Ph.D., THESIS CO-ADVISORS : DISTINGUISHED UNIVERSITY PROF. DIMITRI GIDASPOW, Ph.D., ASST. PROF. PRAPAN KUCHONTHARA, Ph.D., 300 pp.

The fluidized bed systems were modeled using computational fluid dynamics simulation with kinetic theory of granular flow. The proposed numerical models give better result than the previous published models. The models thus are suitable for providing more information about particle cluster and other in-depth parameters those described the hydrodynamics and mass transfer. This knowledge will lead to efficient system design. The computed particle cluster diameters using kinetic theory of granular flow method and particle cluster concentrations using statistical method agree with the published empirical correlations. The models were accurately used to calculate the granular temperatures and the dispersion coefficients. Then, the mass transfer coefficients and the Sherwood numbers were estimated based on particle cluster diameters and were computed using the concept of additive resistances with chemical reaction. The novel system geometry designs were also studied. These results provide the criteria for choosing system geometry with different reaction characteristics. The tapered-out and tapered-in risers will suit for the reactions with fast and slow rates, respectively. Besides, some in-depth hydrodynamics parameters were obtained from real experiment in the fluidized bed system.

Department : ....Chemical Technology.....   Student's Signature Benjapon Chalermsinsuwan
Field of Study : ...Chemical Technology.....   Advisor's Signature ....
Academic Year : 2009..............................   Co-Advisor's Signature ....
                                                        Co-Advisor's Signature ....

ACKNOWLEDGEMENTS

CONTENTS

LIST OF TABLES

LIST OF FIGURES

NOMENCLATURES

General letters

A	Cross-sectional area of a bed (m^2)
$\vec{A}$	Surface area vector (m^2)
Ar	Archimides number (-)
a_v	External surface per volume of catalyst (1/m)
b	Total number of solid particles per unit area in each frame (-)
C	Molar concentration (kgmol/m^3) or Instantaneous velocity fluctuation (m/s)
C_{D0}	Drag function (-)
$C_{surface}$	Surface molar concentration (kgmol/m^3)
C_1	First empirical constant from the experiment (-)
C_2	Second empirical constant from the experiment (-)
c	Instantaneous velocity (m/s)
c_p	Heat capacity at constant pressure (J/kg K)
D	Diameter of column or riser (m)
D	Dispersion coefficient or molecular diffusivity (m^2/s)
D_l	Laminar dispersion coefficient (m^2/s)
$D_{particles\ oscillations}$	Dispersion coefficient due to particle oscillations (m^2/s)
D_t	Turbulent dispersion coefficient (m^2/s)

d_{cl}	Particle cluster diameter (m)
d_p	Solid particle diameter (m)
E	Turbulent kinetic energy (m^2/s^2)
$E(n)$	Energy spectrum or distribution function (m^2/s)
E_a	Activation energy (J/kgmol)
Ex	Radial energy spectrum or distribution function (m^2/s)
Ey	Axial energy spectrum or distribution function (m^2/s)
e	Particle-particle restitution coefficient (-)
e_W	Particle-wall restitution coefficient (-)
$F_{cluster}$	Drag force acting on particle cluster inside the dilute and dense phases (Pa m^2)
F_{dense}	Drag force acting on solid particle inside the dense phase (Pa m^2)
F_{dilute}	Drag force acting on solid particle inside the dilute phase (Pa m^2)
F_{drag}	Drag force (Pa m^2)
f	Dominant frequency (Hz)
G	Circulation rate or mass flux (kg/m^2 s)
g	Gravitational acceleration or gravity force (m/s^2)
g_0	Radial distribution function (-)
h	Height of riser (m)

h	Specific enthalpy (J/kg)
h_{sg}	Heat transfer coefficient between the phases (J/m^3 s K)
I	Unit tensor (-)
J	Diffusive mass flux (kg/m^2 s)
K	Overall resistance (m/s)
k	Thermal conductivity (J/s m K)
$k_{mass\,transfer}$	Mass transfer coefficient (m/s)
$k_{reaction}$	Resistance due to reaction or reaction rate constant (1/s)
k_0	Pre-exponential factor (m^{15}/kg^5 s)
L	Height or length of a bed (m)
l	Total number of time steps (-)
M_c	Number of solid particle per unit volume inside the dense phase (-)
M_f	Number of solid particle per unit volume inside the dilute phase (-)
M_i	Number of particle cluster per unit volume inside the dilute and dense phases (-)
m	Total number of particle clusters (-)
Nu	Nusselt number (-)
n	Unit vector (-)
ΔP	Pressure drop (Pa)

Pr	Prandtl number (-)
p	Gas pressure (Pa)
p_s	Solid pressure (Pa)
Q_{sg}	Intensity of heat exchange between the phases (J/m^3 s)
q	Heat conduction flux (J/m^2 s)
R	Net homogeneous reaction rate (kg/m^3 s)
$R_{universal}$	Universal gas constant (J/kmol K)
Re	Reynolds number (-)
r	Net heterogeneous reaction rate (kg/m^3 s) or radial position (-)
r_p	Reaction rate per unit mass of catalyst (kg /kg catalyst s)
S_φ	Source term of φ (-)
Sh	Sherwood number based on particle diameter (-)
$Sh_{Cluster}$	Sherwood number based on particle cluster diameter (-)
T	Temperature (K)
T_E	Eulerian integral time scale (s)
T_L	Lagrangian integral time scale (s)
t	Time (s)
t'	Time step (s)
u	Superficial velocity (m/s)
V	Arbitrary control volume (m^3)

v	Velocity or hydrodynamic velocity (m/s)
$\vec{v}$	Velocity vector (m/s)
v'	Velocity fluctuation (m/s)
$v_{s,slip}$	Slip velocity of solid particle at the wall (m/s)
$v_{st,W}$	Tangential velocity of solid particle at the wall (m/s)
x	Radial distance from center of riser (m)
Y	Axial or vertical distance (m)
y	Mass fraction (-) or axial distance from bottom of riser (m)

Greek letters

α	Inclined angle (degree) or under-relaxation factor (-)
β_{gs}	Momentum interphase exchange coefficient (kg/m^3 s)
Γ_φ	Diffusion coefficient of φ (-)
γ	Collisional dissipation of fluctuating kinetic energy (kg/m s^3)
γ_W	Collisional dissipation of fluctuating kinetic energy at the wall (kg/m s^3)
ε	Volume fraction (-)
ε_{cl}	Volume fraction of particle cluster (-)
$\varepsilon_{s,max}$	Volume fraction of solid particle phase at maximum packing (-)
θ	Granular temperature (m^2/s^2)
θ_l	Laminar granular temperature (m^2/s^2)

θ_t	Turbulent granular temperature (m^2/s^2)
θ_W	Granular temperature at the wall (m^2/s^2)
κ	Conductivity of fluctuating kinetic energy (kg/m s)
μ	Viscosity (kg/m s)
ξ	Bulk viscosity (kg/m s)
ρ	Density (kg/m^3)
σ	Standard deviation (-)
τ	Stress tensor (Pa)
ϕ	Specularity coefficient (-)
ϕ_s	Sphericity of solid particle (-) or exchange of solid fluctuating kinetic energy between phases ($kg/m\ s^3$)
φ	Scalar variable (-)
ω	Correction factor (-)

Subscripts

Air	Air species
CO_2	Carbon dioxide species
C_3H_8	Propane species
c	Start of turbulent fluidization
g	Gas phase
H_2O	Steam species

i	Component species (Air, CO_2, C_3H_8, H_2O, N_2, O_2 and O_3) or component directions (x-, y- and z- directions)
$inlet$	At the inlet
k	End of turbulent fluidization or component phases (gas and solid)
mb	Minimum bubbling
mf	Minimum fluidization
mp	Minimum pneumatic
N_2	Nitrogen species
O_2	Oxygen species
O_3	Ozone species
$outlet$	At the outlet
s	Solid phase
t	Terminal
tr	Transport
x	Radial direction
y	Axial direction
z	Radial direction
0	Initial condition

CHAPTER I

INTRODUCTION

1.1. Background information and problem statement

Multiphase flows occur in almost all aspects of chemical engineering. Fluidized beds are a type of reactor device that can be used to carry out a variety of multiphase flow chemical reactions. In this type of reactors, a fluid is passed through solid particles at high enough velocities to suspend the solid particles and cause them to behave as a fluid. The reason is that the gravity pull on solid particles is offset by the upward drag of the fluid. As fluid velocity passing through the solid particles increases, a series of changes in the motion of solid particles could occur. These regimes, arranged in order of increasing velocities, are bubbling, turbulent, fast fluidization and pneumatic transport. In bubbling regime or batch fluidization, the solid particles remain in the reactor. In continuous fluidization, the solid particles must be continually added to the reactor to maintain the operation. If the major fraction of solid particles leaving the reactor is captured by a solid separator and recirculated back to the system, the process is called circulating fluidized bed. Either a gas or a liquid can fluidize solid particles. In this study, the focus is purely on gas-solid fluidization. There are many advantages of fluidized beds. Some of the advantages are: easy handling (Kunii and Levenspiel, 1991), good heat control (Basu and Fraser, 1991) and fuel flexibility (Basu, 2006). As a result, the fluidized beds are now used in many industrial processes.

Since the beginning of 1920s, a new chapter has opened in the history of the industrial fluidized beds. Winkler (1922) of Germany introduced gaseous combustion products into the bottom of a crucible containing coke solid particles, creating the demonstration of gasification of coal in a fluidized bed. Winkler saw the mass of solid particles lifted by the gas look like a boiling liquid. This study therefore initiated a new process, called fluidization, and led to commercialization of the fluidized bed reactors. The circulating fluidized bed had an unexpected beginning. Lewis and Gilliland (1950) obtained this new process when they were trying to find an appropriate gas-solid

contacting process in 1938. Incidentally, they invented the circulating fluidized bed similar to the fluidized bed invented earlier by Winkler. The first large scale commercial implementation of the fluidized bed was the fluid catalytic cracking process, which converted heavier petroleum cuts into gasoline in the early 1940s. After that, the fluidized bed technology was applied to a broad number of industrial chemical processes such as combustion, gasification, incineration, calcination, roasting, drying and coating. Currently, there is still much interest in the potential of fluidized bed for power generation or energy conversion due to the increasing world energy demand. There are many novel projects using fluidized bed as a key reactor, for example FutureGen program of the United States (Williams et al., 2006) and HYPOGEN program of the European Union (Christou et al., 2008). However, all the projects encountered many technical and financial issues. The process efficiency dropped below the desired value in some processes (Bajura, 2004; Maurstad, 2005; Liu et al., 2008; Perez-Fortes et al., 2009). In order to use these processes productively, the fluidized beds will need a substantial understanding and improvement. The need to sequester carbon dioxide will require a re-examination of some of the proposed processes, such as FutureGen program (Gidaspow and Jiradilok, 2009).

At present, the fast fluidization regime in circulating fluidized bed has received more attention than the other flow regimes because of its unique characteristics. When comparing to the bubbling regime in fluidized bed, the fast fluidization regime in circulating fluidized beds is a continuous process and has high gas-solid slip velocity which then results in high gas-solid contacting area. When comparing to the turbulent and pneumatic transport regimes in circulating fluidized bed, the fast fluidization regime in circulating fluidized bed has both uniformity and high quantity of solid holdup throughout the reactor. The definition of the fast fluidization regime in circulating fluidized bed is a high velocity gas-solid suspension where solid particles, elutriated by the fluidizing gas above the terminal velocity of individual particles, are returned back to the base of the reactor. The flow structure can be characterized by dilute upwards of solid particles in the core or center region and

downwards movement of aggregates or particle clusters in the annulus or wall region which is widely known as the core-annulus flow structure. Although there are a number of studies on the fast fluidization regime in circulating fluidized bed, most of them are focused on the macroscopic viewpoint such as the alteration of flow structure with various operating conditions (Wang et al., 1995; Zhu and Zhu, 2008; Hu et al., 2009). The study from a microscopic viewpoint is still lacking in the literature, which is the understanding of the fundamental parameters describing the hydrodynamics and ambiguous complex mass transfer. This knowledge will enable scientists and engineers to design better, more efficient, reactors that may effectively deal with the current problem and expand the range of fluidized bed reactor application.

Hydrodynamics of fluidized bed deals with the dynamic phenomena of gas-solid suspensions inside the reactor. From a scientific aspect, the natural characteristic of gas-solid suspensions should be the essential point of interest. From an engineering aspect, the major hydrodynamics issues are the effects of such design factors, as well as operating conditions, on the reactor performance. These scientific and engineering aspects are closely interrelated (mainly interested on the macroscopic viewpoint). One of the emerging hydrodynamic problems for the fast fluidization regime in circulating fluidized beds is how to eliminate the core-annulus flow structure, which is believed to have a negative effect on the chemical reaction conversion. Although the chemical reaction greatly depends on the hydrodynamics, an in-depth study of the chemical reaction in the reactor is still needed. To date, only few research studies have been done to solve the problem of chemical reaction. Also, the study from a microscopic viewpoint is required in order to successfully answer this problem. The parameters describing the hydrodynamics inside the system will provide more insight information, which can explain the reactor dynamic phenomena, such as the gas and solid dispersion coefficients and the solid fluctuating velocity. They can then relate the chemical reaction or process efficiency to general criteria for further consideration of guidelines for the reactor utilization.

Mass transfer is the phrase commonly used for physical processes that involve transport of atoms and molecules within physical systems (Seader and Henley, 1998). The driving force for mass transfer is a difference in concentration; the random motion of molecules causes a net transfer of mass from an area of high concentration to an area of low concentration. The amount of mass transfer can be quantified through the calculation and application of mass transfer coefficient. Transport phenomena texts (e.g. Bird et al., 2002) show that for diffusion control the dimensionless mass transfer coefficient, called the Sherwood number, is two, based on the diameter of a solid particle. Indeed for large particles, Gunn (1978) has shown that the Sherwood number equals to two, the diffusion limit, plus a contribution due to convection expressed in terms of Reynolds and Schmidt numbers. The mass transfer coefficient is known to be much lower for fine particles than those given by correlations for large particles (Kato et al., 1970; Turton and Levenspiel, 1989; Levenspiel, 1999). Breault (2006) reviewed the literature and showed that the Sherwood numbers differ up to seven orders of magnitude. To improve the performance of the reactor, therefore, the information on the mass transfer coefficient is needed to be known. One possible assumption is that the mass transfer coefficient or the Sherwood number for fluidization of small solid particles is low due to particle cluster formation. However, the way to identify and characterize the particle cluster is still in a development stage. The second more plausible assumption is that the mass transfer coefficient or the Sherwood number is low because of its representation in terms of the particle diameter.

Computational fluid dynamics is an important tool for design and optimization of chemical processes. It is one of the branches of fluid mechanics that uses numerical methods and algorithms to solve problems and analyze phenomena that involve fluid and chemically reacting flows. The basic principle of the computational fluid dynamics is the calculation of mass, momentum and energy conservation equations, simultaneously. There are three compelling reasons to use computational fluid dynamics. First, it enables someone to virtually visualize inside his/her design which is difficult to prototype or test through experimentation. Second, it is a quick tool for

predicting what will happen under a given set of circumstances. In a short time, one can test his/her design under various operating conditions until arriving at an optimal result. Third, the foresight gaining from computational fluid dynamics will lead to better, cheaper, faster and safer design that meets environmental regulations and ensures industrial compliance. There are now many commercial and non-commercial computational fluid dynamics programs for example IIT code, MFIX, FLUENT and CFX. For gas-solid or multiphase flow systems, two different approaches might be used for the calculation, namely the Lagrangian and the Eulerian approaches. The Lagrangian approach should be used when the dispersed solid phase in the system occupies a low volume fraction while the Eulerian approach should be used when the volume fraction of dispersed solid phase cannot be occupied by the gas phase. For the fluidized bed reactors, the Eulerian approach thus is suitable for the calculation. This approach separately solves the conservation equations for each phase. Among the various attempts to close the gas-solid flow, the kinetic theory of granular flow has found the widest use as a constitutive equation. This theory is basically an extension of the classical kinetic theory of gases, reviewed by Chapman and Cowling (1970), to dense gas-solid flows, with a description of the solid particle collisions by means of the restitution coefficients. The random movements and the nearly elastic collisions of the solid particles make the kinetic theory ideally suited to describe granular flows. The theory introduces one conservation equation to describe the solid fluctuating kinetic energy called the granular temperature, which is like the thermal temperature in kinetic theory of gases. The solid particle properties can then be obtained as a function of the restitution coefficient and the granular temperature. Although computational fluid dynamics has a promising future and is anticipated to make valuable contributions to predicting the performance of fluidized bed reactors, there are currently no universal computational fluid dynamics models or systematic guidelines available to make appropriate selection of models with a certain gas-solid fluidized bed reactor. Therefore, more attention should be considered in this area. Besides, to support a computational fluid dynamics model, the real experimental data on the fluidized bed reactors is required to provide the crucial information for tuning and validating the model.

1.2. Research objectives

The research objectives of the present study are:

1. Study the hydrodynamics and chemical reaction in fluidized beds using computational fluid dynamics simulation.

2. Identify and characterize the particle cluster properties in fluidized bed and compare the obtained values with the literature correlations.

3. Compute the parameters those described the hydrodynamics and mass transfer in fluidized bed and construct the relation between those parameters and chemical reaction or process efficiency.

4. Propose the alternatives to improve the chemical reaction or process efficiency in fluidized bed.

1.3. Research overviews

In Chapters II and III, the theoretical description of fluidization and kinetic theory based computational fluid dynamics model are discussed, respectively. For Chapter II, the basic properties of fluidization as well as the detail characteristics of each fluidization flow regimes are briefly explained. For Chapter III, the basic computational fluid dynamics model with the kinetic theory of granular flow concept is summarized for modeling of the fluidized bed reactor.

In Chapter IV, the kinetic theory based computational fluid dynamics with the modified interphase exchange coefficient model was developed. It can predict the fast fluidization regime in circulating fluidized bed and can calculate the Reynolds stresses, energy spectra, power spectra, granular temperatures, dispersion coefficients and particle cluster properties. Then, the mass transfer coefficient and the Sherwood number were estimated based on the computed particle cluster diameters.

In Chapter V, the same fluidized bed system and computational fluid dynamics model as employed in Chapter IV with the addition of an ozone decomposition reaction was used to obtain more information on mass transfer. The mass transfer coefficient and the Sherwood number were computed using the concept of additive resistances due to the mass transfer and chemical reaction resistances. Also, the effects of reactor height and reaction rate constant were studied.

In Chapter VI, the novel designs of the riser geometry of circulating fluidized bed were investigated using the kinetic theory based computational fluid dynamics. The new designs were based on the improvement of main factors that had an effect on reaction characteristics which were turbulence, time and temperature. Initially, the hydrodynamics results led to the criteria for choosing riser geometry with different reaction characteristics. Then, the proposed criteria were proved by adding a simple propane combustion reaction. In addition, the parameters those described the hydrodynamics were computed. They were used to explain and find the relationship with the chemical reaction inside these reactors.

In Chapter VII, the particle image velocimetry technique was used to measure the turbulence and dispersion at the wall region in a circulating fluidized bed riser. A method to determine particle velocities and its derivation which are stresses, granular temperatures and dispersions are illustrated. All the values were computed both in the axial and radial directions and classified into two types based on the solid particle characteristic which are individual particle and particle cluster.

In Chapter VIII, the conclusions and recommendations for the future study are provided. About the Appendix sections, the principle of GAMBIT program, the principle of FLUENT 6.2.16 program and the FLUENT program additional user-defined function in Microsoft Visual C++ language are given in Appendices A, B and C, respectively. The new additional user defined function is the interphase exchange coefficient model (the energy minimization multi-scale drag model). In Appendix D, the principle of particle image velocimetry technique is summarized.

CHAPTER II

THEORETICAL DESCRIPTION OF FLUIDIZATION

2.1. Introduction

Fluidization has had a rather turbulent history. It hit the industrial scene in a huge way with fluid catalytic cracking process in 1942 (Avidan and Shinnar, 1990; Avidan, 1997) then it moved into many other areas of industrial chemical process such as combustion, gasification, incineration, calcination, roasting, drying and coating (Basu, 2006). Currently, there is still much interest in the potential of fluidization for power generation or energy conversion due to the increasing of world energy problem (Williams et al., 2006; Christou et al., 2008).

This chapter provides a theoretical description of fluidization, which will cover mainly the subjects that are relevant to this study. The basic properties of fluidization and circulating fluidized bed as well as the detail characteristics of each fluidization flow regimes are briefly explained. In addition, the previous studies on hydrodynamics and mass transfer in fluidized beds are summarized. For more detail information about the fluidization, it can be found in the fundamental textbooks or open source literatures.

2.2. Fluidization concepts

Fluidization is defined as the operation through which fine solid particles are transformed into a fluid-like state through contact with either a gas or a liquid while fluidized bed is a type of reactor device that can be used to carry out a fluidization. Under the fluidized state, the gravitational pulled on solid particles is offset by the upward drag of the fluid. The solid particles therefore remain in a semi-suspended condition. A fluidized bed reflects the properties similar to those of a fluid as explained below with the assist of Figure 2.1.

1. The static pressure at any height is about equal to the weight of solid particles per unit cross sectional area above that level.

2. The solid particle surface maintains a horizontal level, irrespective of how the solid particle is tilted. In addition, the solid particle assumes the shape of the vessel (Figure 2.1 (a)).

3. The solid particles may be drained like a liquid through an orifice at the bottom or on the side of the container (Figure 2.1 (b)).

4. An object denser and lighter than the bulk of the solid particle will sink and float, respectively. Thus, a steel ball sinks in the solid particle bed while a light badminton cock floats on the surface (Figure 2.1 (c)).

5. The solid particles are well mixed and they maintain a nearly homogeneous temperature throughout the body when heated.

To understand how a fluidized bed is formed, imagine a fluid moving up through a bed of solid particles resting on the porous bottom of a column as displayed in Figure 2.2. As the fluid velocity through the solid particles increases, a series of changes in the motion of the solid particles could occur. At a very low velocity, the solid particles remain stationary on the bottom. The column hence is laid on a fixed bed operation. At an adequately high velocity, the fluidized bed operation starts and the solid particles transport out of the column. With changes in fluid velocity, the solid particles move from one state or regime to another. These regimes, arranged in order of increasing velocities, are bubbling, turbulent, fast fluidization and pneumatic transport. In bubbling regime or batch fluidization, the solid particles are remaining in the reactor. In other three regimes or continuous fluidization, the solid particles must be continually added to the column to maintain the operation. Each of the flow regimes has distinct characteristics. The next topic will discuss the features of these flow regimes in gas-solid system. However, the column may also attain slugging or dense suspension upflow regimes under specifically crucial operating conditions. There are many advantages of fluidized beds. Some of the advantages are easy handling (Kunii and Levenspiel, 1991), good heat control (Basu and Fraser, 1991) and fuel flexibility (Basu, 2006).

2.3. Fluidization flow regimes

2.3.1. Bubbling fluidization

If the gas flow rate through the bed of stationary solid particles is increased at a sufficient high velocity, the pressure drop across the bed due to the fluid drag rises. The pressure drop per unit height of a bed ($\Delta P / L$) of uniformly sized solid particles (d_p) is correlated as (Ergun, 1952):

$$\frac{\Delta P}{L} = 150 \frac{\left(1 - \varepsilon_g\right)^2}{\varepsilon_g^{\;3}} \frac{\mu_g u_g}{\left(\phi_s d_p\right)^2} + 1.75 \frac{\left(1 - \varepsilon_g\right)}{\varepsilon_g^{\;3}} \frac{\rho_g u_g^2}{\phi_s d_p} \tag{2.1}$$

where ε_g is the volume fraction of the gas, μ_g is the viscosity of the gas, ϕ_s is the sphericity of the solid particles, ρ_g is the density of the gas. The superficial gas velocity, u_g, is defined as the gas flow rate per unit cross sectional area of the bed. When the u_g reaches a critical value known as the minimum fluidization velocity (u_{mf}) or the velocity where the fluid drag is equal to a solid particle's weight less its buoyancy, the pressure drop across the bed no longer rises and the bed transforms into an incipiently fluidized bed. Since the pressure drop across the bed equals the weight of the bed, the fluid drag (F_{Drag}) is written as:

$$F_{Drag} = \Delta P A = AL\left(1 - \varepsilon_g\right)\left(\rho_s - \rho_g\right)g \tag{2.2}$$

where A is the cross-sectional area of the bed, L is the height of the bed, ρ_s is the density of the solid particles and g is the gravity force. The u_{mf} may be obtained by solving Equations (2.1) and (2.2) at minimum fluidization condition, simultaneously to obtain:

$$150 \frac{\left(1 - \varepsilon_{mf}\right)}{\varepsilon_{mf}^{\;3} \phi_s^2}\left(\frac{\rho_g d_p u_{mf}}{\mu_g}\right) + 1.75 \frac{\left(1 - \varepsilon_{mf}\right)}{\varepsilon_{mf}^{\;3} \phi_s}\left(\frac{\rho_g d_p u_{mf}}{\mu_g}\right)^2 = Ar \tag{2.3}$$

$$Re_{mf} = \frac{\rho_g d_p u_{mf}}{\mu_g} = \left[C_1^2 + C_2 Ar\right]^{0.5} - C_1 \tag{2.4}$$

where ε_{mf} is the volume fraction of the gas at minimum fluidization condition and Ar is the Archimides number ($Ar = \dfrac{\rho_g(\rho_s - \rho_g)gd_p^3}{\mu_g^2}$). To further utilize this equation, the values of the empirical constants C_1 and C_2 from the experiment are required. The C_1 and C_2 values from Grace experiment (1982) are 27.2 and 0.0408, respectively.

At minimum fluidization condition, the body of solid particles behaves like a fluid. For Geldart group B and D particles, a further increase in gas velocity can cause the excess gas to form the bubbles. The gas-solid suspension around the bubbles and elsewhere in the bed is called emulsion phase. The occurrence of bubble phase is the major characteristic of this fluidization flow regime. For Geldart group A particles, the solid particles does not start bubbling as the u_g reaches u_{mf} however the bed starts expanding (Ye et al., 2005). This is due to the role of interparticle force between the solid particles. The bubbles start when the u_g exceeds minimum bubbling velocity (u_{mb}). It can be estimated by Abrahamsen and Geldart correlation (1978) as:

$$u_{mb} = 33d_p\left(\dfrac{\rho_g}{\mu_g}\right)^{0.1} \tag{2.5}$$

Gelderbloom et al. (2003) and Ng and Tan (2008) showed that the u_{mb} approximately equals to u_{mf} for Geldart group B and D particles. For Geldart group C particles, the particles are very fine and very difficult to fluidize. Therefore, there is no bubbling regime for the fluidization of this Geldart group C particle (Basu, 2006).

2.3.2. Turbulent fluidization

When the u_g through a bubbling fluidization is increased above the u_{mb}, the bed of solid particles starts expanding. A continued increase in the velocity may eventually show a change in the pattern of bed expansion, indicating a transition into a new regime called a turbulent fluidization. The transition from bubbling to turbulent fluidizations may be due to an increase in the bubble phase and an expansion and a thinning of the emulsion phase (Nakajima et al., 1991). In the turbulent regime, the

bubble phase loses its identity due to the rapid coalescence and breakup of bubbles. This results in a violently active and highly expanded bed with a change in the pattern of bed expansion throwing solid particles into the freeboard region above the body of solid particles. The bed will have a surface but it is considerably diffused. The turbulent fluidization therefore is characterized by two different coexisting regions which are a dense bubbling at the lower region and dilute dispersed flow at the upper region (Berruti, et al., 1995; Rhodes, 1996; Jiradilok et al., 2006).

The transition between a bubbling to turbulent fluidizations does not occur sharply at one velocity. The onset of this transition begins at the velocity u_c and is completed at the velocity u_k. The velocity u_c is obtained when the amplitude of pressure fluctuation reached a maximum point while the velocity u_k is obtained when the amplitude of pressure fluctuation reduces back to a steady value. There is no well established correlation for calculating the u_c and u_k. However, some correlations from the literatures are given below (Tsukada et al., 1993; Bi and Grace, 1995):

$$Re_c = \frac{\rho_g d_p u_c}{\mu_g} = 0.565 Ar^{0.461} \tag{2.6}$$

$$Re_k = \frac{\rho_g d_p u_k}{\mu_g} = 1.310 Ar^{0.450} \tag{2.7}$$

Fine solid particles enter turbulent fluidization at a velocity sufficiently above their terminal velocity (u_t) while coarser solid particles may enter turbulent fluidization at a velocity below their u_t (Rhodes, 1996). The u_t is the equilibrium velocity where the buoyancy force and the fluid drag balance the effect of gravity. Below the u_t, the solid particles are generally retained within a certain height and there is no large-scale migration of solid particles. Above the u_t, there is large-scale migration of solid particles out of the system. For spherical solid particles, the u_t can be calculated by simplified the force balance and drag coefficient under steady state condition as:

$$Re_t = \frac{\rho_g d_p u_t}{\mu_g} = \left(\frac{Ar}{7.5}\right)^{0.666} \quad \text{for } 0.4 < Re < 500 \tag{2.8}$$

2.3.3. Fast fluidization

The term, fast fluidization, was initially proposed by Yerushalmi et al. (1976b). It was described as a regime lying between turbulent and pneumatic transport fluidizations. The volume fraction of solid particles is somewhat between dense and dilute conditions. In a typical fast fluidization, one observes a non uniform suspension of dilute upwards of solid particles in the core or center region and downwards movement of aggregates or particle clusters in the annulus or wall region. High gas-solid slip velocity, formation and disintegration of particle clusters and extensive back mixing of solid particles are major characteristics of this regime (Yerushalmi and Cankurt, 1979; Avidan and Yerushalmi, 1982). Also, the unique gas-solid suspension called the core-annulus flow structure is another physical characteristic of the fast fluidization (Takeuchi et al., 1986; Chen, 1999).

A clear picture of the transition to and from fast fluidization is still lacking at this moment. However, there is an approximate minimum velocity below which fast fluidization cannot occur. This critical velocity, known as transport velocity (u_{tr}), therefore is the transition velocity from turbulent fluidization to fast fluidization (Smolders and Beayens, 2001; Balasubramanian et al., 2005). According to Yerushalmi and Cankurt experiment (1979), a sudden change of pressure drop disappears when u_g exceeds u_{tr}. If a bed of solid particles is fluidized above the u_t of the individual solid particles, all solid particles will be entrained out of the column unless they are replaced simultaneously. Nevertheless, it takes a certain amount of time to empty the column. As the velocity in excess of the u_t increases, the time needed to empty the column decreases gradually until a critical velocity is reached, above which there is a sudden drop in the time for emptying the column corresponding with the pressure drop variation. An empirical correlation for the u_{tr} is reviewd by Monazam et al. (2005) based on the literature experiments:

$$Re_{tr} = \frac{\rho_g d_p u_{tr}}{\mu_g} = 2.28 Ar^{0.419} \qquad (2.9)$$

2.3.4. Pneumatic transport fluidization

The minimum pressure drop point denotes the transition from fast fluidization to homogeneous pneumatic transport fluidization (Leung, 1980; Klinzing, 1981). The main characteristic of this regime is that all the solid particles will be carried up the column as separate solid particles widely dispersed in the gas phase. The mass flow ratio of solid particle and gas is usually 1:20 which represents a very high volume fraction of gas. Conventional pneumatic transport fluidization operates with high gas velocity approximately $20 u_t$ in order to prevent the settling of solid particles. If the u_g is raised through the fast fluidization regime, the pneumatic transport fluidization is reaches at a gas velocity which there is no accumulation of solid particles at the bottom (Bi et al., 1993, Bi and Grace, 1995). This u_g is designated as the minimum pneumatic velocity (u_{mp}) and is well predicted by an equation due to Bi and Fan (1991) which may be written explicitly as:

$$u_{mp} = 10.1 \left(g d_p \right)^{0.347} \left(G_s / \rho_g \right)^{0.310} \left(d_p / D \right)^{-0.139} Ar^{-0.021} \qquad (2.10)$$

where G_s is the circulation rate or mass flux of the solid particles and D is the column diameter.

Over a wide range of operating conditions, Figure 2.3 summarizes typical distributions of solid volume fraction with position or height in a column (Kunii and Levenspiel, 1991). These curves show that each fluidization flow regime has its own distinctive characteristic as already discussed.

The various transition velocities for the solid particles used in this study are computed and reported in Table 2.1. They are fluid catalytic cracking or FCC particles (d_p = 76 micron and ρ_s = 1,712 kg/m^3), sand particles (d_p = 175 micron and ρ_s = 2,145 kg/m^3) and polyethylene particles (d_p = 750 micron and ρ_s = 863 kg/m^3). These types of solid particles lay in Geldart group A and B particles which are widely used today. For the computation, the gas phase properties are assumed to be the air properties which have ρ_g = 1.2 kg/m^3 and μ_g = 0.00002 kg/m s.

2.4. Circulating fluidized bed concepts

At high superficial gas velocities ($u_g > u_t$), fine solid particles can be elutriated or removed from a fluidized bed. This is common phenomenon in fluidized bed columns with wide particle size distributions or where solid particles are generated from solid particle attrition, fragmentation or chemical reaction. This loss of solid particles from fluidized beds can adversely affect the reactor performance. It can also lead to loss of solid catalyst and air pollution. Therefore, the ability to capture and return entrained solid particles to the bed is crucial. The circulating fluidized bed has come to prominence in terms of this major application. In this type of reactor, the solid particles must be continuously fed to maintain the required solids holdup in a column. This is usually realized by capturing solid particles leaving at the top and returning them to the bottom of the column through a recirculation system (Lim et al., 1995).

A typical configuration for a circulating fluidized bed reactor is shown schematically in Figure 2.4. It consists of a riser, a gas-solid separator called cyclone, a downcomer or standpipe and a return system such as loopseal, seal pot and L-valve. In the riser, the solid particles are introduced into the column usually at the bottom and elutriated out at the top. Most of the chemical reaction occurs in this reactor section. In the cyclone, the entrained solid particles are separated from a gas stream by a radial centrifugal force exerted on solid particles. This force splits the solid particles from the gas by throwing the solid particles to the cyclone wall where they fall to the bottom outlet and being collected. In the downcomer or standpipe, the solid particles flow from the lower pressure region near the outlet of the circulating fluidized bed to a higher pressure region at the bottom where small amount of gas may inject to assist the circulation of the solid particles. Finally, the solid particles are sent back to the riser by the return system. There are two types of return system which are categorized by whether the solid particles are automatically transferred back to the riser (such as loopseal and seal pot) or whether the solid particles flow into the riser is controlled by a valve (such as L-valve). About the fluidization flow regime in circulating fluidized bed, most of them are now generally operated under fast fluidization regime (Das et al., 2008; Breault et al., 2009).

2.5. Studies on hydrodynamics and mass transfer in fluidized beds

As already stated, a large number of circulating fluidized bed reactors have been employed especially in the fast fluidization regime and since the key features of circulating fluidized bed result from the gas-solid suspension flow in the riser, this topic hence mainly concentrates on the previous studies on hydrodynamics and mass transfer in the fast fluidization regime of a circulating fluidized bed riser.

2.5.1. Hydrodynamics

Hydrodynamics of a circulating fluidized bed deals with the dynamics phenomena of gas-solid suspensions. From a scientific aspect, the nature characteristic of gas-solid suspensions should be the essential point of interest. From an engineering aspect, the major hydrodynamics issues are the effects of such design factors, as well as operating conditions, on the reactor performance. Currently, both of these aspects are interested on the macroscopic viewpoint. Only few researches are focused on the microscopic viewpoint such as the understanding about the fundamental parameters those described the system hydrodynamics.

Wang et al. (1995) conducted an experiment in circulating fluidized bed riser to investigate effect of operating temperature on the solids mass flux distribution. As the operating temperature increased, the reduced solids mass flux profile (local solids mass flux divided by cross-sectional mean solids mass flux) became flatter and less parabolic in shape. They suggested that this situation is mainly due to the change in the viscosity of the fluidizing medium gas. The increase in operating temperature would increase gas viscosity, increasing drag force, reducing mean slip velocity, increasing mean solid particles velocity and hence reducing mean suspension density.

Xu et al. (2000) studied the hydrodynamics dependence on circulating fluidized bed riser diameter for two different kinds of solid particles. Three risers with the same height but different diameters were employed. Solid particles of FCC and silica sand were used, which belong to groups A and B of Geldart classification, respectively. In their study, it was found that the riser diameter had opposite influences for Geldart

group A and B particles on the apparent solids concentration. With increasing riser diameter, the apparent solids concentration decreased for Geldart group A but increased for Geldart group B particles. They stated that this difference is due to the bubble effects for Geldart group B particles. If gas velocity is raised to higher values, the riser diameter influence would be the same as for Geldart group A particles.

Therdthianwong et al. (2003) proposed the methods to improve the performance of catalytic ozone decomposition reaction in circulating fluidized beds by studying the effect of operating parameters of the system which were solid catalyst density and reactor configuration. Their results showed that increasing solid catalyst density increased the reaction conversion. The low density catalyst can generally be carried up easier than the high density catalyst and thus is less chance of low density catalyst to occur the chemical reaction. In addition, the reactor with baffles can enhance the radial gas-solid mixing, thereby increasing ozone decomposition conversion.

Jiradilok et al. (2007) calculated the radial and axial solid dispersion coefficients in turbulent and bubbling fluidizations using the autocorrelation technique of turbulent solid velocity. Their results showed that the radial solid dispersion coefficients in turbulent fluidization were two to three orders of magnitude lower than the axial solid dispersion coefficients, but less than an order of magnitude lower for the bubbling fluidization. They suggested that the reported variations in the solid dispersion coefficients may be due to the geometrical effect of the risers and the bubbling beds.

Zhang et al. (2009) estimated the axial solid dispersion coefficient in fluidized beds of FCC particle using the data obtained in a steady state gas tracer experiment. Both baffle-free and baffled fluidized beds were tested in a two-dimensional cold model column. The results showed the axial solid dispersion coefficient of baffle-free fluidized bed ranged from 0.01 to 0.13 m^2/s. Besides, the results in baffled fluidized beds showed that the axial solid dispersion coefficient was significantly reduced when multilayer louver baffles were inserted in the bed, demonstrating louver baffle's strong suppression on solid particles backmixing.

2.5.2. Mass transfer

Mass transfer is the phrase commonly used for physical processes that involve diffusive and convective transport of atoms and molecules within physical systems. The driving force for mass transfer is a difference in concentration. The amount of mass transfer can be quantified through the calculation of mass transfer coefficient or its dimensionless called the Sherwood number. The information on the mass transfer is now required in order to improve the performance of the circulating fluidized bed reactor.

Schoenfelder et al. (1996) developed the numerical model to study the catalytic ozone decomposition reaction in circulating fluidized bed riser. The axial and radial gradients of the ozone concentration were observed under all of their operating conditions. They also reported that near the gas distributor extremely low ozone concentrations were found adjacent to the wall, whereas the total ozone conversion was rather low. As a consequence, they summarized that the circulating fluidized bed riser exhibits significant mass transfer limitations.

Bolland and Nicolai (2001) conducted an experiment in the riser section of a gas-solid circulating fluidized bed. In order to experimentally investigate mass transfer behavior, a suitable low temperature ozone decomposition reaction was applied. The ozone concentration, axial pressure, net solid mass flux as well as solid particle velocity profiles were measured and the relations between these measured variables with the chemical reaction were discussed. Also, the importance of the lower part of the circulating fluidized bed riser with respect to mass transfer was shown similar to the results by Schoenfelder et al. (1996).

Gamwo et al. (2005) simulated the slurry bubble column for converting synthesis gas into liquid fuels. Their computer model was extended to include the effect of the mass transfer coefficient between the liquid and gas and the chemical reaction. In the model, the mass transfer coefficient was an input. It was estimated from a relationship between the fundamental equations of the boundary layers and the solid

turbulent kinetic energy (granular temperature) that was computed by the hydrodynamic model with no chemical reaction. The estimated mass transfer coefficient had a good agreement with the literature values. Their model was then used to determine the optimum solid particle size for the chemical reaction.

Breault (2006) reviewed the state of the art of mass transfer coefficients. Six investigators had reported correlations for the mass transfer coefficient in fluidized systems from research spanning fifty years. The correlation by Gunn (1978) fitted with their data as well as agreed with the other literature for large solid particle experiments. While, for small solid particles, Zabrodsky (1966) showed that the mass transfer coefficient is several orders of magnitude smaller than the diffusion limit. This low Sherwood number is analogous to the low Nusselt number in heat transfer observed by Turton and Levenspiel (1989).

Shuyan et al. (2009) analyzed the interphase heat and mass transfer characteristics in a circulating fluidized bed riser over the stationary isolated and the cluster of naphthalene particles. Distributions of gas concentration, temperature and velocity were obtained. These data then used to compute the heat and mass transfer coefficients using simple convective heat and mass transfer equations, respectively. For the isolated particle, present results reasonably agreed with data found in the reported heat and mass correlations. For the cluster of solid particles, the heat and mass transfers were affected by its neighboring solid particles. Each solid particle inside the cluster had different temperature and concentration due to the heat and mass transfer among the particles inside the cluster being simulated sequentially. The driving force of the different temperature for heat transfer and concentration for mass transfer decreases as ones move from the first to the second solid particles.

Table 2.1 The various transition velocities for the solid particles used in this study.

Solid particle (-)	FCC	Sand	Polyethylene (dilute condition)	Polyethylene (dense condition)
u_{mf} (m/s)	0.004	0.02	0.16	0.16
u_{mb} (m/s)	0.008	-	-	-
u_{c} (m/s)	0.52	0.79	0.90	0.90
u_{k} (m/s)	1.16	1.71	1.89	1.89
u_{t} (m/s)	0.45	-	-	-
u_{tr} (m/s)	1.83	2.49	2.47	2.47
u_{mp} (m/s)	14.98	8.36	8.24	10.24
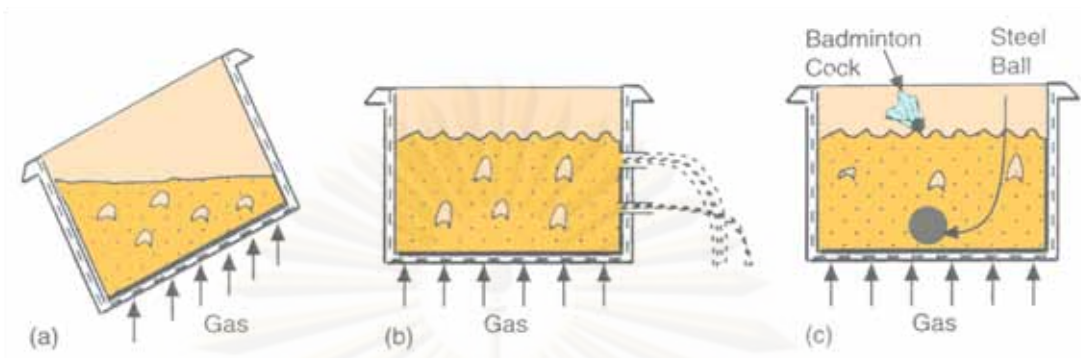
Figure 2.1 Characteristics of a fluidized bed (Basu, 2006).
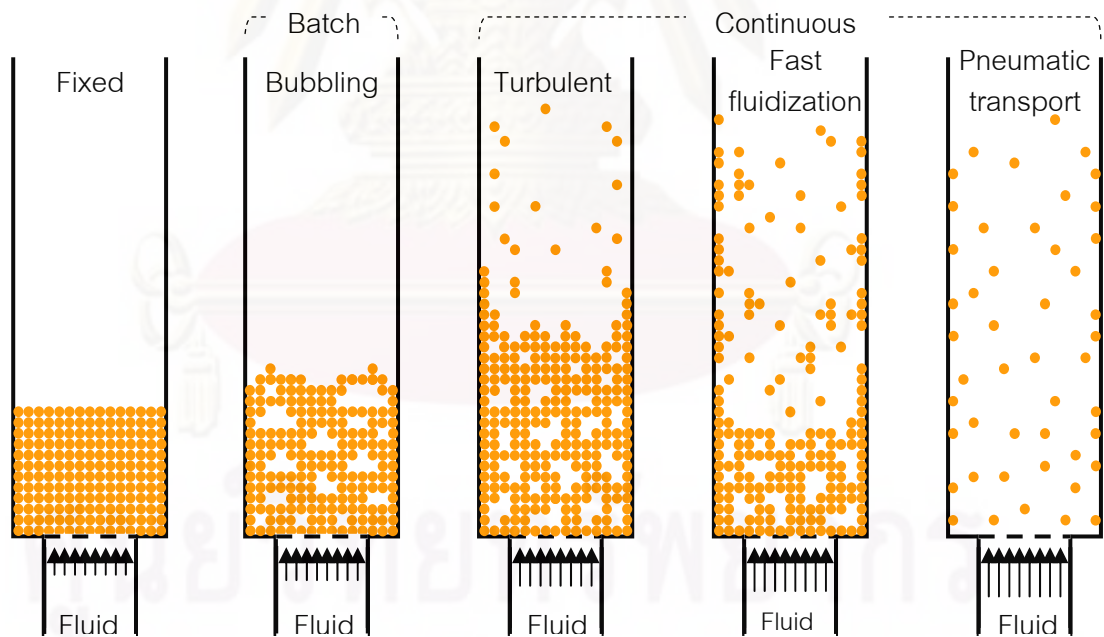
Figure 2.2 Fluidization flow regimes in gas-solid fluidized bed (Grace et al., 1997).
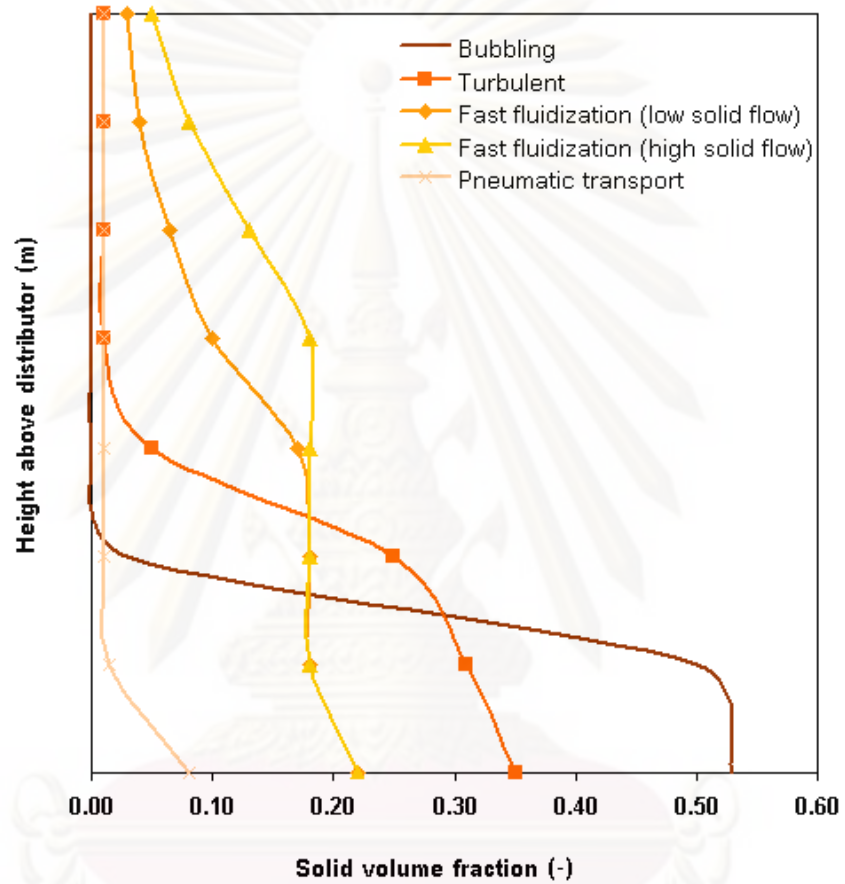
Figure 2.3 Typical solid volume fraction distributions in each fluidization flow regimes
(Kunii and Levenspiel, 1991).
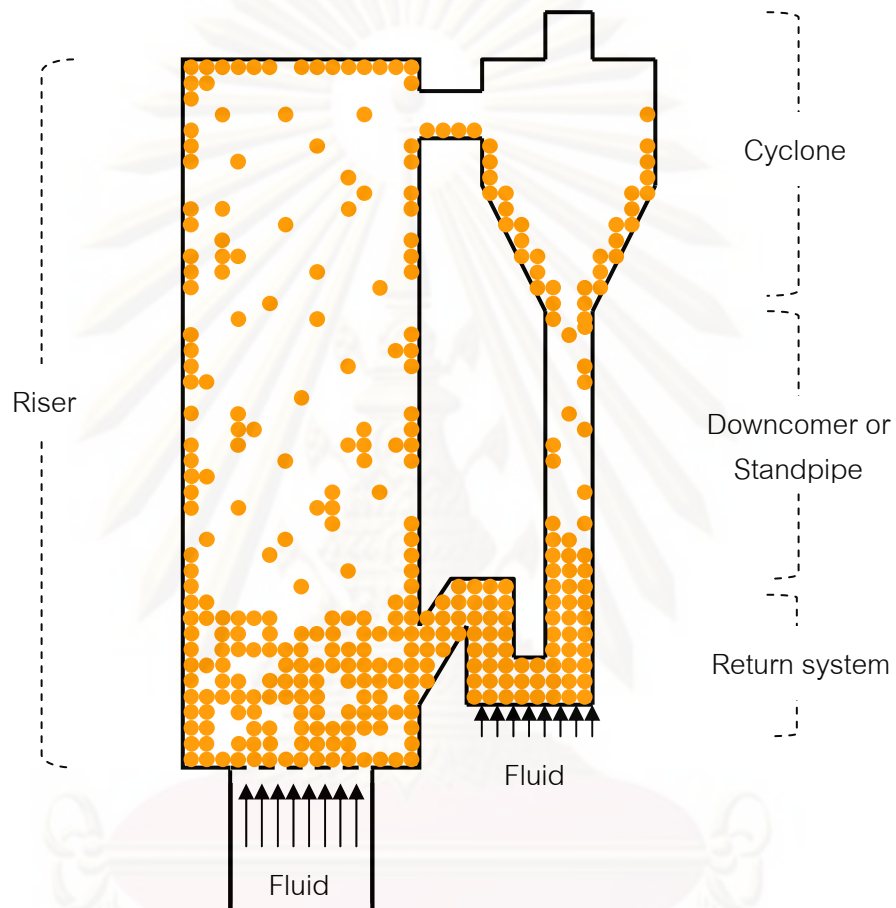
Figure 2.4 Typical configuration for circulating fluidized bed reactor (Grace et al., 1997).

CHAPTER III

THEORETICAL DESCRIPTION OF KINETIC THEORY BASED
COMPUTATIONAL FLUID DYNAMICS MODEL

3.1. Introduction

Computational fluid dynamics is one of the branches of fluid mechanics that uses mathematical or numerical methods and computer algorithms to solve and analyze problems that involve fluid and chemically reacting flows. It is now an emerging technique as can be seen by its many advantages. The computational fluid dynamics gives the virtually visualization inside the design which is difficult to test through experimentation and quickly predicts how the design will perform under various operating conditions. It then helps us save money, meet environmental regulations and ensure industry compliance. There are many successful examples that used computational fluid dynamics to improve the performance of a design in real world industries (Barthod et al., 1999; Stopford, 2002; Gentric et al., 2005; Raynal et al., 2009).

For gas-solid fluidized bed or multiphase flow systems, two difference computational fluid dynamics modeling approaches might be used for the calculation which are the Lagrangian and the Eulerian approaches. The Lagrangian approach calculates the path and motion of each solid particle. The drawbacks of the Lagrangian approach hence are the large memory requirements and the long calculation time. The Eulerian approach treats the solid particle phase as a continuum and averages out motion on the scale of individual solid particles, thus enabling computation by this method to treat the system at realistic size and time. As a result, the Eulerian approach is the appropriate approach for performing multiphase flow studies. Among the various attempts to closure the solid particle properties for Eulerian approach, the kinetic theory of granular flow has found the widest use as a constitutive equation (Gidaspow, 1994; Goldschmidt et al., 2001; Huilin et al., 2003; Jiradilok et al., 2006; Almuttahar and Taghipour, 2008a). This theory is basically an extension of the classical kinetic theory of gases proposed by Chapman and Cowling (1970) to dense gas-solid flows.

This chapter provides a theoretical description of computational fluid dynamics model with the kinetic theory of granular flow concept. Two approaches for multiphase computational fluid dynamics modeling are summarized in detail. Then, the conservation and constitutive equations for the appropriate Eulerian approach are fully discussed. For solid particle phase properties, the well-known kinetic theory of granular flow model is presented. In addition, the previous studies on computational fluid dynamics model in fluidized beds are reviewed. About the numerical solvers and methodologies how the computational fluid dynamics model is solved, it can be found in the Appendix B.

3.2. Approaches for multiphase computational fluid dynamics modeling

Advances in computational fluid mechanics have provided the basis for further insight into the dynamics of multiphase flows. Currently, there are two main multiphase computational fluid dynamics modeling approaches (Ranade, 2002).

3.2.1. The Eulerian-Lagrangian or Lagrangian approach

In the Eulerian-Lagrangian or Lagrangian approach, the continuous phase is modeled using an Eulerian framework while the dispersed phase is explicitly simulated using a Lagrangian framework. Then, the gas phase is treated as a continuum by solving the Navier-Stokes equations and the solid particle phase is solved by tracking a large number of Newtonian equations of motion for each solid particle through the calculated flow field. In this approach, the solid particle phase can exchange momentum, mass and energy with the gas phase and the mechanism of solid particle collision laws can be described by soft-sphere and hard-sphere models (Crowe et al., 1997). In the soft-sphere model, the collisions between solid particles and between solid particle and wall are simulated using Hooke's linear spring, dash pot and friction slider (Cundall and Strack, 1979; Tsuji et al., 1993). On the other hand, in the hard-sphere model, those collisions are taken into account for non-ideal particle interactions with friction by means of empirical coefficients which are restitution, Coulomb friction and tangential restitution (Campbell and Brennen, 1985; Wang and Mason, 1992).

Because a large number of solid particle trajectories must be calculated in order to determine the average behavior of the system, the drawbacks of the Lagrangian approach are the large memory requirements and the long computational time (Grace et al., 1997). Therefore, a fundamental assumption made for this approach is that the solid particle phase should occupy a low volume fraction (gas-solid dilute flow or solid volume fraction < 12%). This makes the model appropriate for the modeling of bubbly, droplet and particle-laden (discrete solid particles in a gas phase) flows, but inappropriate for the modeling of fluidized beds or any application where the volume fraction of the discrete phase is not negligible. However, there are some literature studies in fluidized bed system using this model. It has been used for investigating inter-particle force effect on fluidization characteristics (Kuwagi et al., 2000; Rhodes et al., 2001), mixing and segregation characteristics (Kaneko et al., 1999; Limtrakul et al., 2003) and particle residence time (Wang and Rhodes, 2003). For more information about this approach, it can be found in the literature by Deen et al. (2007).

3.2.2. The Eulerian-Eulerian or Eulerian approach

In the Eulerian-Eulerian or Eulerian approach, the continuous or gas phase and the dispersed or solid particle phase are treated mathematically as interpenetrating continuum via the Navier-Stokes equations. Coupling between the phases is achieved through the pressure and interphase exchange coefficients (momentum, heat and mass). Besides, the Eulerian approach requires additional closure laws to describe the rheology of the solid particles owing to the continuum representation of the solid particle phase. Up to now, the constitutive equations according to the viscosity and kinetic theory of granular flow models are incorporated. The viscosity model gives the solid particle closure based on empirical correlations and experimental values such as solid stress modulus, solid pressure and solid viscosity (Miller and Gidaspow, 1992; Sun and Gidaspow, 1999). On the other hands, the kinetic theory of granular flow model provides explicit closures that take energy dissipation due to inelastic solid particle collisions into account by means of the restitution coefficients (Huilin and Gidaspow, 2003; Jiradilok et al., 2006).

This Eulerian approach can be applied to multiphase flow process containing large volume fraction of dispersed solid particles (gas-solid dense flow) with a relatively small computational effort because it treats the phases as a continuum. Since the volume of a phase cannot be occupied by the other phases, the concept of physic volume fraction is introduced. These volume fractions are assumed to be continuous functions of space and time. Then, the conventional conservation equations for each phase are developed to obtain a set of equations which include the volume fraction interpretation (Gidaspow, 1994; van Wachem et al., 2001). Applications of the Eulerian approach include fluidized beds or other particle suspension columns. There are many literature studies in fluidized bed system using this approach. It has been used for investigating operating condition effect (Mathiesen et al., 2000; Almuttahar and Taghipour, 2008a) and design condition effect (Benyahia et al., 2000; Huilin et al., 2006) on fluidization or characteristics. In the following topic, the mathematical model that utilized this approach is reviewed.

3.3. The Eulerian model

The Eulerian or two-fluid model follows the Eulerian-Eulerian or Eulerian approach. The main governing equations are called conservation equations which consisting of mass and momentum equations for cold flow model (the model without heat transfer or chemical reaction). For hot flow model (the model with heat transfer or chemical reaction), the energy and specie equations are also included as conservation equations. These conservation equations are expressions of the physics laws, written in appropriate forms for flows. They are all based on the consideration of the flux of each state variable flowing into and out of the considered region. If the system has more than one solid particle, each solid particle will define as a phase and need its own equations. The constitutive equations are coupling with the conservation equations to solve the gas and solid particle properties. The conservation and constitutive equations for each phase of this study system are summarized below. To obtain more detail about how each conservation and constitutive equations are derived, it can be referred to the multiphase flow text book written by Gidaspow (1994).

3.3.1. Conservation equations

In this study, the systems are two-dimensional Cartesian coordinate (x- and y- directions) fluidized beds with one gas and one solid particle phase.

- The mass conservation equations

The accumulation of mass in each phase is balanced by the convective mass fluxes. Mass exchanges between the phases, such as due to sublimation or vaporization, are not considered.

For gas phase:

$$\frac{\partial}{\partial t}\left(\varepsilon_g \rho_g\right) + \nabla \cdot \left(\varepsilon_g \rho_g v_g\right) = 0 \tag{3.1}$$

For solid particle phase:

$$\frac{\partial}{\partial t}\left(\varepsilon_s \rho_s\right) + \nabla \cdot \left(\varepsilon_s \rho_s v_s\right) = 0 \tag{3.2}$$

where ε_g is the volume fraction of the gas phase, ε_s is the volume fraction of the solid particle phase, ρ_g is the density of the gas phase, ρ_s is the density of the solid particle phase, v_g the velocity of the gas phase, v_s the velocity of the solid particle phase and t is the time.

- The momentum conservation equations

The accumulation of momentum in each phase is balanced by the convective momentum fluxes and the related forces inside the system which are the forces due to pressure, stress tensor, gravity and momentum interphase exchange coefficient.

For gas phase:

$$\frac{\partial}{\partial t}\left(\varepsilon_g \rho_g v_g\right) + \nabla \cdot \left(\varepsilon_g \rho_g v_g v_g\right) = -\varepsilon_g \nabla p + \nabla \cdot \tau_g + \varepsilon_g \rho_g g - \beta_{gs}\left(v_g - v_s\right)$$

$$\tag{3.3}$$

For solid particle phase:

$$\frac{\partial}{\partial t}\left(\varepsilon_s \rho_s v_s\right) + \nabla \cdot \left(\varepsilon_s \rho_s v_s v_s\right) = -\varepsilon_s \nabla p - \nabla p_s + \nabla \cdot \tau_s + \varepsilon_s \rho_s g + \beta_{gs}\left(v_g - v_s\right)$$

(3.4)

where p is the pressure of the gas phase, p_s is the pressure of the solid particle phase, τ_g is the stress tensor of the gas phase, τ_s is the stress tensor of the solid particle phase, g is the gravity forces and β_{gs} is the momentum interphase exchange coefficient.

- The energy conservation equations

To describe the energy conservation equations, a separate enthalpy equation can be written for each phase. The accumulation of energy in each phase is balanced by the convective energy fluxes, the work due to pressure or volume changes, the heat source due to viscous dissipation (stress) and conduction and the intensity of heat exchange between the phases.

For gas phase:

$$\frac{\partial}{\partial t}\left(\varepsilon_g \rho_g h_g\right) + \nabla \cdot \left(\varepsilon_g \rho_g v_g h_g\right) = -\varepsilon_g \frac{\partial p}{\partial t} + \tau_g : \nabla \cdot v_g - \nabla \cdot q_g - Q_{sg}$$

(3.5)

with $h_g = \int c_{p,g} dT_g$

For solid particle phase:

$$\frac{\partial}{\partial t}\left(\varepsilon_s \rho_s h_s\right) + \nabla \cdot \left(\varepsilon_s \rho_s v_s h_s\right) = -\varepsilon_s \frac{\partial p_s}{\partial t} + \tau_s : \nabla \cdot v_s - \nabla \cdot q_s + Q_{sg}$$

(3.6)

with $h_s = \int c_{p,s} dT_s$

where h_g is the specific enthalpy of the gas phase, h_s is the specific enthalpy of the solid particle phase, $c_{p,g}$ is the heat capacity of the gas phase, $c_{p,s}$ is the heat capacity of the solid particle phase, T_g is the temperature of the gas phase, T_s is the temperature of the solid particle phase, q_g is the heat conduction flux of the gas phase, q_s is the heat conduction flux of the solid particle phase and Q_{sg} is the intensity of heat exchange between the phases.

- The specie conservation equations

The multiphase flow with chemical reaction can be divided into two categories depends on the role of the solid particles which are catalyst or medium and reactant. In this study, the solid particles are catalyst or medium hence only specie conservation equations for gas phase are required. If the solid particles are reactant, the specie conservation equations for solid particle phase are also needed. The mass accumulation of i specie is balanced by the convective mass fluxes of i specie, the diffusive mass fluxes of i specie and the homogeneous and heterogeneous chemical reactions of i specie inside the system.

For gas phase:

$$\frac{\partial}{\partial t}\left(\varepsilon_g \rho_g y_i\right) + \nabla \cdot \left(\varepsilon_g \rho_g v_g y_i\right) = -\nabla \cdot \varepsilon_g J_i + r_i + \varepsilon_g R_i \qquad (3.7)$$

where y_i is the mass fraction of i specie in the gas phase, J_i is the diffusive mass fluxes of i specie in the gas phase (can be substituted by Fick's first law), r_i is the net heterogeneous reaction rate of i specie and R_i is the net homogeneous reaction rate of i specie in the gas phase. However, the diffusive mass fluxes term in the following chapter of this study can be considered as a neglected term because the radial concentration gradients are extremely low (plug flow assumption). Furthermore, the significance of axial diffusion decreases with the increasing gas velocity except for $Re < 1$ (Bolland, 1998; Bolland and Nicolai, 2001). Then, Equation (3.7) takes the form:

$$\frac{\partial}{\partial t}\left(\varepsilon_g \rho_g y_i\right) + \nabla \cdot \left(\varepsilon_g \rho_g v_g y_i\right) = r_i + \varepsilon_g R_i \qquad (3.8)$$

3.3.2. Constitutive equations

Here, the general constitutive equations are summarized. Then, two widely used concepts for the specific constitutive equations of solid phase properties are discussed which are the viscosity and kinetic theory of granular flow models.

- The volume fractions

The description of multiphase flow incorporates the concept of physic volume fractions which represent the space occupied by each phase. These volume fractions are assumed to be continuous function with space and time. The summation of the volume fractions for all the phases must equal one:

$$\varepsilon_g + \varepsilon_s = 1 \tag{3.9}$$

- The stress tensors

The stress is a measure of the average amount of force exerted per unit area of a surface within a deformable body on which internal forces act. In other words, it is a measure of the intensity of the total internal forces acting within a deformable body. The stress tensors of gas and solid particle phases can be represented as:

For gas phase:

$$\tau_g = \varepsilon_g \mu_g \left[\left(\nabla v_g \right) + \left(\nabla v_g \right)^T \right] - \frac{2}{3} \varepsilon_g \mu_g \left(\nabla \cdot v_g \right) I \tag{3.10}$$

For solid particle phase:

$$\tau_s = \varepsilon_s \mu_s \left[\left(\nabla v_s \right) + \left(\nabla v_s \right)^T \right] - \varepsilon_s \left(\xi_s - \frac{2}{3} \mu_s \right) \left(\nabla \cdot v_s \right) I \tag{3.11}$$

where μ_g is the viscosity of the gas phase, μ_s is the shear viscosity of the solid particle phase, ξ_s is the bulk viscosity of the solid particle phase and I is the unit tensor. In the following chapters, these general stress tensors have been proved to be used for fluidized bed reactor simulation.

- The momentum interphase exchange coefficients

The momentum interphase exchange coefficient is a quantity which is used to quantify the drag or resistance of a solid particle in a gas environment. It is typically obtained experimentally from pressure drop measurements in fixed and fluidized or settling beds. Ergun (1952) performed measurements in fixed beds at packed conditions to determine the pressure drop. Wen and Yu (1966) conducted settling experiments of solid particles over a wide range of solid volume fractions and correlated their data and those of others to obtain the momentum interphase exchange coefficient. Until now, there are many momentum interphase exchange coefficient models such as Wen and Yu model (1966) and Syamlal-O'Brien model (1989). In this study, two models which are the classical and the modified ones are selected to use.

Classical momentum interphase coefficient or Gidaspow model (Gidaspow, 1994) is a combination of the Ergun equation and the Wen and Yu model. The Gidaspow model follows Ergun equation for gas volume fractions equal or lower than 0.8 and Wen and Yu model for gas volume fractions higher than 0.8. This model is recommended for dense gas-solid fluidized beds (FLUENT Inc., 2005a).

For $\varepsilon_g \leq 0.8$:

$$\beta_{gs} = 150 \frac{(1-\varepsilon_g)^2 \mu_g}{\varepsilon_g d_p^2} + 1.75 \frac{(1-\varepsilon_g)\rho_g |v_g - v_s|}{d_p} \tag{3.12}$$

For $\varepsilon_g > 0.8$:

$$\beta_{gs} = \frac{3}{4} \frac{(1-\varepsilon_g)\varepsilon_g}{d_p} \rho_g |v_g - v_s| C_{D0} \varepsilon_g^{-2.65} \tag{3.13}$$

with $Re < 1000$; $C_{D0} = \frac{24}{Re}(1 + 0.15 Re^{0.687})$; $Re = \frac{\varepsilon_g \rho_g d_p |v_g - v_s|}{\mu_g}$

$Re \geq 1000$; $C_{D0} = 0.44$

where C_{D0} is the drag function.

Modified momentum interphase coefficient or energy minimization multi-scale (EMMS) model (Yang et al., 2003, 2004) is a combination of the Ergun equation and the modified Wen and Yu model. The energy minimization multi-scale model follows Ergun equation for gas volume fractions equal or lower than 0.74 and modified Wen and Yu model for gas volume fractions higher than 0.74. This model is corrected to account for particle cluster formation of fine solid particles inside the fluidized beds (Naren et al., 2007). The concept of the energy minimization multi-scale model is to include the effect of heterogeneous structure parameters in the momentum interphase coefficient model. The gas and solid particles are considered to be either in the particle-rich dense phase or in the gas-rich dilute phase. The mechanisms of gas-solid interactions then can be analyzed for different scales: the interaction between a single solid particle and the nearby gas inside both dense and dilute phases (micro-scale) and the interaction between particle cluster and the surrounding for both dilute and dense phases (meso-scale). The drag force is calculated from these three interactions as follows:

$$F_{drag} = M_c F_{dense} + M_f F_{dilute} + M_i F_{cluster} \qquad (3.14)$$

where F_{drag} is the drag force, F_{dense} is the drag force acting on solid particle inside the dense phase, F_{dilute} is the drag force acting on solid particle inside the dilute phase, $F_{cluster}$ is the drag force acting on particle cluster inside the dilute and dense phases, M_c is the number of solid particle per unit volume inside the dense phase, M_f is the number of solid particle per unit volume inside the dilute phase and M_i is the number of particle cluster per unit volume inside the dilute and dense phases. For the macro-scale, it encompasses the global system of the gas-solid suspension within its boundaries. Therefore, this scale of interaction already includes by the effect of boundaries. With these assumptions, the momentum interphase coefficient model can be formulated as a non-linear optimization problem which is based on the postulate of minimum energy consumption for suspension and transport of gas-solid suspension. Since it is too time consuming to solve this optimization problem for each iteration, the problem is solved once for the considered operating conditions and the momentum exchange coefficient model is obtained depending on the solids volume fraction:

For $\varepsilon_g \leq 0.74$:

$$\beta_{gs} = 150 \frac{\left(1-\varepsilon_g\right)^2 \mu_g}{\varepsilon_g d_p^{\,2}} + 1.75 \frac{\left(1-\varepsilon_g\right)\rho_g \left|v_g - v_s\right|}{d_p} \tag{3.15}$$

For $\varepsilon_g > 0.74$:

$$\beta_{gs} = \frac{3}{4} \frac{\left(1-\varepsilon_g\right)\varepsilon_g}{d_p} \rho_g \left|v_g - v_s\right| C_{D0}\,\omega\!\left(\varepsilon_g\right) \tag{3.16}$$

with $\quad 0.74 < \varepsilon_g \leq 0.82$; $\omega\!\left(\varepsilon_g\right) = -0.5769 + \dfrac{0.0214}{4\!\left(\varepsilon_g - 0.7463\right)^2 + 0.0044}$

$0.82 < \varepsilon_g \leq 0.97$; $\omega\!\left(\varepsilon_g\right) = -0.0101 + \dfrac{0.0038}{4\!\left(\varepsilon_g - 0.7789\right)^2 + 0.0040}$

$\varepsilon_g > 0.97$; $\omega\!\left(\varepsilon_g\right) = -31.8295 + 32.8295\varepsilon_g$

where $\omega\!\left(\varepsilon_g\right)$ is the correction factor. Yang et al. (2004) mentioned that the correction factor in this model is much smaller than that computed in Wen and Yu model, which is reasonable agreement with the observation from experimental results that the drag coefficient decreases dramatically due to the formation of particle clusters.

- The heat conduction fluxes

The heat conduction is the transfer of thermal energy between neighboring molecules in a same substance due to a temperature gradient. By using Fourier's law, the heat conduction fluxes of gas and solid particle phases can be written as:

For gas phase:

$$q_g = -\varepsilon_g k_g \nabla T_g \tag{3.17}$$

For solid particle phase:

$$q_s = -\varepsilon_s k_s \nabla T_s \tag{3.18}$$

where k_g is the thermal conductivity of the gas phase and k_s is the thermal conductivity of the solid particle phase.

- The heat exchange between the phases

The heat exchange between the phases or heat convection is the transfer of thermal energy between a solid surface and the nearby motion gas. This can be contrasted with heat conduction, which is the transfer of energy by vibrations at a molecular level. The heat exchange between the phases can be defined as:

$$Q_{sg} = h_{sg}\left(T_s - T_g\right) \tag{3.19}$$

with

$$h_{sg} = \frac{6k_g \varepsilon_s \varepsilon_g Nu_s}{d_p^2} \text{ and from Gunn's correlation;}$$

$$Nu_s = \left(7 - 10\varepsilon_g + 5\varepsilon_g^2\right)\left(1 + 0.7 Re_s^{0.2} Pr^{1/3}\right) + \left(1.33 - 2.4\varepsilon_g + 1.2\varepsilon_g^2\right)Re_s^{0.7} Pr^{1/3}$$

$$Re_s = \frac{\rho_g d_p \left|v_s - v_g\right|}{\mu_g}$$

$$Pr = \frac{c_{p,g} \mu_g}{k_g}$$

where h_{sg} is the heat transfer coefficient between the phases.

- The viscosity model concept

The viscosity model is one of the models to use as constitutive equations for solid particle properties in the multiphase modeling. The solid modulus, solid pressure and solid viscosity based on empirical correlations and experimental values are employed in this model. There are many investigators defined the solid modulus and solid viscosity correlations as a function of the gas phase volume fraction (Tsuo and Gidaspow, 1990; Miller and Gidaspow, 1992; Sun and Gidaspow, 1999). The solid pressure is then based on the obtained solid modulus. The requirement of these input correlations therefore is the shortcoming of the utilization of this viscosity model.

- The kinetic theory of granular flow model concept

The kinetic theory of granular flow model is basically an extension of the classical kinetic theory of gases proposed by Chapman and Cowling (1970) to dense gas-solid flows, with describing the inelastic solid particle collisions by means of the restitution coefficients. Constitutive equations for this model were developed by Lun et al. (1984) using a methodology analogous to the methods employed in deriving the Chapman-Enskog dense gas kinetic theory. This model is more advantage than the viscosity model because the solid pressure and solid viscosity are estimated by solving solid fluctuating kinetic energy or granular temperature equation which is obtained by subtracting the mechanical energy balance from the total energy balance. As a result, there is no need for an empirical correlations or experimental values. Such a solid fluctuating kinetic energy equation can be predicted by solving with the mass, momentum and energy equations. Then, the solid pressure and viscosity can be computed as a function of granular temperature and the interactions due to solid particle collisions (Gidaspow, 1994). Because there is no requirement of the empirical correlations, the kinetic theory of granular flow model has found the widest use as a constitutive equation. Therefore, it was selected to use in this study. The constitutive equations from this kinetic theory of granular flow model are summarized in the next topic.

3.4. The kinetic theory of granular flow model

- The solid fluctuating kinetic energy or granular temperature

The granular temperature for the solid particle phase is proportional to the fluctuating kinetic energy of the random motion of the solid particles. The solid fluctuating kinetic energy transport equation derived from kinetic theory of granular flow takes the form:

$$\frac{3}{2}\left[\frac{\partial}{\partial t}(\varepsilon_s \rho_s \theta) + \nabla \cdot (\varepsilon_s \rho_s v_s \theta)\right] = (-p_s I + \tau_s) : \nabla v_s + \nabla \cdot (\kappa_s \nabla \theta) - \gamma_s + \phi_s$$

(3.20)

where θ is the solid fluctuating kinetic energy or granular temperature, κ_s is the conductivity of solid fluctuating kinetic energy, γ_s is the collisional dissipation of solid fluctuating kinetic energy and ϕ_s is the exchange of solid fluctuating kinetic energy between phases.

- The solid pressure

The solid pressure is composed of a kinetic term that dominates in the dilute regions and a second term due to particle collisions that is significant in the dense regions:

$$p_s = \varepsilon_s \rho_s \theta [1 + 2g_0 \varepsilon_s (1+e)] \tag{3.21}$$

where g_0 is the radial distribution function and e is the particle-particle restitution coefficient.

- The solid shear viscosity

The solid shear viscosity is also composed of a kinetic and a collisional terms arising from particle momentum exchange due to translation and collision:

$$\mu_s = \frac{4}{5} \varepsilon_s \rho_s d_p g_0 (1+e) \sqrt{\frac{\theta}{\pi}} + \frac{10 \rho_s d_p \sqrt{\pi \theta}}{96(1+e)g_0 \varepsilon_s} \left[1 + \frac{4}{5} g_0 \varepsilon_s (1+e) \right]^2 \tag{3.22}$$

- The solid bulk viscosity

The solid bulk viscosity accounts for the resistance of the granular solid particles to compression and expansion:

$$\xi_s = \frac{4}{3} \varepsilon_s \rho_s d_p g_0 (1+e) \sqrt{\frac{\theta}{\pi}} \tag{3.23}$$

- The radial distribution function

The radial distribution function is a correction factor that modifies the probability of collisions between solid particles when the solid particles become dense:

$$g_0 = \left[1 - \left(\frac{\varepsilon_s}{\varepsilon_{s,max}} \right)^{1/3} \right]^{-1}$$

(3.24)

where $\varepsilon_{s,max}$ is the volume fraction of the solid particle phase at maximum packing.

- The conductivity of solid fluctuating kinetic energy

The conductivity of solid fluctuating kinetic energy describes the diffusion of granular energy:

$$\kappa_s = \frac{150 \rho_s d_p \sqrt{\theta \pi}}{384(1+e)g_0} \left[1 + \frac{6}{5} \varepsilon_s g_0 (1+e) \right]^2 + 2 \rho_s \varepsilon_s^2 d_p (1+e) g_0 \sqrt{\frac{\theta}{\pi}}$$

(3.25)

- The collisional dissipation of solid fluctuating kinetic energy

The collisional dissipation of solid fluctuating kinetic energy represents the rate of energy dissipation within the solid particle phase due to collisions between solid particles:

$$\gamma_s = 3\left(1-e^2\right)\varepsilon_s^2 \rho_s g_0 \theta \left(\frac{4}{d_p} \sqrt{\frac{\theta}{\pi}} \right)$$

(3.26)

- The exchange of solid fluctuating kinetic energy between phases

The transfer of solid fluctuating kinetic energy from the solid particle phase to gas phase is defined by:

$$\phi_s = -3\beta_{gs}\theta$$

(3.27)

3.5. Studies on computational fluid dynamics model in fluidized beds

Although computational fluid dynamics has a promising future and is anticipated to make valuable contributions to predicting the performance of fluidized bed reactors, currently, there are no universal computational fluid dynamics models available to make appropriate selection of models with a certain gas-solid fluidized bed. Therefore, more attention should be considered in this area. This topic mainly focuses on the previous studies on computational fluid dynamics model in the fast fluidization regime of circulating fluidized bed risers both from the model using viscosity and the kinetic theory of granular flow concepts.

van Wachem et al. (2001) reviewed the gas-solid computational fluid dynamics models in the literature. They stated that these models often differ in terms of both the form of the conservation and the constitutive equations, resulting in much confusion. Then, they performed the simulation with various fluidized bed systems to compare the effects of conservation and constitutive equations. The predictions with different conservation equations and solid stress models or radial distribution functions were very similar. The application of different drag models, however, significantly impacted the gas-solid suspension flow. To explain this situation, they analyzed the individual terms on the momentum conservation equation for the solid particle phase and found that drag and gravity are the most dominating terms.

Cabezas-Gómez and Milioli (2003) studied the influence of various physical aspects over hydrodynamics of gas-solid two-phase flow in the riser of a circulating fluidized bed. An Eulerian continuum formulation was applied for both phases. The addressed features were focused on the solid viscosity and the momentum interphase coefficient correlations. It was observed that for high values of solid viscosity there was an accumulation of solid particles near the outlet forming large particle clusters. For inviscid solid particle phase, no particle cluster formation was observed. Quite different results were obtained for different correlations of momentum interphase coefficient and there was a poor agreement between computed and experimental data. Thus, they suggested that necessity of further studies is required for this correlation.

Huilin et al. (2005) proposed two-fluid model using a cluster-based approach for predicting the flow behaviour of particle clusters in circulating fluidized bed riser. The model was assumed that the solid particles move as particle clusters in the riser rather than identical-sized single solid particles. The particle cluster sizes were estimated from the existing correlations found in the literatures and applied as the constitutive equations. The distributions of pressure drops, solid particle concentrations and both gas and solid particle velocities were predicted. A core-annular flow structure in risers was observed from simulations and the results were in agreement with experimental data.

Cabezas-Gómez et al. (2008) studied methodology for identification and characterization of particle clusters with the hydrodynamic results of numerical simulation generated for the riser of a circulating fluidized bed. The simulation was performed using the two-fluid model and the solid particle properties were computed using the viscosity model. It was shown that the present model caught a smaller particle cluster quantity in comparison to literature experiment. The main reason for these discrepancies is still not yet well understood, indicating the need of more research in this area. They proposed that one possible solution is the use of a more sophisticated numerical model as that based on the kinetic theory of granular flow.

Almuttahar and Taghipour (2008b) carried out a computational fluid dynamics simulation of circulating fluidized bed riser with fluid catalytic cracking particles. The implementation of correct inlet conditions was found to be critical for the successful simulation. The simulated profiles of gas and solid particle velocity were in good agreement with the data in the literature. However, due to the difficulties in accurate modeling, the solid volume fraction was under predicted near the walls. Then, the effects of modeling parameters including different wall restitution coefficient values and solid slip conditions were evaluated. While the wall restitution coefficient did not exhibit a significant effect on the riser hydrodynamics, the appropriate slip condition aided in predicting the solid segregation toward the wall.

CHAPTER IV

KINETIC THEORY BASED COMPUTATION OF FAST FLUIDIZATION REGIME IN PSRI RISER: PART I - ESTIMATION OF MASS TRANSFER COEFFICIENT WITH PARTICLE CLUSTER CONCEPT

4.1. Introduction

4.1.1. Reduced mass transfer

Conventional fluidized bed reactor design requires knowledge of mass transfer coefficients. Kunii and Levenspiel (1991) has defined two different mass transfer coefficients: the single particle and the overall. The single particle mass transfer coefficient represents the mass transfer between a single particle and fluidizing environment. The overall mass transfer coefficient considers the mass transfer of the overall solid particles by a fluidizing gas. Here, the focus is on the latter point of view due to the impractical to follow a single particle. Transport phenomena textbooks (Kunii and Levenspiel, 1991; Bird et al., 2002) show that the diffusion controlled dimensionless mass transfer coefficient called the Sherwood number or the Nusselt number for related heat convection is two. Indeed for large particles, Gunn (1978) and many investigators before him, e.g. Kato et al. (1970), have shown that the Sherwood number equals two, the diffusion limit, plus a contribution due to convection expressed in terms of Reynolds and Schmidt numbers. Unfortunately for fine particles, it has been known for over a half century (Zabrodsky, 1966) that the mass transfer coefficient is several orders of magnitude smaller than the diffusion limit. Levenspiel (Turton and Levenspiel, 1989) has discussed this problem at several conferences. Recently, Breault (2006) has reviewed the literature and has shown that the mass transfer coefficients differ up to seven orders of magnitude and that a satisfactory model is still not available. One possible explanation for this phenomenon is the formation of particle clusters in fluidized beds. The fluidizing gas must pass through the solid particles inside the particle clusters. The mass transfer coefficient thus accounts for these transfer resistances. Computational fluid dynamics models, e.g. Tsuo and Gidaspow (1990), are now being used to compute

particle clusters in fluidized beds. In such a situation, the particle size becomes the much larger particle cluster size, leading to a greatly reduced mass transfer coefficient.

In this chapter, the kinetic theory based computational fluid dynamics with the modified interphase exchange coefficient model was developed. It can predict the fast fluidization regime in circulating fluidized bed riser and can calculate the Reynolds stresses, energy spectra, power spectra, granular temperatures, solid viscosity, dispersion coefficients and particle cluster properties. The mass transfer coefficient and the Sherwood number were then estimated based on the computed particle cluster diameters. We compute the particle cluster size to be several orders of magnitude larger than the individual particle size, which may explain why the Sherwood number becomes smaller than the diffusion controlled limit based on particle diameter. In the next chapter, we compute the reduced mass transfer coefficient for the circulating fluidized bed riser with chemical reaction concept.

4.1.2. Particle clusters

The occurrence of particle clusters in fluidized beds has been known since Yerushalmi et al. (1976a) first presented the particle cluster hypothesis. Gidaspow et al. (1989) obtained a movie of particle clusters near the wall in a circulating fluidized bed riser. Horio and Kuroki (1994), Tartan and Gidaspow (2004) and Jung et al. (2005) observed the existence of particle clusters in both the bubbling and circulating fluidized beds and found downward moving, stagnant and even upward moving particle clusters. While the occurrence of particle clusters was well accepted, little information was available about the identification and characterization of particle clusters. Soong et al. (1995) developed criteria using statistical methodology to identify particle clusters based on their experimental data. Sharma et al. (2000) used a similar approach as Soong et al. (1995) to study the effect of particle size and superficial gas velocity on particle cluster dynamics. Those dynamics were the mean duration time, the frequency of occurrence, the existence time fraction and the mean solid concentration. Recently, the same criterion has proved to be useful for characterization of particle cluster dynamics from numerical simulation described by Cabezas-Gómez et al. (2008). In

addition, Andrews and Sundaresan (2005) are developing a new methodology to compute particle cluster sizes. They use the concepts of filtering common in the direct numerical simulation of single-phase flow (Kim et al., 1987).

Gu and Chen (1998) summarized the curve fitting correlations from other publications and used them in their numerical simulations. Their results were matched with the literature experimental measurements. They are as follows:

Gu's correlations;

For particle cluster diameter:

$$\overline{d}_{cl} = d_p + \left(0.027 - 10d_p\right)\overline{\varepsilon}_s + 32\overline{\varepsilon}_s^6 \tag{4.1}$$

For particle cluster concentration:

$$\overline{\varepsilon}_{cl} = \varepsilon_{s,max}\left[1 - \left(1 - \frac{\overline{\varepsilon}_s}{\varepsilon_{s,max}}\right)^{3.4}\right] \tag{4.2}$$

where $\varepsilon_{s,max} = 0.60$.

Harris et al. (2002) presented correlations for predicting the properties of cluster of particles traveling near the riser wall. The correlations were developed from experimental data published in the literature for vertical risers ranging from laboratory to industrial scale. They are as follows:

Harris's correlation;

For particle cluster diameter:

$$\overline{d}_{cl} = \frac{\overline{\varepsilon}_s}{40.8 - 94.5\overline{\varepsilon}_s} \tag{4.3}$$

For particle cluster concentration:

$$\overline{\varepsilon}_{cl} = \frac{0.58\overline{\varepsilon}_s^{1.48}}{0.013 + \overline{\varepsilon}_s^{1.48}} \tag{4.4}$$

Figure 4.1 (a) and (b) show the plot of particle cluster diameter and concentration calculated from Gu's and Harris's correlations as a function of average particle concentration or particle solid volume fraction. Both correlations show similar trends of predicted values. The particle cluster diameter and concentration increase with particle concentration for a certain value (Gu and Chen, 1998; Harris et al., 2002). These trends are consistent with the experimental data observed by many researchers.

4.1.3. Particle cluster diameter

A physical definition of particle cluster diameter based on the kinetic theory of granular flow (Gidaspow, 1994) is the radial characteristic length of particles. It can be obtained from the radial diffusivity or the radial dispersion coefficient shown below:

$$Cluster\ diameter = \frac{D_x(r)}{Radial\ oscillating\ velocity} \tag{4.5}$$

where the radial oscillating velocity is obtained from the square root of the radial normal Reynolds stress or the *Radial oscillating velocity* $= \sqrt{\overline{v'_x v'_x}(r)}$. The radial normal Reynolds stress is defined by Equation (4.6) below:

$$\overline{v'_x v'_x(r)} = \frac{1}{l}\sum_1^l \left(v_{x,k}(r,t) - \overline{v}_x(r)\right)\left(v_{x,k}(r,t) - \overline{v}_x(r)\right) \tag{4.6}$$

where $\overline{v}_x(r) = \frac{1}{l}\sum_1^l v_{x,k}(r,t)$ and l is the total number of time steps.

Also, from the kinetic theory of granular flow (Jiradilok et al., 2006, 2007), the radial dispersion coefficient is defined as a function of radial normal Reynolds stress times the Lagrangian integral time scale or Eulerian integral time scale as shown in Equation (4.7). Tenekes and Lumley (1972) stated that the Eulerian integral time scale can approximately equal to Lagrangian integral time scale in order to estimate the order of magnitude of the diffusivity or dispersion coefficient.

$$D_x(r) = \overline{v'_x v'_x(r)}T_L = \overline{v'_x v'_x(r)}T_E \tag{4.7}$$

where the Lagrangian integral time scale or Eulerian integral time scale is obtained by autocorrelation function using Equation (4.8):

$$T_L = T_E = \int_0^\infty \frac{\overline{v'(t)v'(t+t')}}{\overline{v'^2}} dt' \tag{4.8}$$

where v' is velocity fluctuation.

4.1.4. Particle cluster concentration

This study uses the statistical methodology proposed by Sharma et al. (2000) to identify and characterize the particle clusters. They define the particle clusters as:

"The particle cluster is detected when the instantaneous solid fraction becomes larger than the time-averaged solid fraction plus two times the standard deviation (2σ)."

After the particle cluster is defined, the particle cluster concentration or particle cluster solid volume fraction is computed as the sum of the time-averaged solid fractions for all the clusters over the total number of clusters detected in the observation period:

$$\bar{\varepsilon}_{cl} = \frac{\sum_1^m \bar{\varepsilon}_{cl}}{m} \tag{4.9}$$

where m is the total number of particle clusters detected in the observation period.

4.2. Computational fluid dynamics simulation

4.2.1. Mathematical model

Although computational fluid dynamics has a promising future and is anticipated to make valuable contributions for predicting the performance of fluidized bed reactors, there are currently no universal mathematical models available to make

appropriate selection of models with a certain fluidized bed reactor. In this study, a set of governing equations, mass and momentum conservation equations, with constitutive equations were solved. The equations used in this study are based on the kinetic theory of granular flow, as reviewed by Gidaspow (1994). Here, the modified Wen and Yu drag law (Yang et al., 2003, 2004) has been replaced with that obtained from the energy minimization multi-scale (EMMS) approach. The EMMS drag model has been proved to be an effective way for modeling a high solid mass flux system of FCC particles. This study uses the commercial CFD program FLUENT 6.2.16 for modeling the system. There are several numerical models for gas-solid two-phase flow in the program such as, the Lagrangian model and the Eulerian model. In this case, the Eulerian model was selected. A summary of the governing equations and constitutive equations is already given in Chapter III. Since the EMMS drag model is not available in the FLUENT 6.2.16 program, the new additional user-defined function code (Fluent Inc., 2005a, 2005b) in C programming language was added. According to the previous literature, there has not been enough information given on the values of operating parameters which are the restitution coefficients and the specularity coefficient. Some adjustment process of these values has been done to find the suitable condition that matches with the experimental data and to obtain optimized parameter values as summarized in Table 4.1.

4.2.2. System description and computational domain

To validate the numerical results in this study, the Particulate Solid Research, Inc. (PSRI) challenge problem I, Knowlton et al. (1995), was chosen as the reference case. The system for Fluidization VII benchmark test is shown in Figure 4.2. The particles in the system were FCC particles. The diameter (D) and the height (h) of their riser were 0.2 m and 14.2 m, respectively. Since a three dimensional model requires long computation time and since the location of measurement was not known, this study uses a two dimensional model for the simulation. The schematic drawing of the riser is depicted in Figure 4.3 (a). This simplified schematic drawing is based on Benyahia et al.'s papers (2000, 2002). It was a two inlet-outlet design used to approximate the two dimensional riser to simulate the three dimensional riser

experiment. This was done because a one inlet-outlet design for the two dimensional riser could not capture the realistic mixing throughout the height of the riser. A full discussion of this topic is in the results and discussion section. The gas was fed to the system at the bottom of the riser. The solid particles were fed from the two side-inlets at 0.3 m above the bottom of the riser with a width of 0.1 m. The gas and solid exited through two symmetric side outlets at 0.3 m below the top of the riser with the same width as the solid-inlets. The other conditions for simulation are listed in Table 4.1.

The computational domain of the riser used in this study is illustrated in Figure 4.3 (b). The computational domain consists of 19 non-uniform grids in radial or horizontal direction and 285 uniform grids in axial or vertical direction, with a total of 5,415 computational cells. The grid independence study is described in Appendix 4A. The models were solved by using a computer with Pentium 1.80 GHz CPU 2 GB RAM. It took approximately seven days of computer time to obtain 40 s of simulation time.

4.2.3. Initial and boundary conditions

At the inlet, the velocity and volume fraction in each phase were specified. On the other hand, at the outlet, the system pressure was specified as atmospheric pressure. Initially, there were no gas and solid phases in the riser. At the wall, a no-slip condition was applied for all velocities, except for the tangential velocity of the solid phase and the granular temperature. Here, the boundary conditions of Johnson and Jackson (1987) were used. These conditions were first applied to kinetic theory of granular flow modelling by Sinclair and Jackson (1989). They are;

$$v_{st,W} = -\frac{6\mu_s \varepsilon_{s,max}}{\pi\phi\rho_s \varepsilon_s g_0 \sqrt{3\theta}} \frac{\partial v_{st,W}}{\partial n} \tag{4.10}$$

$$\theta_W = -\frac{\kappa_s \theta}{\gamma_W} \frac{\partial \theta_W}{\partial n} + \frac{\sqrt{3}\pi\phi\rho_s \varepsilon_s v_{s,slip}^2 g_0 \theta^{\frac{3}{2}}}{6\varepsilon_{s,max}\gamma_W} \tag{4.11}$$

where $\gamma_W = \dfrac{\sqrt{3}\pi\left(1-e_W^2\right)\varepsilon_s \rho_s g_0 \theta^{3/2}}{4\varepsilon_{s,max}}$.

4.3. Results and discussion

4.3.1. Comparison of simulation result to PSRI experiment

Figure 4.4 displays the computed time-averaged solid mass flux versus radial distance at 3.9 m above the bottom of the riser. The simulation using the Gidaspow or non-modified interface exchange coefficient model does not match with the experiment, while the EMMS or modified interface exchange coefficient model agrees with the experiment, especially in the near wall region. According to the literature (Gidaspow et al., 1989), there was significant particle cluster formation in the near wall region for the FCC or Geldart group A particles. The EMMS model used in this study modifies the interface exchange coefficient using the particle cluster concept. This makes the modified interface exchange coefficient model match the experimental data, rather than the non-modified interface exchange coefficient model, especially in the near wall region.

A comparison of the one and two inlet-outlet configurations is shown in Figure 4.5. From the computed time-averaged solid mass flux profiles versus radial distance at 3.9 m above the bottom of the riser, the two inlet-outlet configuration gives a more symmetrical profile than the one inlet-outlet configuration. The one inlet-outlet configuration had upflow at one side and downflow at the other side. Consequently, the one inlet-outlet configuration could not capture real phenomena inside the riser system. The reason is maybe because the two inlet-outlet configuration compensates the local mixing effect in a real three dimensional experimental system. Then, the two inlet-outlet configuration was used for subsequent analysis in this study.

Figure 4.6 shows the computed time-averaged solid mass flux at 3.9 m above the bottom of the riser versus the radial distance for two time-average ranges. Besides, the experimental values were plotted in the figure. Increasing the simulation time to 40 s, changed the result only slightly. This implies that this numerical simulation has reached the quasi steady state condition since the simulation time was 20 s. However, the 20-40 s time-averaged range result was selected to represent this system.

The transient distributions of solid volume fraction contour and solid axial velocity vector at 3.9 m above the bottom of the riser are displayed in Figure 4.7. The results are at 20, 30 and 40 s. These results are consistent with the results in previous figures. The numerical simulations predict the core-annular flow structure in the riser, similar to the experimentally observed flow pattern. This core-annular flow structure is made up of a very dilute flow in the center region (core) and a relatively dense phase near the wall region (annulus). It seems that the present model predicts more accurate time-averaged solid mass fluxes than the previous models (Benyahia et al., 2000, 2002) especially in the near wall region, which is the region with most particle clusters.

The computed values were compared to other measured variables for the same experimental condition. Figure 4.8 shows a comparison of the computed time-averaged solid density distribution at 3.9 m height inside the riser with the experimental values. The simulation result obtained by Sun and Gidaspow (1999) using viscosity based computation is also plotted in the figure. The viscosity based computation uses the empirical correlation from the experiment for particulate phase viscosity, stress and pressure. In kinetic theory based computation, the particulate phase properties are automatically computed. A reasonable agreement is obtained in between the kinetic theory based and the viscosity based computation results. All the results show the same distribution reflecting the establishment of a core-annular regime, as discussed in Figure 4.7. However, there is a slight difference in numeric values between the experiment and the computations. A little change in the position or angle of measurement can have an effect on measured results. In addition, the computations are obtained at only one position or angle in the real three dimensional experiment. Therefore, the difference may be due to the position of experimental measurement.

The computed time-averaged pressure drop versus the riser height is displayed in Figure 4.9. There is a reasonable agreement between the results obtained from the experiments and the computations. The high pressure drop at the top and the bottom of the riser is due to the effect of inlet and outlet configurations. The pressure drop decreases along the height of the riser due to the decreasing solids volume

fraction. This pressure drop profile matches the fast fluidization regime, as described by Kunii and Levenspiel (1991). Figures 4.4 to 4.9 confirm the validity of the developed model that can capture the phenomena in this riser system. Therefore, this computational fluid dynamics simulation provides more information and is suitable for analysis of particle cluster than the previous publication of Cabezas-Gómez et al. (2008) in which the results were not match with the experimental measurement. Some turbulent properties were also extracted from this simulation. These variables are the Reynolds stresses, the energy spectrum, the power spectrum, the granular temperatures, FCC viscosity and the dispersion coefficients. Also, the results from this fast fluidization riser were compared with those from turbulent fluidization riser by Jiradilok et al. (2006, 2007) to study the effect of fluidization regime on those properties as the followings.

4.3.1.1. Reynolds stresses

The principal characteristic of turbulent flow is the production of additional stresses due to random velocity fluctuations, called Reynolds stresses. From the numerical simulation, the hydrodynamic velocities $v_{ik}(r,t)$ were obtained. The method to define the averaged quantities, the mean velocity of particles, $\bar{v}_i(r)$ and solid phase normal Reynolds stresses, $\overline{v_i' v_i'}$, is shown by Equation (4.6). However, the subscript "x" is changed to "i" because the normal Reynolds stresses are in both the axial (y) and the radial (x) directions. A similar method was used by Pan et al. (1999) to analyze the particle image velocimetry data. Matonis et al. (2002) used the same method for computation of the stresses for three-phase flow. The method used here is essentially that of Jiradilok et al. (2006, 2007).

Figure 4.10 shows the turbulence intensities, $\overline{v_i' v_i'}$, at three different heights. The anisotropic characteristics of the particle fluctuations can be seen clearly. These three heights are 3.5 m, 7.0 m and 10.5 m. In fast fluidization riser, the pressure drop at these heights did not change much when compared to the turbulent fluidization riser, where the pressure drop at the bottom section was higher than that at the top section (Kunii and Levenspiel, 1991). Hence, these three heights can be used to represent the hydrodynamics in this riser system. Figure 4.10 (a) shows the radial

distribution of the normal Reynolds stresses in axial direction, at three different heights. At all riser heights, the oscillations are low in the center region and high near the wall. These profiles are not similar to those of a turbulent fluidization riser, as they had flat profiles at the bottom section of the riser due to low oscillations in the dense phase (Jiradilok et al., 2006, 2007). The time-averaged values of the normal Reynolds stresses in the radial direction as a function of position are plotted in Figure 4.10 (b). The fluctuations in the radial direction are opposite to those in the axial direction, high in the center region and low near the wall. These results are in agreement with those obtained in a turbulent fluidization riser. The comparisons between the normal Reynolds stresses in axial and radial directions can also be seen in this figure. The velocity fluctuations are large in the direction of the flow. It can be seen that the values of the normal Reynolds stresses do not differ much at these three heights. This is because the flow structure was changed slightly at the selected positions of the riser height. This is the difference between the turbulent fluidization riser and this system.

4.3.1.2. Energy spectrum

Spectral analysis of turbulent oscillations is common in the study of turbulent single phase flow (Hinze, 1959). Frequently the energy spectrum rises sharply with the wave number, reaches a maximum at a low frequency and finally follows the Kolmogorov -5⁄3 power law at high frequencies. We can estimate the axial energy spectrum or the distribution function, $Ey(n)$, from the Fourier transforms of $v'_y v'_y$ using the fast Fourier transform (FFT) technique. Also $Ex(n)$ can be determined from the Fourier transforms of $v'_x v'_x$.

Hinze (1959), Tennekes and Lumley (1972), McComb (1990), Hunt and Vassilicos (2000), Mathieu and Scott (2000) and Pope (2000) stated that if the turbulence contains only large eddies, the distribution function, $E(n)$, will exist mainly in the energy-containing range; if there are only small eddies, $E(n)$ will exist mainly in the inertial range. In the transition from the energy-containing range to the inertial range, the large eddy breaks and transfers the energy to the small eddies. Figure 4.11 shows the computed (a) near wall region and (b) central region vertical spectrum in a riser at

three different heights. For all the axial positions in Figure 4.11 (a), the famous -5⁄3 Kolmogorov power law is obeyed in the inertial range at high frequencies while at low frequencies the gravity wave and the internal solids circulation played an important role. Similar to that for single-phase flow and the turbulent fluidization riser, the energy-containing range and inertial range can be identified in the energy spectrum. At 7.0 m and 10.5 m in Figure 4.11 (b), there also exists the famous -5⁄3 Kolmogorov power law in the inertial range at high frequencies and the gravity wave and the internal solids circulation at low frequencies. At 3.5 m, there is only the gravity wave and the internal solids circulation range at all the frequencies. This is because this riser system has only large eddies at that position.

To determine the frequency of energy-containing range and inertial range, a comparison of horizontal (a) near wall region to the (b) central region energy spectrum in solids phase are obtained and analyzed at three different heights in the riser, as displayed in Figure 4.12. The energy spectra for the central and the near wall regions show significant differences to single-phase flow and turbulent fluidization riser. At 3.5 m and 10.5 m in Figure 4.12 (a), there exists the famous -5⁄3 Kolmogorov power law in the inertial range at high frequencies and the gravity wave and the internal solids circulation at low frequencies. At 7.0 m in Figure 4.12 (a) and for all positions in Figure 4.12 (b), there are only the gravity wave and the internal solids circulation range at all the frequencies. Figures 4.11 and 4.12 also indicate that the turbulent energies in the vertical direction are much stronger than that in the horizontal direction due to high Reynolds stress in direction of flow.

4.3.1.3. Power spectrum

We can estimate the power spectrum from the Fourier transforms of solid volume fraction. This methodology is commonly used to find the signal repeating pattern or periodic situation. A power spectrum of density fluctuations can distinguish between a well-defined structure, such as a large bubble or a core-annular regime and turbulent flow. When a well-defined structure exists, a sharp peak spectrum is obtained at a certain frequency called the dominant frequency (Du et al., 2003). For the core-annulus

fast fluidization flow in the IIT riser, the dominant frequency was about 0.2 Hz (Gidaspow et al., 2001).

The time series solids holdup characteristics at 3.5 m and 10.5 m from the bottom of the riser, on the right side wall, were obtained. Figure 4.13 illustrates the power spectrum densities corresponding to the fluctuations of the solids holdup computed at those two heights. The magnitudes of the fluctuations are approximately the same at these two heights. From the figures, the diagram highlights a dominant frequency at about 0.04 Hz. These frequencies are surprisingly low. However, these values are in reasonable agreement with the power spectrum for the similar riser system reported by Sun and Gidaspow (1999). Also, the obtained dominant frequencies are different from the turbulent fluidization riser, as the magnitude of the fluctuations in the dilute section was higher than in the dense section. The profile of power spectrum was almost flat in the dense section which is due to the restrictive space to oscillate. Dominant frequencies obtained by Jiradilok et al. (2006), for the bottom and top sections of the turbulent fluidization riser were 0.16 and 0.28 Hz, respectively.

4.3.1.4. Granular temperature

Tartan and Gidaspow (2004) used their kinetic theory based particle image method to determine the oscillations, both due to particles and due to particle clusters. Jung et al. (2005) showed using a kinetic theory based particle image velocity method that there are two kinds of turbulence in fluidization:

1. A "laminar" type, due to random oscillations of individual particles, measured by the classical granular temperature, and

2. A "turbulent" type, caused by the motion of clusters of particles or bubbles, measured by the average particle normal Reynolds stress.

These two kinds of turbulence give rise to two kinds of mixing, one on the level of particles and the other on the level of particle clusters or bubbles. To compute the granular temperature, the related equations have to be programmed into the CFD

codes. The code itself computes the classical granular temperature (θ_l), similar to the calculation of single-phase turbulence by direct numerical computation. The turbulent granular temperature (θ_t) is defined as the average of the normal Reynolds stresses, which are the average of the three squares of the velocity components in the three directions, by using the following definition:

$$\theta_t(t, x) \cong \frac{1}{3}\overline{v_x' v_x'} + \frac{1}{3}\overline{v_y' v_y'} + \frac{1}{3}\overline{v_z' v_z'} \tag{4.12}$$

Assuming the velocity fluctuations in *x*- and *z*- directions, the non-flow directions, to be equal, the turbulent granular temperature can be calculated as follows:

$$\theta_t(t, x) \cong \frac{2}{3}\overline{v_x' v_x'} + \frac{1}{3}\overline{v_y' v_y'} \tag{4.13}$$

The turbulent kinetic energy (E) in the solid phase can be calculated by:

$$E = \frac{1}{2}\overline{v_x' v_x'} + \frac{1}{2}\overline{v_y' v_y'} + \frac{1}{2}\overline{v_z' v_z'} \tag{4.14}$$

The simple relation between turbulent granular temperature and the turbulent kinetic energy becomes:

$$\theta_t = \frac{2}{3}E \tag{4.15}$$

Table 4.2 summarizes a comparison of the computed granular temperatures due to the particle and particle cluster oscillations and the turbulence kinetic energy at three different heights in this riser system. The sum of the granular temperatures due to the particle oscillations and due to the particle cluster oscillations is the total granular temperature. This quantity, therefore, can demonstrate the overall system oscillations. At all heights the computed granular temperatures due to the particle cluster oscillations are higher than those due to particle oscillations, which is consistent with the literature experimental results. In the riser studies at IIT (Gidaspow and Huilin, 1996, 1998b) for the flow of FCC particles, visible wall particle clusters formed. Most of the particles move as clusters for Geldart group A particles. Hence, the

turbulent granular temperature should dominate the oscillations in this riser system. At all heights, the computed total granular temperatures are of the same order of magnitude. The oscillations are about same throughout this riser. These results are different from those obtained in turbulence fluidization riser. In the later case, the total granular temperatures increased with increase in height in the riser. This is due to the fact that in the turbulent fluidization riser system, there is a co-existence of dense and dilute phases at the bottom and top sections of the riser, respectively. In the dilute section, the oscillations are higher than those in the dense section because of the available space between the particles or particle clusters. A comparison of the computed total granular temperatures with the literature experimental data is displayed in Figure 4.14. It can be seen that the computed values match the experimental data within the same range of gas velocity.

Figure 4.15 shows the computed time-averaged total granular temperature versus the radial distance at three different heights. The range of computed values matches the FCC experimental data, as reviewed by Gidaspow et al. (2004). The maximum values of total granular temperature are off-center at all riser heights. In the center and near wall regions, the total granular temperatures drop. In the core section, this implies that there is a reduction of fluctuations by the shear term ($\frac{\partial v_s}{\partial y} \approx 0$) in the solid phase fluctuating energy equation. In the annular section, this is probably because of the zero stresses.

4.3.1.5. FCC viscosity

The solids viscosity is one of the transport properties. In the kinetic theory of granular flow (Gidaspow, 1994), it is a function of granular temperature. The total granular temperature, which is the overall system oscillation, is substituted in Equation (3.22) to calculate the solids viscosity. Figure 4.16 displays its computed values as a function of solid concentration. The solid viscosity increases with increasing solid concentration. In the figure, the computed trendline from FCC experimental data correlation (Gidaspow and Huilin, 1998a) is also shown. Their correlation is as follows;

$$\mu_s = 0.014 \varepsilon_s^{1/3} g_0 \tag{4.16}$$

There is an excellent agreement between the computed FCC viscosity and the correlation at low solid volume fraction. On the other hand, at high solid volume fractions, the result deviates, because this correlation was obtained for much lower solids fluxes.

4.3.1.6. Dispersion coefficient

A measure of the quality of mixing is the particle diffusivity or dispersion coefficient. Similar to the granular temperature we can identify two types of dispersion coefficients (Jiradilok et al., 2007):

1. due to individual particle oscillations, or a "laminar" type and

2. due to particle cluster or bubble oscillations, or a "turbulent" type

4.3.1.6.1. Dispersion coefficient due to individual particles oscillations

An order of magnitude estimate of the dispersion coefficient due to individual particle oscillations can be obtained using the methodology as illustrated by Jung et al. (2005) and Jiradilok et al. (2006). They stated that the dispersion coefficients appear to correlate roughly with the granular temperature. The dispersion coefficient is calculated from the laminar granular temperature divided by the dominant frequency as follows:

$$D_{particle\ oscillations} \approx \frac{\theta_l}{f} \tag{4.17}$$

At 3.5 m and 10.5 m, the dominant frequency is 0.04 Hz and the laminar granular temperatures are 0.016 m^2/s^2 and 0.027 m^2/s^2, respectively. Therefore, the order of magnitude estimates of dispersion coefficients due to individual particle motion are approximately 0.4 m^2/s to 0.7 m^2/s.

4.3.1.6.2. Dispersion coefficient due to particle cluster oscillations

Dispersion coefficients due to particle cluster oscillations or turbulent can be obtained as a function of normal Reynolds stress using the Lagrangian integral time scale. The long-time diffusion coefficients are expressed in Equation (4.7) but the subscript "x" is changed to "i" because the dispersion coefficients are in both the axial (y) and the radial (x) directions.

A comparison of the radial and axial solid and gas dispersion coefficients at various heights is summarized in Table 4.3. The solid dispersions are lower than the gas dispersions. This is due to the slip velocity between the phases. At these three heights, the dispersion coefficients are approximately the same. The simulations also show that the radial dispersion coefficients in the riser are two to three orders of magnitude lower than the axial dispersion coefficients.

The comparisons between the computed solid dispersion coefficients due to particle cluster oscillations and the literature surveyed by Jiradiok et al. (2007), for axial and radial directions are shown in Figures 4.17 and 4.18, respectively. The computations show that the solid dispersion coefficients are close to each other in agreement with the measurements. Considering the solid dispersion coefficient at each height, the coefficients in this riser system are also close to each other. Figures 4.19 and 4.20 display the comparisons of computed axial and radial gas dispersion coefficients with the literature surveyed by Breault (2006). The calculated gas dispersion coefficients are also in the range of the literature experimental data.

Table 4.4 shows the comparison of some quantitative dispersion coefficient values from the turbulent fluidization riser (Jiradilok et al., 2006, 2007) and the fast fluidization riser in this study. As already discussed, the turbulent fluidization riser has a coexistence of the dense and dilute regimes. To compare the results, data are selected at the interface section for turbulent fluidization riser and at 7.0 m height for fast fluidization riser. These sections have approximately the same solid volume fraction. All the dispersion coefficients of turbulent fluidization riser are lower than those in this study.

This implies that the turbulent fluidization riser has less mixing when compared with the fast fluidization riser system.

4.3.2. Computation and comparison of particle cluster diameter and concentration

Figure 4.21 illustrates the computed instantaneous solids volume fractions at 30 s in this continuous riser system. From the figure, it can be seen that the solids volume fractions are high at the bottom of the riser and decrease slightly with the height in the riser. This situation is consistent with the results of the time-averaged pressure drop, as shown in Figure 4.9. Concerning the particle cluster information, it can be clearly seen from the expanded riser section that the particle clusters occur near the wall region. The particle cluster concentration or solids volume fraction is about 0.40 with the diameter of particle cluster approximately 0.0100 m.

Table 4.5 summarizes the computed information on particle cluster diameter at three different heights of the riser. It consists of the radial solid dispersion coefficient, oscillating velocity and particle cluster diameter. The particle cluster diameters in this study were computed using Equation (4.5). All the computed values were time- and cross-sectional area averaged over the riser diameter. The diameters of particle clusters vary slightly in the axial directions. In the lower section, the particle cluster diameter is the highest. This is due to the accumulation of the particle clusters in the lower section. However, it can be seen that all of the computed values are approximately the same at three different heights. This result is consistent with the stability of flow structure in this riser system.

Figure 4.22 displays the computed (a) particle and (b) particle cluster concentration versus radial distance at three different heights. These results are based on the statistical methodology as described in the introduction section. The profiles show a similar behavior to each other, but the particle cluster concentrations have a higher value than the particle concentration. This figure also illustrates the core-annular flow structure. At the wall, the particle cluster concentration is larger than at the center of

the riser. The value of particle cluster concentration at the wall is approximately 0.40 which is consistent with the contour value observed in Figure 4.21.

After we identify the cluster, the comparisons with the previous empirical correlation are shown. Table 4.6 shows the comparison of the values of the particle cluster diameter with the previous literature correlations (Gu and Chen, 1998; Harris et al., 2002). In the table, the values are shown both at three different heights and the averaged values from these three heights. At each height, the minimum and maximum values are also summarized. For the values from this study, the minimum and maximum values are obtained from the lowest and highest riser position data, respectively. In this study, the minimum particle cluster diameter is 0.0027 m while the maximum particle cluster diameter is 0.0238 m. For the values from the previous empirical correlations, the minimum values are calculated based on the averaged particle concentrations and the maximum values are calculated based on the averaged particle cluster concentrations. The computed results are match with the literature empirical correlations. The overall averaged values of particle cluster diameter and minimum particle cluster diameters from the three different heights are approximately the same. Only, the correlation values of maximum particle cluster diameters from three different heights are slightly lower which maybe because of the outlier data. Therefore, the qualitative results from this study are in agreement with the previous experimental publication data. They can also capture more realistic higher particle cluster diameters. This confirms the validity of this computational method.

Table 4.7 summarizes the comparison of the particle cluster concentration or solid volume fraction with the previous literature correlations (Gu and Chen, 1998; Harris et al., 2002). In the table, the values are shown both at three different heights and the averaged values at these three heights. The correlation of Harris is used to compare the particle cluster concentration at the wall region and the correlation of Gu is used to compare the averaged particle cluster concentration from all the riser position data. All the values from the previous correlations are both in quantitative and qualitative agreement with the values of this study. The particle cluster concentration is higher at

the wall than the averaged values. This also confirms the validity of this computational method for particle cluster concentration.

4.3.3. Computation of Sherwood number and mass transfer coefficient

The Sherwood number and mass transfer coefficient were computed based on the particle cluster results. The conventional Sherwood number for a single spherical particle is two. In this study, the conventional Sherwood number is multiplied by the scale factor to get the new reasonable Sherwood number. The assumption is that the Sherwood number is low due to the particle cluster formation. The used scale factor is thus the ratio between the real particle diameter and the computed particle cluster diameter. The mass transfer coefficient is then calculated using the relation with the Sherwood number ($Sh = \dfrac{k_{mass\,transfer}d_p}{D}$). In this study, the obtained averaged particle cluster diameter is approximately 10^{-2} m. Hence, the computed Sherwood number is of the order of 10^{-2} and the computed mass transfer coefficient is of the order of 10^{-3} m/s. These two values are in reasonable agreement with the observations from the literature experimental data (Kunii and Levenspiel, 1991). They also fall in the range given in the review by Breault (2006).

This computation leads us to make the hypothesis that the Sherwood number for fluidization of small particles, Geldart groups A particles, are low due to particle cluster formation. Therefore, this reduction of Sherwood number or mass transfer coefficient can be explained by the particle cluster formation in the system. When the particle clusters formed, the fluidizing gas must pass through the solid particles inside the particle clusters. The mass transfer resistance of the system is thus increased. This phenomenon makes the Sherwood number and mass transfer coefficient of the system much lower than the diffusion controlled value based on particle diameter.

4.4. Conclusions

1. The PSRI challenge problem I data for flow of FCC particles in a riser with a high solids flux and low gas velocity was modeled using the kinetic theory of granular flow with the non-modified and modified interface exchange coefficient models. In the dense regime, the modified interface exchange coefficient model or the EMMS drag law gives a closer comparison of the computed solid mass flux, solid density and pressure drop than the standard drag law.

2. The computer model was also used to calculate axial and radial normal Reynolds stresses, energy spectra, power spectra, granular temperature, the FCC viscosity, and axial and radial dispersion coefficients, accurately.

3. Particle cluster sizes were computed from the radial dispersion coefficient divided by the radial oscillating velocity. The particle cluster diameters agree with published empirical correlations.

4. From the cluster diameter, the computed Sherwood number is of the order of 10^{-2} and the mass transfer coefficient is of the order of 10^{-3} m/s, in agreement with the experimental data for fluidization of fine particles.

Appendix 4A. The grid independence study

No numerical simulation is complete without a study of grid independence. To confirm that the results are independent of grid size, the increments of grid numbers in the radial direction, in the axial direction and in both the radial and axial directions were performed. Figure 4.23 (a) shows the computed time-averaged pressure drops with the change in the radial direction grid number. The computational domains consist of 19, 29 and 38 non-uniform grids in radial direction and 285 uniform grids in axial direction. The computed time-averaged pressure drops with the change in the axial direction grid number are shown in Figure 4.23 (b). The computational domains consist of 19 non-uniform grids in radial direction and 285, 428 and 570 uniform grids in axial direction. Figure 4.23 (c) displays the computed time-averaged pressure drops with the change in both the radial and axial directions grid number. The computational domains consist of 19 × 285, 29 × 428 and 38 × 570 grids (non-uniform grids in radial direction × uniform grids in axial direction). From the figure, all the grid number cases predict similar pressure drop distributions. Also, the Sherwood numbers and the mass transfer coefficients with the change in grid number are summarized in Table 4.8. The computed values are approximately the same for all the grid number cases. The minimum and maximum mass transfer coefficient error percentages as compared with the lowest grid number case are only 0.12 and 8.88 %, respectively. This indicates that all the grid number cases are sufficiently fine for providing reasonably grid independence results. In general, the continuous increase in mesh density may lead to slightly better results that are more grid independence. However, the computational time is still a significant restriction when using a finer grid. In this study, the computational domain consisting of 19 non-uniform grids in radial direction and 285 uniform grids in axial direction was selected to use.

Table 4.1 Parameters used for the simulation.

Symbol	Description	Value
D	Diameter of riser	0.20 m
h	Height of riser	14.20 m
ρ_g	Gas density	1.2 kg/m^3
μ_g	Gas viscosity	2×10^{-5} kg/m s
ρ_s	Particle density	1712 kg/m^3
d_p	Diameter of particle	76 μm
v_g	Gas inlet velocity	5.200 m/s
v_s	Solid inlet velocity	0.476 m/s
ε_s	Solid inlet volume fraction	0.60
e	Restitution coefficient between particles	0.95
e_W	Restitution coefficient between particle and wall	0.90
ϕ	Specularity coefficient	0.50

Table 4.2 A comparison of computed laminar, turbulent and total granular temperatures
and turbulent kinetic energy at three different heights.

Height (m)	Granular temperatures (m^2/s^2)			Turbulent kinetic energy (m^2/s^2)
	Laminar	Turbulent	Total	
3.5	0.016	1.841	1.857	2.785
7.0	0.028	2.273	2.300	3.450
10.5	0.027	2.010	2.036	3.055

Table 4.3 A comparison of computed axial and radial dispersion coefficients
at three different heights.

Height (m)	Solid dispersion coefficients (m^2/s)		Gas dispersion coefficients (m^2/s)	
	Axial	Radial	Axial	Radial
3.5	1.959	0.002	3.959	0.017
7.0	3.644	0.003	3.983	0.018
10.5	2.118	0.002	2.856	0.020

Table 4.4 A comparison of computed dispersion coefficients of the turbulent fluidization riser and the fast fluidization riser.

Variable	Riser system	
	Turbulent fluidization riser (at interface section)	Fast fluidization riser (at 7.0 m)
Inlet gas velocity (m/s)	3.25	5.20
Solid mass flux (kg/m^2 s)	98.80	489.00
Normal Reynolds stress at riser center		
- Axial (m^2/s^2)	3.000	5.000
- Radial (m^2/s^2)	0.010	0.125
Granular temperature		
- Laminar (m^2/s^2)	0.016	0.028
- Turbulent (m^2/s^2)	1.014	2.273
Solid dispersion coefficient		
- Axial (m^2/s)	1.221	3.644
- Radial (m^2/s)	0.001	0.003
Gas dispersion coefficient		
- Axial (m^2/s)	2.032	3.983
- Radial (m^2/s)	0.002	0.018

Table 4.5 The computed information on particle cluster diameter

at three different heights of the riser.

Height (m)	Radial solid dispersion coefficient (m^2/s)	Oscillating velocity (m/s)	Particle cluster diameter (m)
3.5	0.002	0.224	0.010
7.0	0.003	0.259	0.010
10.5	0.002	0.243	0.009

Table 4.6 The comparison of the particle cluster diameter

with the previous literature correlations.

Method	Height (m)	Particle cluster diameters (m)		
		Minimum	Maximum	Averaged
This study	3.5	0.0064	0.0232	0.0101
	7.0	0.0040	0.0238	0.0095
	10.5	0.0027	0.0150	0.0087
	Averaged	0.0027[a]	0.0238[b]	0.0095
Harris's correlation	3.5	0.0033	0.0151	0.0092
	7.0	0.0035	0.0149	0.0092
	10.5	0.0034	0.0165	0.0099
	Averaged	0.0033[a]	0.0165[b]	0.0095
Gu's correlation	3.5	0.0028	0.0154	0.0091
	7.0	0.0030	0.0149	0.0089
	10.5	0.0029	0.0175	0.0102
	Averaged	0.0028[a]	0.0175[b]	0.0094

[a] the minimum value from the overall data

[b] the maximum value from the overall data

Table 4.7 The comparison of the particle cluster concentration
with the previous literature correlations.

Method	Height (m)	Particle cluster concentration (-)	
		Wall	Averaged
This study	3.5	0.3884	0.2541
	7.0	0.4016	0.2522
	10.5	0.4194	0.2628
	Averaged	0.4031	0.2564
Harris's correlation	3.5	0.4229	-
	7.0	0.4292	-
	10.5	0.4253	-
	Averaged	0.4258	-
Gu's correlation	3.5	-	0.2855
	7.0	-	0.2940
	10.5	-	0.2887
	Averaged	-	0.2894

Table 4.8 The comparison of the Sherwood numbers and the mass transfer coefficients
with the change in grid number.

Grid number (radial direction × axial direction)	Sherwood number (-)	$k_{mass\ transfer}$ (m/s)
19 × 285	0.0161	0.0042
Change in the radial direction;		
29 × 285	0.0154	0.0041
38 × 285	0.0160	0.0042
Change in the axial direction;		
19 × 428	0.0157	0.0041
19 × 570	0.0150	0.0040
Change in both the radial and axial directions;		
29 × 428	0.0148	0.0039
38 × 570	0.0161	0.0042
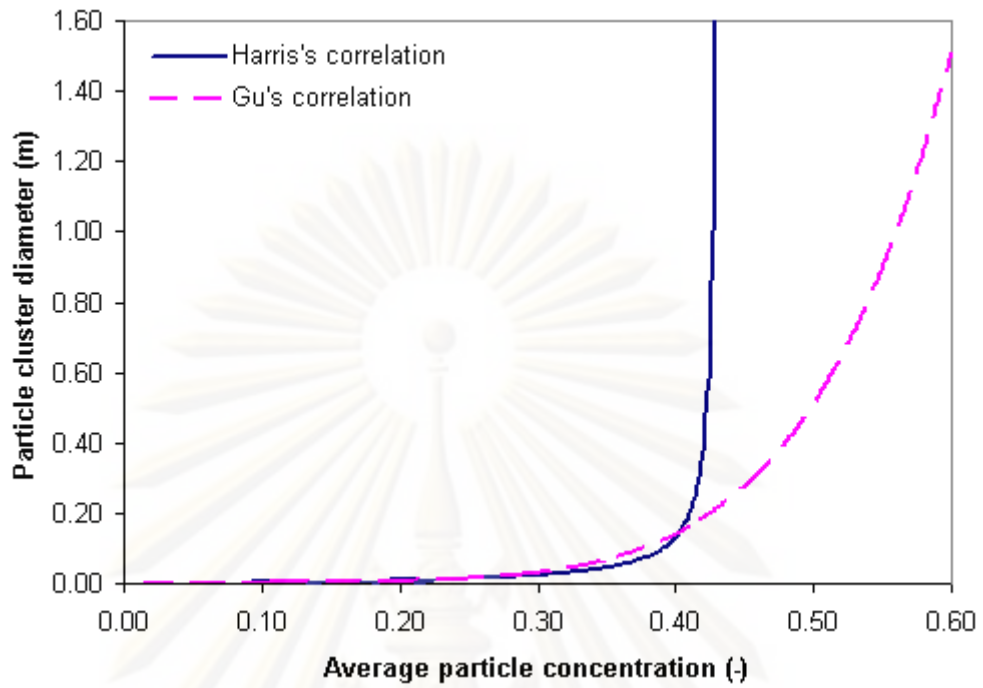
(a)
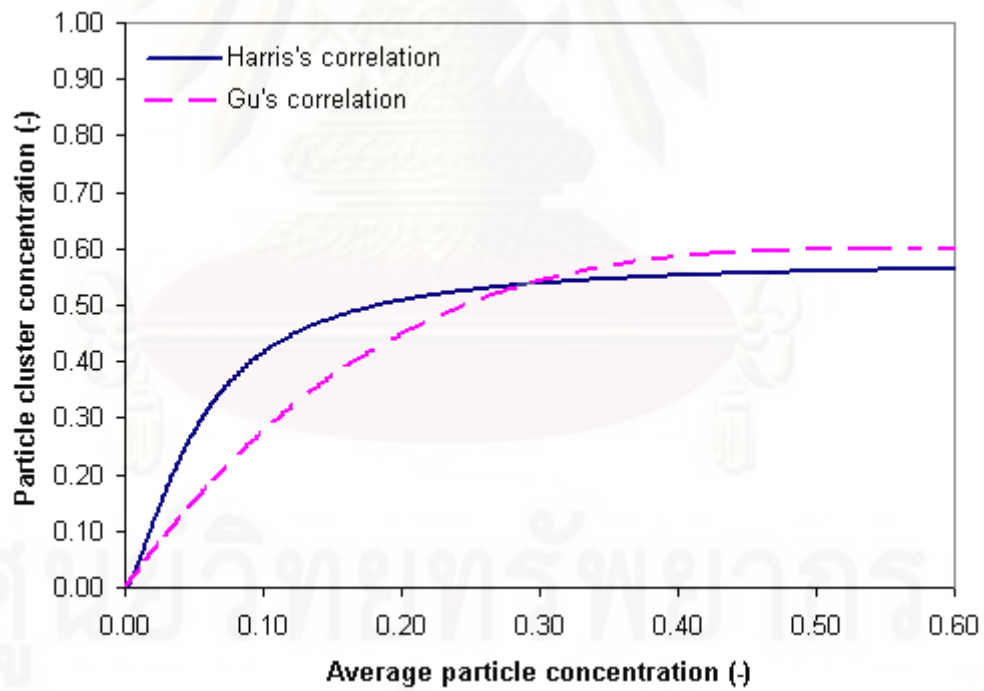
(b)

Figure 4.1 Particle cluster (a) diameter and (b) concentration calculated from

Gu's (Gu and Chen, 1998) and Harris's (Harris et al., 2002) correlations.
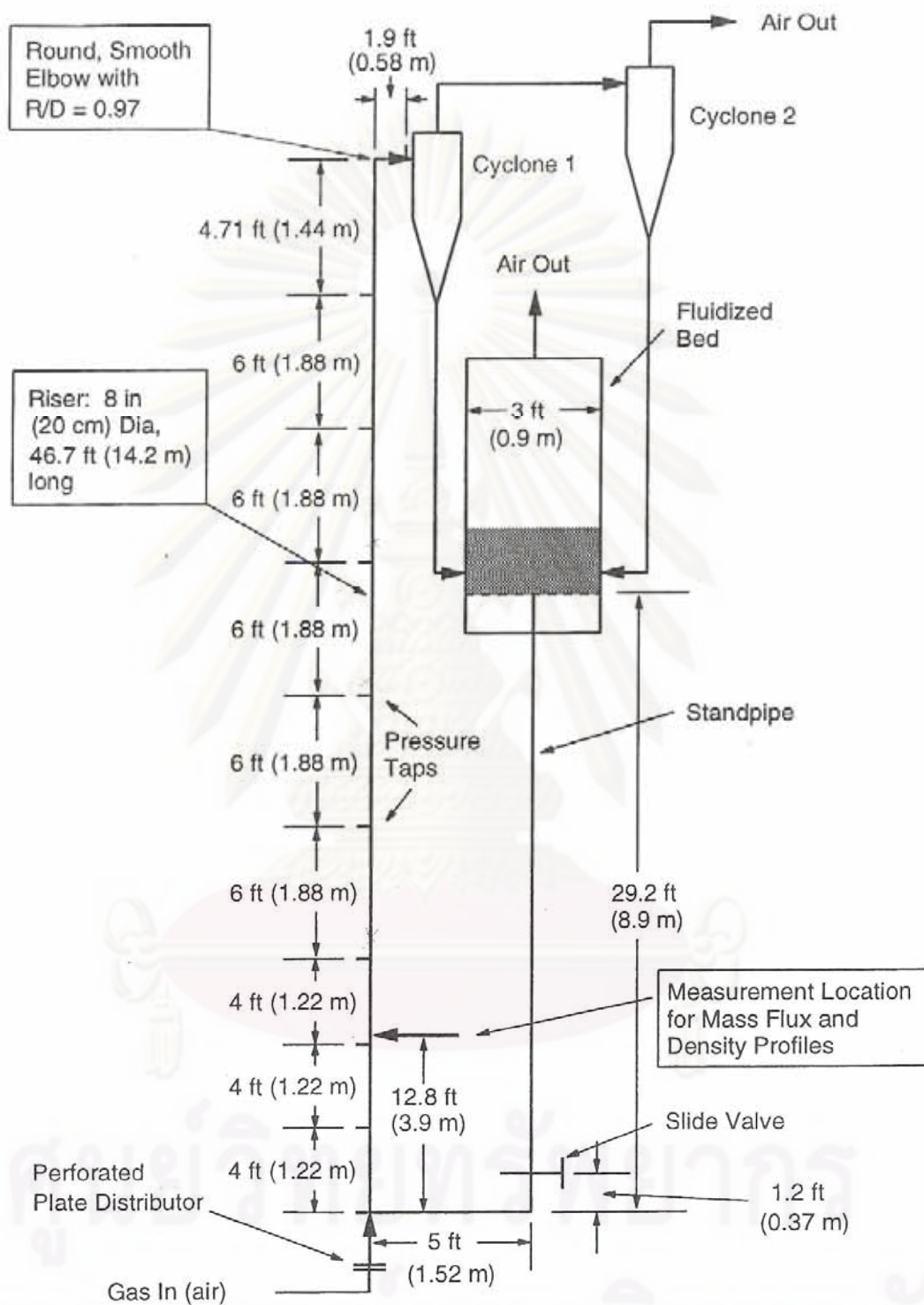
Figure 4.2 Schematic drawing of a 20 cm diameter circulating fluidized bed test unit

for the Fluidization VII benchmark test.

(a)   (b)
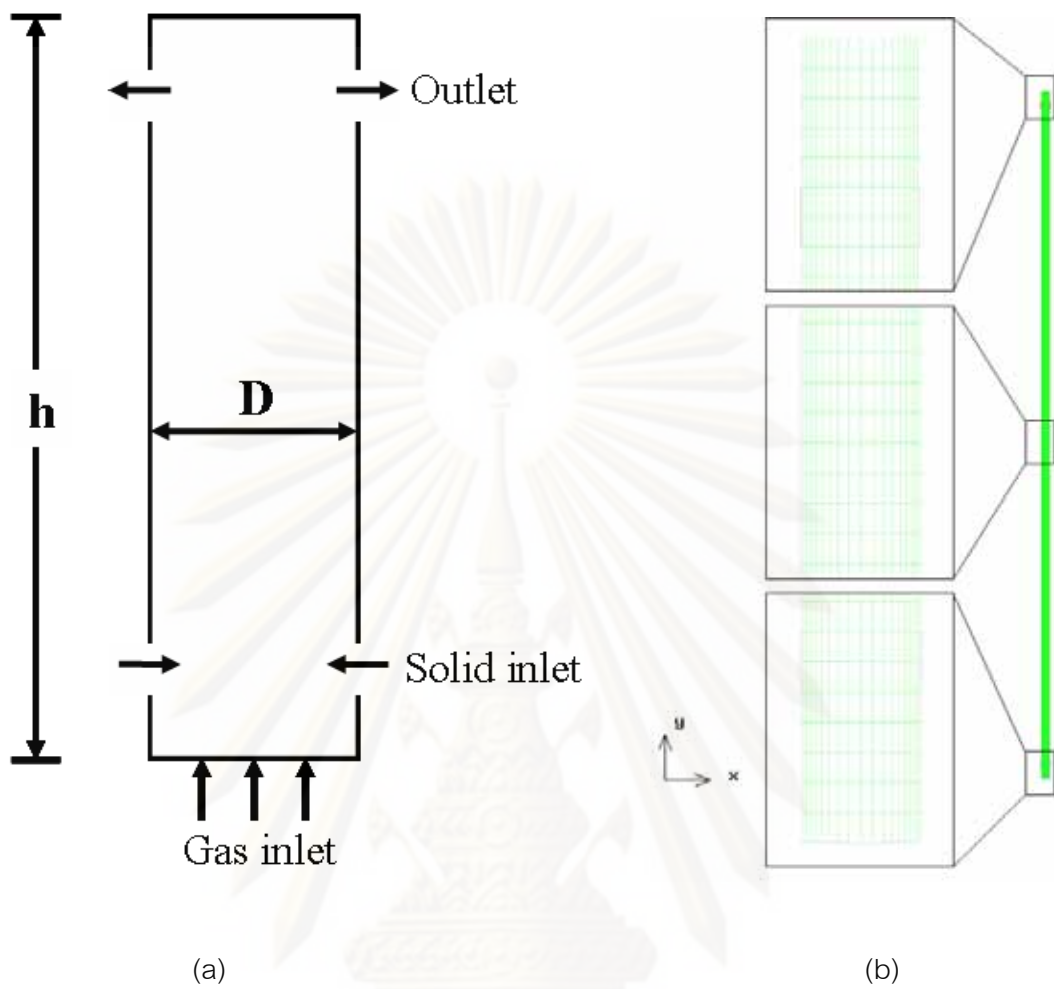
Figure 4.3 (a) Schematic drawing and (b) computational domain with their boundary
conditions of a simplified riser used in this study.
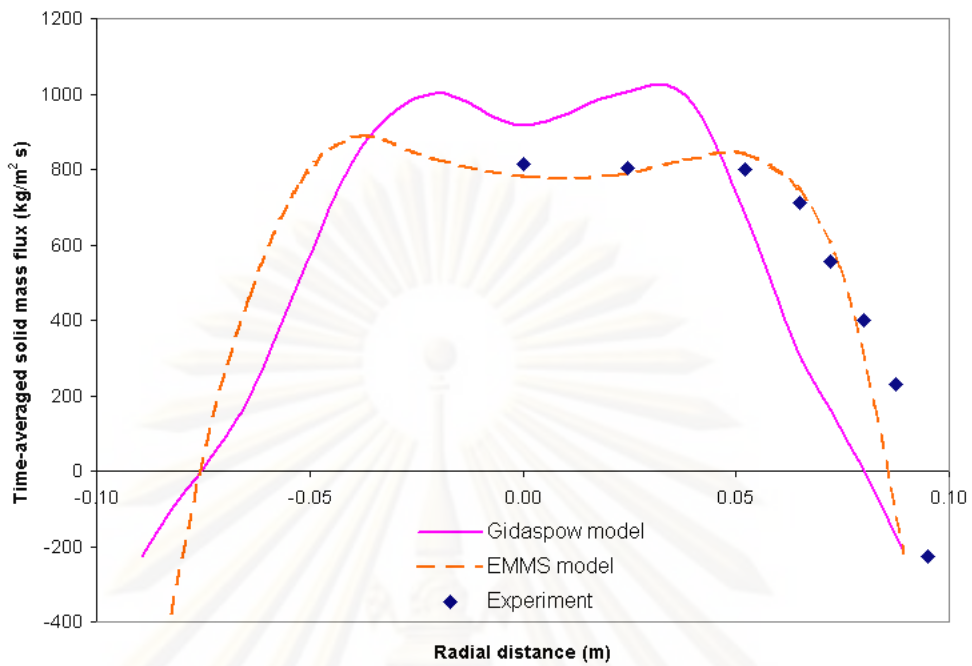
Gidaspow model;

$\varepsilon_g > 0.80$ $\beta_{gs} = 150 \dfrac{(1-\varepsilon_g)^2 \mu_g}{\varepsilon_g d_p^2} + 1.75 \dfrac{(1-\varepsilon_g)\rho_g |v_g - v_s|}{d_p}$

$\varepsilon_g \leq 0.80$ $\beta_{gs} = \dfrac{3}{4} \dfrac{(1-\varepsilon_g)\varepsilon_g}{d_p} \rho_g |v_g - v_s| C_{D0} \varepsilon_g^{-2.65}$

EMMS model;

$\varepsilon_g < 0.74$ $\beta_{gs} = 150 \dfrac{(1-\varepsilon_g)^2 \mu_g}{\varepsilon_g d_p^2} + 1.75 \dfrac{(1-\varepsilon_g)\rho_g |v_g - v_s|}{d_p}$

$\varepsilon_g \geq 0.74$ $\beta_{gs} = \dfrac{3}{4} \dfrac{(1-\varepsilon_g)\varepsilon_g}{d_p} \rho_g |v_g - v_s| C_{D0} \omega(\varepsilon_g)$

with;

$0.74 \leq \varepsilon_g \leq 0.82$ $\omega(\varepsilon_g) = -0.5760 + \dfrac{0.0214}{4(\varepsilon_g - 0.7463)^2 + 0.0044}$

$0.82 \leq \varepsilon_g \leq 0.97$ $\omega(\varepsilon_g) = -0.0101 + \dfrac{0.0038}{4(\varepsilon_g - 0.7789)^2 + 0.0040}$

$\varepsilon_g > 0.97$ $\omega(\varepsilon_g) = -31.8295 + 32.8295\varepsilon_g$

$Re < 1000$ $C_{D0} = \dfrac{24}{Re}(1 + 0.15 Re^{0.687})$

$Re \geq 1000$ $C_{D0} = 0.44$

Figure 4.4 Computed time-averaged solid mass flux at 3.9 m using two drag models.
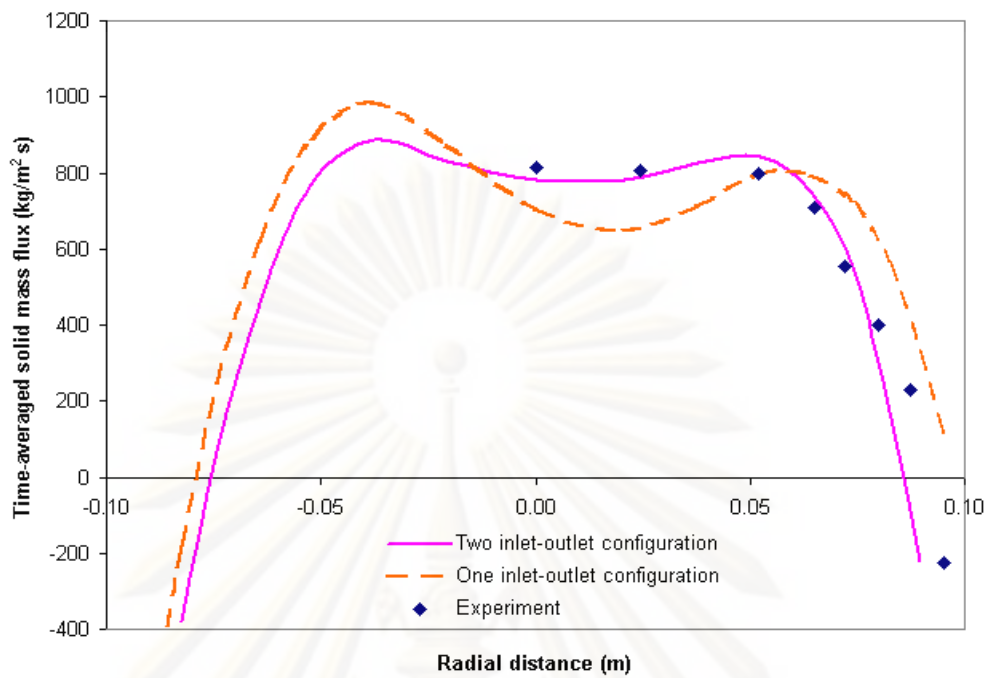
Two inlet-outlet configuration;   One inlet-outlet configuration;
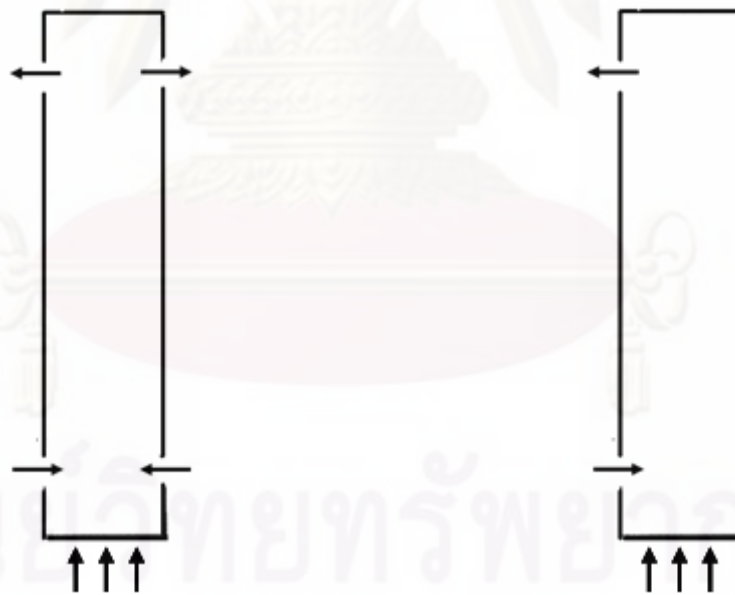
Figure 4.5 Computed time-averaged solid mass flux at 3.9 m
with different inlet-outlet configurations.
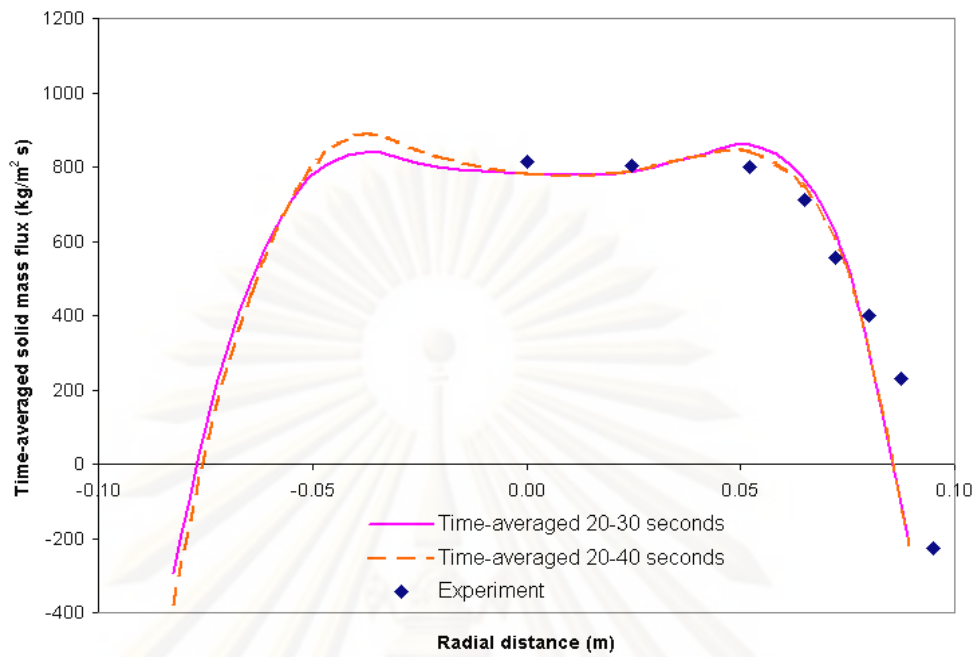
Time-averaged 20-30 seconds;

Time-averaged 20-40 seconds;

$$\bar{v}_x(r) = \frac{1}{l}\sum_1^l v_{ik}(r,t)$$

Figure 4.6 Computed time-averaged solid mass flux at 3.9 m

with different time-averaged ranges.
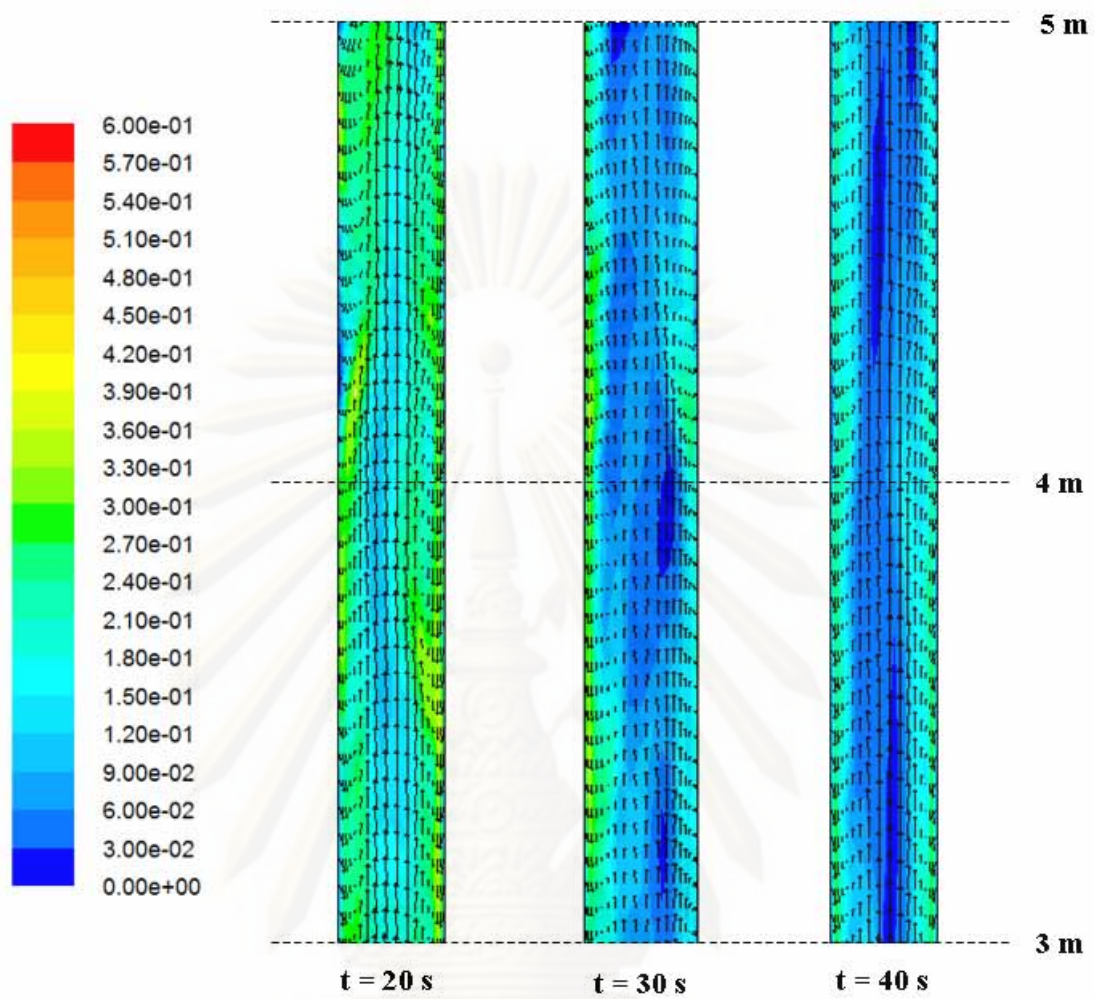
Figure 4.7 Transient distributions of solid volume fraction and solid velocity at 3.9 m

for the Fluidization VII benchmark test (h = 3.0 - 5.0 m).
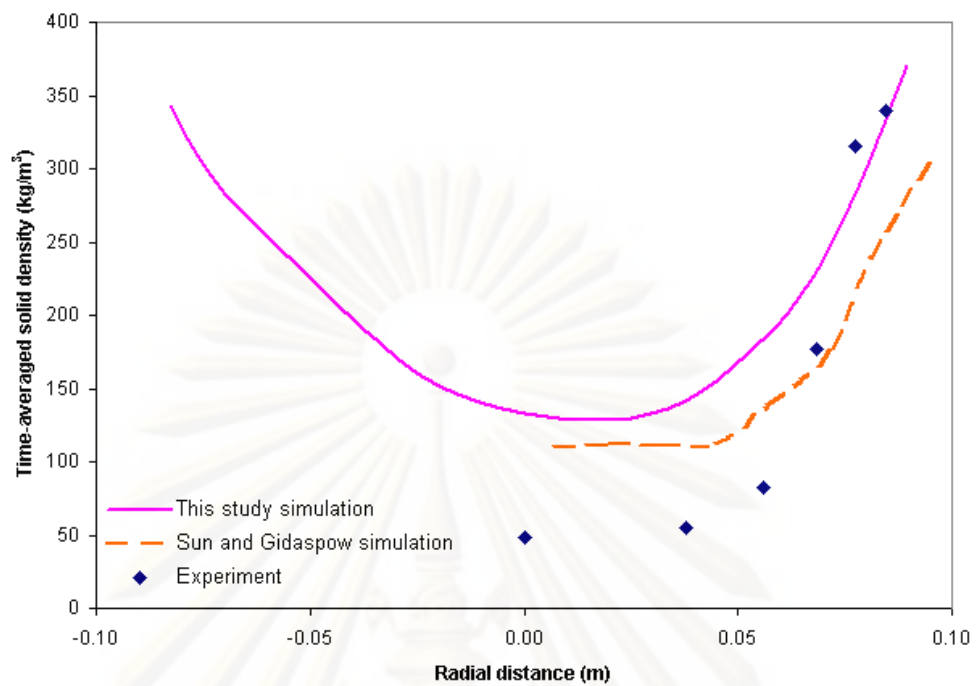
Figure 4.8 Computed time-averaged solid density at 3.9 m compared with the

experiment and Sun and Gidaspow (1999) simulation.
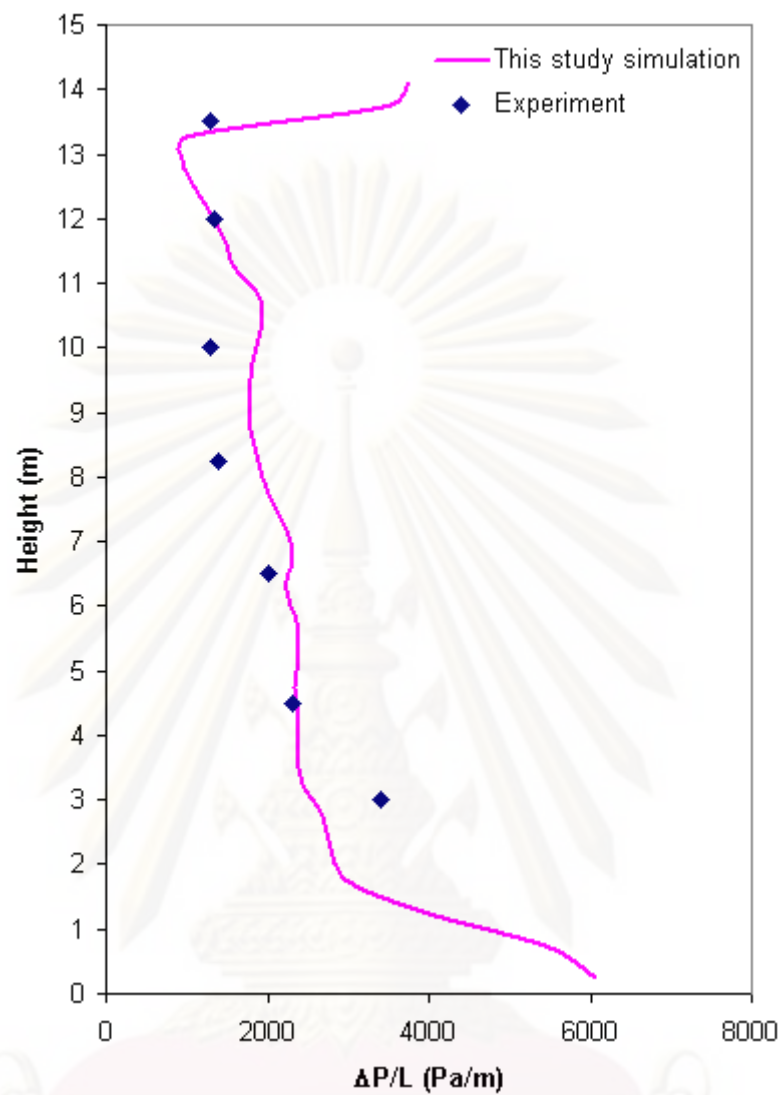
Figure 4.9 A comparison of the computed time-averaged pressure drop for the

Fluidization VII benchmark test.
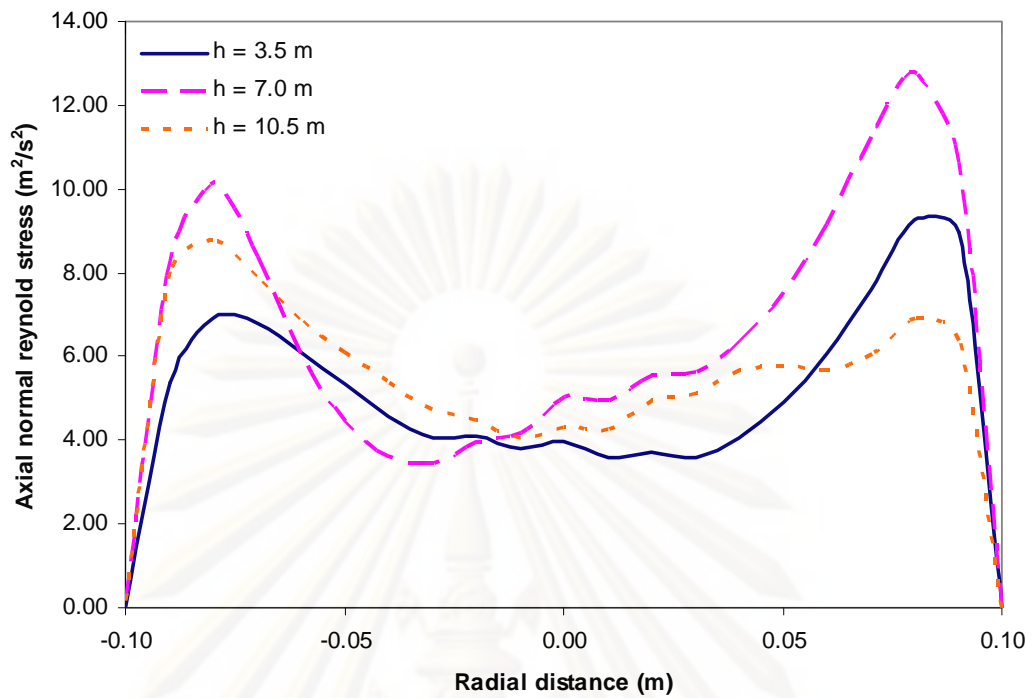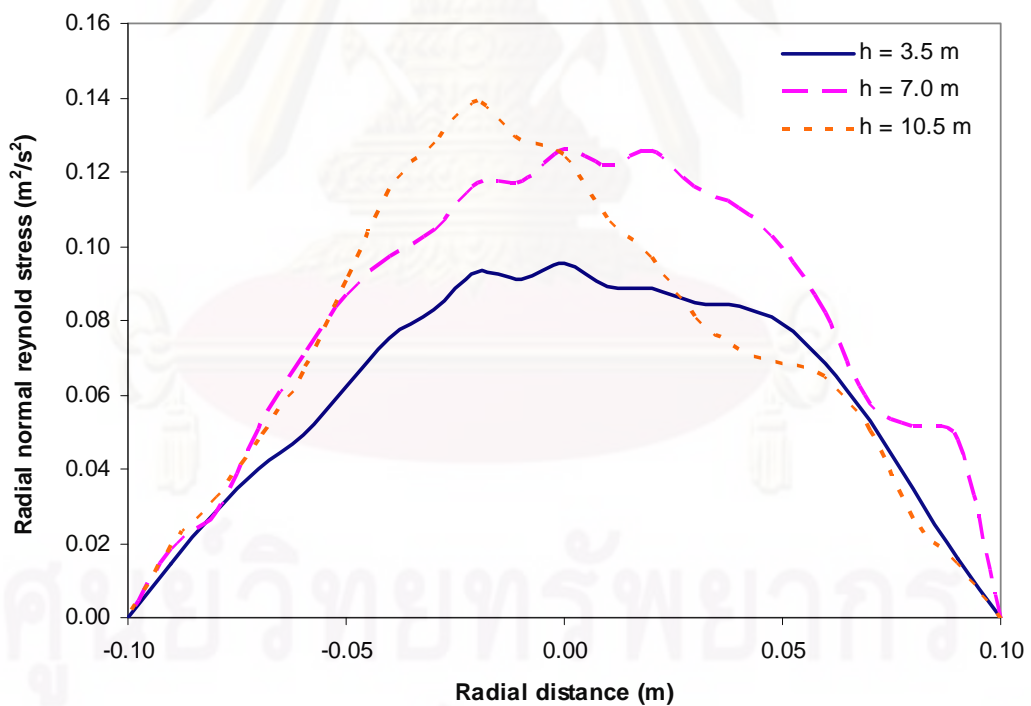
Figure 4.10 Radial distributions of the computed normal (a) axial and (b) radial Reynolds

stresses at three different heights.
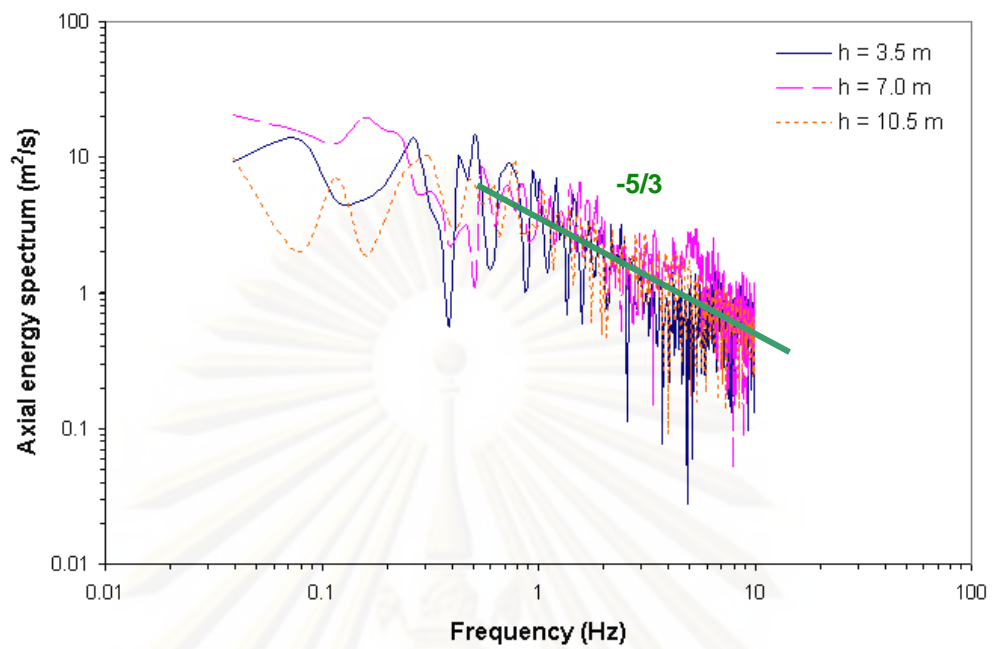
(a)
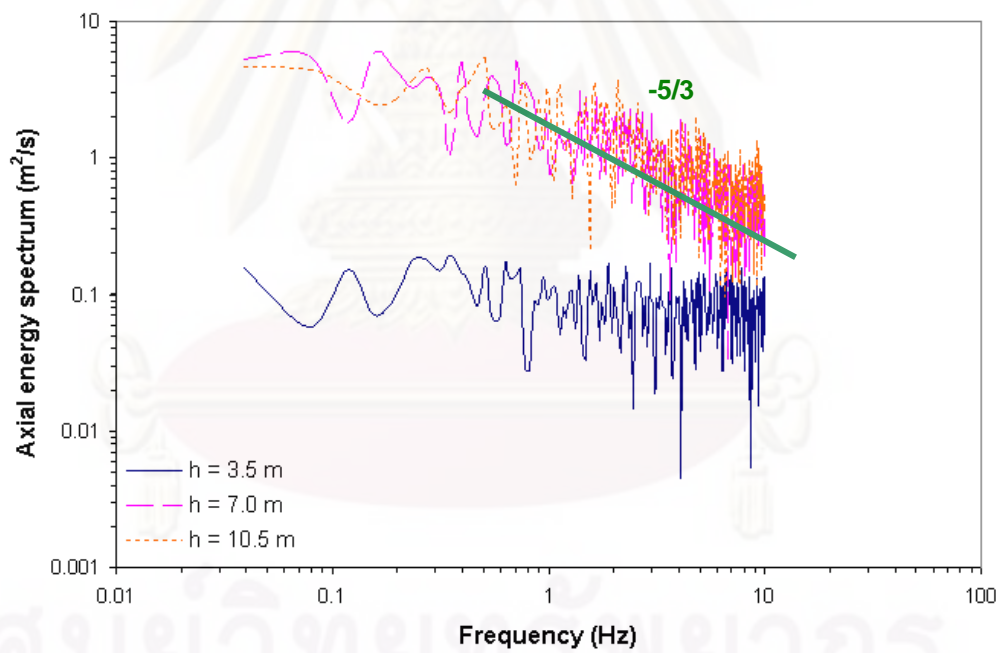
(b)

Figure 4.11 Computed (a) near wall region and (b) central region axial energy spectrum in a riser at three different heights.
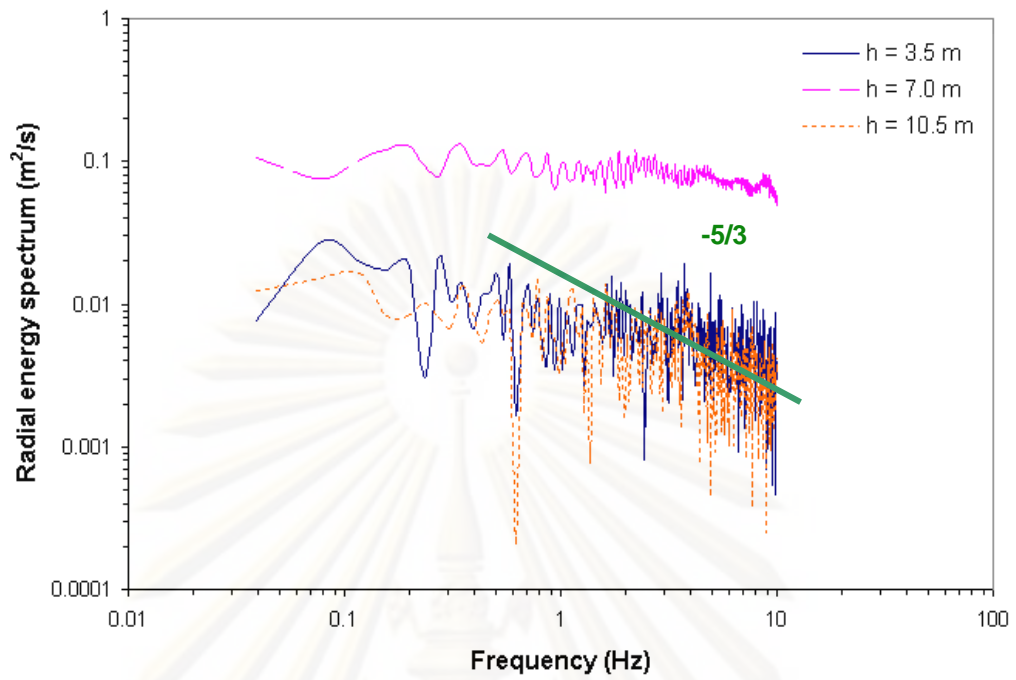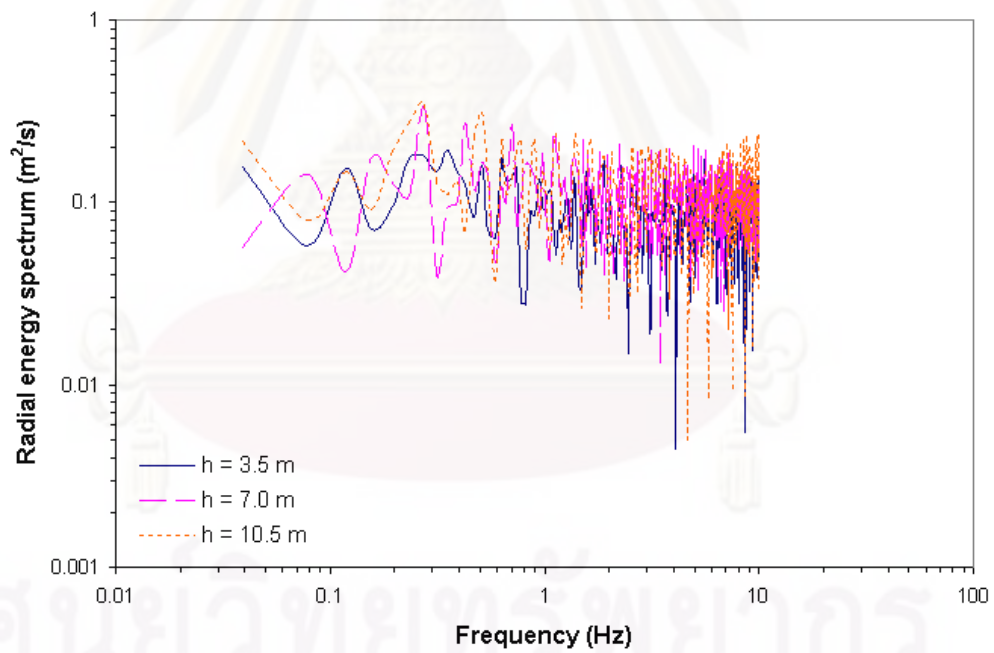
Figure 4.12 Computed (a) near wall region and (b) central region radial energy
spectrum in a riser at three different heights.
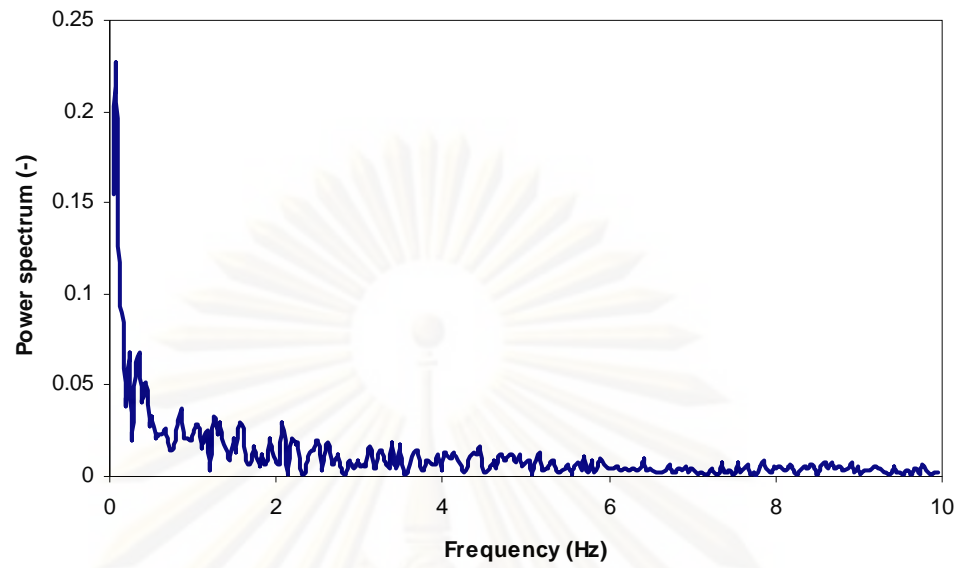
(a)
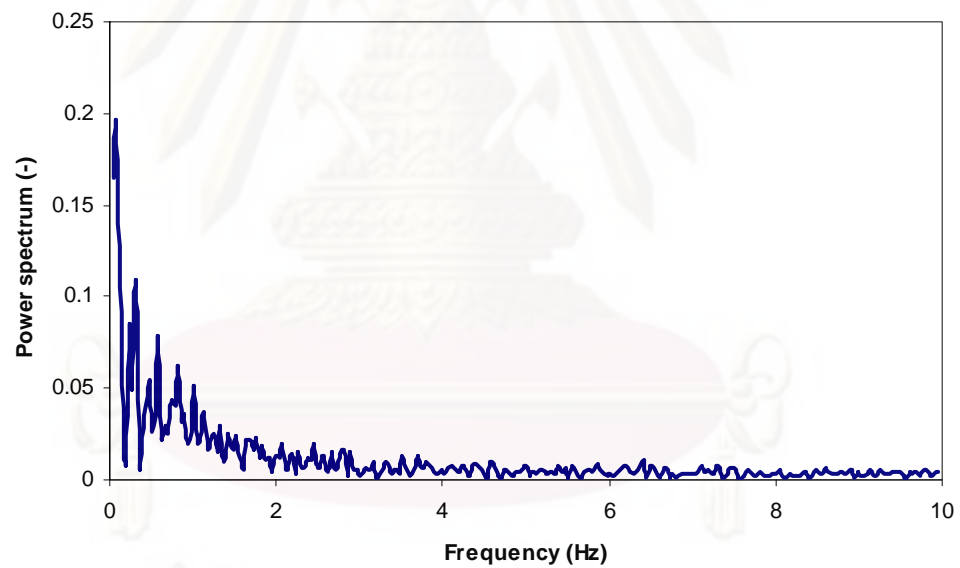
(b)

Figure 4.13 Power spectrum density of the solid volume fraction fluctuations at

(a) 3.5 m and (b) 10.5 m on right-hand side wall in the riser.
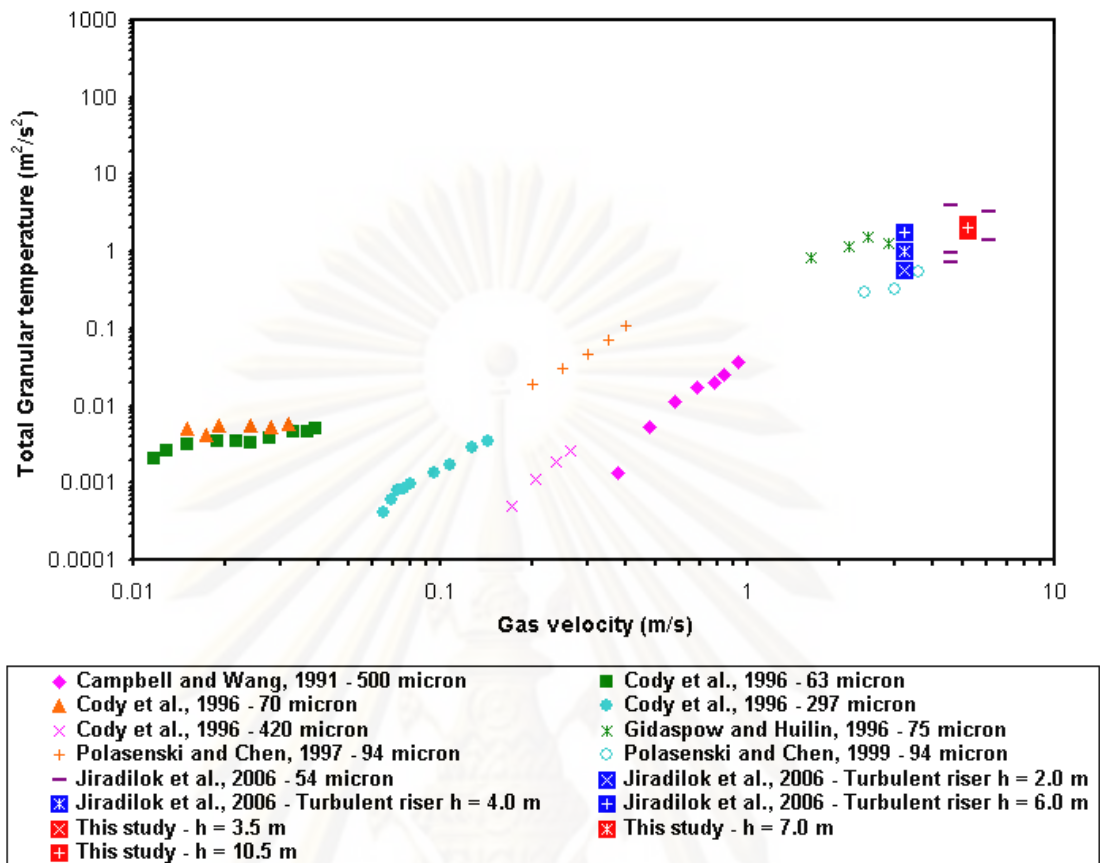
Figure 4.14 Effect of the gas velocity on experimental and computed total granular
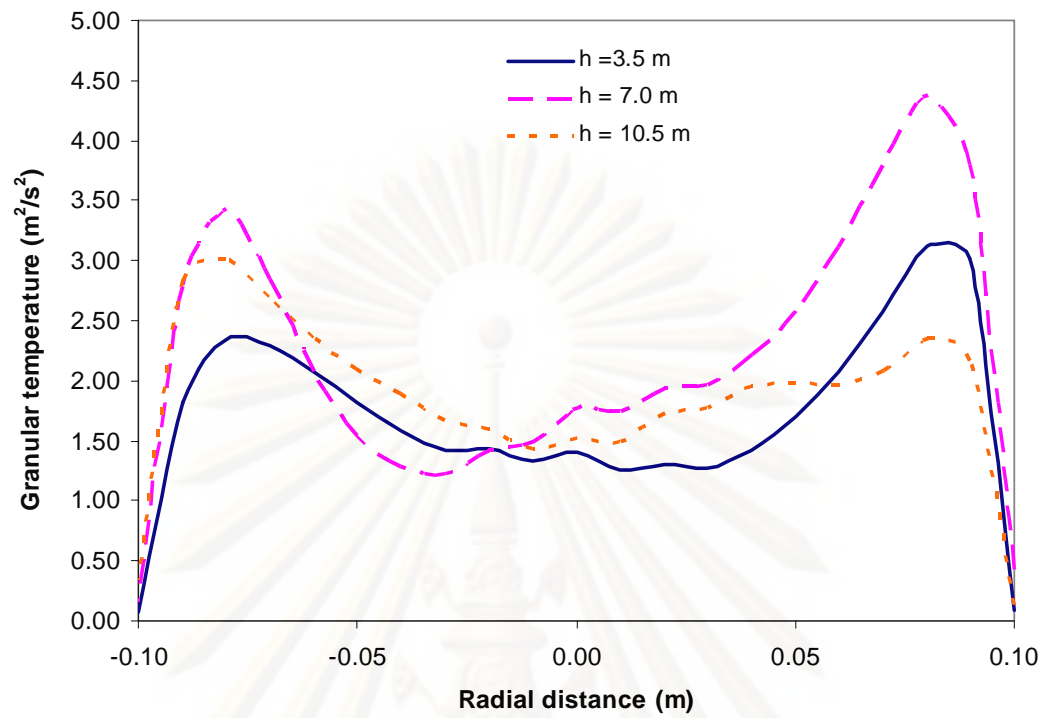
temperatures.

Figure 4.15 Radial distributions of computed time-averaged total granular temperature at three different heights.
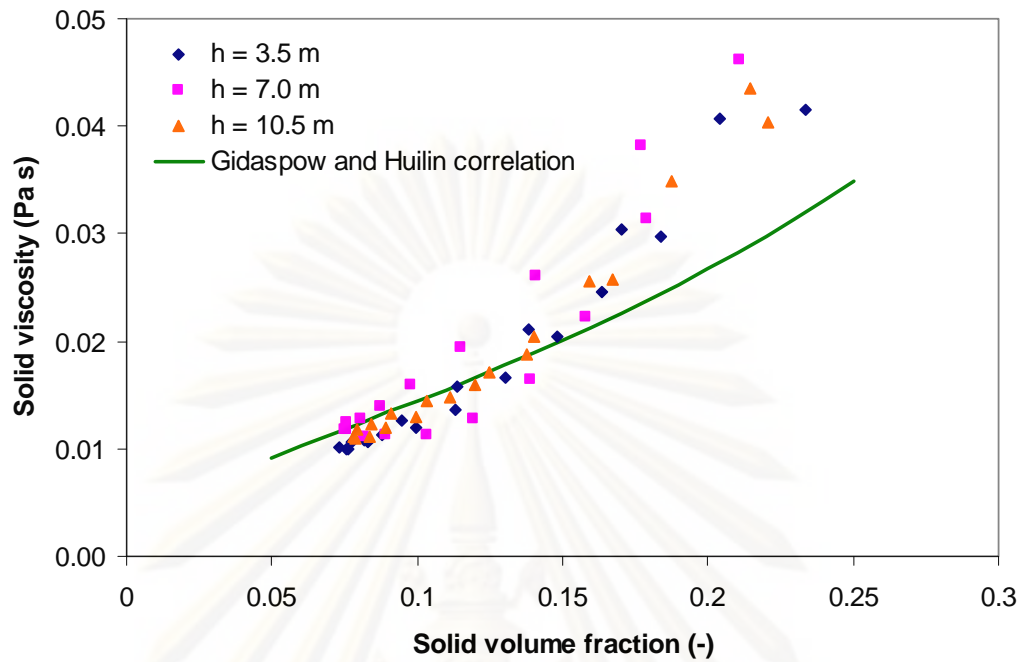
Figure 4.16 Computed solid viscosity based on total granular temperature as a function
of solid volume fraction.
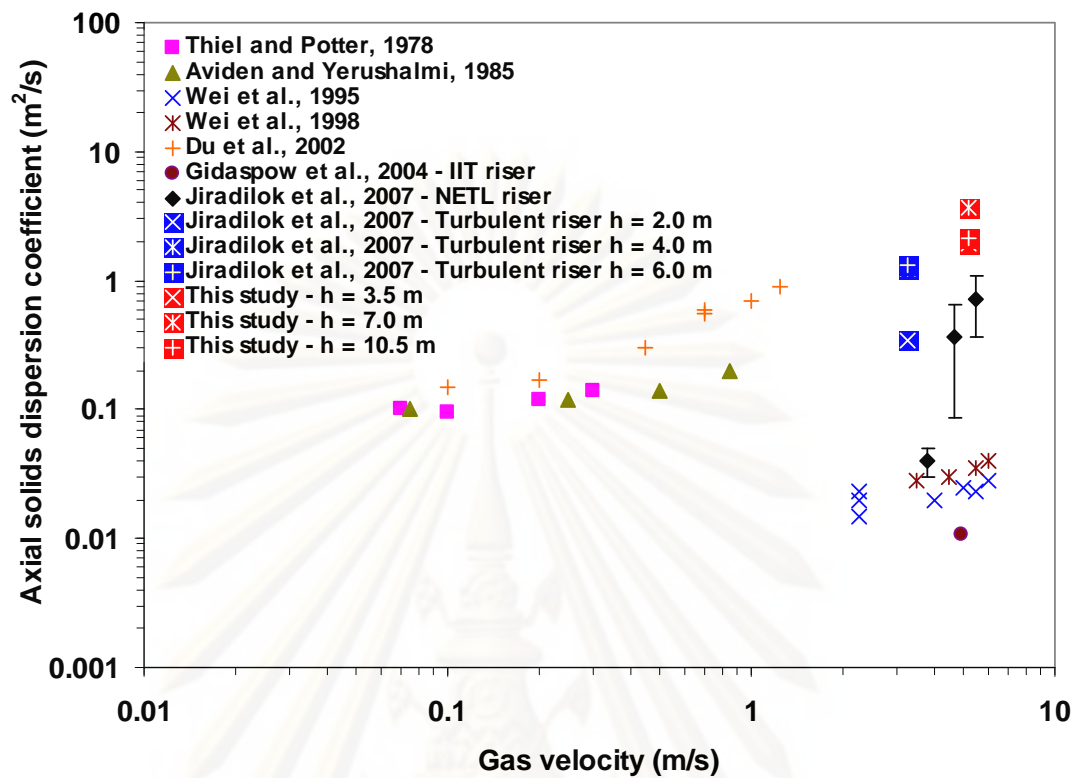
Figure 4.17 Effect of the gas velocity on experimental and computed axial solid

dispersion coefficients.
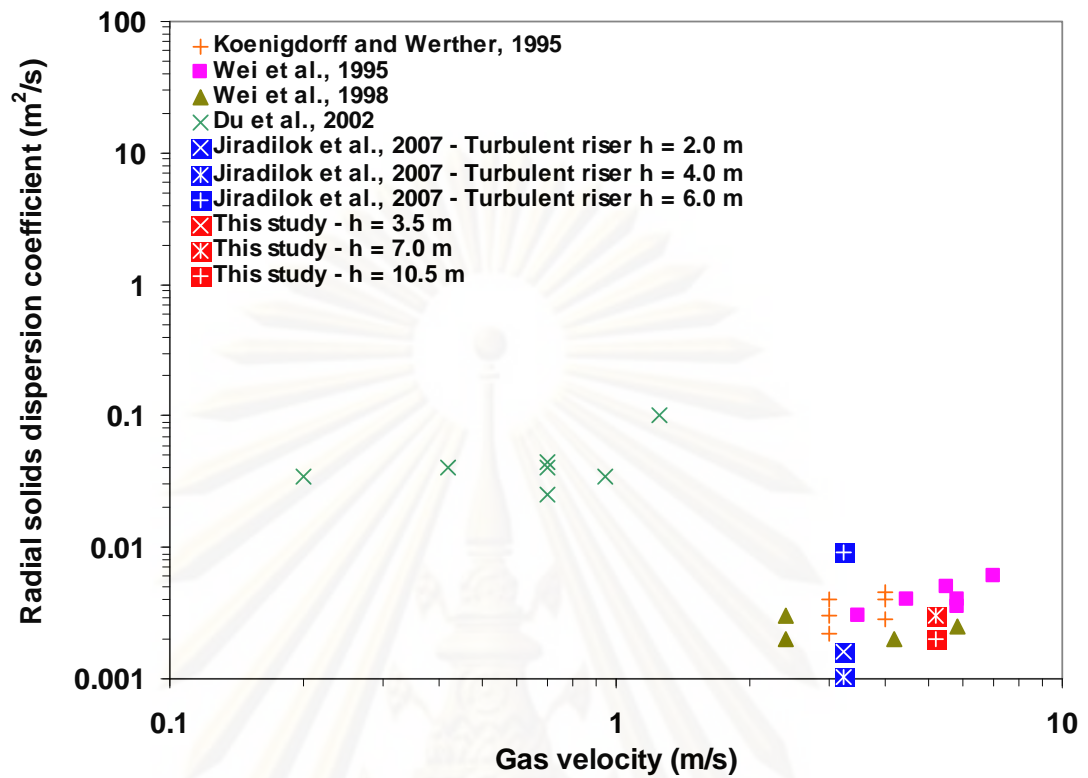
Figure 4.18 Effect of the gas velocity on experimental and computed radial solid

dispersion coefficients.
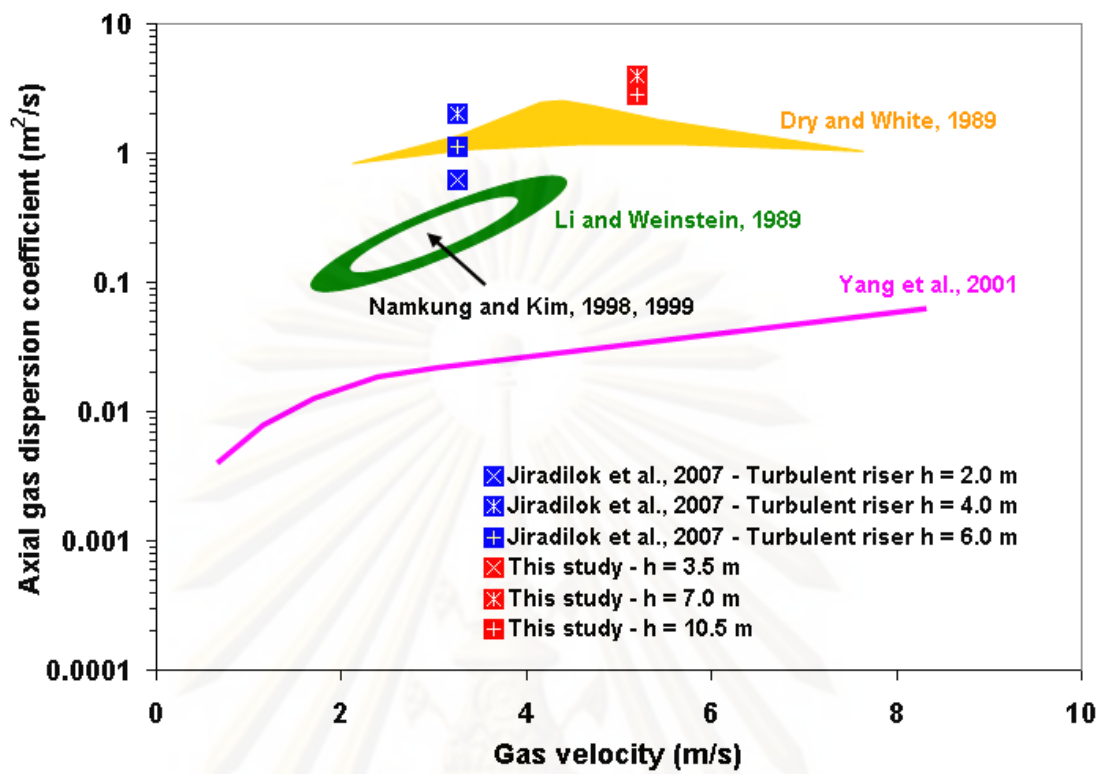
Figure 4.19 Effect of the gas velocity on experimental and computed axial gas

dispersion coefficients.
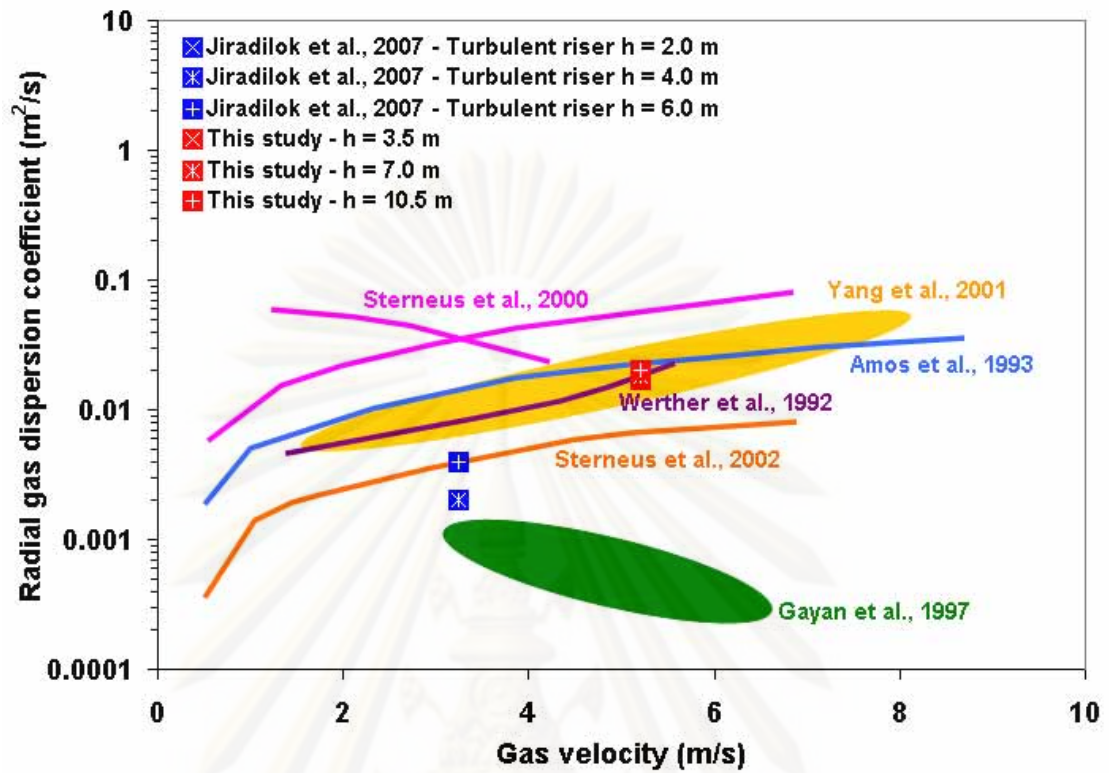
Figure 4.20 Effect of the gas velocity on experimental and computed radial gas

dispersion coefficients.
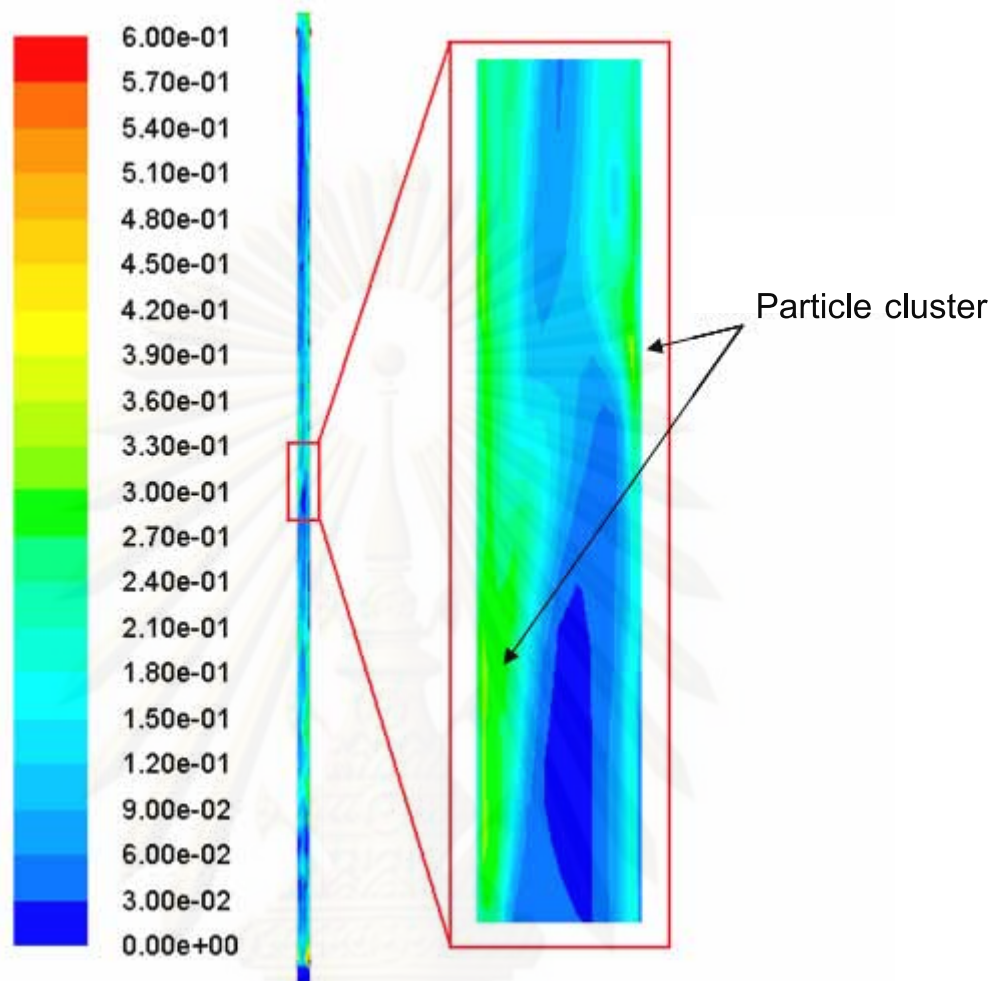
Figure 4.21 Computed instantaneous solid volume fraction at 30 s.
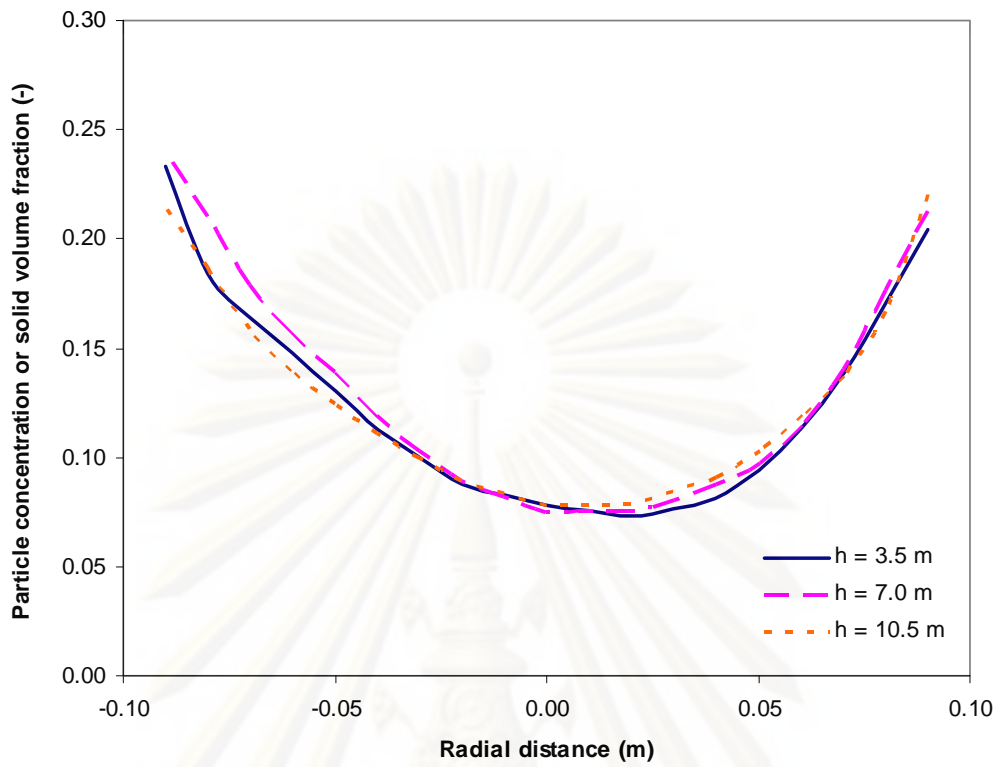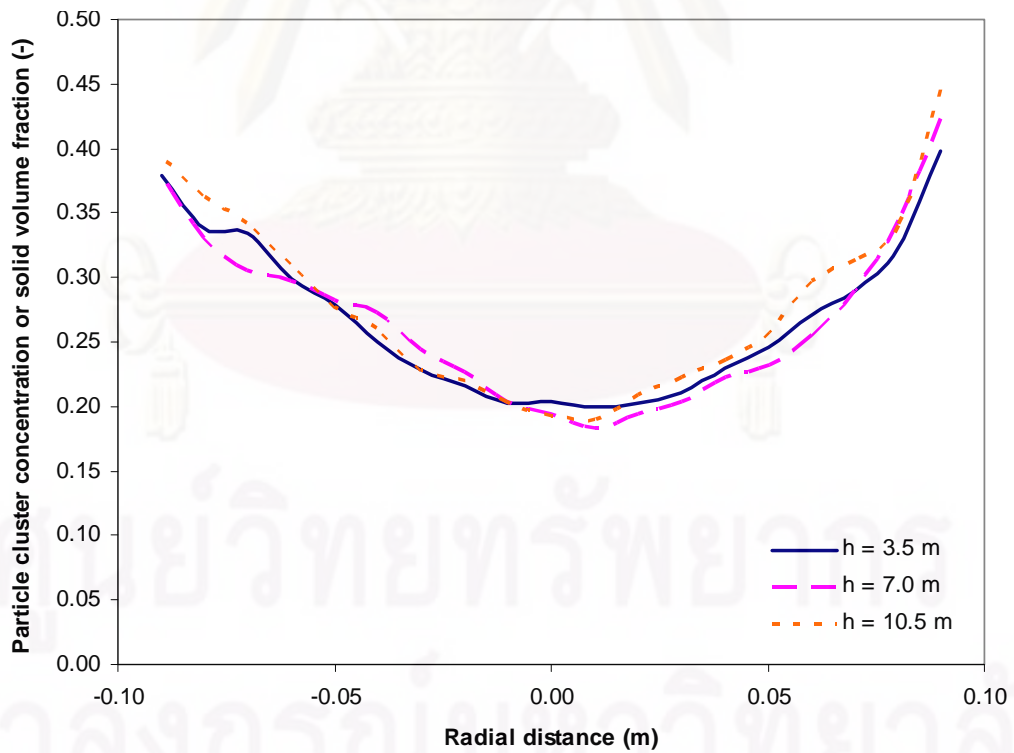
Figure 4.22 Computed (a) particle concentration and (b) particle cluster concentration

at three different heights in the riser.
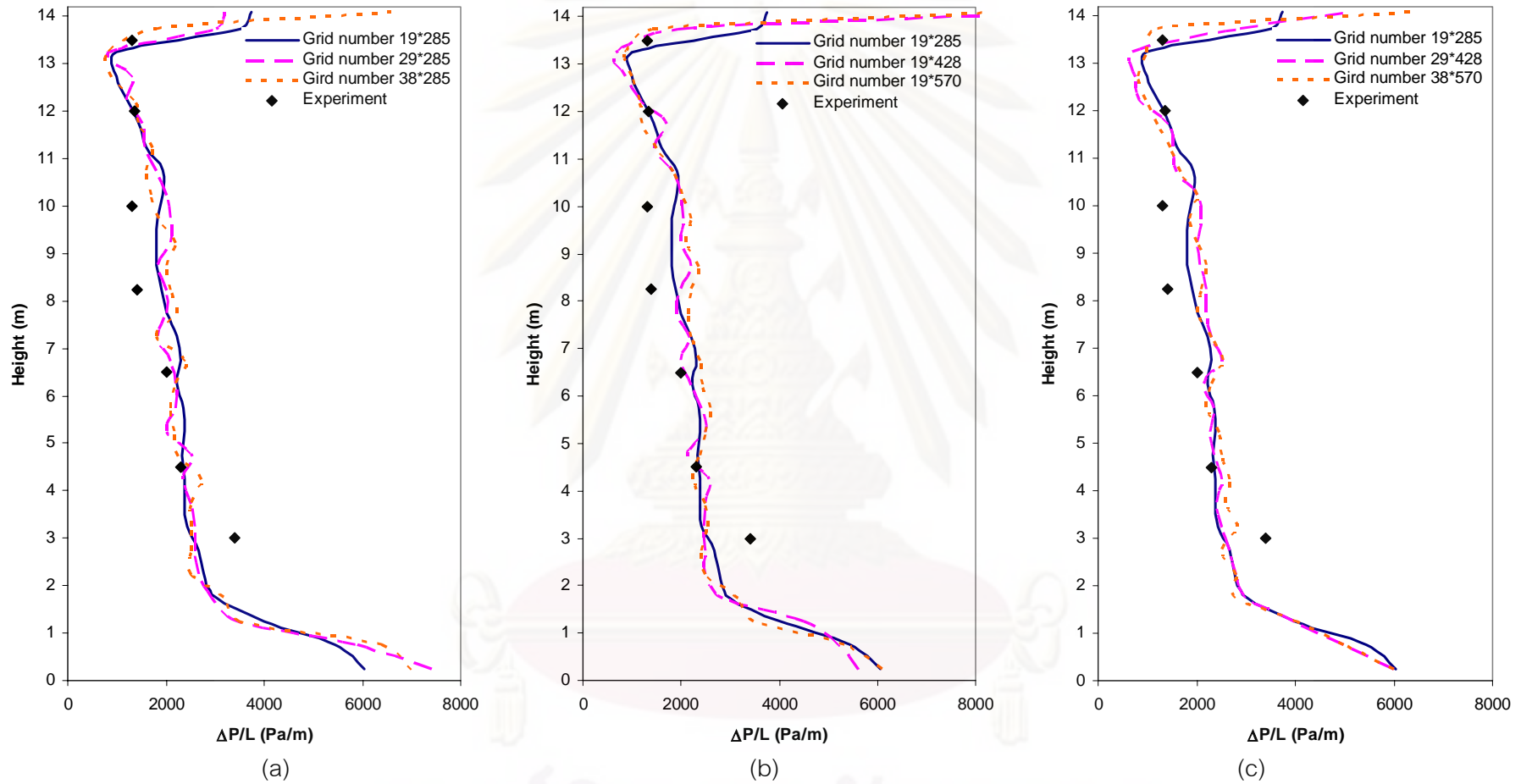
Figure 4.23 Computed time-averaged pressure drops with the change in (a) the radial direction grid number, (b) the axial direction grid number and

(c) both the radial and axial directions grid number.

CHAPTER V

KINETIC THEORY BASED COMPUTATION OF FAST FLUIDIZATION REGIME IN PSRI RISER: PART II - COMPUTATION OF MASS TRANSFER COEFFICIENT WITH CHEMICAL REACTION CONCEPT

5.1. Introduction

The design of circulating fluidized bed systems, such as gasifiers (Yoon et al., 1987; Gidaspow and Jiradilok, 2007), also requires the knowledge of mass transfer coefficients or Sherwood numbers. The heat and mass transfer coefficients are known to be much lower for fine particles than those given by correlations for large particles (Zabrodsky, 1966; Turton and Levenspiel, 1989; Kunii and Levenspiel, 1991). As mentioned in the previous chapter that the Sherwood numbers could differ up to seven orders of magnitude ranging from a low value of 10^{-5}, (Bolland and Nicolai (2001). The formation of particle clusters could be the explanation. The other explanation is that the conventional method of computing mass transfer coefficients in fluidized beds shows the effect of concentration distribution and has little to do with diffusion to an individual particle. Hence, the representation in terms of the Sherwood number is misleading.

In the previous chapter, the methodology for estimation of the Sherwood numbers is described. In this chapter, a different methodology for computation of the very low Sherwood numbers and mass transfer coefficients, with the chemical reaction is proposed. The computed Sherwood numbers agree with very small values reported in the literature. The variation of the Sherwood numbers with reactor length is similar to those found from the Leveque solution of laminar convection problems and experimental observations. The Sherwood numbers are high in the entrance region and reach a constant value.

5.2. Ozone decomposition reaction

The ozone decomposition or dissociation reaction is one of the frequently used chemical reactions for studying reactions in the circulating fluidized bed systems (Fryer and Potter, 1976; Samuelsberg and Hjertager, 1995). The ozone reactant is converted to oxygen product. The reaction can be written as;

$$2O_{3(g)} \rightarrow 3O_{2(g)}$$
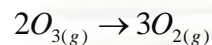
This decomposition reaction is a simple irreversible first-order catalytic reaction (Hansen et al., 2004). The rate of heterogeneous reaction (r_{O_3}) for ozone species is shown below;

$$Ozone\ decompostion\ reaction\ rate = r_{O_3} = -k_{reaction}C_{O_3}\varepsilon_s$$

where $k_{reaction}$ is the reaction rate constant, C_{O_3} is the ozone molar concentration and ε_s is the solids volume fraction or particle concentration of catalyst used in the reaction.

The first order reaction permits the total resistance to be expressed as the sum of reaction and diffusion resistances. This reaction requires only low concentrations of ozone reactant. Due to the low concentration of the reactant, the heat produced by the chemical reaction is negligible. The ozone decomposition reaction takes place at low temperature, ambient, and is therefore easy to carry out experimentally. The ozone concentration detection is rapid and accurate using fairly simple detection methods (Syamlal and O'brien, 2003). Hence, the ozone decomposition reaction is selected as the base reaction for this study.

5.2.1. Previous experimental studies on ozone decomposition reaction

There have been several attempts to analyze the experimental results from ozone decomposition in circulating fluidized bed systems. Jiang et al. (1991) investigated the baffle effects on the performance of ozone decomposition with FCC particles. It was found that, the riser with baffles gives a higher solid holdup and ozone

conversion in the gas phase than that without baffles. This was because baffles could enhance the gas-solid contact efficiency by promoting radial gas and solid mixing. Ouyang et al. (1993, 1995) measured the ozone concentration profiles in a riser of a circulating fluidized bed with impregnated FCC as the catalyst. The axial ozone concentration profiles showed a significant deviation from plug flow profiles. The radial profiles showed that the ozone concentration was lower in the wall region than in the core region, consistent with the observations of near wall region flow of solid particles. Bolland and Nicolai (2001) studied the mass transfer between gas and solids in the riser section. The highest rate of reaction was found to be in the lower section and the lowest in the upper zone of the riser. This phenomenon can be explained by means of mass transfer control in the upper zone. Zevenhoven and Järvinen (2002) computed the slip velocity between the solid particles and the surrounding gas. They obtained improved gas-solid mass and heat transfer predictions when the slip velocity was high.

5.2.2. Previous computational studies on ozone decomposition reaction

A two-dimensional model for ozone decomposition in a circulating fluidized bed reactor was studied by Schoenfelder et al. (1996). They developed their model based on the empirical data from the experiment, including the height of bottom dense zone and top dilute zone, as well as axial and radial solids concentration profiles. Therdthianwong et al. (2003) modified a two-dimensional model of Schoenfelder et al. (1996) by using two different models for solid viscosity, a semi-empirical and a kinetic theory of granular flow model. Their model gave reasonable predictions of experimentally measured values. Syamlal and O'Brien (2003) also simulated the bubbling fluidized bed reactor with the ozone decomposition to test the capability of their computational fluid dynamics code, MFIX. The MFIX code quantitatively captured the effect of hydrodynamics on the chemical reaction in the bubbling bed system. This study is the first one to compute the low mass transfer coefficients and Sherwood numbers observed experimentally in fluidized beds of fine particles.

5.3. Computational fluid dynamics simulation

5.3.1. Mathematical model

In this study, a set of governing equations, continuity, momentum, energy and gas mass species (O_3, O_2 and N_2 (air)) conservation equations with constitutive equations were solved numerically. The equations used are based on the kinetic theory of granular flow, as reviewed by Gidaspow (1994). This theory has proved its validity by many researchers (Ding and Gidaspow, 1990; Neri and Gidaspow, 2000; Gidaspow et al., 2004; Jiradilok et al., 2006, 2007). Here the modified Wen and Yu drag law (Yang et al., 2003, 2004) has been replaced with that obtained from the Energy Minimization Multi-Scale (EMMS) approach. The EMMS drag model has been proved to be an effective way for modeling a high solid mass flux system of FCC particles. The commercial CFD program FLUENT 6.2.16 was also used for modeling the system by using the Eulerian model. With this approach, governing equations in each phase are solved separately. In this study, the governing equations and constitutive equations are the same set as given in Chapter IV with the addition of the conservation of energy and species equations. The summary of the equations is given in Chapter III. Table 5.1 shows the parameters used in the simulation.

5.3.2. System description and computational domain

The Particulate Solid Research, Inc. (PSRI) challenge problem I, Knowlton et al. (1995), was also used for validating the numerical results, with the addition of the catalytic chemical reaction. The system for Fluidization VII benchmark test is shown in Figure 5.1. The validation and model verification were already shown in the previous chapter. The catalyst particles in the system were FCC particles, which are commonly used in circulating fluidized bed. The diameter (D) and height (h) of their riser were 0.2 m and 14.2 m, respectively. Since a three dimensional model requires long computation time, this study uses a two-dimensional model. The schematic drawing of the riser is depicted in Figure 5.2 (a). This simplified schematic drawing is the same as mentioned in Chapter IV. The other conditions for this simulation are listed in Table 5.1.

The computational domain of the riser used in this study, illustrated in Figure 5.2 (b), was consists of 19 non-uniform grids in radial or horizontal direction and 285 uniform grids in axial or vertical direction, with a total of 5,415 computational cells. The grid independence study is described in Appendix 5A. The models were solved by using a computer with Pentium 1.80 GHz-CPU, 2 GB RAM. It took approximately ten days of computer time to obtain 40 s of simulation time.

5.3.3. Initial and boundary conditions

At the inlet, the velocity, volume fraction, temperature and gas species composition were specified, as summarized in Table 5.1. On the other hand, at the outlet, the system pressure was specified as atmospheric pressure. Initially, there were no gas and solid phases in the riser. At the wall, an adiabatic condition was employed and a no-slip condition was applied for all velocities, except for the tangential velocity of the solid phase and the granular temperature. Here, the boundary conditions of Johnson and Jackson (1987) were used. These conditions were first applied in the kinetic theory of granular flow modeling by Sinclair and Jackson (1989). They are;

$$v_{st,W} = -\frac{6\mu_s \varepsilon_{s,max}}{\pi \phi \rho_s \varepsilon_s g_0 \sqrt{3\theta}} \frac{\partial v_{st,W}}{\partial n} \tag{5.1}$$

$$\theta_W = -\frac{\kappa_s \theta}{\gamma_W} \frac{\partial \theta_W}{\partial n} + \frac{\sqrt{3}\pi \phi \rho_s \varepsilon_s v_{s,slip}^2 g_0 \theta^{\frac{3}{2}}}{6\varepsilon_{s,max}\gamma_W} \tag{5.2}$$

where $\gamma_W = \frac{\sqrt{3}\pi\left(1-e_W^2\right)\varepsilon_s \rho_s g_0 \theta^{3/2}}{4\varepsilon_{s,max}}$.

5.3.4. Chemical reaction conditions

The information needed for chemical reaction is the reaction rate constant. From the previous experimental data, the values of reaction rate constant for ozone decomposition reaction are varied by three orders of magnitude with the activity of catalyst particle. This decomposition reaction can be catalyzed with many types of catalyst compositions, such as FCC catalyst coated with ferric nitrate (Ouyang et al.,

1993, 1995), FCC catalyst coated with ferric oxide (Jiang et al., 1991) and γ-alumina catalyst coated with ferric oxide (Pagliolico et al., 1992). In this study, four different values of reaction rate constants are used to study the effect of this parameter on the Sherwood number and mass transfer coefficient. The range of these values is selected from the literature experiments. The chosen reaction rate constants are summarized in Table 5.1.

5.4. Results and discussion

5.4.1. Calculation of Sherwood number and mass transfer coefficient

From the conservation of species equation:

$$\frac{\partial}{\partial t}\left(\varepsilon_g \rho_g y_i\right) + \nabla \cdot \left(\varepsilon_g \rho_g v_g y_i\right) = r_i \tag{5.3}$$

where t is the time, ε_g is the volume fraction of gas phase, ρ_g is the density of gas phase, v_g is the velocity of gas phase, y_i is the mass fraction of specie "i" and r_i is the reaction rate.

Integration of Equation (5.3) over time and over the riser radius (x- and z-directions) for ozone species gives the one dimensional steady state balance:

$$v_y \varepsilon_g \frac{dC_{O_3}}{dY} = r_i \tag{5.4}$$

where v_y is the velocity of gas phase in axial or vertical direction and Y is the axial or vertical distance.

The decomposition of ozone is a first order reaction. Hence, the reaction rate constant is independent of the gas concentration. Substitution of the rate of reaction in Equation (5.4) gives:

$$v_y \varepsilon_g \frac{dC_{O_3}}{dY} = -K C_{O_3} \varepsilon_s \tag{5.5}$$

where K is the overall resistance.

Solving Equation (5.5) gives:

$$\ln C_{O_3} = \ln C_{O_3,0} - \frac{K\varepsilon_s}{v_y \varepsilon_g} Y \qquad (5.6)$$

where the subscript "0" is the initial molar concentration of ozone.

In fluidized bed reactors, one measures the ozone concentration and obtains the overall resistance from Equations (5.5), (5.6) or the finite difference form of Equation (5.5). In this simulation, Equation (5.6), the time averaged, area averaged result, gives the overall resistance. The linear plot of natural logarithm of ozone molar concentration versus the height of the riser gives the slope, which further gives the overall resistance. Then, the conventional additive resistance concept permits us to compute the mass transfer coefficient. At steady state, the external mass transfer in terms of global rate is equated to the mass transfer from the bulk gas to catalyst surface (Fogler, 1999; Levenspiel, 1999; Bolland and Nicolai, 2001; Welty et al., 2001):

$$k_{mass\ transfer} a_v \left(C_{O_3} - C_{O_3,surface} \right) = k_{reaction} C_{O_3,surface} \qquad (5.7)$$

where $k_{mass\ transfer}$ is the mass transfer coefficient, a_v is the external surface per volume of catalyst and $C_{O_3,surface}$ is the surface molar concentration of ozone.

Eliminating $C_{O_3,surface}$ from Equation (5.7) and expressing the global reaction rate per unit mass of catalyst (r_p) in terms of C_{O_3} gives:

$$r_p \rho_s \varepsilon_s = \frac{1}{\dfrac{1}{k_{mass\ transfer} a_v} + \dfrac{1}{k_{reaction}}} C_{O_3} \varepsilon_s = K C_{O_3} \varepsilon_s \qquad (5.8)$$

The result from Equation (5.8) and the overall resistance from Equation (5.6) give the mass transfer coefficient as follows:

$$\frac{1}{K} = \frac{1}{k_{mass\ transfer} a_v} + \frac{1}{k_{reaction}} \qquad (5.9)$$

The Sherwood number (Sh) is then given by Equation (5.10) below:

$$Sh = \frac{k_{mass\,transfer}d_p}{D}$$

(5.10)

where d_p is the diameter of the catalyst particle and D is molecular diffusivity. Bolland and Nicolai (2001) had analyzed their ozone decomposition data in a fluidized bed using this exact method.

5.4.2. Computation and interpretation of Sherwood number and mass transfer coefficient

Figure 5.3 shows the variation of the computed time-averaged ozone molar concentration with the riser height for various reaction rate constants used in this study. Due to the reaction, all the ozone concentrations decrease with riser height. For the lowest reaction rate constant or $k_{reaction}$ = 3.96 s^{-1} case, the ozone reactant leaves the riser partially unreacted. For $k_{reaction}$ = 39.60, 99.00 and 198.00 s^{-1} cases, the ozone reactants are almost used up due to the higher of reaction rate constant.

For a first order reaction, with or without mass transfer, and constant catalyst concentration, the natural logarithm of the ozone molar concentration varies linearly with height, as given by Equation (5.6). Hence, in Figure 5.4, the ozone concentrations are presented to test these assumptions and to enable the determination of the mass transfer coefficient. The natural logarithms of computed time-averaged ozone molar concentration with the riser height for various reaction rate constants are displayed in Figure 5.4. All the graph lines are approximately linear, which verify the assumptions used in the ozone species mass balance.

The fitted equation parameters, which are the slope and the intercept, for each graph are summarized in Table 5.2. These fitted slopes are consistent with the profiles of computed ozone molar concentration in Figure 5.3. For the highest reaction rate constant or $k_{reaction}$ = 198.00 s^{-1} case, the highest slope value is obtained. The slopes decrease with decreasing reaction rate constants. The lowest slope is obtained

for the lowest reaction rate constant or $k_{reaction}$ = 3.96 s^{-1} case. From the experimental observation that the Sherwood numbers or mass transfer coefficients are not constant along the entire riser section, the slope values are separated into three regions for each graph. These three heights are at 3.5 m, 7.0 m and 10.5 m, that is the middle section of the riser. From the results in the previous chapter, these three heights have the same flow structure. However, all the slopes with the same reaction rate constant are not significantly different which also verifies with the assumption used in this study.

Table 5.3 summarizes the computed information on the Sherwood numbers and mass transfer coefficients at three different heights of the riser for various reaction rate constants. For the lowest reaction rate constant or $k_{reaction}$ = 3.96 s^{-1} case, the reaction rate constant is too low and, thus, controls the system. Therefore, the mass transfer coefficient cannot be computed using the present method of additive resistances for mass transfer and reaction. In this case, the diffusional resistances are zero. Once the reaction rate constants become high or $k_{reaction}$ = 39.60, 99.00 and 198.00 s^{-1} cases, the diffusional resistances become large and can be computed using the concept of additive resistances. Appendix 5B shows a typical numerical example. Since the overall resistance (K) is close to reaction rate constant ($k_{reaction}$), this implies that the mass transfer has an insignificant role in the chemical reaction. The reason for the low Sherwood number is its representation in terms of the particle diameter or surface area per unit volume, a_v. Equation (5.10) rewritten as,

$$Sh = \frac{k_{mass\,transfer}d_p}{D} = \frac{6k_{mass\,transfer}}{a_v D} \qquad (5.11)$$

The equation shows that for large a_v, small particles, the mass transfer coefficient must be extremely high to give a Sherwood number of two. The conventional method of computation presented here captures the small differences between the bulk and the surface concentration that are due the hydrodynamics of the fluidized bed, not due to the diffusion between the bulk and the surface concentration. The mass transfer is not as poor as is implied by the extremely small values of the Sherwood numbers, although the particle cluster formation does decrease the mass transfer.

Figure 5.5 illustrates the effect of reaction rate constants on the computed Sherwood numbers and mass transfer coefficients for three different heights of the riser. The computed Sherwood numbers and mass transfer coefficients have a similar trend because the diameter of the catalyst particle and molecular diffusivity in used this study are constant. At the height of 3.5 m or at the lower section, the Sherwood number and mass transfer coefficient have a minimum value. For the low reaction rate constant or $k_{reaction}$ = 39.60 s^{-1} case, the ozone reactant is slowly converted. This makes the reaction resistance dominant this system and results in the high values of Sherwood numbers and mass transfer coefficients. For the high reaction rate constant or $k_{reaction}$ = 198.00 s^{-1} case, the ozone reactant is almost used up. Consequently, the rate of reaction is slow. This also gives high values of Sherwood numbers and mass transfer coefficients. Thus, there exists an optimum condition at the suitable moderately reaction rate constant, at $k_{reaction}$ = 99.00 s^{-1} in this simulation. At the height of 7.0 m and 10.5 m or at the higher section, the ozone reactant is mostly converted. The conversion is higher, directly proportional to the reaction rate constant. Hence, the Sherwood numbers and mass transfer coefficients increase when the reaction rate constant increases.

Figure 5.6 shows the effect of reaction rate constants on the computed riser height-averaged Sherwood numbers and mass transfer coefficients. The average values are calculated at three different heights. The computed values of Sherwood numbers and mass transfer coefficients increase with the increasing of reaction rate constant. The explanation of this phenomenon is similar to the reason for the case at the higher section or at the height of 7.0 m and 10.5 m in the riser as shown in Figure 5.5. Thus, we can state that the mass transfer resistance decreases when the reaction rate constants increases. These study results confirm the literature results that there is a dependence of the mass transfer coefficient or Sherwood number on the reaction rate constant (Solbrig and Gidaspow, 1967; Kulacki and Gidaspow, 1967; Bird et al., 2002).

The effect of riser height on the computed Sherwood numbers and mass transfer coefficients for various reaction rate constants is displayed in Figure 5.7. The computed Sherwood numbers and mass transfer coefficients decrease with the riser

height and reach constant values at the top section for all cases. This variation of the Sherwood numbers is similar to the typical behavior in convective mass transport. The computed trend from experimental data correlation (Kato et al., 1970) is also plotted in the figure. A reasonable agreement is obtained between this study and Kato's correlations. As can be seen from Figure 5.3, the highest and lowest conversions of the ozone are obtained at the bottom and the top sections of the riser, respectively. This confirms the low mass transfer resistance and results in the high values of Sherwood numbers and mass transfer coefficients near the inlet region. Also, the mass transfer resistance is high at the upper section. The values of Sherwood numbers and mass transfer coefficients therefore decrease.

The effect of Reynolds number on experimental and computed Sherwood numbers is displayed in Figure 5.8. In this figure, the comparison of the computed Sherwood number from the particle cluster diameter concept is also shown. The computed Sherwood numbers obtained in this chapter and those from the previous chapter are lower than the experimental Sherwood numbers for large particles in fluidized and fixed bed systems. The values of Sherwood numbers and mass transfer coefficients are in reasonable agreement with the phenomena from the experimental data (Kunii and Levenspiel, 1991) and fall in the range as reviewed by Breault (2006). The Sherwood number and mass transfer coefficient from chemical reaction are of the same order of magnitude as the values from the particle cluster diameter.

5.4.3. Confirmation of reduced Sherwood number and mass transfer coefficient

The computed time-averaged ozone molar concentration versus radial distance at three different heights, with $k_{reaction}$ = 39.60 s^{-1} case, is illustrated in Figure 5.9. The results obtained only for the case with $k_{reaction}$ = 39.60 s^{-1} are shown because similar trends are observed with other reaction rate constants. The results are similar to those shown by previous researchers (Ouyang et al., 1993, 1995; Bolland and Nicolai, 2001). There is a very little ozone concentration due to the high catalyst concentration near the wall. The highest ozone concentration is at the center region.

The computed time-averaged and natural logarithm of computed time-averaged bulk and surface ozone molar concentrations with $k_{reaction}$ = 39.60 s^{-1} are displayed in Figures 5.10 (a) and 5.10 (b), respectively. The surface ozone molar concentrations are calculated using Equation (5.7). From the figures, the surface ozone molar concentration is slightly lower than the bulk ozone molar concentration due to the diluteness of the ozone molar concentration inside the catalyst or particle clusters.

Figure 5.11 shows plots of the computed instantaneous solids volume fraction and ozone molar concentrations with $k_{reaction}$ = 39.60 s^{-1} at the observed particle cluster position in Figure 5.12. The ozone concentration is not symmetric within the particle cluster due to the unequal surrounding reactant concentrations, as shown in Figure 5.9. The ozone concentration decreases when the solid volume fraction increases or when it passes through the catalyst. The Sherwood number or the mass transfer coefficient, hence, measures the effect of the ozone molar concentration distribution and reflects this mal-distribution. The formation of particle cluster increases the mass transfer resistance in the system. This makes the Sherwood number and mass the mass transfer coefficient much lower than the diffusional limit of Sherwood number, which is equal to 2. Also, the reason for low Sherwood number for fine particles can be explained using arithmetic. From Equation (5.10), a fine particle with high surface to volume ratio will have the Sherwood number lower than a large particle with low surface to volume ratio. To verify the explanation, the conventional and new computed Sherwood numbers with $k_{reaction}$ = 39.60 s^{-1} is displayed in Figure 5.13. For the new computed Sherwood number, the particle diameter in Equation (5.10) is changed to the particle cluster diameter. The results are plotted versus the riser height and compared with the computed trend from experimental data correlation (Kato et al., 1970). The computed Sherwood numbers based on particle diameter are significantly lower than the computed Sherwood numbers based on particle cluster diameter. These results also infer that the convection to diffusion ratio of fine particle is lowered than large particle.

The reduction of the Sherwood number or mass transfer coefficient has thus been confirmed which can be explained by the particle cluster formation.

5.5. Conclusions

1. From additive diffusional and chemical resistance concept, the computed Sherwood number is of the order of 4×10^{-3} and the mass transfer coefficient is of the order of 2×10^{-3} m/s, in agreement with measured literature experimental data for fluidization of small particles.

2. The Sherwood number or mass transfer coefficient is high near the inlet section, and decreases to a constant value with the height of the riser. This is similar to the normal behavior of the Sherwood number in convective mass transfer process (Kato et al., 1970).

3. The Sherwood number or mass transfer coefficient varies slightly with reaction rate constant. For the higher reaction rate constant case, the ozone reactant is almost used up which makes the rate of reaction to be slower. Therefore, the computed values of Sherwood numbers and mass transfer coefficients increase with the increasing reaction rate constant.

4. In this study, two explanations are possible for the low Sherwood numbers measured in the fluidization of fine particles. One explanation is due to the particle cluster formation studied in the previous chapter. The second explanation is that the conventional method of computing the mass transfer coefficients does not measure the diffusional resistance to the particles implied by the conventional Sherwood number representation. However, it shows the effect of concentration mal-distribution.

Appendix 5A. The grid independence study

To confirm that the results are grid independent of grid size, the increments of grid numbers in both the radial and axial directions were performed. The comparison of the Sherwood numbers and the mass transfer coefficients with the change in grid number is summarized in Table 5.4. Four different values of reaction rate constants were selected for study. For each reaction rate constant, the computed values are approximately same with all the grid number cases. The minimum and maximum mass transfer coefficient error percentages compared with the lowest grid number case are 0.29 and 4.52 %, respectively. This indicates that all the grid number cases are sufficiently fine for providing reasonably good grid independence results. However, the computational power currently available is still a significant restriction for using large number of grids. Therefore, the computational domain which consists of 19 non-uniform grids in radial direction and 285 uniform grids in axial direction was chosen in this study.

Appendix 5B. An example of Sherwood number and mass transfer coefficient calculation, explaining our argument for good mass transfer in fluidized beds

An example of Sherwood number and mass transfer coefficient calculation is illustrated for the reaction rate constant equal to 39.60 s^{-1} case at a height of 3.5 m. The computed time-averaged and natural logarithm of computed time-averaged ozone molar concentration are displayed in Figures 5.3 and 5.4, respectively. The obtained slope and the intercept are shown in Table 5.2. The slope for this case is -0.7584 and the intercept is -13.8290. From the simulation, the computed volume fraction of the solid phase is 0.1289, the computed volume fraction of the gas phase is 0.8711 and the velocity of gas phase in axial direction is 6.0115 m/s. Substitution of all the values into Equation (5.6) to obtain the overall resistance gives:

$$-\frac{K(0.1289)}{(6.0115)(0.8711)} = -0.7584$$

Overall mass transfer coefficient, $K = 30.81$ s^{-1}.

The mass transfer coefficient is calculated from Equation (5.9):

$$\frac{1}{K} = \frac{1}{k_{mass\ transfer}a_v} + \frac{1}{k_{reaction}} \qquad (5.9)$$

With $\qquad d_p \qquad = 76 \times 10^{-6}$ m

$\qquad\qquad\qquad a_v \qquad = (3 \times 4\pi(\text{particle radius}^2)) / (4\pi(\text{particle radius}^3))$

$\qquad\qquad\qquad\qquad = 3/\text{particle radius}$

$\qquad\qquad\qquad\qquad = 3/(d_p/2)$

$\qquad\qquad\qquad\qquad = 3/((76 \times 10^{-6})/2) = 78947.37$ m^{-1}

$\qquad\qquad\qquad k_{reaction} = 39.60$ s^{-1}

Note that the overall resistance, $1/K$, and the reaction resistance, $1/k_{reaction}$, are close to each other. This implies that the mass transfer resistance is small.

Therefore, $\quad k_{mass\ transfer}a_v \quad$ = 138.71 s^{-1} $\quad$ and

$$k_{mass\ transfer} \quad = 0.0018\ \text{m/s}$$

The Sherwood number is calculated from Equation (5.10);

$$Sh = \frac{k_{mass\ transfer}d_p}{D} \tag{5.10}$$

With $\quad\quad D \quad$ = 2.88×10^{-5} m^2/s

Therefore, $\quad Sh \quad$ = 0.0046

Figure 5.13 shows that the Sherwood number based on the particle cluster diameter, calculated to be 0.0087 to 0.0101 m in the previous chapter, is 0.62, close to a typical value for diffusion to a particle.

Table 5.1 Parameters used for the simulation.

Symbol	Description	Value
D	Diameter of riser	0.20 m
h	Height of riser	14.20 m
ρ_g	Gas density	1.2 kg/m^3
μ_g	Gas viscosity	2×10^{-5} kg /m s
ρ_s	Particle density	1712 kg/m^3
d_p	Diameter of particle	76 μm
v_g	Gas inlet velocity	5.200 m/s
T_g	Gas inlet temperature	298.15 K
y_{O_3}	Ozone species mass fraction inlet	0.00004
y_{Air}	Air species mass fraction inlet	0.99996
v_s	Solid inlet velocity	0.476 m/s
T_s	Solid inlet temperature	298.15 K
ε_s	Solid inlet volume fraction	0.60
e	Restitution coefficient between particles	0.95
e_W	Restitution coefficient between particle and wall	0.90
ϕ	Specularity coefficient	0.50
$k_{reaction}$	Reaction rate constant	3.96, 39.60, 99.00 and 198.00 s^{-1}

Table 5.2 The fitted equation parameters with various reaction rate constants used in this study.

Model equation: $ln\ C_{O3}$ = Slope × Y + Intercept

No.	$k_{reaction}$ (s^{-1})	Riser height (m)	Slope	Intercept
1	3.96	3.5	-0.1680	-13.8290
		7.0	-0.1375	-13.8290
		10.5	-0.1236	-13.8290
2	39.60	3.5	-0.7584	-13.8290
		7.0	-0.6630	-13.8290
		10.5	-0.6319	-13.8290
3	99.00	3.5	-1.4370	-13.8290
		7.0	-1.3074	-13.8290
		10.5	-1.2216	-13.8290
4	198.00	3.5	-2.3236	-13.8290
		7.0	-2.0776	-13.8290
		10.5	-1.9759	-13.8290

Table 5.3 Computed information on the Sherwood numbers and mass transfer

coefficients at three different heights of the riser.

No.	$k_{reaction}$ (s⁻¹)	Riser height (m)	$k_{mass\ transfer}a_v$ (s⁻¹)	$k_{mass\ transfer}$ (m/s)	Sherwood number (-)
1	3.96	3.5	-	-	-
		7.0	-	-	-
		10.5	-	-	-
		Averaged	Reaction controlled	Reaction controlled	Reaction controlled
2	39.60	3.5	138.71	0.0018	0.0046
		7.0	86.35	0.0011	0.0029
		10.5	78.90	0.0010	0.0026
		Averaged	101.32	0.0013	0.0034
3	99.00	3.5	132.18	0.0017	0.0044
		7.0	110.07	0.0014	0.0037
		10.5	109.51	0.0014	0.0037
		Averaged	117.25	0.0015	0.0039
4	198.00	3.5	182.33	0.0023	0.0061
		7.0	136.23	0.0017	0.0046
		10.5	132.60	0.0017	0.0044
		Averaged	150.38	0.0019	0.0050

Table 5.4 The computed Sherwood numbers and mass transfer coefficients due to the effect of grid number.

No.	$k_{reaction}$ (s^{-1})	Grid number (radial direction × axial direction)	$k_{mass\,transfer}a_v$ (s^{-1})	$k_{mass\,transfer}$ (m/s)	Sherwood number (-)
1	3.96	19 × 285	-	-	-
		29 × 428	-	-	-
		38 × 570	-	-	-
2	39.60	19 × 285	101.32	0.0013	0.0034
		29 × 428	99.02	0.0013	0.0033
		38 × 570	96.74	0.0012	0.0032
3	99.00	19 × 285	117.25	0.0015	0.0039
		29 × 428	115.30	0.0015	0.0039
		38 × 570	116.92	0.0015	0.0039
4	198.00	19 × 285	150.38	0.0019	0.0050
		29 × 428	153.23	0.0019	0.0051
		38 × 570	151.77	0.0019	0.0051
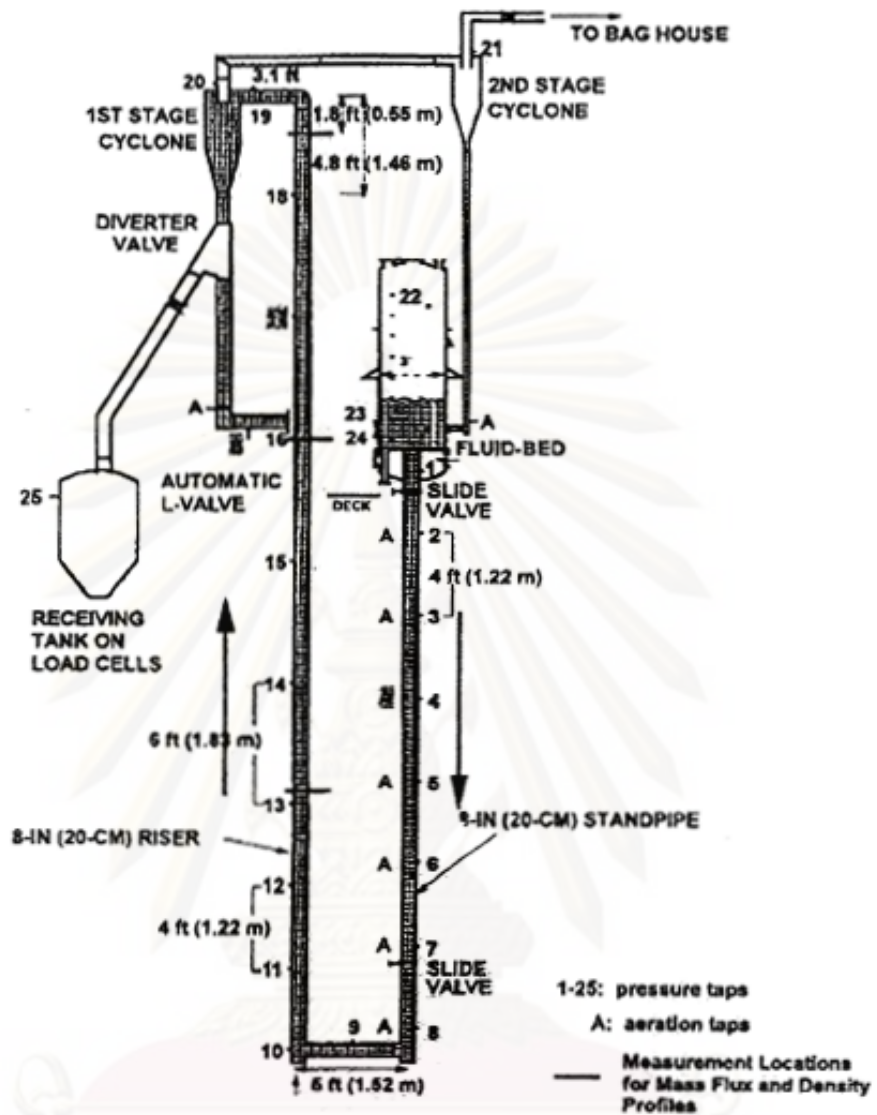
Figure 5.1 Schematic drawing of a 20 cm diameter circulating fluidized bed test unit

for the Fluidization VII benchmark test.
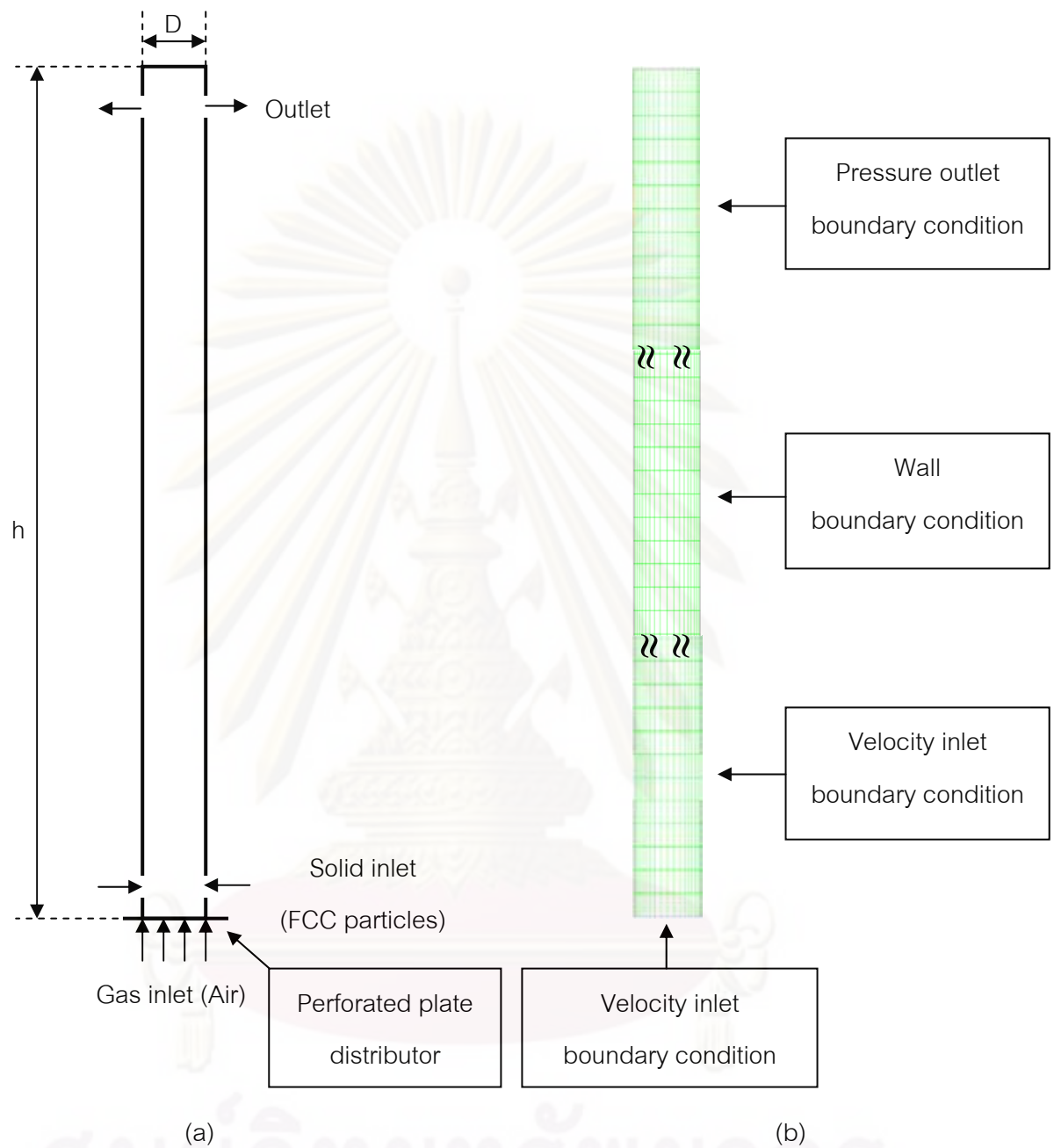
Figure 5.2 (a) Schematic drawing and (b) computational domain with their boundary

conditions of a simplified riser used in this study.
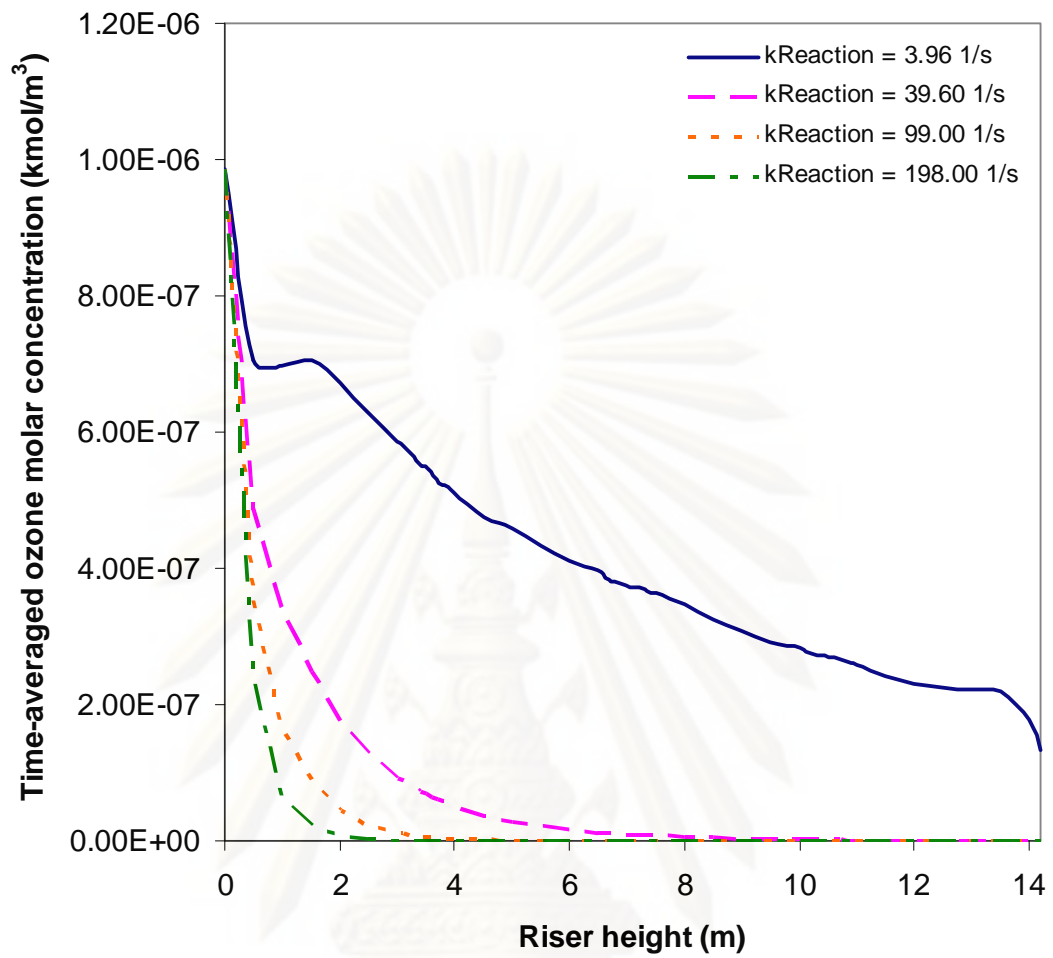
Figure 5.3 Computed time-averaged ozone molar concentration with various reaction rate constants.
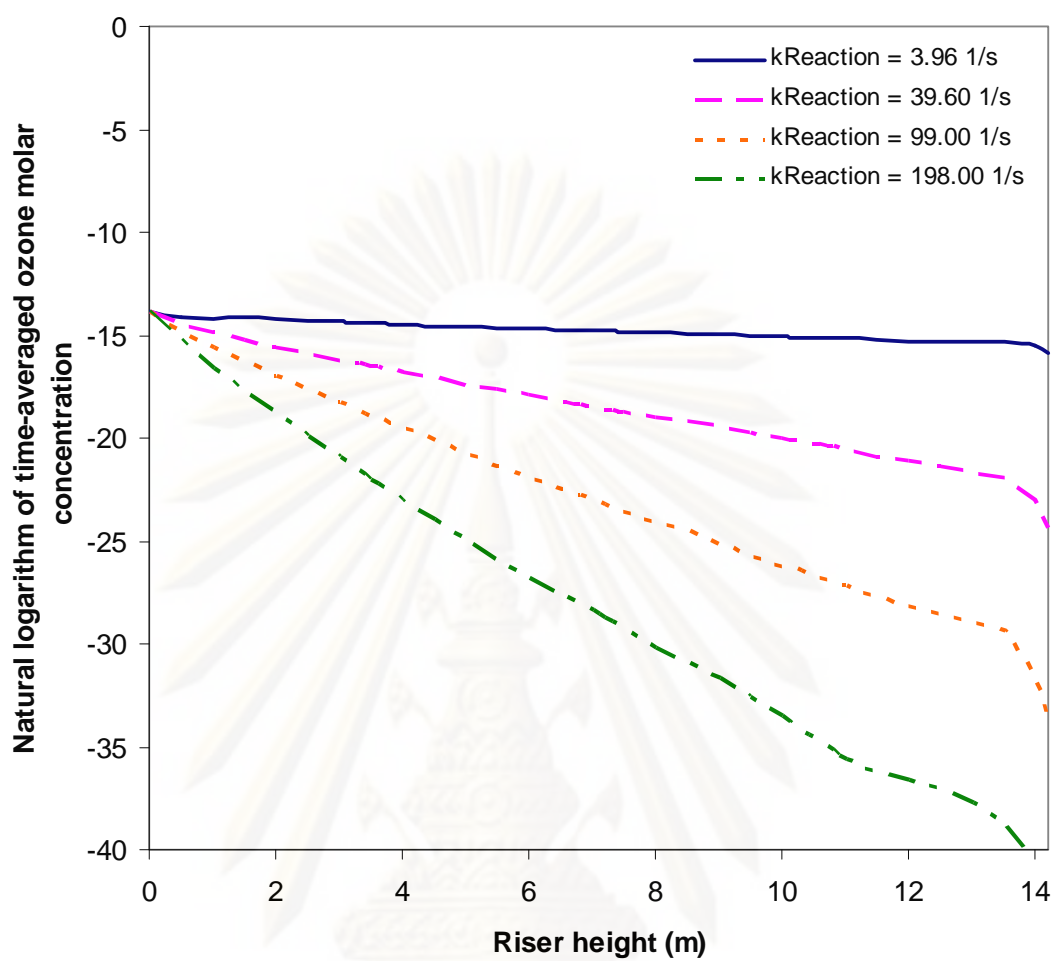
Figure 5.4 Test of model for computation of mass transfer coefficients.
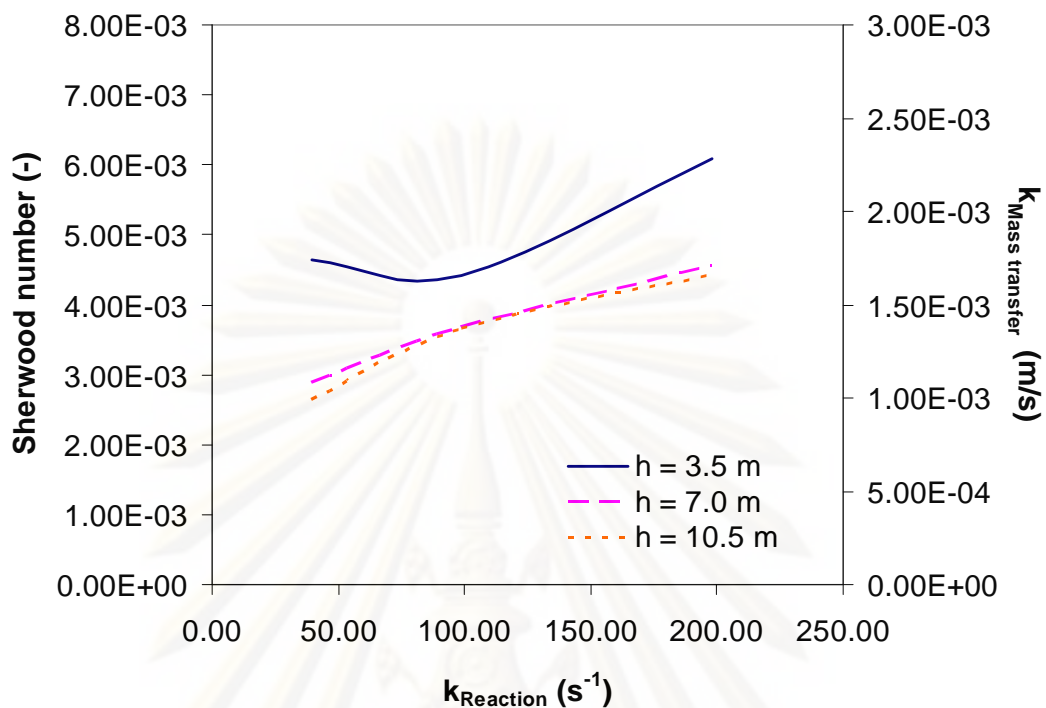
Figure 5.5 Effect of reaction rate constants on computed Sherwood numbers and mass transfer coefficients.
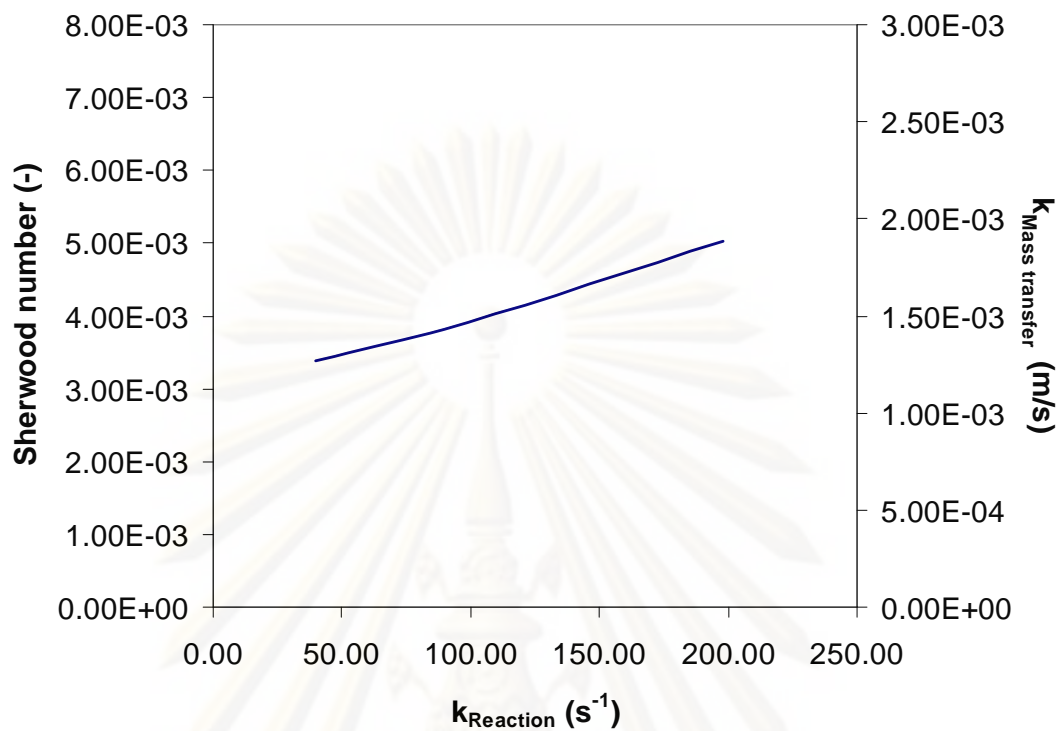
Figure 5.6 Effect of reaction rate constants on computed riser height-averaged

Sherwood numbers and mass transfer coefficients.
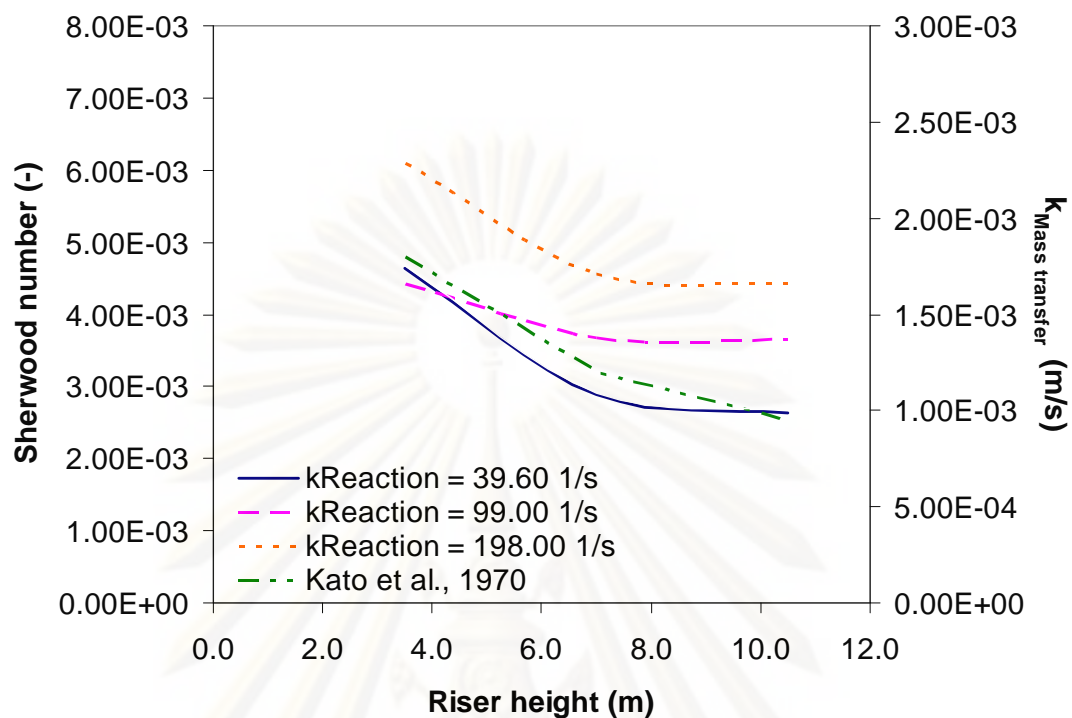
Figure 5.7 Effect of riser height on computed Sherwood numbers and
mass transfer coefficients.
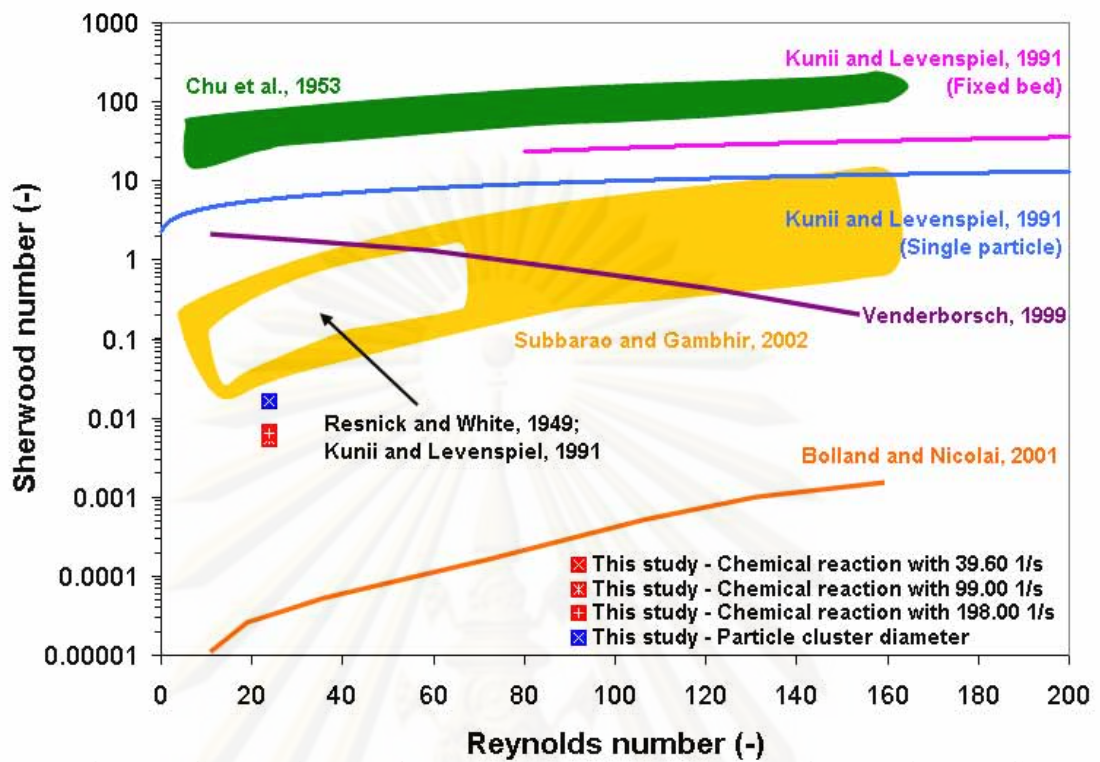
Figure 5.8 Effect of Reynolds number on experimental and

computed Sherwood numbers.
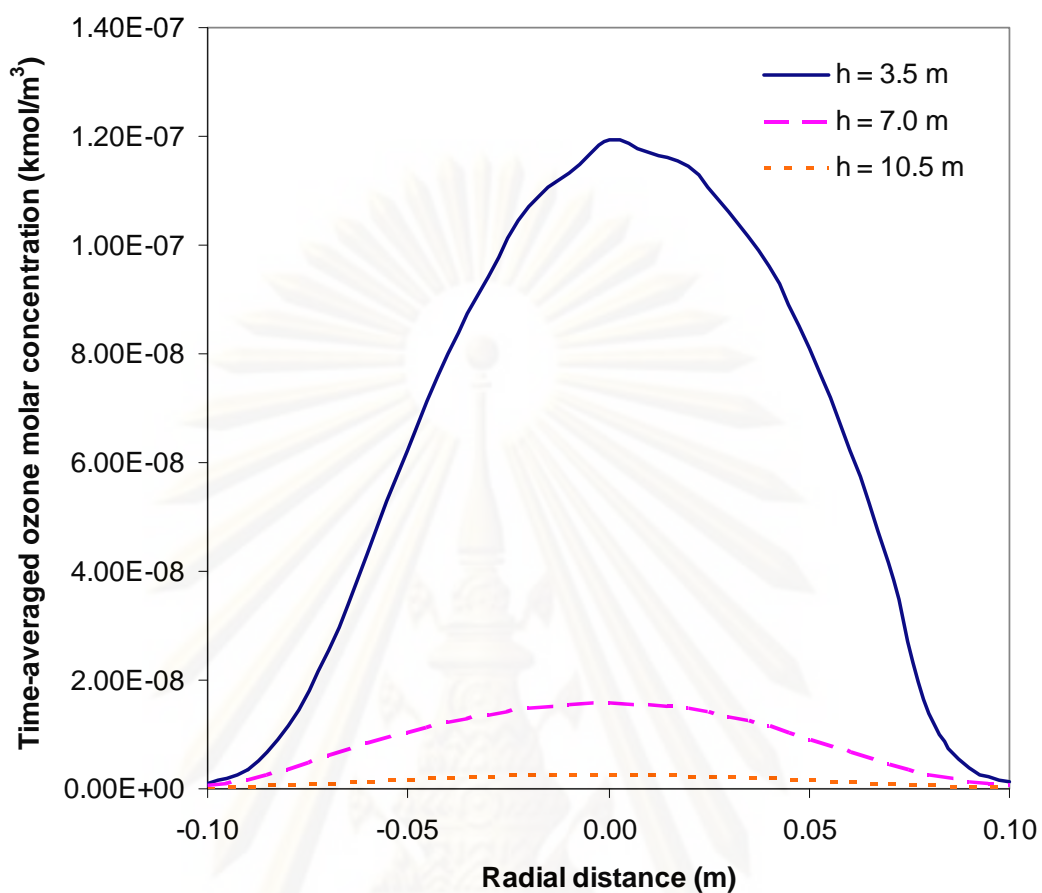
Figure 5.9 Radial distribution of computed time-averaged ozone molar concentration at three different heights with $k_{reaction}$ = 39.60 s^{-1}.
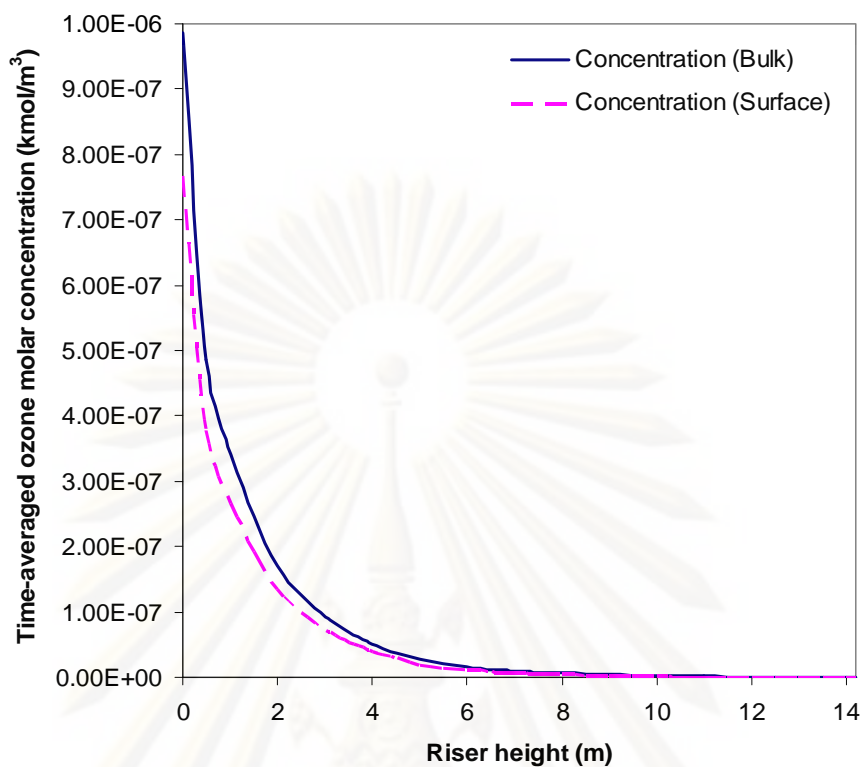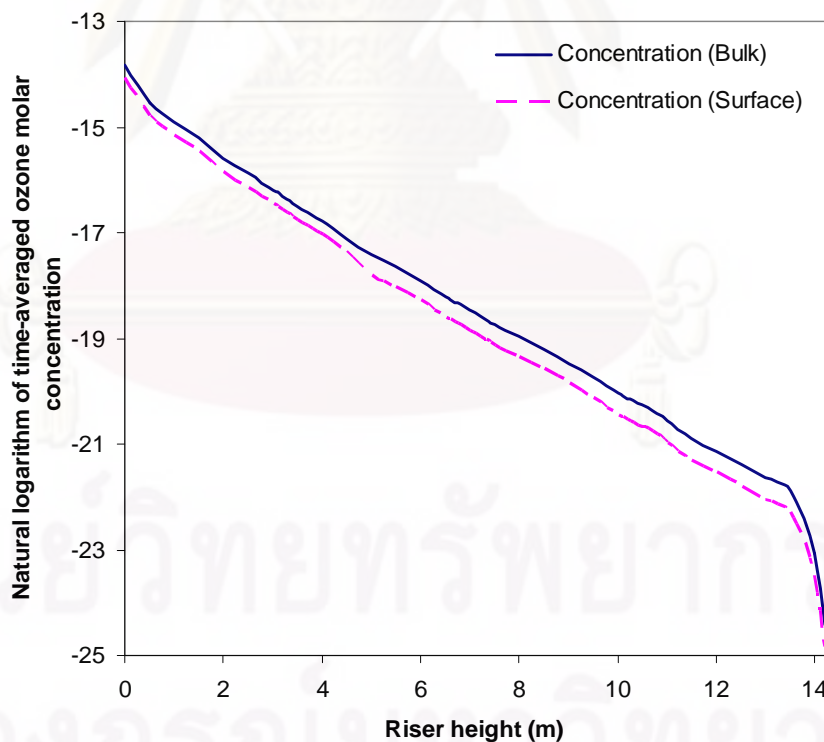
Figure 5.10 (a) Computed time-averaged and (b) natural logarithm of computed time-averaged of bulk and surface ozone molar concentrations with $k_{reaction}$ = 39.60 s^{-1}.
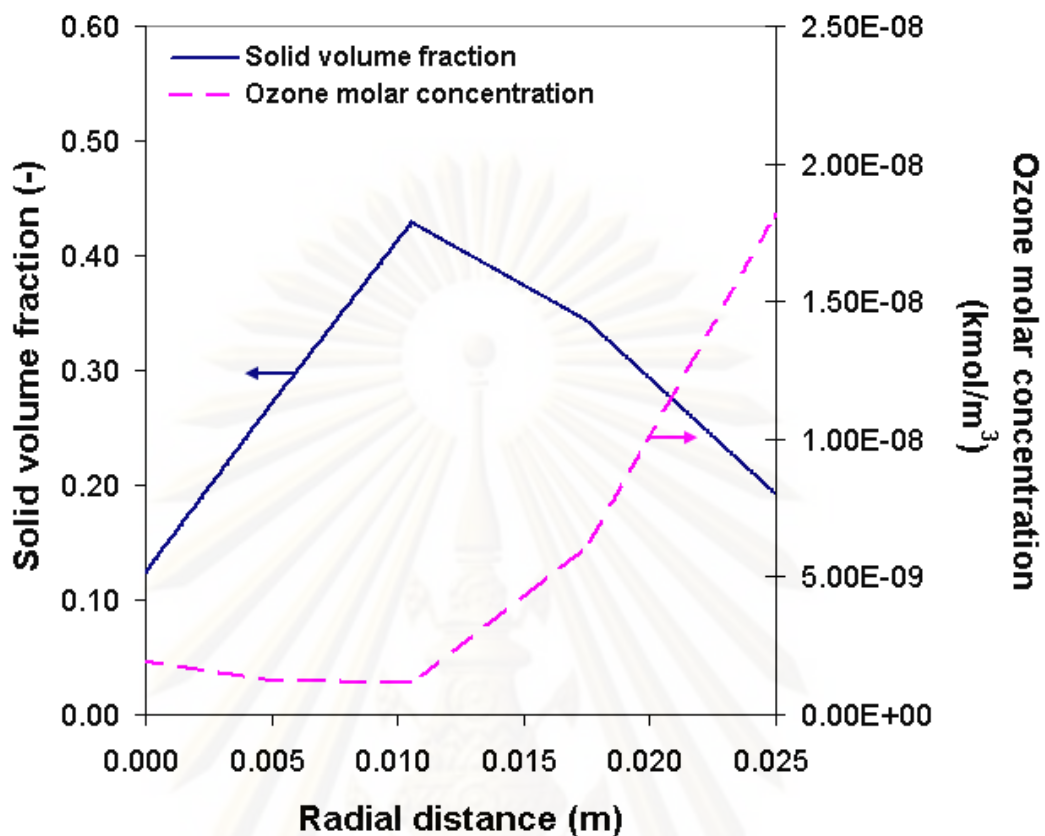
Figure 5.11 Variation of instantaneous solid volume fraction and ozone molar concentration profiles with $k_{reaction}$ = 39.60 s^{-1} in the observed particle cluster.
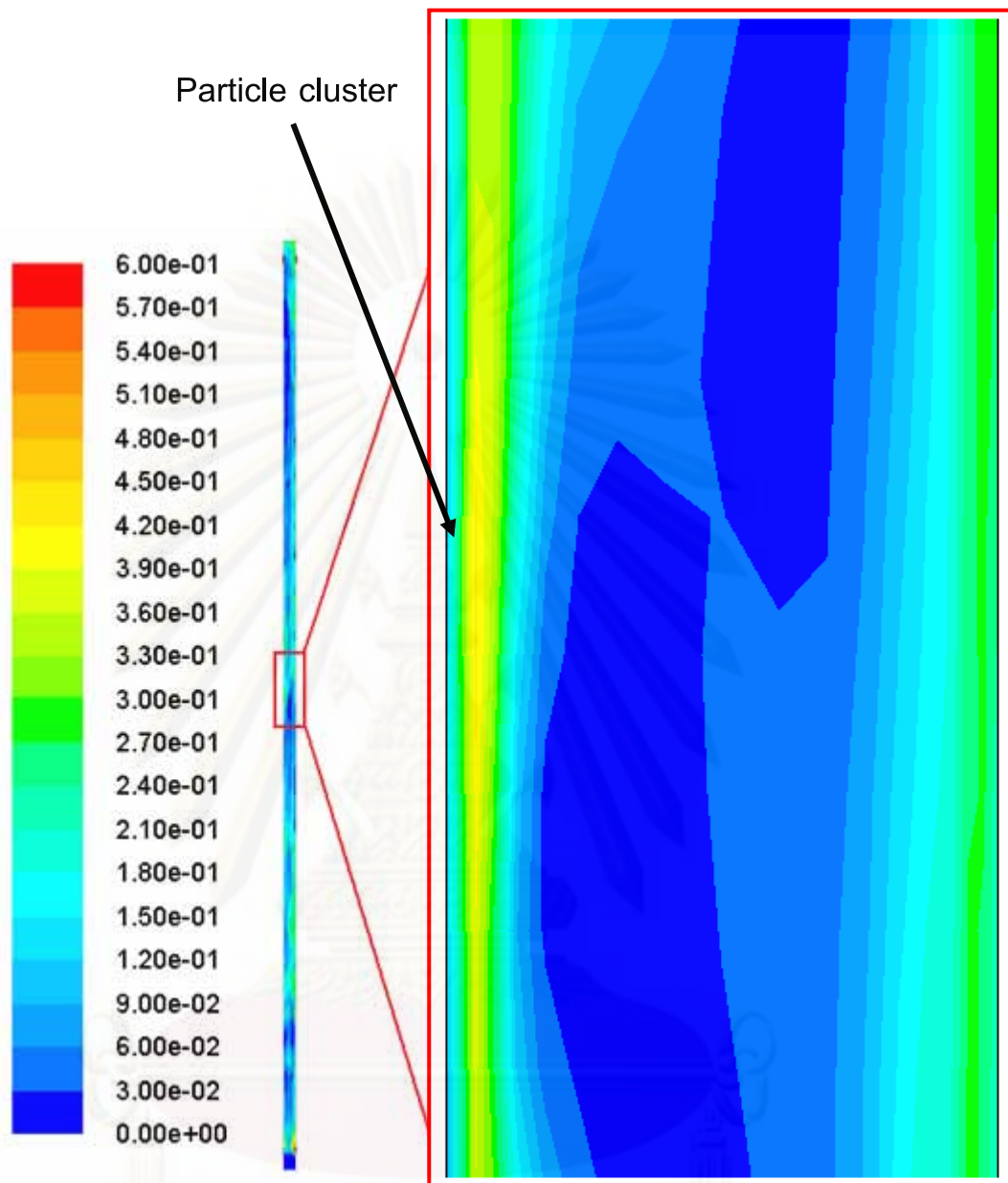
Figure 5.12 Contour of the computed instantaneous solid volume fractions

in the riser at 30 s.
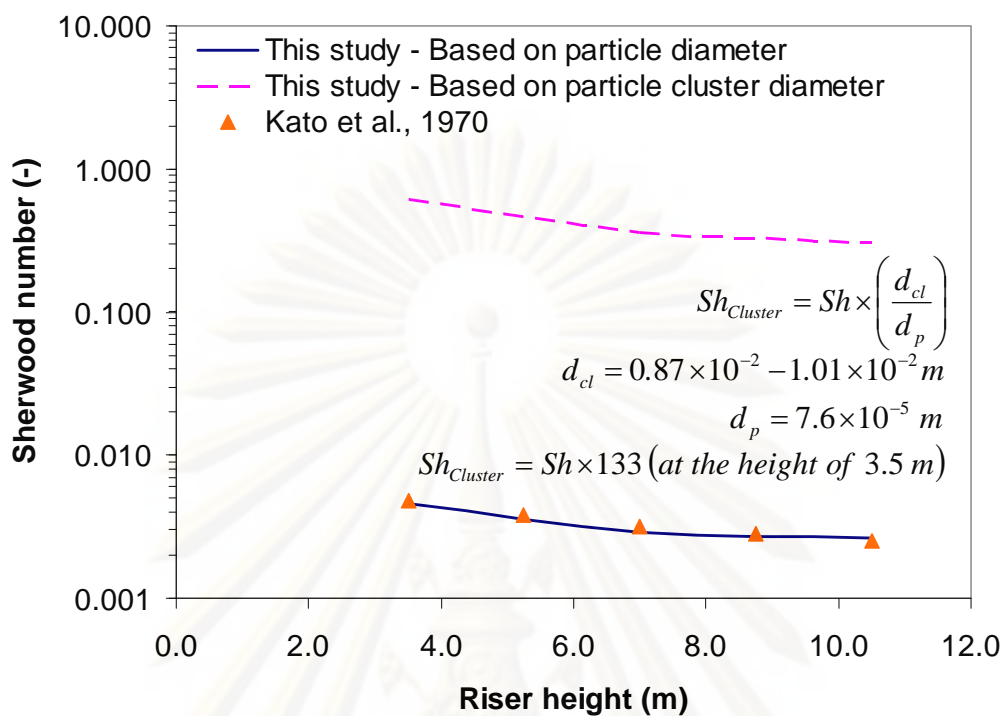
Figure 5.13 Comparison of the computed Sherwood numbers based on particle

diameter (Sh) and particle cluster diameter ($Sh_{Cluster}$) with $k_{reaction}$ = 39.60 s^{-1}.

For $Sh = 0.0046$, $Sh_{Cluster} = 0.62$ at the height of 3.5 m.

CHAPTER VI

EFFECT OF CIRCULATING FLUIDIZED BED REACTOR RISER
GEOMETRIES ON CHEMICAL REACTION RATES BY USING CFD
SIMULATIONS

6.1. Introduction

According to many advantages such as the continuous process coupled with high gas and solids throughputs and the ease of solid handling, a circulating fluidized bed reactor (CFBR) has been widely used in many industrial processes (Grace et al, 1997). Typically, this kind of the reactors is used for cracking, combustion and gasification processes. The Fluid Catalytic Cracking (FCC) or cracking reaction is used for converting crude oil into variety of higher-value light products, such as gasoline. Inside the riser, the feed vapor is cracked and the reaction is enhanced by the catalyst. The mean size of the FCC particles (catalysts) is about 40-80 μm and particle densities 1,000-1,800 kg/m^3, representing Geldart group A. The net solids flux is 400-1,200 kg/m^{2}s. In combustion and gasification reactions, the medium solids are coarser and denser than those in the FCC, with the particle sizes of 100-300 μm and particle densities of 1,800-2,600 kg/m^3 (Geldart group B), such as silica sands. The fuels used include coal, petroleum coke, biomass and different municipal wastes. The typical reactor, net solids flux is 10-100 kg/m^{2}s. These chemical reactions have their own characteristics such that combustion has fast reaction rate. On the contrary, the rate of gasification is slow. According to the old rules of thumb, time, temperature, and turbulence are three major factors for a good chemical reaction. The excellent internal and external particle recirculations provide long residence time and adequate energy to the particles. The high degree of gas-solid mixing in the CFBR provides the turbulence that is necessary for good reaction conversion.

In the CFBR, the riser section is the part that the chemical reaction normally occurred. Considering this section, the suitable geometric design can greatly enhance the reaction characteristics. There are many research groups focusing on

designing this section. Gupta and Burruti (2000) found that the core-annulus structure was changed due to exit bended angle. van der Meer et al. (2000) used square cross-sectional riser system and observed slightly higher solids downward flux halfway between the corners, near the walls. They explained that their high solids downflow might be due to secondary flow in the square duct which conveyed solids from the center of the riser towards the corners, forced them to travel along the walls and returned them back to the center at the halfway between the corners. Kersten et al. (2003) observed that dividing the riser into stages could minimize the back-mixing of gas and particles in the system. The effect of the riser exits has shown a modest influence upon the particle residence time distribution (Harris et al., 2003). Huilin et al. (2003) found that the increase of riser diameter lead to higher particle concentration at the riser walls, while lower particle concentration at the center. Huilin et al. (2006) also observed that the uniform particle distribution could be achieved by changing the riser geometry. Wang et al. (2008) performed an experiment in the CFBR with baffles and found that positioning the baffles at different heights was more effective in increasing the solid density of the center region. Similar to CFBR, there are many investigators trying to investigate the effect of geometry for other flow systems. Sparrow et al. (1988) and Sparrow and Ruiz (1988) conducted an experiment with convergent and divergent single-phase flow channels. They stated that the changing angle was strongly affected the system temperature profile. Chen et al. (1996) analyzed particle concentration in a convergent channel by tracing particle motions and found that the deposition rate of particles depended on the convergent angle of system channel. Nevertheless, all of the previous researches have only designed new system geometry to solve the hydrodynamics problems. No ones has been designed this section yet to solve the problem of the chemical reactions.

In this chapter, the novel designs of the riser section have been studied by using commercial CFD (Computational Fluid Dynamics) simulation package, FLUENT 6.2.16. The concept of the new designs is to study the parameters on reactor geometry that will have effects on the chemical reactions. The results can be divided into two main

sections. In the first section, the hydrodynamics responses under different riser geometries and conditions were simulated and used their results to develop the criteria for specifying different riser geometry with different reaction characteristics. In the second section, the proposed criteria were proved by adding a simple propane combustion reaction. The chemical reaction responses under different riser geometries and conditions were studied. In addition, the in-depth parameters those described the hydrodynamics were computed. They were used to describe the observed chemical reaction responses.

6.2. Novel design of the riser geometries

In this topic, the new designs of riser column were explained. The new designs are based on the improvement of main factors that have an effect on reaction characteristics which are turbulence, time and temperature. The assumption is that altering riser cross-sectional area can change the hydrodynamics and system conversion. Figure 6.1 (a) illustrates the base case of riser geometry that is a typical riser. The first design concept is to obtain the turbulence or better mixing in the riser column (Huilin et al., 2006). This riser is designed to be tapered-out as shown in Figure 6.1 (b). The second design concept is to enhance both residence time and temperature distribution in the riser (Kersten et al., 2003). This riser is designed to be tapered-in as depicted in Figure 6.1 (c). All of these risers have the same height (h). Diameters (D) of these risers are the same at the middle height of each riser (h/2). The along column diameter of typical riser is D. Tapering is defined by the inclined angle (α) which is also based on the middle height. The inclined angles were varied. Therefore, the diameter at the inlet and outlet of tapered-out riser are $D + h \tan \alpha$ and $D - h \tan \alpha$, respectively. On the other hand, the diameter at the inlet and outlet of tapered-in riser are $D - h \tan \alpha$ and $D + h \tan \alpha$, respectively.

6.3. CFD modeling of CFBR risers: hydrodynamics responses

6.3.1 Computational fluid dynamics simulation

6.3.1.1. Mathematical model

Here, a set of governing equations, mass and momentum conservation equations, and constitutive equations were solved numerically. The numerical solution is considered because of the complexity to solve as analytical solution. To completely describe the governing equations, appropriate constitutive equations were specified to describe the physical properties in each phase. The equations used in this work are based on the kinetic theory of granular flow developed by Gidaspow (1994). This theory has been proven its validity by many researchers (Sun and Gidaspow, 1999; Neri and Gidaspow, 2000; Huilin and Gidaspow, 2003; Yunhau et al., 2006; Andreux et al., 2007). Later on modified Wen and Yu drag law, Yang et al. (2003, 2004) applied the theory with energy minimization multi-scale (EMMS) approach to calculate the interphase exchange coefficient (drag model) by a concept of cluster. EMMS drag model has also been proven to be an effective way for modeling co-existence of dilute and dense regimes. In this section, in case of low solid mass flux system, the original Gidaspow drag model was used. In case of high solid mass flux system, the new EMMS drag model was employed to improve the accuracy of the computational results. There are several numerical models for gas-solid two-phase flow simulation such as Lagrangian model and Eulerian model. Here, the Eulerian model was selected because the volume fractions of the solid or granular phase in this system cannot be occupied by the gas phase. With this approach, governing equations in each phase are solved separately. A summary of the governing equations and constitutive equations are given in Chapter III. Since the EMMS drag model is not available in the FLUENT 6.2.16 program, the new additional UDF (user-defined function) code in C programming language was added as shown in Appendix C. According to the previous literatures, there has not been enough information on the values of operating parameters, especially for the riser system using Geldart group B particles. The optimization of these values has been done to get the

optimized parameter values as summarized in Table 6.1. All of these make the models different from the other previous models that had been used in this kind of system.

6.3.1.2. System description and computational domain

To verify the numerical models, the experimental results by Knowlton et al. (1995) were chosen as the base case. The particles in their system were FCC particles (Geldart group A) and silica sands (Geldart group B), which are two commonly used particles in CFBR. Their riser section was referred as a typical riser. The diameter (D) and height (h) of the riser were 0.2 m and 14.2 m, respectively. Since three dimensional model requires long computation time, this section uses two dimensional model for the simulation. The schematic drawing of the riser is depicted in Figure 6.1 (a). This schematic drawing is based on Benyahia et al.'s result (2000, 2002) which was a two inlet-outlet design for the two dimensional riser to obtain the simulation result for three dimensional riser experiment. This was done because a one inlet-outlet design for two-dimensional riser could not capture the realistic mixing throughout the height of the riser. This simplified schematic drawing is the same as mentioned in Chapter IV. The gas was fed to the system at the bottom of the riser. The solid particles were fed from the two side-inlets at 0.3 m above the bottom of the riser with a width of 0.1 m. The gas and solid exited through two symmetric side outlets at 0.3 m below the top of the riser with a width of 0.1 m (similar width to the side-inlets). The other conditions for this simulation are listed in Table 6.1.

After validating the typical riser model, the new designs of the riser geometry have been constructed and simulated with the inclined angle of 0.3 degree (for Geldart group A and B particles) and 0.5 degree (for only Geldart group A particles) for both tapering-in and tapering-out risers. The schematic drawings of these risers are depicted in Figures 6.1 (b)-(c). To compare the results with the typical riser, other input conditions were fixed as the base case of Knowlton et al.'s experiment. After that, such condition has been tested to get better performance of the system.

The computational domains for the typical, tapered-out and tapered-in risers are illustrated in Figures 6.2 (a)-(c), respectively. The computational domain consists of 19 non-uniform grids in radial direction and 285 uniform grids in axial direction, with a total of 5,415 computational cells. The constant time step of 0.001 s was used in these computations. The real fluidization time for time-averaged results was examined in the results and discussion topic. The models were solved by using a computer with Pentium 2.14 GHz CPU 2 GB RAM. It took approximately five days of computer time for 40 s simulation time.

6.3.1.3. Initial and boundary conditions

At the inlet, the velocity and volume fraction in each phase were specified. On the other hand, at the outlet, the system pressure was specified at atmospheric pressure. Initially, no gas phase and solid phase were in the riser. At the wall, no-slip conditions were applied for all velocities, except the tangential velocity of solid phase and granular temperature. Here, the Johnson and Jackson conditions (Johnson and Jackson, 1987) were used. These conditions were first applied to kinetic theory of granular flow modeling by Sinclair and Jackson (1989). They are;

$$v_{st,W} = -\frac{6\mu_s \varepsilon_{s,max}}{\pi\phi\rho_s \varepsilon_s g_0 \sqrt{3\theta}} \frac{\partial v_{st,W}}{\partial n} \tag{6.1}$$

$$\theta_W = -\frac{\kappa_s \theta}{\gamma_W} \frac{\partial \theta_W}{\partial n} + \frac{\sqrt{3}\pi\phi\rho_s \varepsilon_s v_{s,slip}^2 g_0 \theta^{\frac{3}{2}}}{6\varepsilon_{s,max}\gamma_W} \tag{6.2}$$

where $\gamma_W = \frac{\sqrt{3}\pi\left(1-e_W^2\right)\varepsilon_s \rho_s g_0 \theta^{3/2}}{4\varepsilon_{s,max}}$.

6.3.2. Results and discussion

6.3.2.1. Simulation of Knowlton et al. experiments

Knowlton's riser was constructed and simulated by using CFD package. The results obtained from the simulation were compared with the Knowlton's experimental results (1995) to check its validity. The results can be divided into two

parts by system solid particle. Figure 6.3 shows the plot of various time-averaged solid mass fluxes versus radial position with the experimental result for Geldart group A particles. The results are at 3.9 m above the bottom of the riser with the bottom gas inlet velocity of 5.2 m/s. In this case, the EMMS drag model was used due to the high solid mass flux in the system. The 20-30 s time-averaged result is not fitted well with the experimental data. The reason is that this time-averaged result is not yet reaching the quasi steady state or stationary operating condition. Increasing the simulation time to 40 s, the 20-40 s time-averaged result is fitted with the experimental data. Further, increasing the simulation time to 50 s, the result is changed slightly. This implies that this time-averaged result has reached the steady-state condition. Thus, the time-averaged of 20-40 s was selected to represent the simulation results. According to Figure 6.3, it also exhibits that the simulation results are fitted well with the experimental data. Both simulation and experiment predict the core-annulus flow structure in the riser. This core-annulus (gas–solid) flow structure is made up of very dilute in the center region (core) and relatively dense near the wall region (annulus).

Another experimental condition was used to verify this numerical model. The same experimental condition was used, by changing the bottom gas inlet velocity to 7.6 m/s. The solid mass flux versus radial position at 3.9 m above the bottom of the riser is plotted as shown in Figure 6.4. It was found the reasonable agreement between the experiment and the computation results. The core-annulus flow structure in the riser is still observed. However, the downward flow of particles near the wall for the bottom gas inlet velocity of 5.2 m/s is changed to the upward flow for that of 7.6 m/s. Both testing conditions confirm the validity of the developed model. Therefore, this numerical model can be used for predicting the responses of new riser geometries for Geldart group A particles.

Then, the system solid particle was changed to Geldart group B particles. With the same model as Geldart group A particles, the simulation result is not match with the experimental data. As a consequence, some parts of the model must be changed, such as drag force or interphase exchange coefficient model and solid-wall

restitution coefficient, as summarized in Table 6.1. The drag force model in this system was changed to Gidaspow model that predicted well with the dilute system (low solid mass flux). The solid-wall restitution coefficient was 0.99999. The collision characteristic between solid-wall in the case of Geldart group B particles is more elastic than that of Geldart group A particles. This is due to the large wall friction loss in Geldart group A particles. Figure 6.5 shows the various time-averaged solid densities versus radial position with the experimental result for Geldart group B particles. The results are at 3.9 m above the bottom of the riser with the bottom gas inlet velocity of 4.0 m/s. As can be seen from the figure, the time-averaged of 20-40 s was also selected to represent the simulation result with the same reason as for Geldart group A particles. About the accuracy of the model, the solid density in the system is higher near the wall and more dilute at the center of the riser, which is typical flow structure of CFBR. It is observed that the result in near wall region is little overpredicted. This is because the numerical model is not able to include all of the physical factors. Nevertheless, the model used in this work gives closer values in comparison with the other previous models. Thus, this model is suitable for predicting the Geldart group B particles system.

6.3.2.2. Simulation of novel riser geometries

In this topic, the new designs of the riser geometries were simulated with the inclined angle of 0.3 (for Geldart group A and B particles) and 0.5 (for only Geldart group A particles) degrees both tapered-out and tapered-in risers. The numerical models and other input conditions were fixed as the base case of Knowlton et al.'s experiments. To get better understanding the hydrodynamics response in these riser geometries, the discussions were divided into three topics. For the effect on turbulence or mixing, the results were separated into the effects of axial and radial mixings. The effects on residence time and temperature were discussed together since they are closely related. When the system has long residence time, the temperature profiles in the system will be more uniform. Eventually, the effect on chemical reactions would be summarized.

6.3.2.2.1. Effect on mixing

- Effect on axial mixing

Figures 6.6 and 6.7 illustrate the contour of instantaneous solid volume fraction at five different times in the typical, 0.3 degree tapered-out and 0.3 degree tapered-in risers for Geldart group A and B particles, respectively. From the figures, the computational results of both Geldart group particles have similar trend. It can be seen that the tapered-out riser has the best homogeneous solid volume fraction along the riser column. In this riser, few particles appear near the wall (annulus) region. The distributions of particles are, therefore, uniform. Although the solid particles entrain out of the tapered-out riser, the solid particles are continuously feed to compensate the loss solid particles. For the case of typical riser (Simulation of Knowlton et al. experiments in topic 6.3.2.1), more downward flow of particles are observed near the wall at the bottom of the riser. This makes the system more heterogeneity. The tapered-in riser has the worst homogeneous solid volume fraction along the riser, especially at the upper and lower sections of the riser. More downward flow of particles was found, indicating the particle cluster formed near the riser wall. This situation makes this riser to be non-uniform particle distribution when compares with the other riser geometries.

Figure 6.8 shows the time-averaged axial solid volume fraction along the riser height in the typical, 0.3 degree tapered-out, 0.5 degree tapered-out, 0.3 degree tapered-in and 0.5 degree tapered-in risers for Geldart group A particles. Figure 6.9 displays the time-averaged axial solid volume fraction along the riser height in the typical, 0.3 degree tapered-out and 0.3 degree tapered-in risers for Geldart group B particles. It is observed that the results are consistent with that of Figures 6.6 and 6.7. The tapered-out riser has minimum variation of time-averaged axial solid volume fraction along the riser. This indicates that the tapered-out riser provides better mixing in axial direction. On the other hand, the tapered-in riser has maximum variation of time-averaged axial solid volume fraction along the riser. There are high solid volume fractions in the upper top and lower sections. Thus, tapered-in riser is improper mixing in axial direction. This is due to the change of pressure drops in the system. The

pressure drop is inversely proportional to the cross-sectional area of the riser and is directly proportional to the solid volume fraction. Therefore, the pressure drop and the solid volume fraction in the system will be changed with the change of the inclined angle. For example, in case of tapered-in riser, when the inclined angle is increased, the pressure drop of the system decreases. Subsequently, the solid volume fraction decreases in the upper section and increases in the lower section. Furthermore, increasing the inclined angle, the upward gas velocity does not have enough momentum to support for high solid holdup when comparing to other riser geometries. This is the reason why the 0.3 degree tapered-in riser for Geldart group B particles profile has the high solid volume fraction at the middle of the riser. However, the solid volume fraction in the upper top section of all geometries of riser may be influenced by the configuration of the riser outlet.

- Effect on radial mixing

When considering radial mixing, there are three variables to be studied, which are the radial distribution of solid volume fraction, radial solid velocity and axial solid velocity. The riser geometries, with higher range value of radial solid velocity, imply better mixing of gas and particles in the system. Figures 6.10 and 6.11 illustrate the comparison of the magnitude of the radial solid velocities and the axial solid velocities (at 40 s simulation time) in the typical, tapered-out and tapered-in risers for Geldart group A and B particles, respectively. In all riser geometries, the contour of radial solid velocity is constant along the riser height and lower than the axial ones about an order of magnitude. This is because axial direction is the main flow direction. Hence, it is assumed that the radial solid velocity has insignificant effects on radial mixing and was not taken into account.

The radial distribution of time-averaged solid volume fraction in the middle of riser's geometry for Geldart group A and B particles are presented, in Figures 6.12 and 6.13, respectively. At this middle position, the diameters of all riser geometries, typical, tapered-in, and tapered-out, are the same. Similar to the axial mixing results, different types of particles do not change the radial mixing results. The simulation results

clearly exhibit the inherent core-annulus flow structure in the typical riser. In the tapered-out riser, the time-averaged solid volume fraction appears to be flatter than that in the case of the typical riser. This means that, for tapered-out riser, the solid volume fraction is more uniform distribution in the radial direction. On the other hand, in the case of the tapered-in riser, the time-averaged solid volume fraction is not symmetry. The minimum value of the solid volume fraction, which used to be in the center of the column, is shifted to the right side of the riser column. This phenomenon would be attributable to the accumulation of particles in the upper section of tapered-in riser. It induces the distribution of the solid volume fraction, along the riser, to be non-uniform.

Figures 6.14 and 6.15 show the radial distribution of time-averaged axial solid velocity in the middle of each riser's geometry for Geldart group A and B particles, respectively. For the equality of gas phase inlet velocity, the time-averaged axial solid velocity at this position would not be equal, due to the change in cross-sectional areas along the risers, for taper risers. Therefore, the magnitude of the time-averaged axial solid velocity could not be compared (magnitude of the time-averaged axial solid velocity: 0.5 degree tapered-out riser > 0.3 degree tapered-out riser > typical riser > 0.3 degree tapered-in riser > 0.5 degree tapered-in riser). For all of the riser geometries, the time-averaged axial solid velocities are high in the center and low near the wall except in the case of tapered-in riser (the maximum point is located between the center and the wall of the riser). The tapered-out riser has flat time-averaged axial solid velocity profile, which is identical to that obtained from the result of time-averaged solid volume fraction. Fewer downward flows near the wall appear in this riser. On the contrary, more particles have been found near the wall in the typical riser. In the tapered-in riser, the profile is not symmetry, which is consistent with the result appeared in Figures 6.12 and 6.13. Therefore, the time-averaged axial solid velocities on each side of the riser are not similar.

It can be concluded that the better mixing in a system, both axially and radially, can be obtained from the tapered-out riser geometry. On the contrary, the worst mixing are obtained from the tapered-in riser geometry.

6.3.2.2.2. Effect on residence time and temperature

Figures 6.16 and 6.17 illustrate the vector of instantaneous solid velocity (at 40 s simulation time) in the middle of the typical, tapered-out and tapered-in risers for Geldart group A and B particles, respectively. In the figures, the contours of axial solid velocity are also shown. These results show the similar trend of both particle groups that particles flow downward near the wall region while they spout upward in the center region. This flow pattern indicates somewhat particle recirculation over the riser geometries. Regarding the result in the previous topic, the tapered-out riser exhibits less core-annulus structure than the other riser geometries. In the typical riser, the core-annulus structure is pronounced and it is even more obvious when the riser is tapered-in. The riser geometry, with core-annulus structure, is the riser that has longer residence time and uniform temperature. Thus, the tapered-in riser would have longer residence time and uniform temperature than the typical and tapered-out risers, respectively. It can be seen in Figures 6.16 and 6.17 that the maximum instantaneous solid axial velocity of the tapered-in riser is less than the typical and tapered-out risers, respectively. This means that the gas and particles in the system will reside longer in this riser geometry when compared with the other two geometries.

Table 6.2 summarizes the particle residence time in each riser's geometry for both types of particle. The values in this table are minimum, maximum, average and standard deviation of the residence times. The result in this table was obtained by simulating the injection of pulse tracer particles in each riser's geometry under the stable operating system. The procedure begins with simulating the considered riser's geometry until the steady-state flow field was reached (after 20 s simulation time). Then, the tracer particles, which have similar properties as the system solid particle, were introduced into the system at the solid side inlets and allowed them to travel in the riser until they moved out of the system at the outlet. The time that particles spent in the system outlet was recorded and summarized in the table. It can be stated that the tapered-in risers provide longer residence time and uniform temperature profile than the typical and tapered-out risers, respectively.

6.3.2.3. Criteria for choosing riser geometry with reaction characteristic

According to the simulation results in topic 6.3.2.2 (Simulation of novel riser geometries), one can observe that the tapered-out riser gives better mixing and creates more turbulence motion. The tapered-in riser provides long residence time which can be inferred to the uniform temperature distribution in the system. These situations occur when the system solid particle are both Geldart group A and B particles, which are mainly used in cracking, combustion and gasification reaction in CFBR. Due to the difference in hydrodynamics response inside each riser's geometry, it can be used to specify the criteria for choosing riser geometry to suit with different chemical reaction characteristics.

In a CFBR, chemical reactions typically take place in the riser section. The reactions might be divided into two main categories: the fast and the slow reaction rate processes. The tapered-out riser will suit with the fast reaction rate processes, such as cracking (Issangya et al., 1999) and combustion (Yin et al., 2002; Basu, 2006). Because it does not need a long residence time or uniform temperature, only better mixing along the height of the riser or having more gas-solid contacting area to enhance the conversion of this kind of reaction are required. On the other hand, the tapered-in riser will suit with the reaction with slow rate, such as gasification (Kersten et al., 2003; Jianzhi et al., 1992; Fang et al., 2001; Fletcher et al., 1998; Fletcher et al., 2000), since this reaction needs more time to react. For example, in the case of gasification, this reaction requires longer residence time and uniform temperature distribution for decomposing tar to low molecular weight molecules by reacting with gasifying agents, e.g. oxygen or steam. The better mixing in this system would not much improve the conversions of this reaction. The reason would be the feedstocks do not have enough time to reach the complete reaction in the riser. The summary of the specified criteria are as follows:

Fast reaction rate (combustion and cracking) → Tapered-out riser

Slow reaction rate (gasification) → Tapered-in riser

In addition, the influence of solid volume fraction on the proposed criteria was investigated by altering the gas velocity. When the gas velocity decreases, solid particles are more accumulated. Figure 6.18 shows the time-averaged axial solid volume fraction along the riser height in the typical and 0.5 degree tapered-out risers for Geldart group A particles. Decreasing the gas velocity from 5.2 m/s to 2.5 m/s obviously increases the total solid volume fraction. As can be seen, all the profiles have slightly difference of solid volume fraction distribution in the middle section of the riser. However, the tapered-out riser still gives more uniform solid distribution than the typical riser especially at the bottom section. The radial distribution of time-averaged solid volume fraction in the middle of typical and 0.5 degree tapered-out risers for Geldart group A particles is presented in Figures 6.19. The tapered-out riser also has more uniform distribution of solid volume fraction in the radial direction than the typical riser even though the gas velocity is decreased. Therefore, it can be concluded that the proposed criteria for choosing riser geometries can be employed even in the system with different solid volume fraction.

6.4. CFD modeling of CFBR risers: hydrodynamics descriptions and chemical reaction responses

6.4.1 Computational fluid dynamics simulation

6.4.1.1. Mathematical model

In this second section, the modeling can be divided into cold flow and hot flow. The model verification and in-depth hydrodynamics responses, as well as system turbulent properties, were discussed in the cold flow simulations topic. In the hot flow simulations topic, the riser geometries with the addition of chemical reaction were simulated to obtain the chemical reaction responses and to prove the proposed criteria from the previous section. For cold flow simulations, a set of governing equations which consists of mass and momentum conservation equations were solved numerically (similar to the first section). For hot flow simulations, energy and species (C_3H_8, CO_2, H_2O, O_2 and N_2 (air)) conservation equations were added and solved with original two

governing equations. To completely describe the governing equations, appropriate constitutive equations were specified to describe the physical properties in each phase such as the gas phase stress and the solid phase viscosity. The constitutive equations are based on the kinetic theory of granular flow, as reviewed by Gidaspow (1994). The drag force model for this system was Gidaspow model that predicted well with the low solid mass flux or dilute system (Neri and Gidaspow, 2000). A summary of the governing equations and constitutive equations are already given in Chapter III. According to the previous literatures, there was no information given on the values of operating parameters which are the restitution coefficients and the specularity coefficient. Some adjustment procedure thus was done to find the suitable operating condition as summarized in Table 6.3.

6.4.1.2. System description and computational domain

The same experimental results of PSRI (Particulate Solid Research Inc.) challenge problem I, published by Knowlton et al. (1995), were chosen as the reference case for validating the proposed CFD model. Their riser section was next referred as a typical riser. However, the considered solid particle in this section was only silica sands. The diameter (D) and height (h) of their riser were 0.2 m and 14.2 m, respectively. Since a three-dimensional model requires long computation time, this section uses two-dimensional model for modeling the system. The schematic drawing of the typical riser is already shown in Figure 6.1 (a). The other conditions for the modeling are listed in Table 6.3. Also, two tapered riser geometries were modeled and compared with the typical riser results. The inclined angle of 0.3 degree was selected for both tapered-out and tapered-in risers. To compare the results with the typical riser, the other input conditions were fixed as the reference case. The tapered-out and tapered-in riser geometries are already displayed in Figures 6.1 (b) and 6.1 (c), respectively.

The computational domains of the typical, tapered-out and tapered-in risers are illustrated in Figures 6.2 (a)-(c), respectively. All of the riser geometries consist of 19 non-uniform grids in radial or horizontal direction and 285 uniform grids in axial or vertical direction, with a total of 5,415 computational cells. The constant time step of

0.001 s was used. The CFD models were solved by using a computer with Pentium 2.14 GHz CPU and 2 GB RAM. It took 5 and 10 days of computing time for 40 s of simulating time in case of the cold and the hot flow simulation cases, respectively.

6.4.1.3. Initial and boundary conditions

The initial and boundary conditions for cold flow and hot flow simulations are indicated in Table 6.3. At the inlet, the velocity and volume fraction in each phase were specified for cold flow simulations while the temperature and gas compositions in each phase were also required for the hot flow simulations. On the other hand, at the outlet, the system pressure was specified at atmospheric pressure. Initially, there were no gas and solid phases inside the system. At the wall, an adiabatic condition was employed and a no-slip condition was applied for all velocities, except for the tangential velocity of the solid phase and the granular temperature. Here, the boundary conditions of Johnson and Jackson (1987) were used.

6.4.1.4. Chemical reaction model

The required information for modeling the chemical reaction is the reaction rate equation. Considering the solid particles in the system, silica sand is a typical bed material that is used as heating media to provide heat for combustion of solid fuels in CFBR combustor. Due to the uncertainty of reaction rate equation in the literatures and the aim of this section is not to develop the details of gas and solid chemical reaction. Thus a simplified propane combustion reaction was employed. The reaction rate equation for this reaction is given in a database of FLUENT 6.2.16 program. The chemical reaction and reaction rate equation ($R_{C_3H_8}$) for homogeneous propane combustion reaction can be expressed as:

$$C_3H_8 + 5O_2 \rightarrow 3CO_2 + 4H_2O \tag{6.3}$$

$$R_{C_3H_8} = -k_0 e^{-E_a/R_{universal}T} C_{C_3H_8} C_{O_2}^5 \tag{6.4}$$

where $C_{C_3H_8}$ is the propane concentration, C_{O_2} is the oxygen concentration, E_a is the activation energy, k_0 is the pre-exponential factor, $R_{universal}$ is the universal gas constant and T is the temperature. The reactivity of the propane combustion is characterized by the activation energy and the pre-exponential factor via the Arrhenius's equation. However, from the results of Hurt et al. (1998) and Yunhau et al. (2006), the pre-exponential factor had less effect on the reaction rate equation than the activation energy. Thus, the activation energy would be the only parameter being varied for adjusting the reaction rates to be slow, medium or fast for the purpose of proving our previous proposed criteria. The reaction conditions of each case are given in Table 6.4. It is noted that a default activation energy value for the propane combustion reaction in the FLUENT program is 1.26×10^8 J/kgmol.

6.4.2. Results and discussion

6.4.2.1. Cold flow simulations

6.4.2.1.1. Validation of the computational fluid dynamics model to PSRI experiment

Figure 6.20 illustrates a comparison of the computed time-averaged solid density distributions at 3.9 m above the bottom of the riser with two different time-average ranges. The riser geometry in the simulation was a typical riser. Also, the measured PSRI experimental values are plotted. From the figure, the 20-30 s time-averaged simulation result is fitted well with the experimental data. Increasing the simulating time to 40 s only slightly changes the result. This implies that this riser system has reached the quasi steady state condition since the simulating time was 20 s. The solid density in the system is higher near the wall or annulus region and more dilute at the center or core region, which is typical core-annulus flow structure in CFBR system and consistent with the observed experimental data. This qualitative and quantitative accuracy makes the CFD model suitable for predicting the response of this riser system. For the next subsequent simulations, this CFD model with time-averaged between 20 s and 40 s was selected as a system representative.

Besides solid density, the modeling results were compared to other measured experimental values, which are solid mass flux and pressure drop. Figure 6.21 displays the computed time-averaged solid mass flux versus radial distance at 3.9 m above the bottom of the riser and the measured experimental values. The modeling and the experiment results are consistent with each others. However, there is a slightly difference in numeric values in the center region of the riser. This may be due to the measurement uncertainty. Additionally, the modeling is obtained only at one position or angle in the real three-dimensional experiment. Therefore, the difference may be resulted from the position of experimental measurement. Considering the system flow behavior, the solid mass flux profile is high at the center region and low at the wall region, which is the opposite direction to the solid density. This solid mass flux distribution also reflects the establishment of a core-annular flow structure, as discussed in Figure 6.20 and previous literature by Benyahia et al. (2000).

The computed time- and area- averaged pressure drop versus the riser height is depicted in Figure 6.22. There is a reasonable agreement between the result trends obtained from the modeling and the experimental measurement but the modeling values are slightly higher than the experimental values. This discrepancy may be attributable to the simplified system geometry. The increasing of pressure drop at the bottom and the top of the riser system are attributed to the inlet and outlet configurations, respectively. This behavior confirms the large influence of inlet and outlet configurations as published in many literatures (Cheng et al., 1998; Kim et al., 2008). In the system, the pressure drop decreases along the riser height owing to the decreasing of solid particles. This pressure drop distribution matches with the fast fluidization regime pressure drop profile (Figure 2.3) as described by Kunii and Levenspiel (1991) and confirms the observed core-annulus flow structure. Figures 6.21 and 6.22 validate that the developed CFD model can capture the phenomena in this riser system.

No numerical modeling is complete without a study of grid independence. Before moving to the next sections, the effect of grid numbers on modeling results was investigated. To prove that the results are independent of grid

numbers, the increments of grid numbers in both the radial and axial directions were performed. Ideally, the grid should be sufficiently fine so that further refinement does not change the results. Figure 6.23 shows the computed time-and area- averaged pressure drop profiles versus the riser height with three different grid numbers. The computational domains consist of 19✕285, 29✕428 and 38✕570 grids (non-uniform grids in radial direction✕uniform grids in axial direction). All the grid numbers predict similar pressure drop profiles. This indicates that all the grid numbers are sufficiently fine for providing reliable results. In general, continuous increasing in grid numbers may lead to slightly better results. However, it will introduce large computational time which is unfavorable. Therefore, the proper grid size is necessary. In this simulation, the computational domain consisting of 19 non-uniform grids in radial direction and 285 uniform grids in axial direction was chosen.

6.4.2.1.2. Comparison the hydrodynamics responses in tapered riser to typical riser

- Solid volume fractions

Figure 6.24 illustrates the transient distributions of solid volume fraction in the typical, tapered-out and tapered-in risers. The solid velocity vectors are also plotted in the figure to demonstrate the direction of solid particle flows. The instantaneous results from the unsteady state results are at 20, 30 and 40 s. It can be seen from the contour color that the solid volume fraction of tapered-out riser along the riser column is more homogeneous than the typical and tapered-in risers, respectively. In the tapered-out riser, most of the solid particles flow upward in the center region. Only, few solid particles flow downward in the wall region. The distribution of solid particles is, hence, uniform or exhibit less core-annulus flow structure. In the typical and tapered-in risers, more downward flow of solid particles is observed near the wall region. This makes these systems more heterogeneity and indicates somewhat more recirculated solid particles over the riser system geometries.

The time- and area- averaged solid volume fraction profiles along the riser section of the typical, tapered-out and tapered-in risers are depicted in Figure 6.25. It is observed that the results are consistent with the results in Figure 6.24. There are high solid volume fractions at the bottom and the top sections in all the riser system geometries due to the inlet and outlet configurations as already discussed. The tapered-out riser result has lowest variation of time- and area- averaged solid volume fraction along the riser. This indicates that the tapered-out riser provides better mixing in axial direction. On the other hand, the tapered-in riser has highest variation of time- and area-averaged solid volume fraction along the riser especially at the bottom section. Thus, the tapered-in riser provides improper mixing in the axial direction. These variations of solid volume fraction are due to the change of pressure drops which are inversely proportional to the cross-sectional area of the riser system and directly proportional to the solid volume fraction. Also, these variations of solid volume fraction can be physically clarified by the insufficient force to support the weight of solid particles.

- Solid and gas velocities

Both the solid and gas velocities can be divided into the axial and radial velocities. The axial distributions of the time- and area- averaged solid axial and radial velocities with three different riser geometries are shown in Figure 6.26. From Figure 6.26 (a), the time- and area- averaged solid axial velocity in the typical riser is almost constant throughout the riser height after a point inside the system. This behavior is referred to a fully developed flow structure. In contrast, the time- and area- averaged solid axial velocities in the tapered-out and tapered-in risers are changing throughout the riser height. The explanation for this behavior is also owing to the altering of inclined angle or cross-sectional area of riser system. The solid axial velocity increases and decreases when the cross-sectional area of the riser system is reduced and expanded, respectively. Besides, the changing of pressure drop along the riser height as already discussed can be the indirect reason for these observed phenomena. From Figure 6.26 (b), the time- and area- averaged solid radial velocities in all riser geometries are constant along their heights and are lower than the axial ones. The reason is that the

axial direction is the main direction of system flow. Therefore, it can be implied that the solid radial velocity or mixing has less effect on these system flow behaviors.

Figure 6.27 illustrates the time- and area- averaged gas axial and radial velocity along the riser section of the typical, tapered-out and tapered-in risers. All the time- and area- averaged velocity profiles of gas phase have similar trends when compared to the solid phase. The explanation thus should be the same. However, there is a slip velocity between these two phases due to their density difference. The gas phase has higher velocity than the solid phase. Next, some system turbulent properties were extracted from the solid and gas velocities. These variables are the normal Reynolds stresses, the granular temperatures and the dispersion coefficients.

- Normal Reynolds stresses

The main characteristic of system turbulent is the production of additional stresses due to velocity fluctuations, called normal Reynolds stresses ($\overline{v_i'v_i'}$). The subscript "i" represents the direction. The solid and gas normal Reynolds stresses can be computed in both axial (y) and radial (x) directions. From the modeling, the hydrodynamic velocities ($v_i(t)$) were obtained. The method to define the normal Reynolds stresses is shown below:

$$\overline{v_i'v_i'} = \frac{1}{l}\sum_1^l \left(v_i(t)-\overline{v}_i\right)\left(v_i(t)-\overline{v}_i\right) \qquad (6.5)$$

where $\overline{v}_i = \frac{1}{l}\sum_1^l v_i(t)$ and l is the total number of time steps.

Figure 6.28 shows the axial distributions of computed time- and area- averaged solid normal Reynolds stresses for axial and radial directions in typical, tapered-out and tapered-in risers. The axial distributions of computed time- and area- averaged gas normal Reynolds stresses for axial and radial directions with three different riser geometries are depicted in Figure 6.29. Both solid and gas normal Reynolds stress trends are similar. However, the magnitude of velocity fluctuation in the gas phase is higher than that in the solid phase. The value of gas normal Reynolds

stress in the axial direction is about factor two of that of the solid one. For normal Reynolds stresses in axial direction, the velocity fluctuation is almost constant in the typical riser while they are significantly changed in the tapered-out and tapered-in risers. The axial velocity fluctuations of tapered-out and tapered-in risers are highest at the top and the bottom, respectively. The high velocity fluctuation implies high energy content. This can explain why at the top of tapered-in riser does not have enough force to support the weight of solid particles which, then, affects the overall system solid circulation rate. From the figures, it can also be seen that the oscillations for normal Reynolds stresses in the radial direction are approximately constant in all of the riser geometries.

The radial distributions of computed time-averaged solid normal Reynolds stresses for both axial and radial directions at the height of 7.0 m in typical, tapered-out and tapered-in risers are plotted in Figure 6.30. Figure 6.31 illustrates the radial distributions of computed time-averaged gas normal Reynolds stresses for axial and radial directions at the same height with three different riser geometries. At this position, the diameters of all riser geometries are the same. The anisotropic characteristics of the velocity fluctuations can be clearly seen. For normal Reynolds stresses in the axial direction, the oscillations are low in the center region and high in the wall region except the solid axial normal Reynolds stresses in the tapered-out riser case (Figure 6.30). Comparing with the axial normal Reynolds stresses, the radial normal Reynolds stresses and the exceptional case of axial normal Reynolds stresses show the velocity fluctuation distributions in the opposite trend, the values are high in the center region and low in the wall region which can be observed in the figures. In terms of the magnitude, the velocity fluctuations are much larger in the direction of the flow.

- Granular temperatures

Tartan and Gidaspow (2004) used the kinetic theory based particle image velocimeter method to determine the oscillations; both due to individual solid particles called "laminar granular temperature" and due to clusters of solid particles called "turbulent granular temperature". To compute the granular temperature, the

related equations have to be programmed into the CFD models. The code itself computes the laminar granular temperature. The turbulent granular temperature (θ_t) is defined as the average of the normal Reynolds stresses in the three-dimensional system, by using the following equation:

$$\theta_t(t) \cong \frac{1}{3}\overline{v'_x v'_x} + \frac{1}{3}\overline{v'_y v'_y} + \frac{1}{3}\overline{v'_z v'_z}$$ (6.6)

For two-dimensional modeling, the velocity fluctuations in non-flow or radial direction are assumed to be equal. Therefore, the turbulent granular temperature is defined as:

$$\theta_t(t) \cong \frac{2}{3}\overline{v'_x v'_x} + \frac{1}{3}\overline{v'_y v'_y}$$ (6.7)

The sum of the granular temperatures due to the individual solid particles and due to the cluster of solid particles is the total granular temperature. This quantity, therefore, can demonstrate the overall system oscillations.

Table 6.5 summarizes a comparison of the computed laminar, turbulent and total granular temperatures at three different heights in the typical, tapered-out and tapered-in risers. These three heights are at 3.5, 7.0 and 10.5 m representing the middle section of the riser. The height-averaged values are also shown in the table. In the typical riser, the computed laminar and turbulent granular temperatures are close to each others. The computed laminar granular temperatures in tapered-out riser are higher than the computed turbulent granular temperatures whereas the computed laminar granular temperatures in tapered-in riser are lower than the computed turbulent granular temperatures. These granular temperature values are consistent with the hydrodynamics responses. The turbulent granular temperature of the system which has more clusters of solid particles should dominate the system oscillations. Considering the riser geometry, the computed total granular temperature of tapered-out riser is higher than those of the typical and tapered-in risers, respectively. The system oscillations are higher in the dilute system than those in the dense system because of the available space among the solid particles or clusters of solid particles. The normal Reynolds

stress and granular temperature results therefore provide the explanation why the tapered-out riser has solid particle residence time shorter than the typical and tapered-in risers as observed in the previous section. At all heights, the total computed granular temperatures in the typical riser are of the same order of magnitude. This infers that the flow structures are similar. The total computed granular temperatures in the tapered-out and tapered-in risers are increased and decreased with the riser height, respectively. These results are also seen in Figure 6.32, which displays axial distributions of computed time- and area- averaged total granular temperature with three different riser geometries.

The radial distributions of computed time- and area- averaged total granular temperature at the height of 7.0 m with three different riser geometries are shown in Figure 6.33. The maximum values of total granular temperature are off-center in all the riser geometries. The total granular temperatures drop in the center and near wall regions. In the center region, there is a reduction of fluctuations by the shear term. In the wall region, this is due to the zero stresses observed by Tartan and Gidaspow (2004). These granular temperature results show the related trends with the normal Reynolds stresses.

Figure 6.34 compares the height-average of the total granular temperatures in the typical, tapered-out and tapered-in risers with the literature values. All the computed values match the experimental data within the same range of gas velocity. This also validates the CFD model used in this section.

- Solid and gas dispersion coefficients

A measure of the quality of system mixing is dispersion coefficient. Similar to the granular temperature we can identify two types of the dispersion coefficients: one due to individual solid particles oscillations or laminar and the other due to clusters of solid particles oscillations or turbulent. In order to compare solid and gas dispersion coefficients, we focus on the dispersion coefficient due to particle cluster oscillations or turbulent. Axial dispersion coefficient (D_y) and radial dispersion

coefficient (D_x) can be obtained as a function of normal Reynolds stress and the Lagrangian integral time scale (T_L) as expressed below:

$$D_y = \overline{v'_y v'_y}\, T_L \qquad\qquad (6.8)$$

$$D_x = \overline{v'_x v'_x}\, T_L \qquad\qquad (6.9)$$

where $T_L = \int_0^\infty \dfrac{\overline{v'_y(t)v'_y(t+t')}}{\overline{v'^2_y}} dt'$ for D_y and $T_L = \int_0^\infty \dfrac{\overline{v'_x(t)v'_x(t+t')}}{\overline{v'^2_x}} dt'$ for D_x.

A comparison of the solid and gas axial and radial dispersion coefficients at three different heights in the typical, tapered-out and tapered-in risers are shown in Table 6.6. Also, the height-averaged values are summarized. For all of the riser geometries, the dispersion coefficient trends are similar. The gas dispersion coefficients are higher than the solid dispersion coefficients which are due to the slip velocity between the phases and the radial dispersion coefficients are lower than the axial dispersion coefficients. When focused on each riser's geometry, the dispersion coefficients vary from bottom to top of the riser. The axial dispersion coefficients in the tapered-out riser are lower than those in the tapered-in and typical risers, respectively. For radial dispersion coefficients, the trends are moving in the opposite direction except for the case of solid dispersion coefficients between the typical and tapered-in risers in which the values are quite similar. The radial dispersion coefficient of the tapered-out riser becomes the one with the highest value. The low axial and high radial solid dispersion coefficients show that the solid particles have well mixed. This explains the previous section results that the better solid mixing in a system could be obtained from the tapered-out riser. The high axial and low radial solid dispersion coefficients imply that the solid particles have worst mixing. In our previous section result, the mixing behavior is only concluded from the non-uniform solid volume fraction and solid velocity profiles. Unlike the good solid mixing, the worst solid mixing in the tapered-in riser case cannot clearly be explained using the computed dispersion coefficient. Both the axial and radial solid dispersion coefficients in the tapered-in riser are lower than that in the typical riser. Therefore, the effect of solid particle residence time or the force inside the

system may be the importantly additional reason for the observed hydrodynamics results. The core-annulus flow structure can make the system to be heterogeneity and inferior in mixing. The same explanation can also be used for gas mixing. In this section, the calculated solid and gas dispersion coefficients are in the range as shown in the literature.

6.4.2.2. Hot flow simulations

6.4.2.2.1. Comparison of the chemical reaction responses in tapered risers to typical riser

The hot flow simulations were carried out with various activation energies to explore the effect of riser geometries on the selected combustion reaction responses. Figures 6.35 to 6.37 show the contour of mass fraction distributions of gas compositions with various reaction rates in the typical, tapered-out and tapered-in risers, respectively. The gas compositions include propane (C_3H_8), oxygen (O_2), nitrogen (N_2), carbon dioxide (CO_2) and steam (H_2O) and the reaction rates are fast, medium and slow.

From all the figures, it can be seen that the C_3H_8, O_2 and N_2 were supplied into the riser system at the bottom of the riser. N_2 is an inert gas which was fed into the system as a part of air with O_2. The result shows that C_3H_8 and O_2 mass fractions are depleted along the riser height while the mass fractions of CO_2 and H_2O are increased due to the combustion reaction. To compare the chemical reaction responses, the results are mainly concentrated on the product gas compositions which are CO_2 and H_2O gases. The mass fractions of CO_2 are observed to be higher than those of H_2O. This is relevant to the chemical reaction stoichiometry in mass unit. Considering the effect of riser system geometries with constant reaction rate, the mass fractions of CO_2 and H_2O in the tapered-in riser are higher than those in the typical and tapered-out risers, respectively. The explanation can be attributed to the system residence time for both in the homogeneous and heterogeneous reaction cases. For homogeneous reaction, as already shown in the solid and gas velocities section, the tapered-in and tapered-out risers have the lowest and highest gas axial velocities

throughout the riser height, respectively. The low gas axial velocity infers that the gas phase reactants will have more opportunity or time to react and convert to system products. For heterogeneous reaction, as discussed in the granular temperature section, the tapered-in and tapered-out risers have the highest and lowest solid particle residence time inside the system, respectively. The high solid particle residence time also increases the opportunity for chemical to react. In each figures, the effect of reaction rate are also observed. These results confirm that the mass fractions of CO_2 and H_2O are increased when the combustion reaction rate is increased or activation energy is decreased. Lower activation energy means that the chemical reaction requires less energy to take place.

Figures 6.38 to 6.42 display the outlet weight percent and the outlet content of product gases in three different riser geometries with medium, fast, faster, slow and slower reaction rates, respectively. The outlet weight percent gives the outlet mass composition or qualitative aspect of product gases while the outlet content provides the outlet mass flow rate or quantitative aspect of product gases. In all the figures, the outlet weight percent trends and explanations are similar to each others and the results in Figures 6.35 to 6.37. About the outlet content, the obtained results are varied depending on the chemical reaction characteristic. This is due to the difference in the system flow rate resulting from the area changing of CFBR riser geometries and the occurrence of the chemical reaction. For medium reaction rate, the mass flow rates of CO_2 and H_2O in the typical riser are higher than those in the tapered-out and tapered-in risers, respectively. For fast and faster reaction rates, the outlet content of product gases in the tapered-out riser is higher than that in the typical and tapered-in risers, respectively while, for the slow and slower reaction rates, the outlet content of product gases in the tapered-in riser is higher than that in the tapered-out and typical risers, respectively. The results in the cold flow and the hot flow sections can be used to clarify the obtained results. The tapered-out riser gives better mixing and creates more turbulent motion in the system. The tapered-in riser provides long system residence time and uniform temperature distribution.

In this simulation, the content of product gases are not high because these system outlet gases and solid particles are entrained out of the system and not circulated back as in the case of normal CFBR riser system. The temperature change in these systems, thus, is not significant and it is not taken into account.

6.4.2.2.2. Verification of the previous proposed criteria

As already declared in the previous section, the criteria for choosing CFBR riser geometry with chemical reaction characteristics were proposed. The tapered-out riser would suit for fast reaction rate processes because it does not need a long residence time or uniform temperature. Only better mixing along the height of the riser or having more gas-solid contacting area are required to enhance the reaction conversion. On the other hand, the tapered-in riser would fit slow reaction rate processes, since this kind of reaction need more time to react. The reactants require having enough time to reach the completeness of the chemical reaction. The better mixing in this system will not much improve the reaction conversion.

To verify the proposed criteria, the riser system which provides more content or quantitative amount of product gases is the proper geometry for a certain reaction rate. From the comparison of chemical reaction behaviors, it can be seen that the slow and slower reaction rates are appropriate with the tapered-in riser while the fast and faster reaction rates are appropriate with the tapered-out riser. The medium reaction rate then suits for the typical riser. The reasons for these modeling results have already shown. Consequently, this section results verify the criteria for choosing riser geometry with chemical reaction characteristics.

6.5. Conclusion

1. The novel designs of the riser geometries have been studied by computer simulation using a two dimensional transient Eulerian model combined with kinetic theory of granular flow.

2.   In the first section, the concept of the new designs is proposed on the improvement of the factors that have effects on the chemical reaction via the hydrodynamics inside the riser. It is found that different types of particles (Geldart group A and B) do not affect the simulation result. The tapered-out riser could improve the turbulence or mixing in the system. On the other hands, the tapered-in riser could enhance the particle residence time and give uniform temperature distribution in the system. This result leads to the criteria for choosing riser geometry with different reaction characteristics. The tapered-out riser will suit the reactions with fast reaction rate, while the tapered-in riser will fit to the reactions with slow reaction rate.

3.   In the second section, the proposed model was used for predicting in-depth hydrodynamics responses and computing system turbulent properties in the typical and tapered-riser geometries. The tapered-in riser enhances the solid particle residence time and gives uniform temperature distribution in the system. The explanation is due to this riser geometry not having enough force to support the weight of solid particles as justified by the normal Reynolds stresses and the granular temperatures. The tapered-out riser improves the turbulence or mixing in the system which can be clarified by the dispersion coefficients. In addition, the chemical reaction responses were directly modeled and used to prove the proposed criteria. These modeling results prove the criteria for choosing riser geometry with reaction characteristics. It can be used as alternatives in the designing stage of the CFBR system.

Table 6.1 Parameter used for first section simulations.

Symbol	Description	Typical riser	Tapered-out riser	Tapered-in riser
D_{inlet}	Inlet diameter of riser	0.2000 m[*]	0.2744 m and 0.3239 m	0.1256 m and 0.0761 m
D_{outlet}	Outlet diameter of riser	0.2000 m[*]	0.1256 m and 0.0761 m	0.2744 m and 0.3239 m
D	Diameter of riser at middle height	0.2000 m[*]	0.2000 m	0.2000 m
h	Height of riser	14.2000 m[*]	14.2000 m	14.2000 m
ρ_g	Gas density	1.2 kg/m^3	1.2 kg/m^3	1.2 kg/m^3
μ_g	Gas viscosity	2×10^{-5} kg /m s	2×10^{-5} kg /m s	2×10^{-5} kg /m s

[*] from reference by Knowlton et al. (1995).

Symbol	Description	Typical riser	Tapered-out riser	Tapered-in riser
For Geldart group A particles;				
ρ_s	Particle density	1720 kg/m^{3*}	1720 kg/m^3	1720 kg/m^3
d_p	Diameter of particle	76 μm[*]	76 μm	76 μm
α	Inclined angle	0.0^o	0.3^o and 0.5^o	0.3^o and 0.5^o
v_g	Gas inlet velocity	5.2 m/s[*] (2.5 and 7.6 m/s)	5.2 m/s (2.5 m/s)	5.2 m/s
v_s	Solid inlet velocity	0.4760 m/s	0.4760 m/s	0.4760 m/s
ε_s	Solid inlet volume fraction	0.60	0.60	0.60
e	Restitution coefficient between particles	0.95	0.95	0.95
e_W	Restitution coefficient between particle and wall	0.90	0.90	0.90
ϕ	Specularity coefficient	0.50	0.50	0.50

[*] from reference by Knowlton et al. (1995).

Symbol	Description	Typical riser	Tapered-out riser	Tapered-in riser
For Geldart group B particles;				
ρ_s	Particle density	2145 kg/m^{3*}	2145 kg/m^3	2145 kg/m^3
d_p	Diameter of particle	175 μm*	175 μm	175 μm
α	Inclined angle	0.0°	0.3°	0.3°
v_g	Gas inlet velocity	4.0 m/s*	4.0 m/s	4.0 m/s
v_s	Solid inlet velocity	0.2392 m/s	0.2392 m/s	0.2392 m/s
ε_s	Solid inlet volume fraction	0.10	0.10	0.10
e	Restitution coefficient between particles	0.95	0.95	0.95
e_w	Restitution coefficient between particle and wall	0.99999	0.99999	0.99999
ϕ	Specularity coefficient	0.40	0.40	0.40

* from reference by Knowlton et al. (1995).

Table 6.2 The particle residence time in each riser's geometry.

No.	Geometry	Residence time (s)			
		Minimum time	Maximum time	Average time	Standard deviation time
For Geldart group A particles;					
1	0.5 degree tapered-out riser	1.418	2.194	1.605	0.2660
2	0.3 degree tapered-out riser	1.655	2.746	2.037	0.3664
3	Typical riser	1.895	2.749	2.192	0.2162
4	0.3 degree tapered-in riser	2.217	2.751	2.499	0.1815
5	0.5 degree tapered-in riser	2.554	4.262	3.872	0.3577
For Geldart group B particles;					
6	0.3 degree tapered-out riser	2.362	4.019	3.481	0.5347
7	Typical riser	3.983	4.997	4.561	0.3298
8	0.3 degree tapered-in riser	4.246	6.102	5.357	0.6250

Table 6.3 Parameter used for second section simulations.

Symbol	Description	Typical riser	Tapered-out riser	Tapered-in riser
D_{inlet}	Inlet diameter of riser	0.2000 m[*]	0.2744 m	0.1256 m
D_{outlet}	Outlet diameter of riser	0.2000 m[*]	0.1256 m	0.2744 m
D	Diameter of riser at middle height	0.2000 m[*]	0.2000 m	0.2000 m
α	Inclined angle	0.0°	0.3°	0.3°
h	Height of riser	14.2000 m[*]	14.2000 m	14.2000 m
e	Restitution coefficient between particles	0.95	0.95	0.95
e_W	Restitution coefficient between particle and wall	0.99999	0.99999	0.99999
ϕ	Specularity coefficient	0.40	0.40	0.40
ρ_g	Gas density	1.2 kg/m^3	1.2 kg/m^3	1.2 kg/m^3
μ_g	Gas viscosity	2×10^{-5} kg /m s	2×10^{-5} kg /m s	2×10^{-5} kg /m s
ρ_s	Particle density	2145 kg/m^{3}[*]	2145 kg/m^3	2145 kg/m^3
d_p	Diameter of particle	175 μm[*]	175 μm	175 μm

[*] from reference by Knowlton et al. (1995).

Symbol	Description	Typical riser	Tapered-out riser	Tapered-in riser
For gas inlet - bottom inlet;				
v_g	Inlet velocity	4.0 m/s[*]	4.0 m/s	4.0 m/s
T_g	Inlet temperature	550 K	550 K	550 K
$y_{C_3H_8}$	Inlet propane species mass fraction	0.0000	0.0000	0.0000
y_{CO_2}	Inlet carbon dioxide species mass fraction	0.0000	0.0000	0.0000
y_{H_2O}	Inlet steam species mass fraction	0.0000	0.0000	0.0000
y_{O_2}	Inlet oxygen species mass fraction	0.2320	0.2320	0.2320
y_{N_2}	Inlet nitrogen species mass fraction	0.7680	0.7680	0.7680
For solid inlet - side inlet;				
ε_s	Inlet solid volume fraction	0.10	0.10	0.10
v_s	Inlet velocity	0.2392 m/s	0.2392 m/s	0.2392 m/s
T_s	Inlet temperature	550 K	550 K	550 K
$y_{C_3H_8}$	Inlet propane species mass fraction	1.0000	1.0000	1.0000
y_{CO_2}	Inlet carbon dioxide species mass fraction	0.0000	0.0000	0.0000
y_{H_2O}	Inlet steam species mass fraction	0.0000	0.0000	0.0000
y_{O_2}	Inlet oxygen species mass fraction	0.0000	0.0000	0.0000
y_{N_2}	Inlet nitrogen species mass fraction	0.0000	0.0000	0.0000

[*] from reference by Knowlton et al. (1995).

Table 6.4 Reaction rate conditions for modeling.

No.	Reaction rate condition	Activation energy (J/kgmol)	Pre-exponential factor (m^{15}/kg^5 s)
1	Slower reaction rate	1.88×10^8	4.836×10^9
2	Slow reaction rate	1.78×10^8	4.836×10^9
3	Medium reaction rate	1.44×10^8	4.836×10^9
4	Fast reaction rate	1.36×10^8	4.836×10^9
5	Faster reaction rate	1.26×10^8	4.836×10^9

Table 6.5 A comparison of computed laminar, turbulent and total granular temperatures with three different riser geometries.

No.	System	Height (m)	Granular temperature (m^2/s^2)		
			Laminar	Turbulent	Total
1	Typical riser	3.5	1.2923	1.3672	2.6594
		7.0	0.9352	1.3072	2.2425
		10.5	1.2449	1.4432	2.6881
		Averaged	0.9117	1.2122	2.1239
2	Tapered-out riser	3.5	1.1692	1.0720	2.2412
		7.0	1.3584	1.0141	2.3725
		10.5	2.6718	0.6678	3.3396
		Averaged	1.6951	0.7980	2.4931
3	Tapered-in riser	3.5	0.6987	1.6828	2.3815
		7.0	0.2183	1.0618	1.2801
		10.5	0.1523	0.8878	1.0401
		Averaged	0.3046	1.0496	1.3542

Table 6.6 A comparison of computed axial and radial dispersion coefficients with three different riser geometries.

No.	System	Height (m)	Solid dispersion (m^2/s)		Gas dispersion (m^2/s)	
			Axial	Radial	Axial	Radial
1	Typical riser	3.5	2.5780	0.0324	5.9696	0.0238
		7.0	2.2215	0.0167	4.9896	0.0275
		10.5	3.2264	0.0225	6.4751	0.0237
		Averaged	2.6753	0.0239	5.8115	0.0250
2	Tapered-out riser	3.5	0.7197	0.0397	1.6317	0.0595
		7.0	0.8273	0.0206	1.6625	0.0434
		10.5	0.7792	0.0171	1.5903	0.0266
		Averaged	0.7754	0.0258	1.6282	0.0432
3	Tapered-in riser	3.5	1.7138	0.0288	3.0655	0.0298
		7.0	1.8617	0.0191	3.4663	0.0280
		10.5	0.7214	0.0135	1.1213	0.0232
		Averaged	1.4323	0.0205	2.5510	0.0270
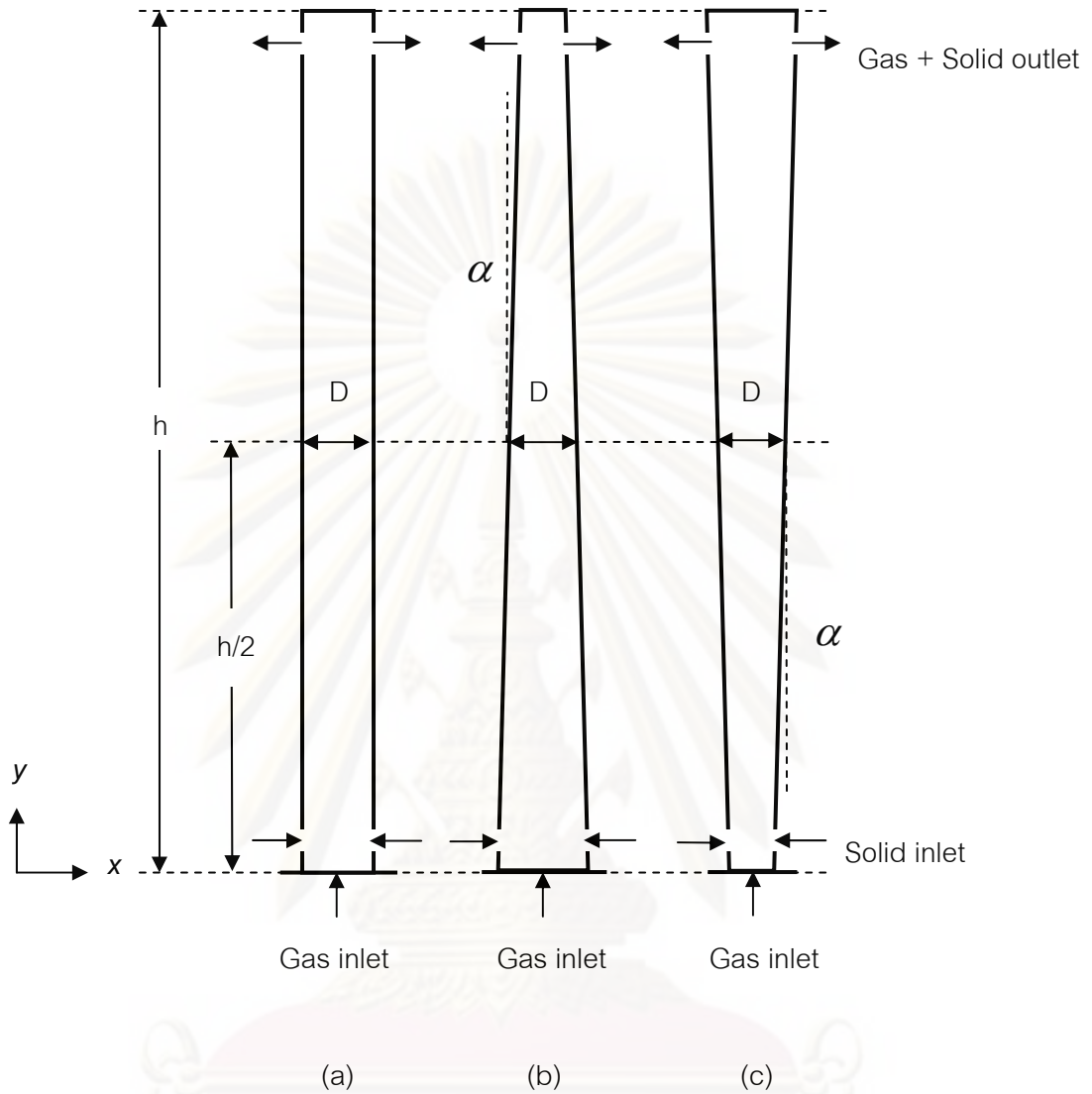
Figure 6.1 Schematic drawing of the (a) typical, (b) tapered-out and (c) tapered-in
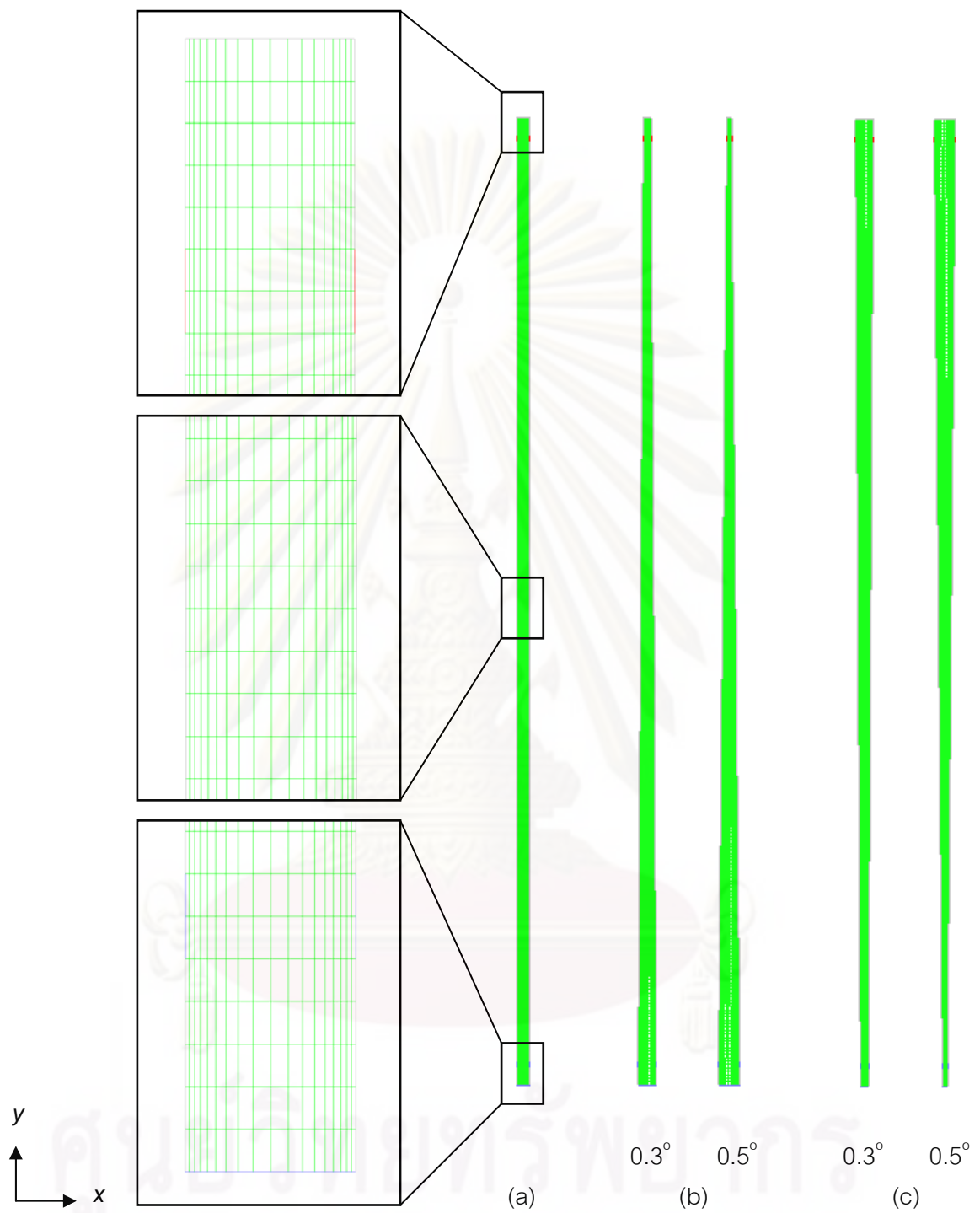
risers.

Figure 6.2 Computational domains of the (a) typical, (b) tapered-out and (c) tapered-in risers with their boundary conditions.
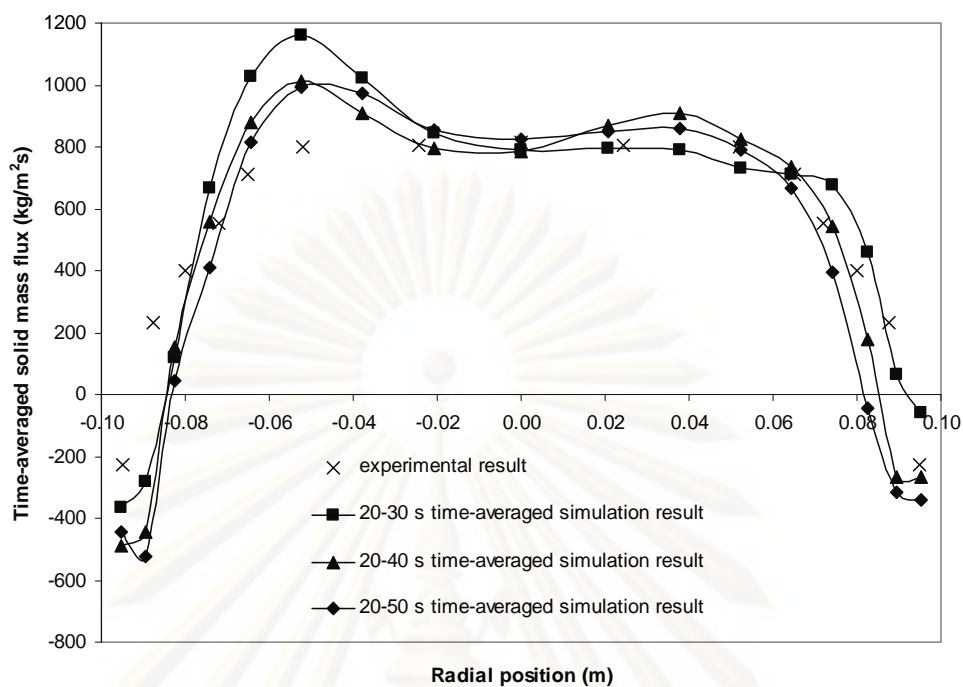
Figure 6.3 The various time-averaged solid mass fluxes at 3.9 m above the bottom of the

riser with the bottom gas inlet velocity of 5.2 m/s for Geldart group A particles

using EMMS drag model.
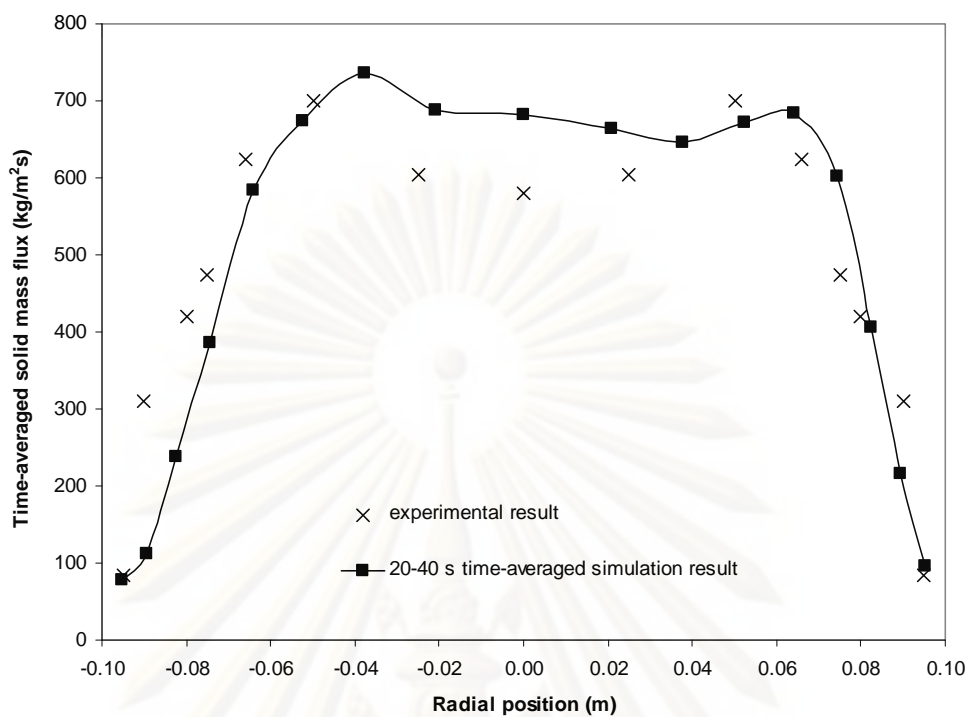
Figure 6.4 The various time-averaged solid mass fluxes at 3.9 m above the bottom of the riser with the bottom gas inlet velocity of 7.6 m/s for Geldart group A particles using EMMS drag model.
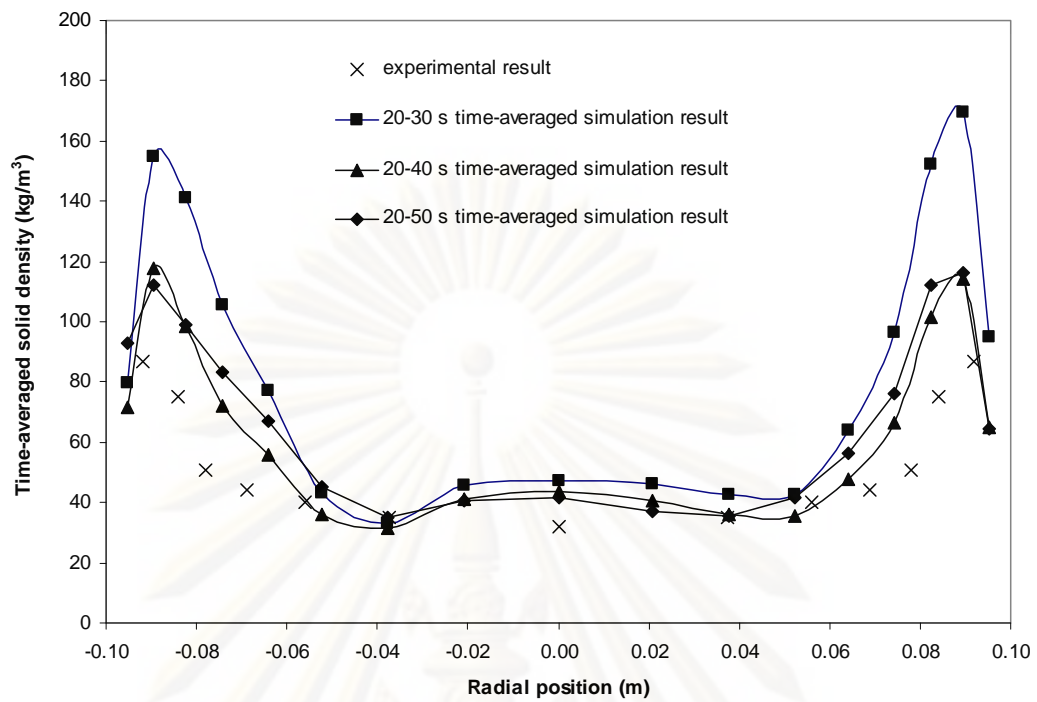
Figure 6.5 The various time-averaged solid densities at 3.9 m above the bottom of the riser with the bottom gas inlet velocity of 4.0 m/s for Geldart group B particles using Gidaspow drag model.
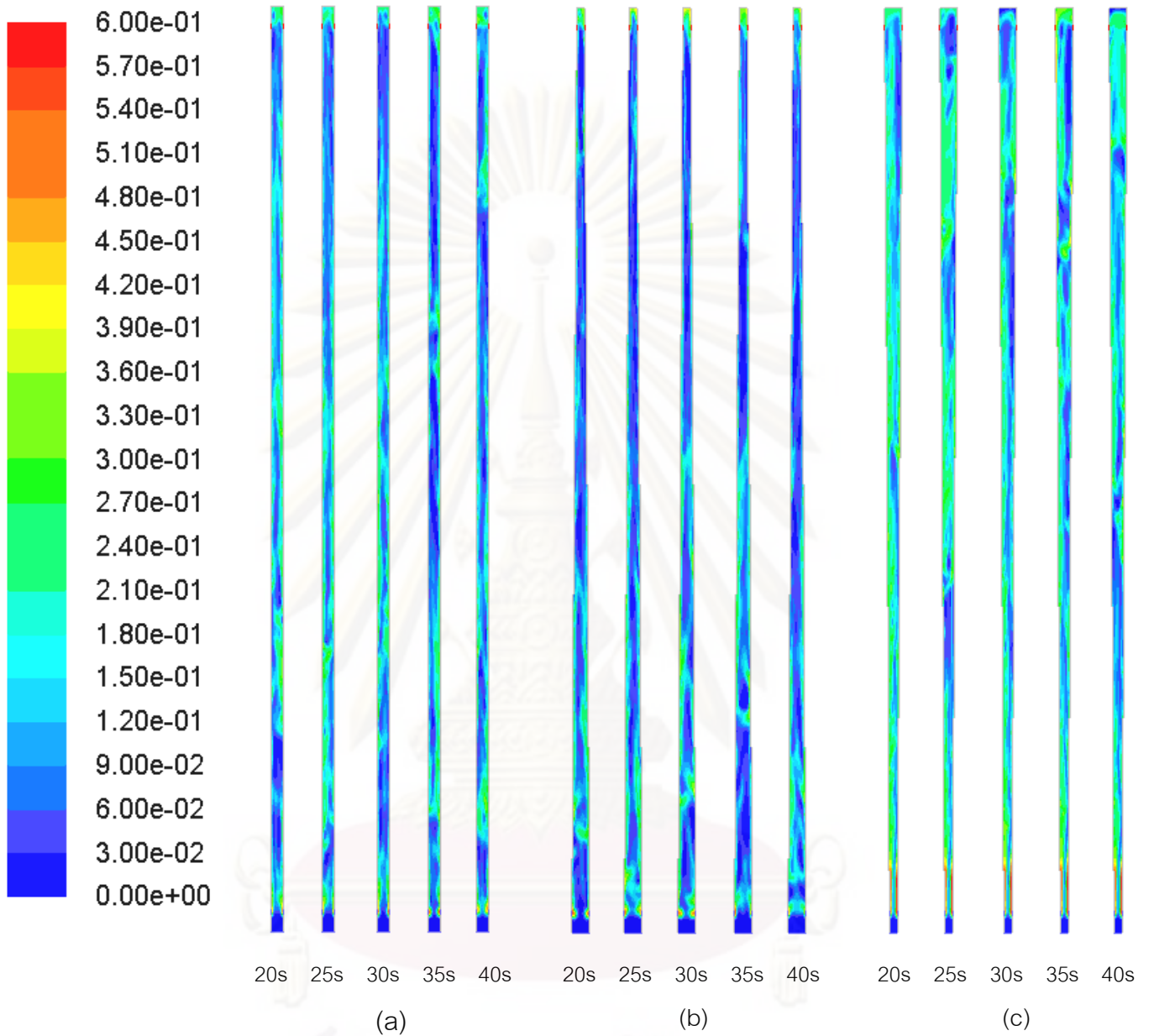
Figure 6.6 Contour of instantaneous solid volume fraction at five different times in

(a) typical, (b) 0.3 degree tapered-out and (c) 0.3 degree tapered-in risers

for Geldart group A particles.
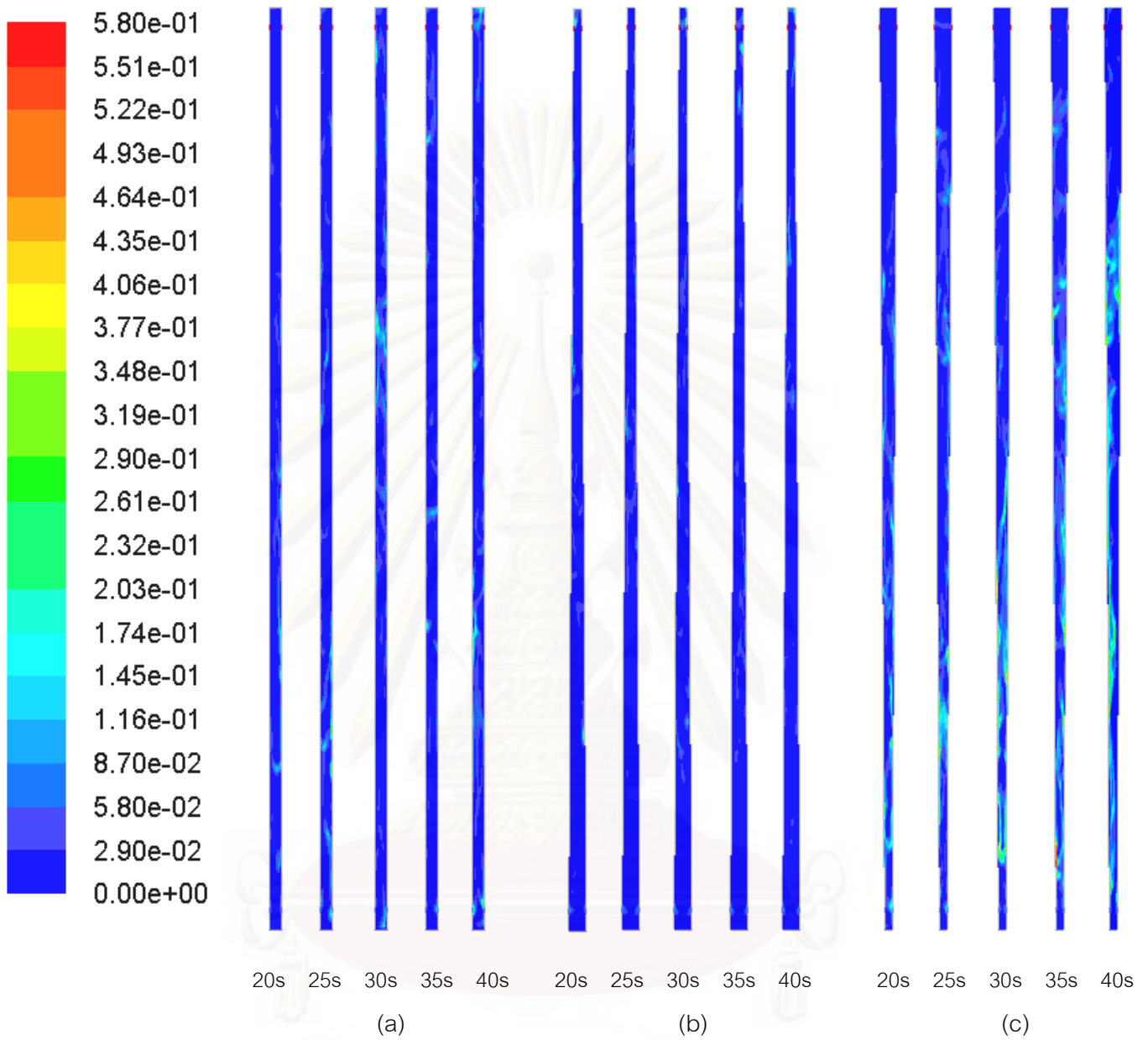
Figure 6.7 Contour of instantaneous solid volume fraction at five different times in

(a) typical, (b) 0.3 degree tapered-out and (c) 0.3 degree tapered-in risers

for Geldart group B particles.
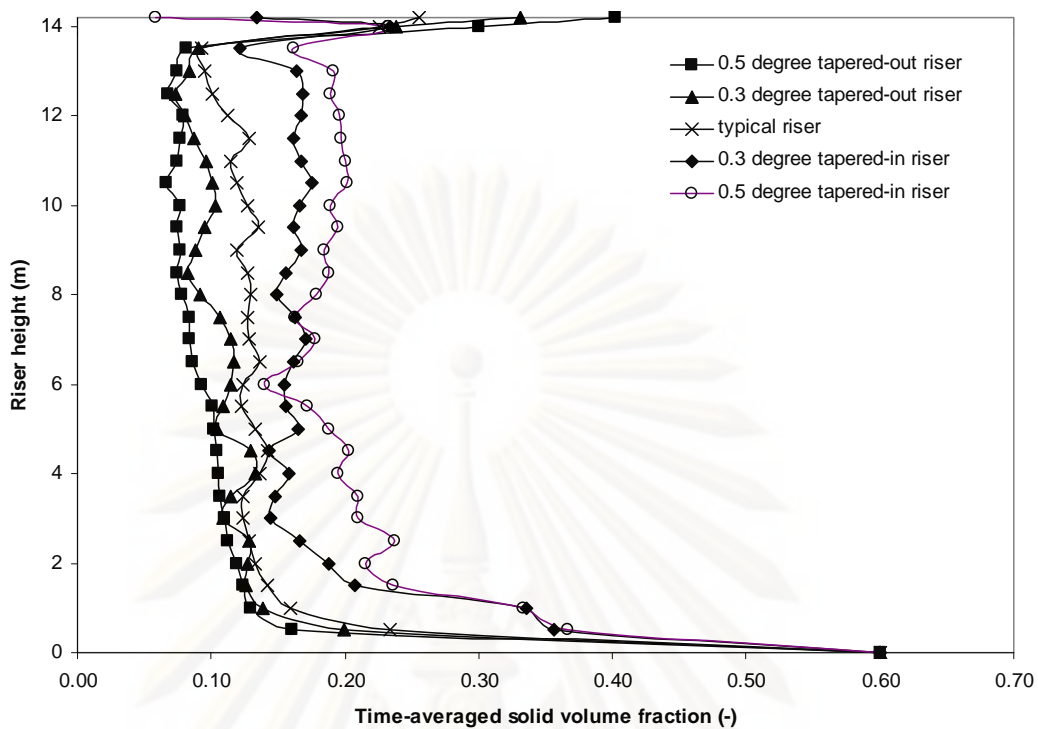
Figure 6.8 The time-averaged axial solid volume fraction along the height of each riser's

geometry with the bottom gas inlet velocity of 5.2 m/s for Geldart group A particles.
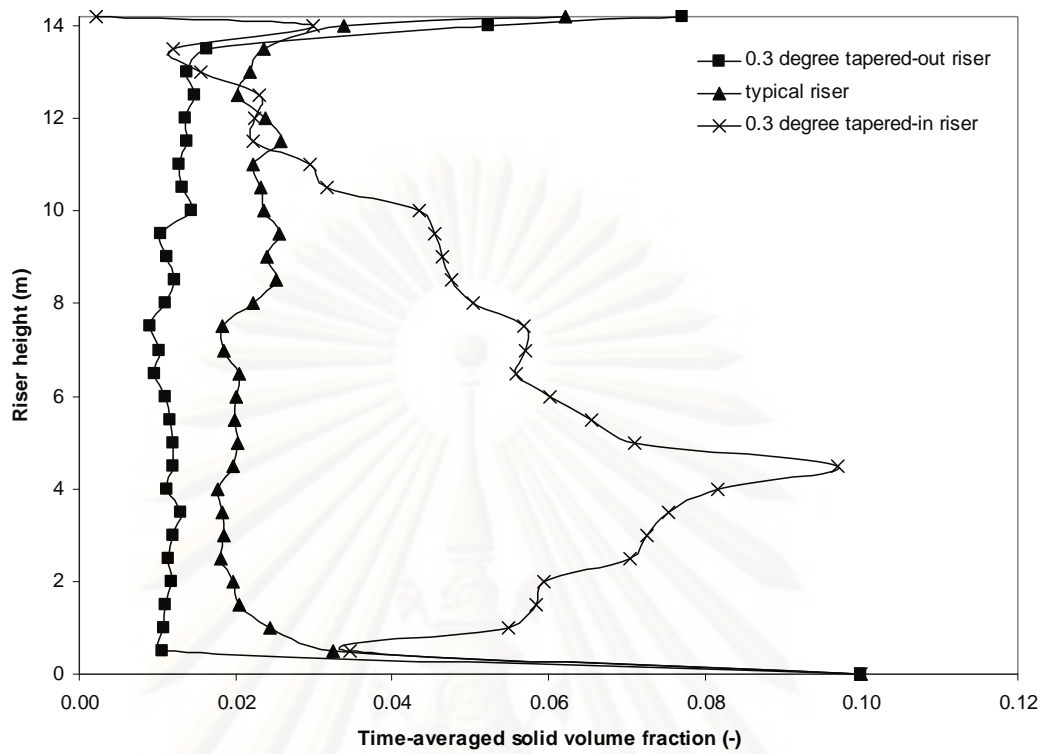
Figure 6.9 The time-averaged axial solid volume fraction along the height of each riser's geometry with the bottom gas inlet velocity of 4.0 m/s for Geldart group B particles.
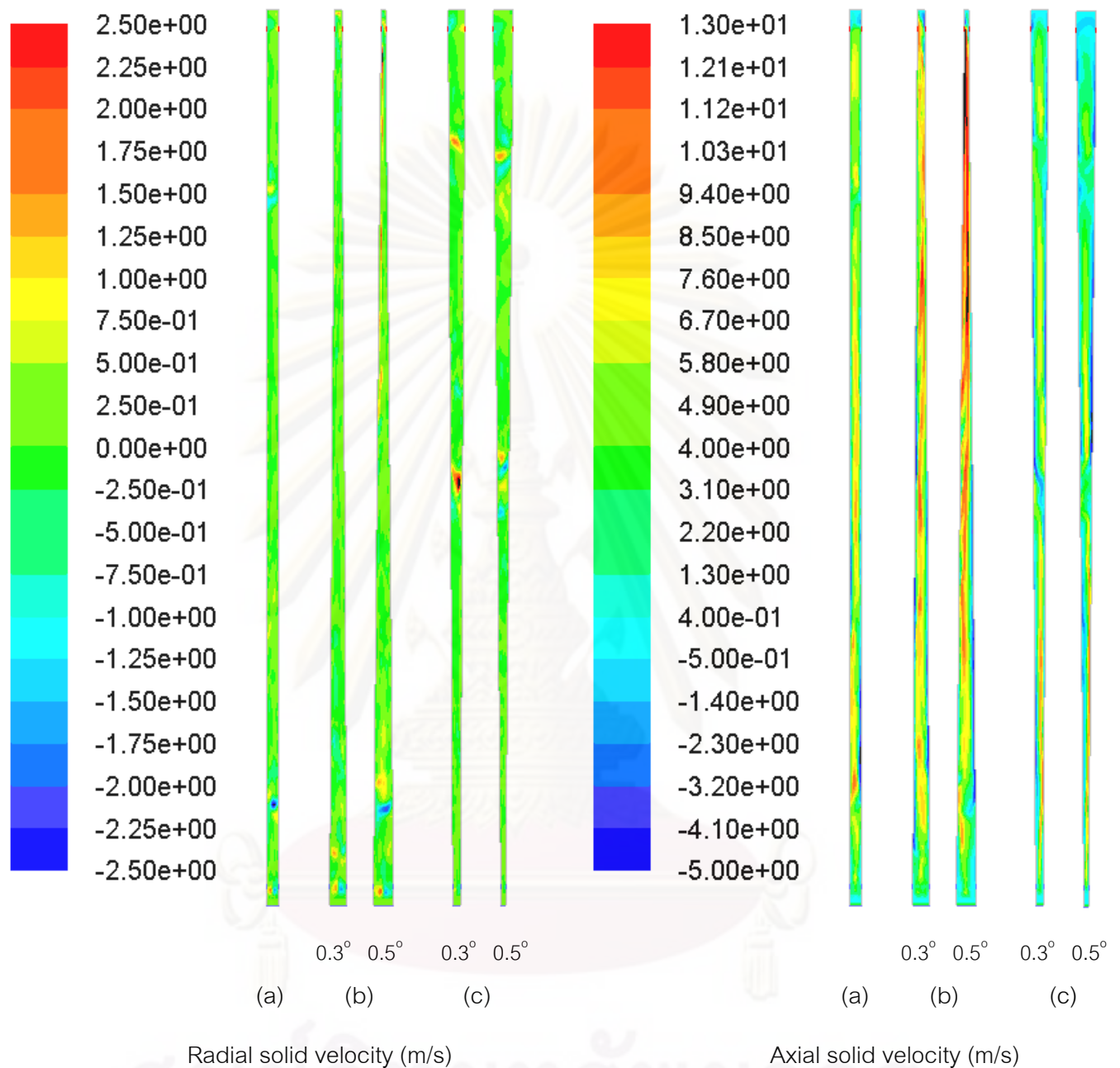
Figure 6.10 Contour of the radial and axial solid velocities at 40 s simulation time in the

(a) typical, (b) tapered-out and (c) tapered-in risers for Geldart group A particles.
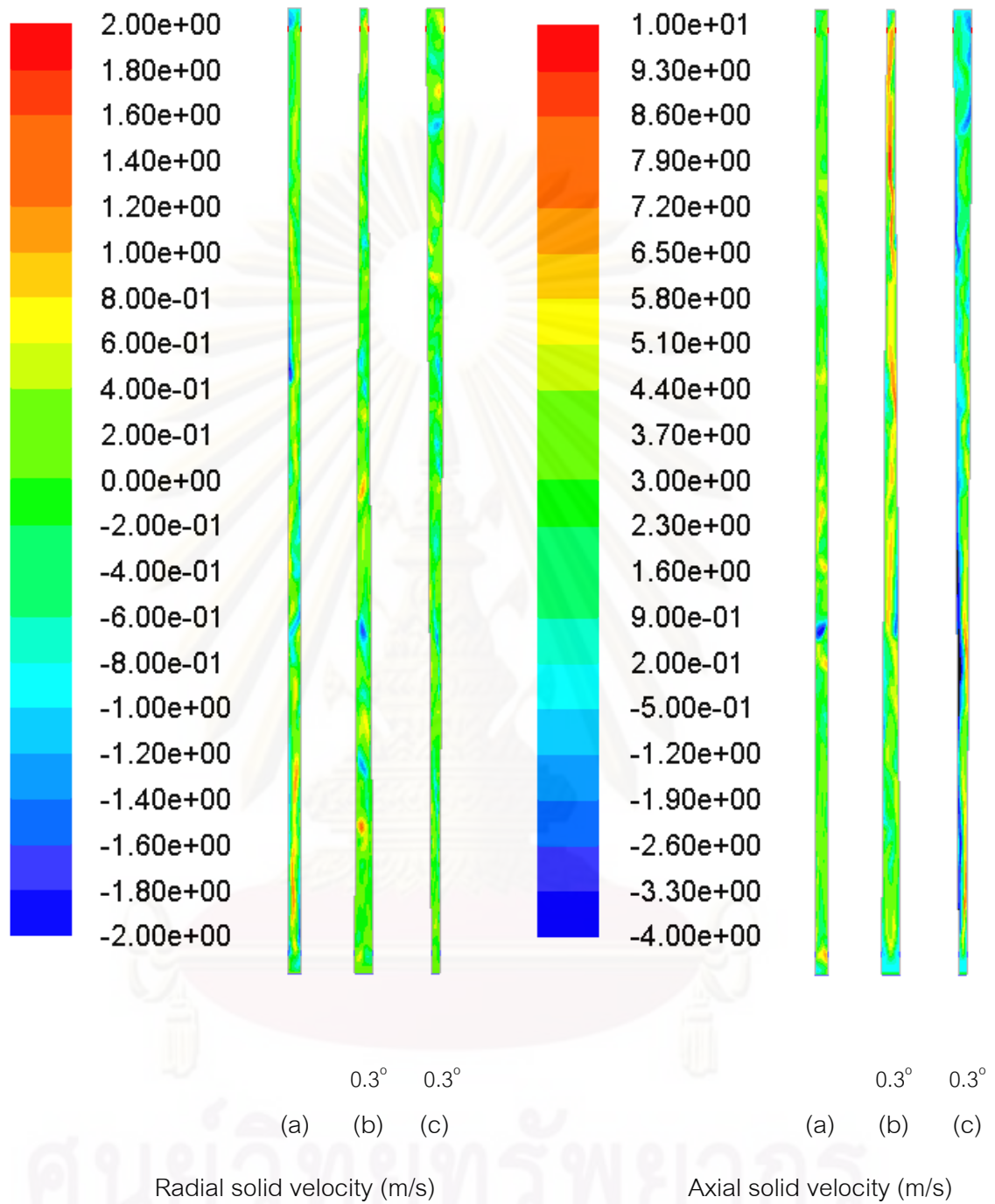
Figure 6.11 Contour of the radial and axial solid velocities at 40 s simulation time in the
(a) typical, (b) tapered-out and (c) tapered-in risers for Geldart group B particles.
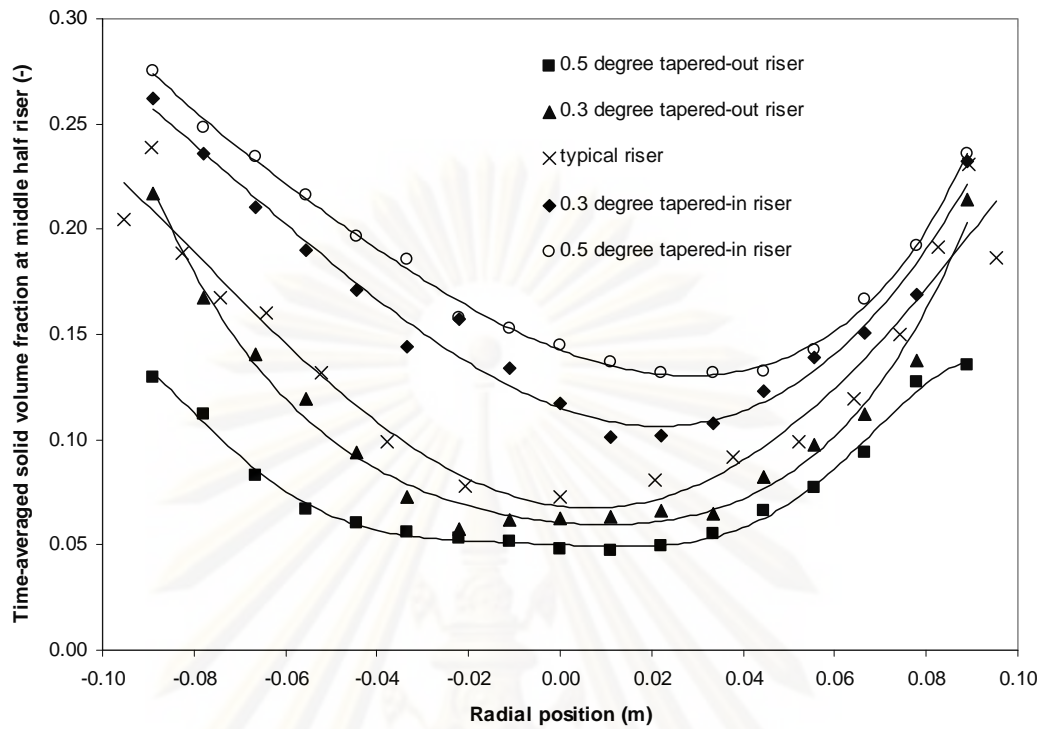
Figure 6.12 The radial distribution of time-averaged solid volume fraction in the middle of each riser's geometry for Geldart group A particles.
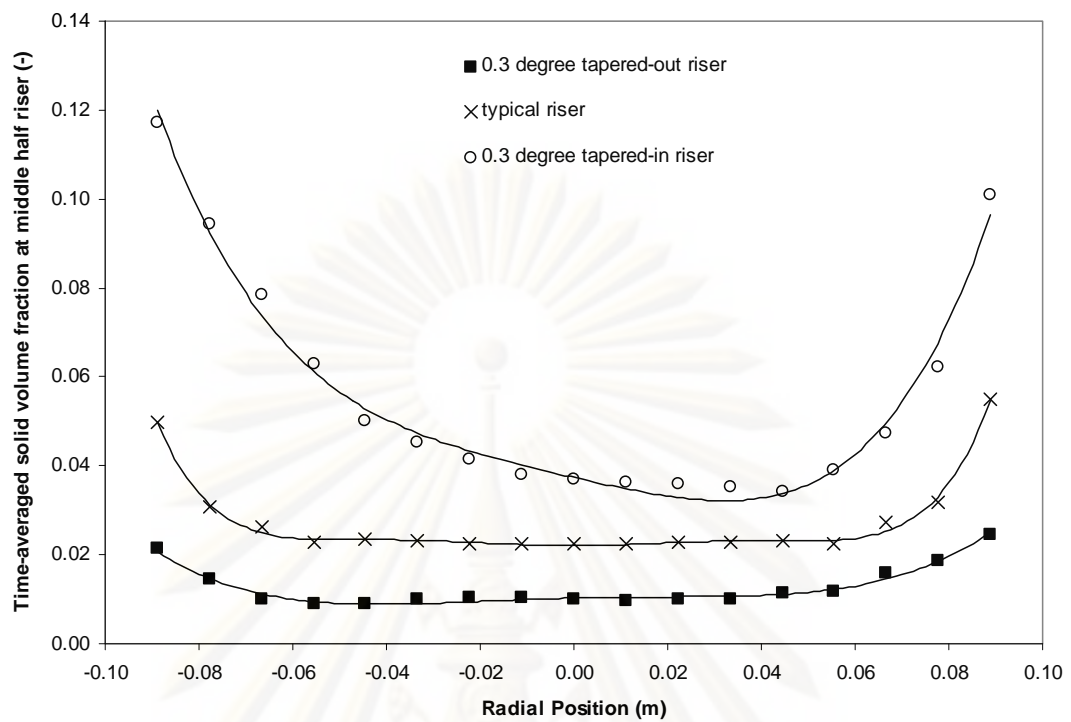
Figure 6.13 The radial distribution of time-averaged solid volume fraction in the middle of each riser's geometry for Geldart group B particles.
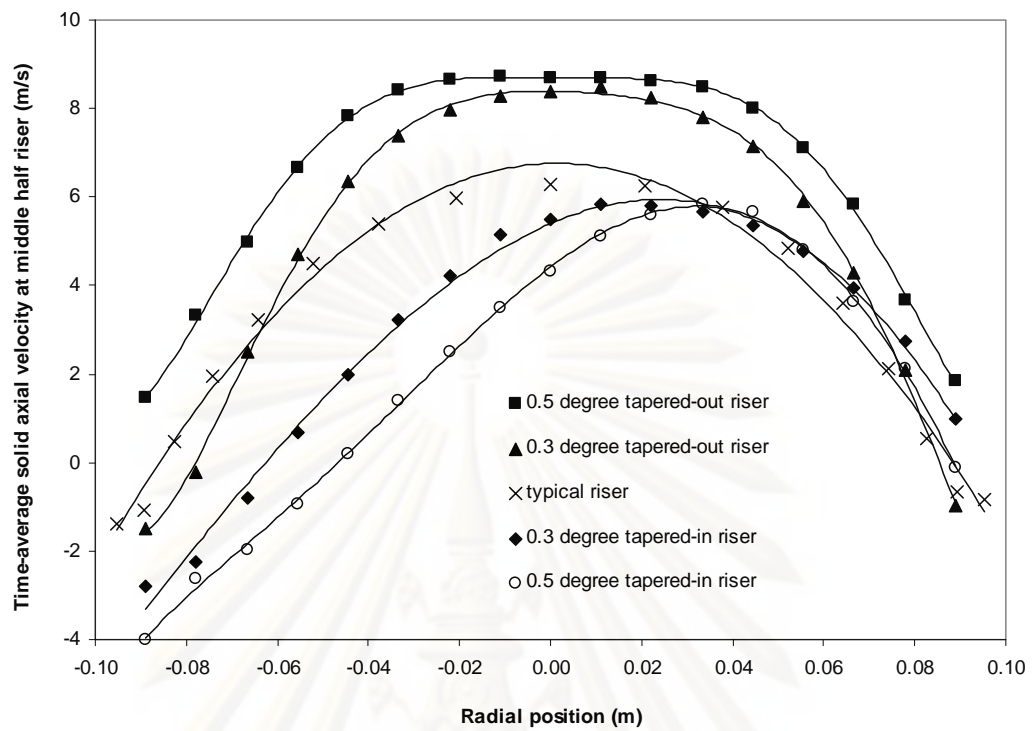
Figure 6.14 The radial distribution of time-averaged axial solid velocity in the middle of each riser's geometry for Geldart group A particles.
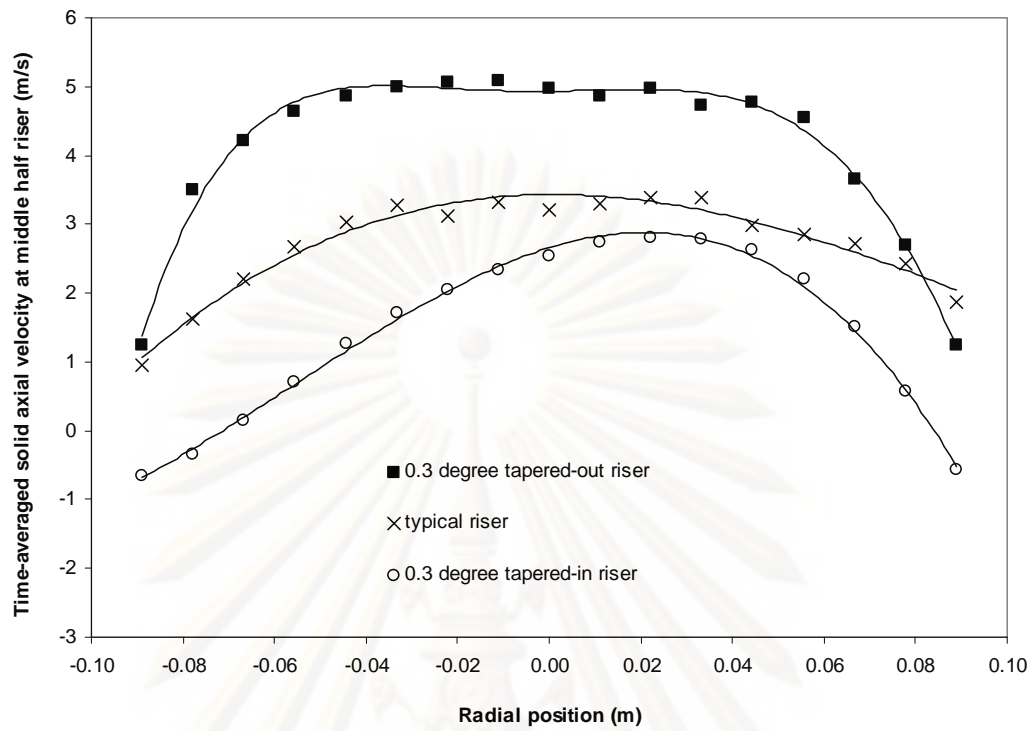
Figure 6.15 The radial distribution of time-averaged axial solid velocity in the middle of

each riser's geometry for Geldart group B particles.
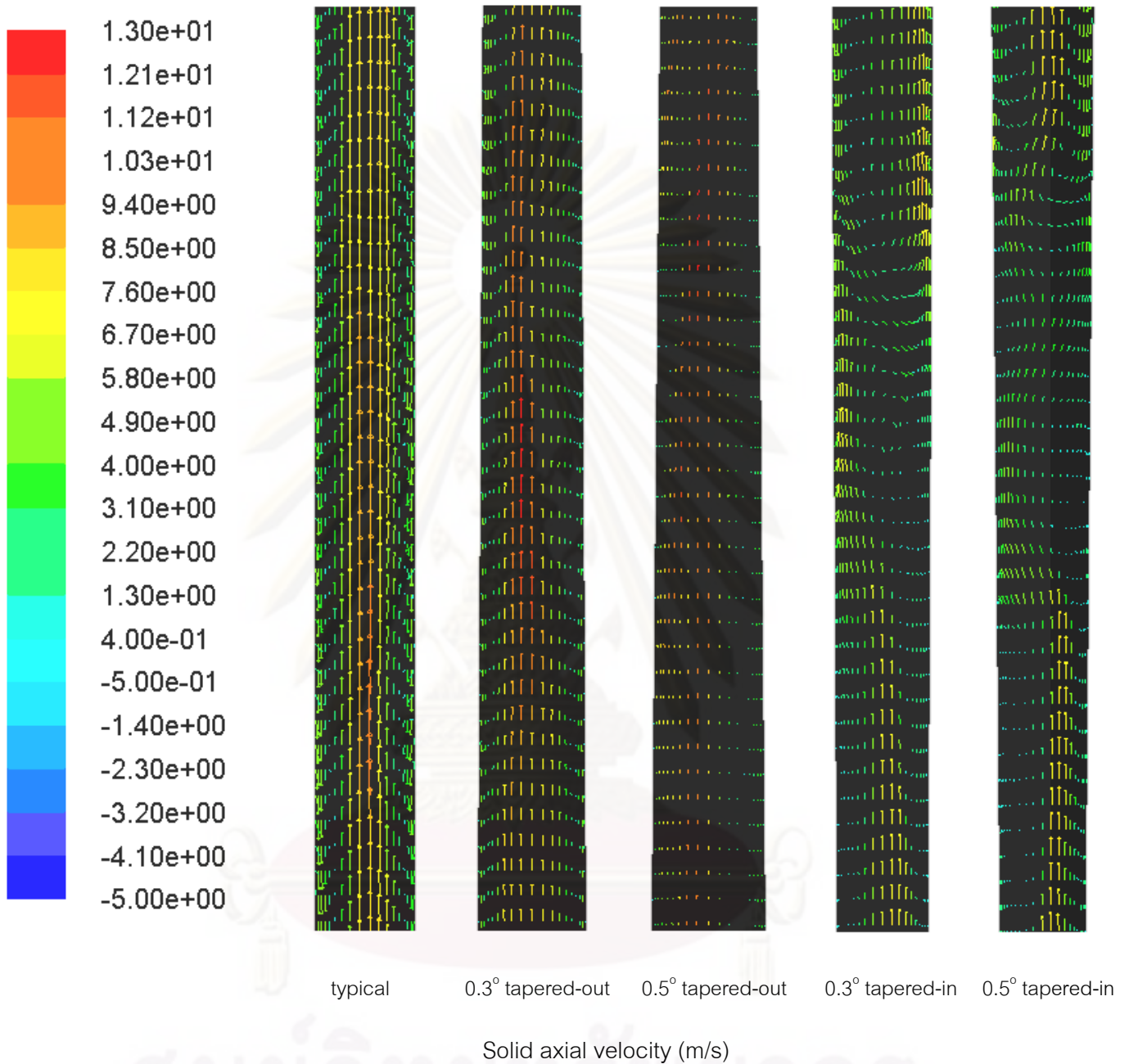
Figure 6.16 The vector of instantaneous solid velocity and contour of instantaneous axial

solid velocity (at 40 s simulation time) in the middle of each riser's geometry

for Geldart group A particles.

typical   0.3° tapered-out   0.3° tapered-in

Solid axial velocity (m/s)
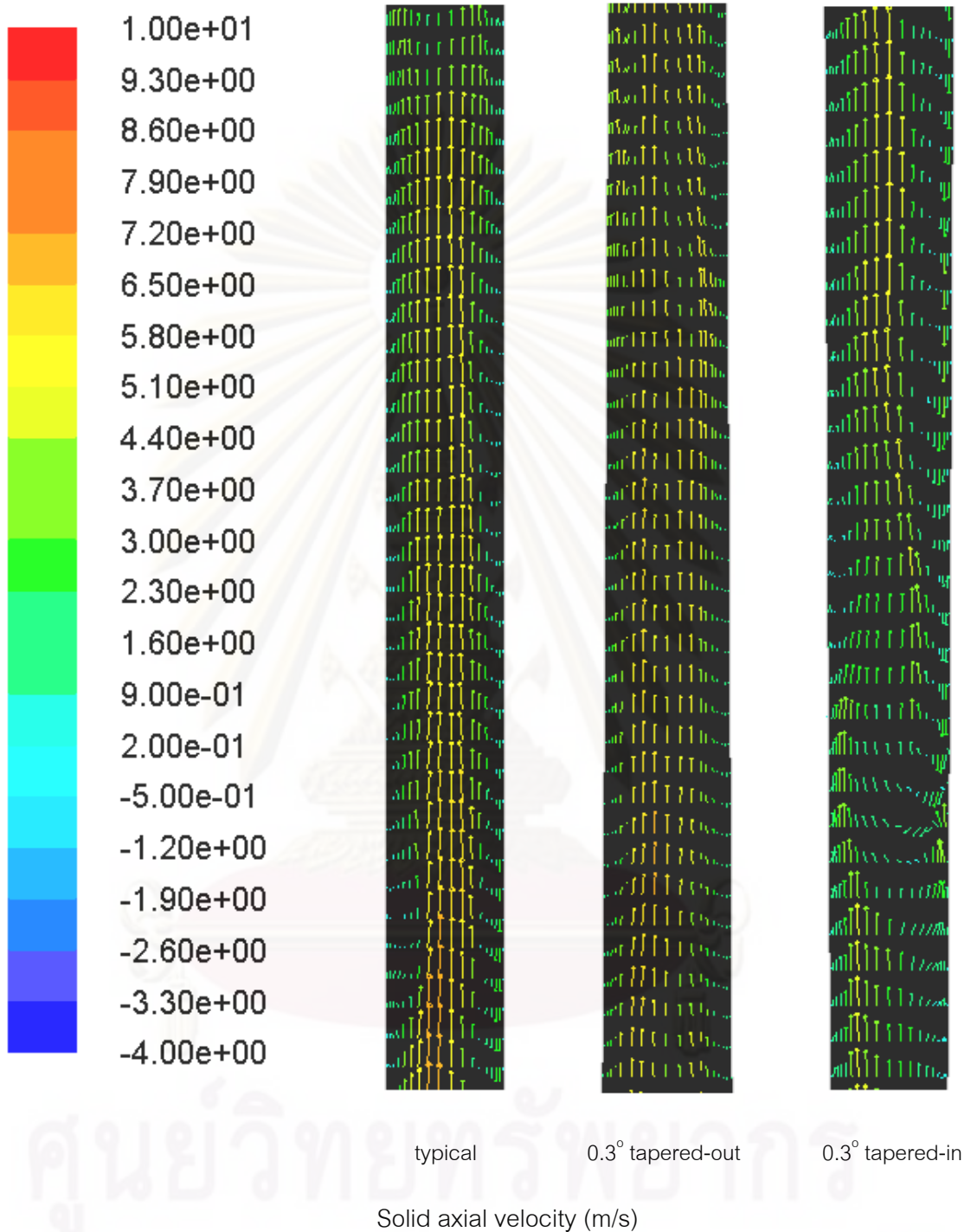
Figure 6.17 The vector of instantaneous solid velocity and contour of instantaneous axial

solid velocity (at 40 s simulation time) in the middle of each riser's geometry

for Geldart group B particles.
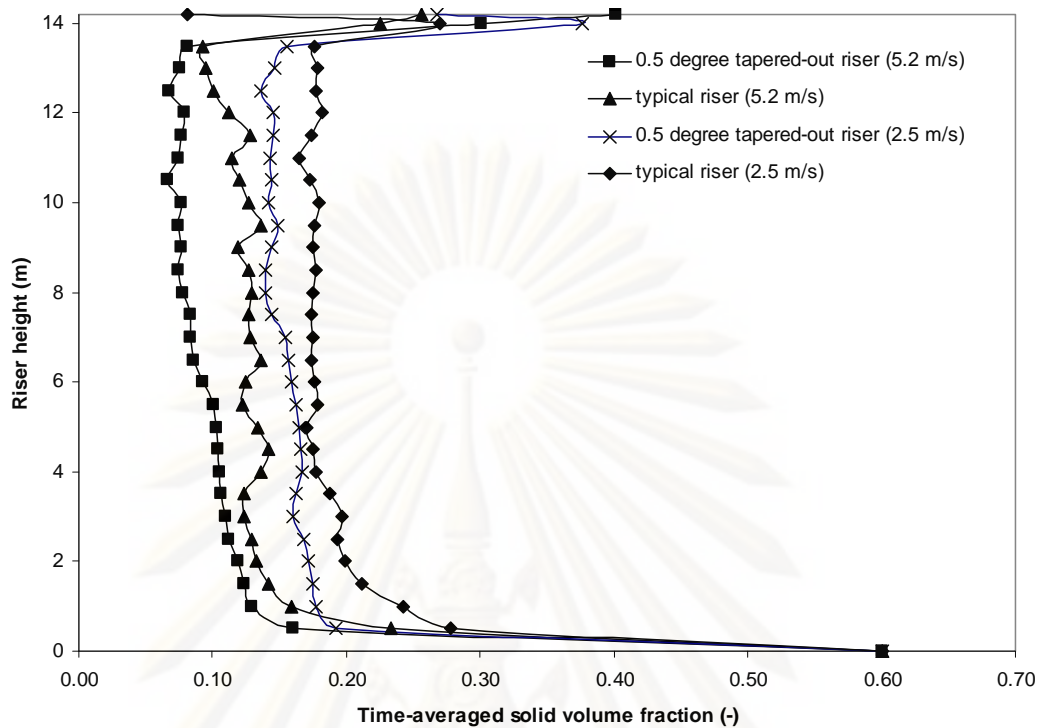
Figure 6.18 The time-averaged axial solid volume fraction along the height of each

riser's geometry with the bottom gas inlet velocity of 2.5 and 5.2 m/s

for Geldart group A particles.
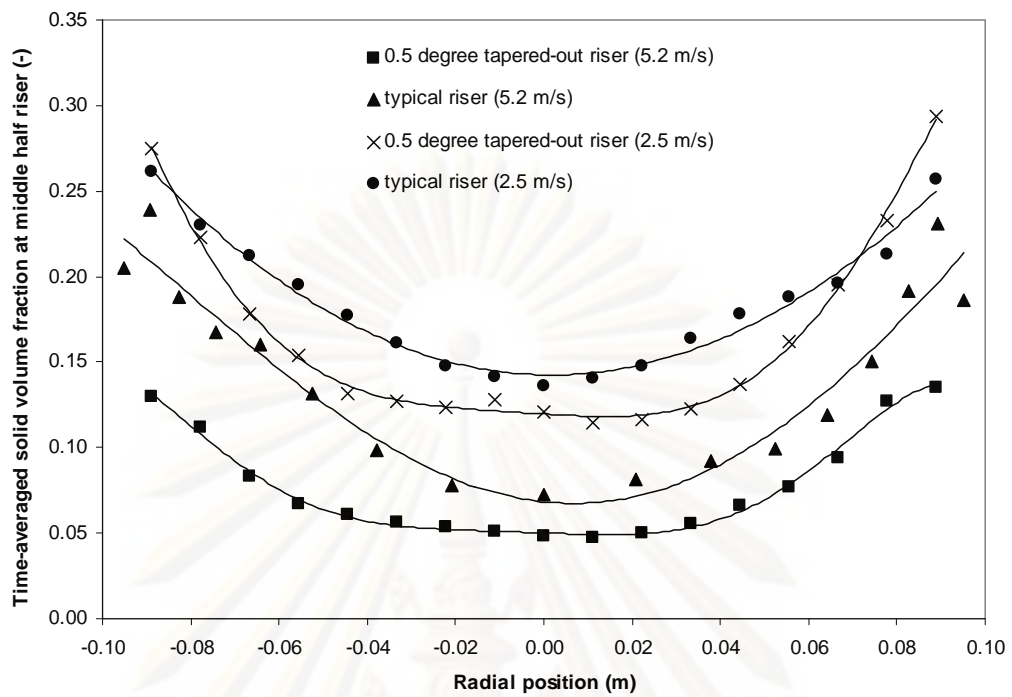
Figure 6.19 The radial distribution of time-averaged solid volume fraction in the middle of

each riser's geometry with the bottom gas inlet velocity of 2.5 and 5.2 m/s

for Geldart group A particles.
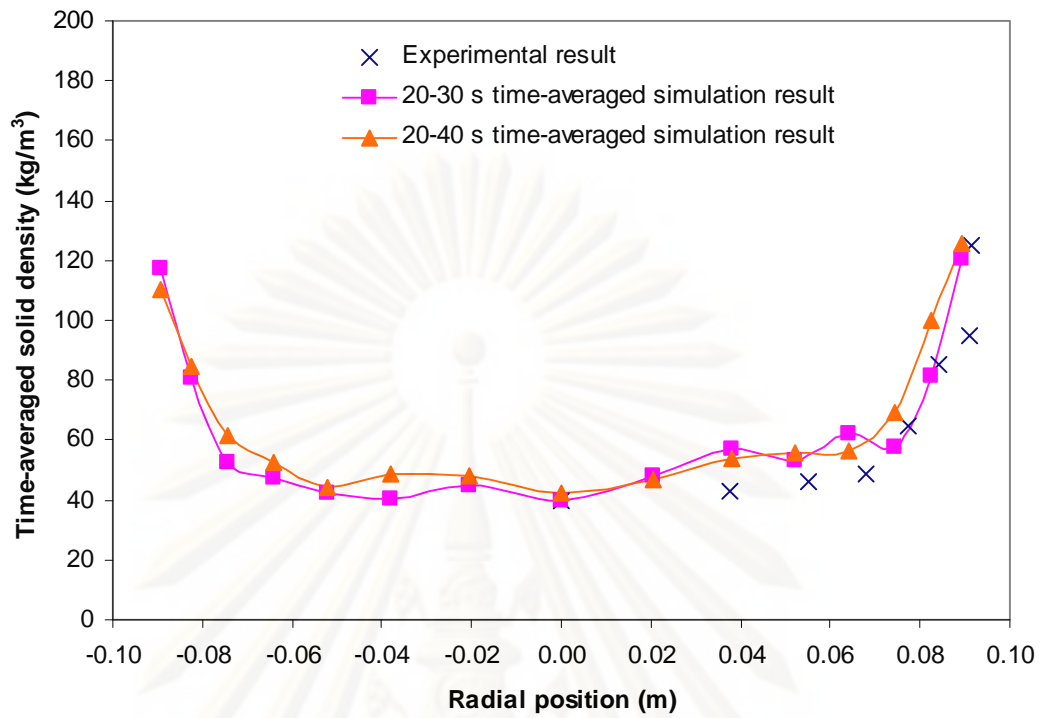
Figure 6.20 Measured and computed time-averaged solid densities at 3.9 m above the

bottom of the riser with two different time-average ranges.
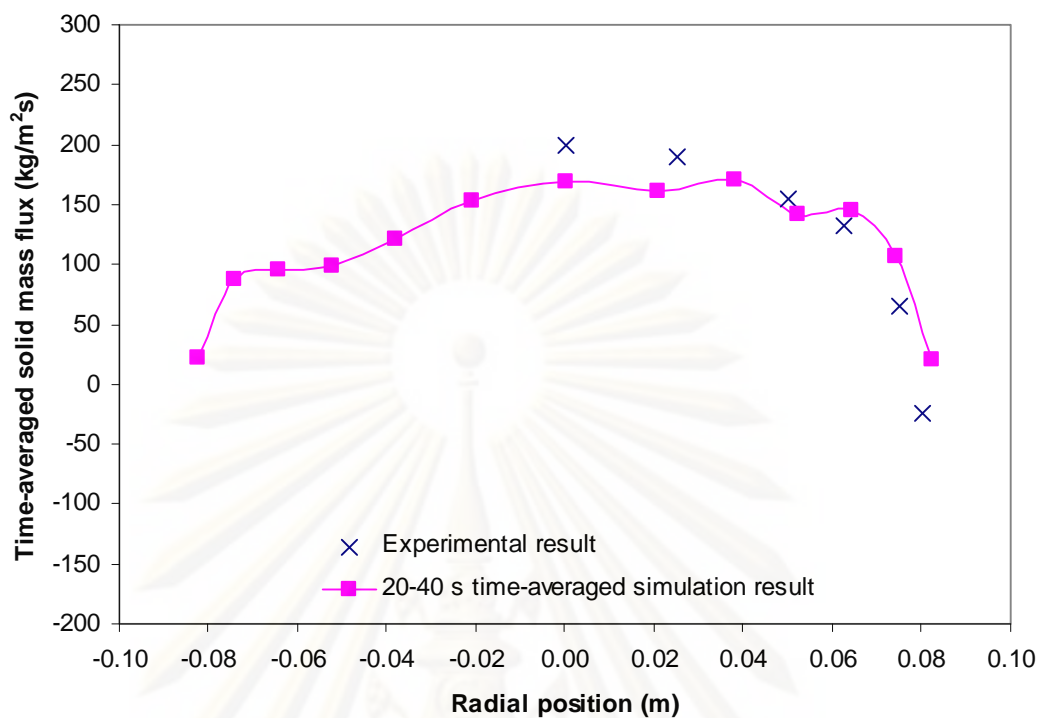
Figure 6.21 Measured and computed time-averaged solid mass fluxes at 3.9 m above

the bottom of the riser.
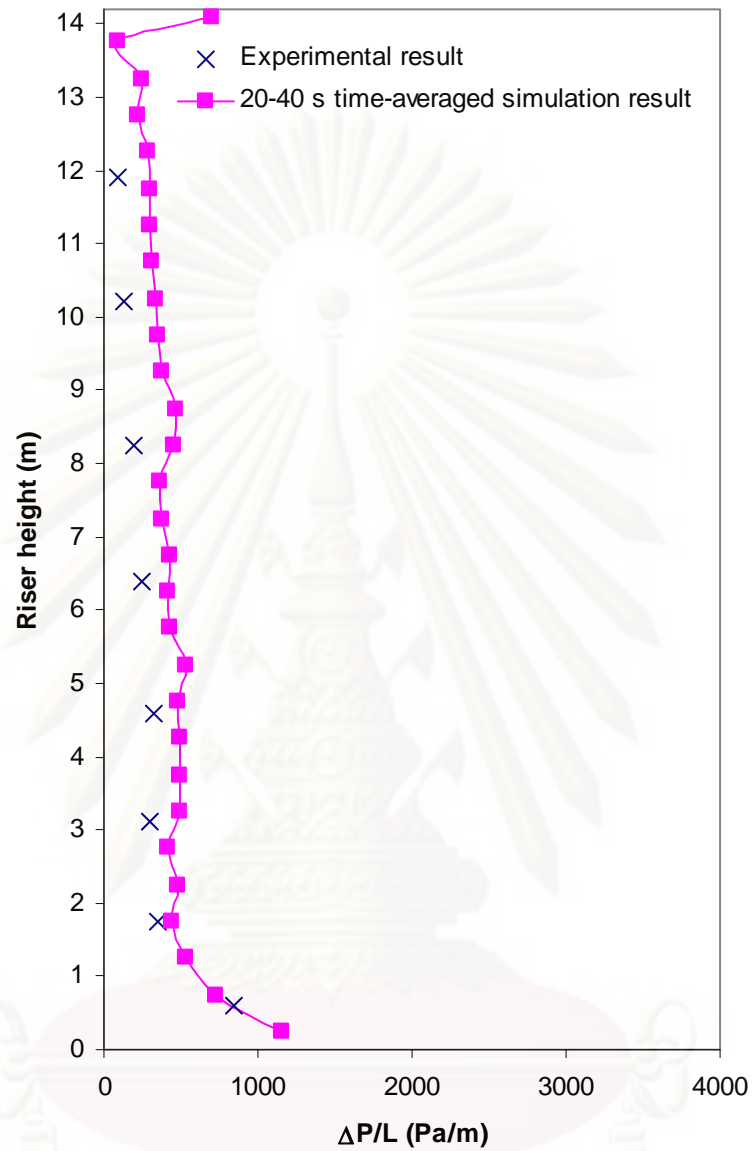
Figure 6.22 Measured and computed time- and area- averaged pressure drop profiles in the riser of the PSRI challenge problem I benchmark test.
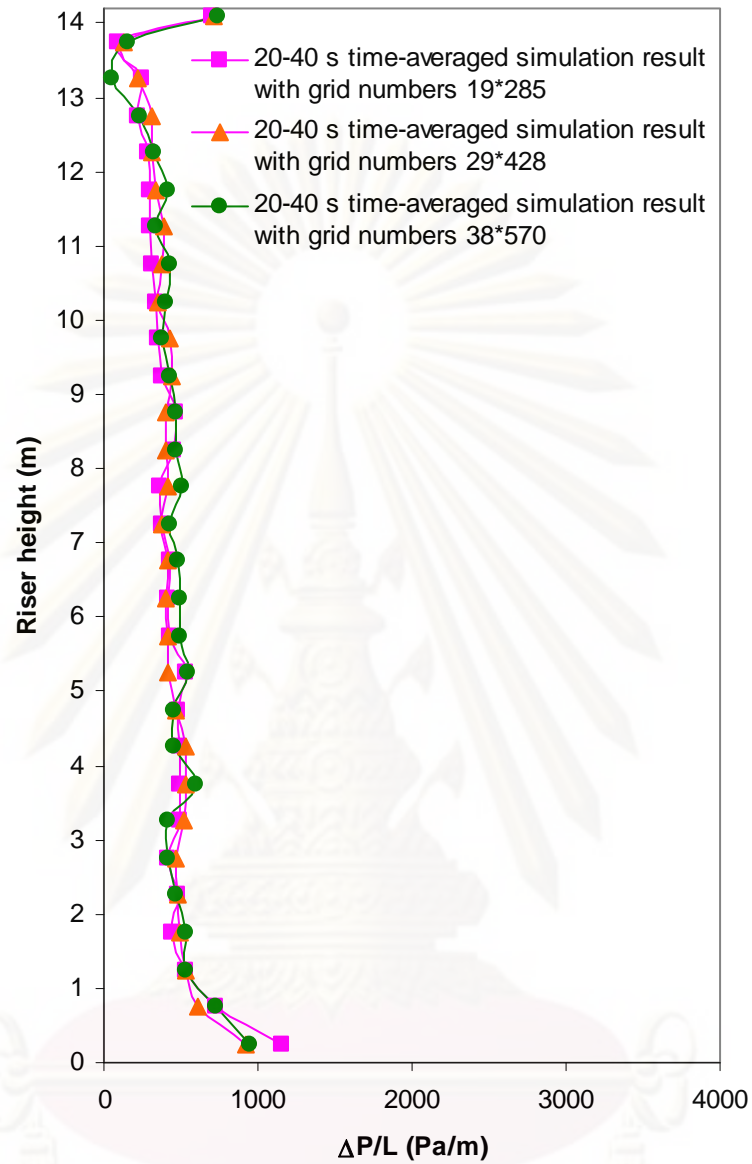
Figure 6.23 Computed time- and area- averaged pressure drop profiles in the riser with three different grid numbers.
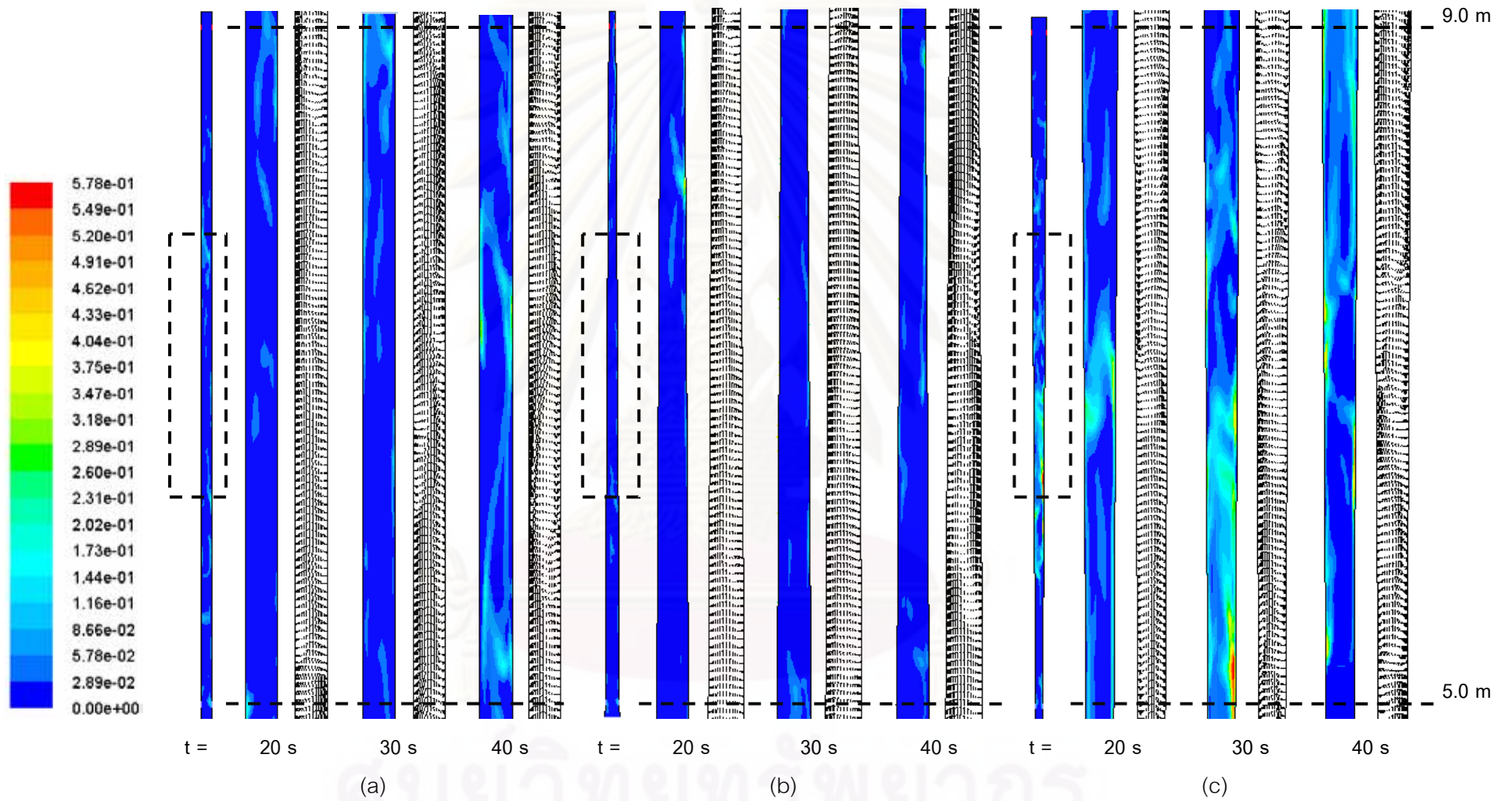
Figure 6.24 Transient distributions of solid volume fraction and solid velocity in the (a) typical, (b) tapered-out and (c) tapered-in risers.
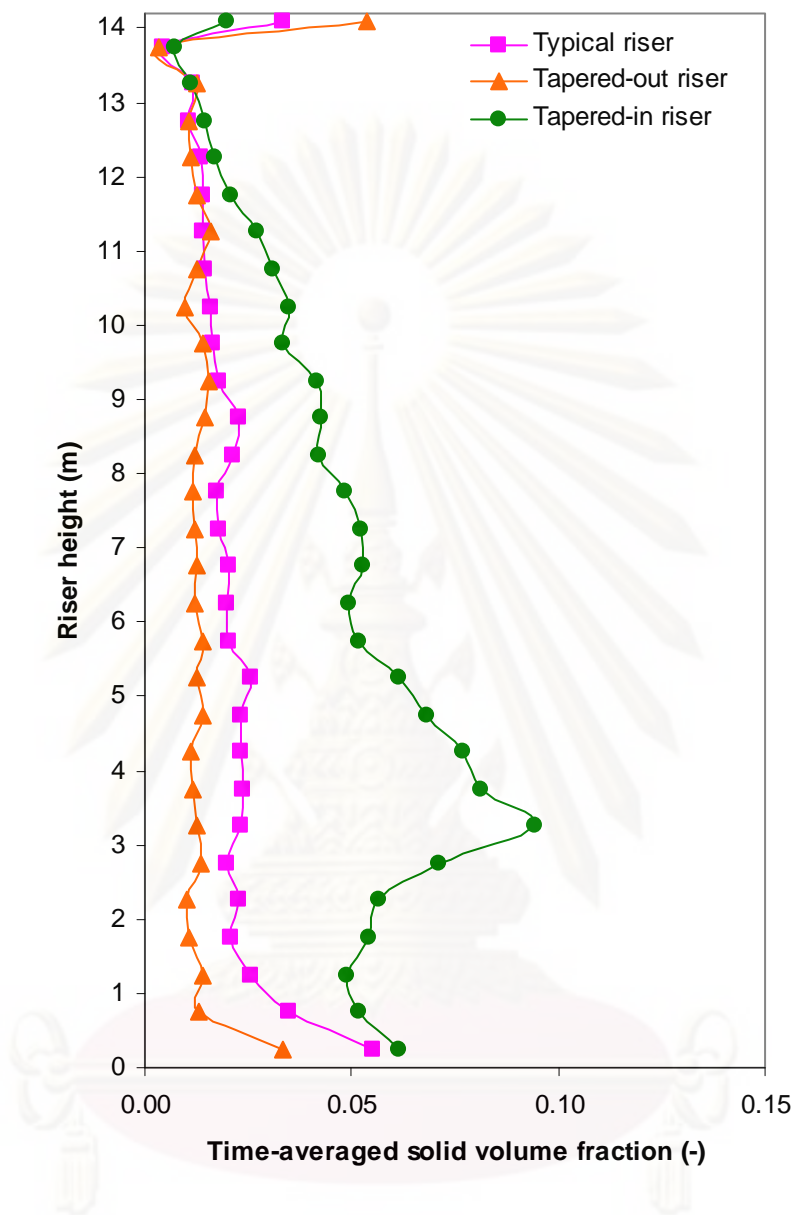
Figure 6.25 Computed time- and area- averaged solid volume fraction profiles in the
riser with three different riser geometries.
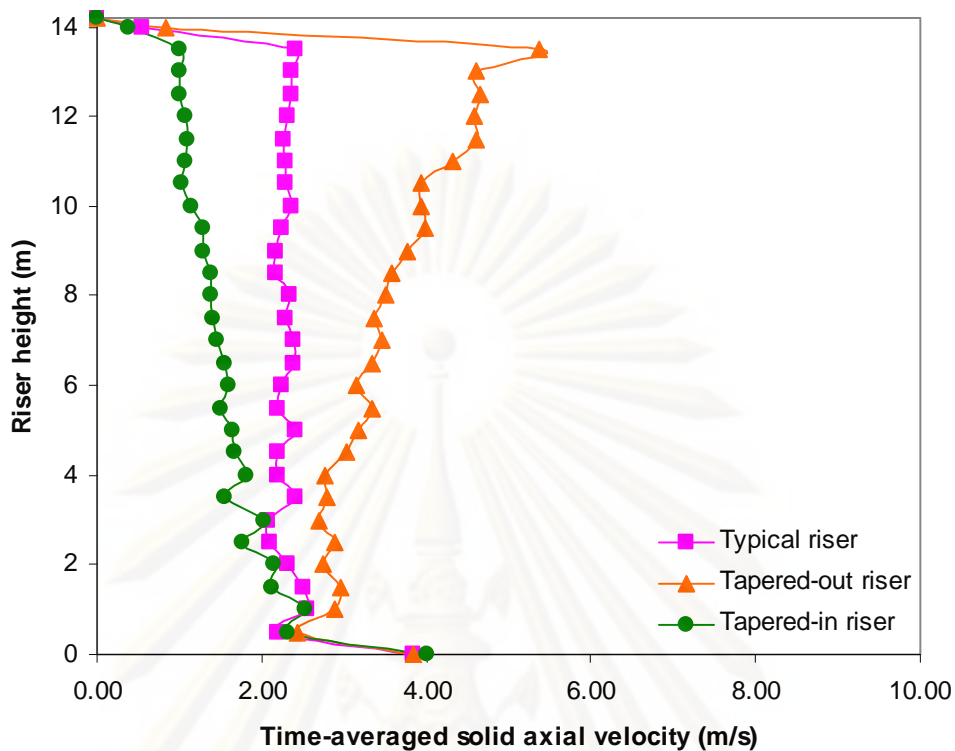
(a)
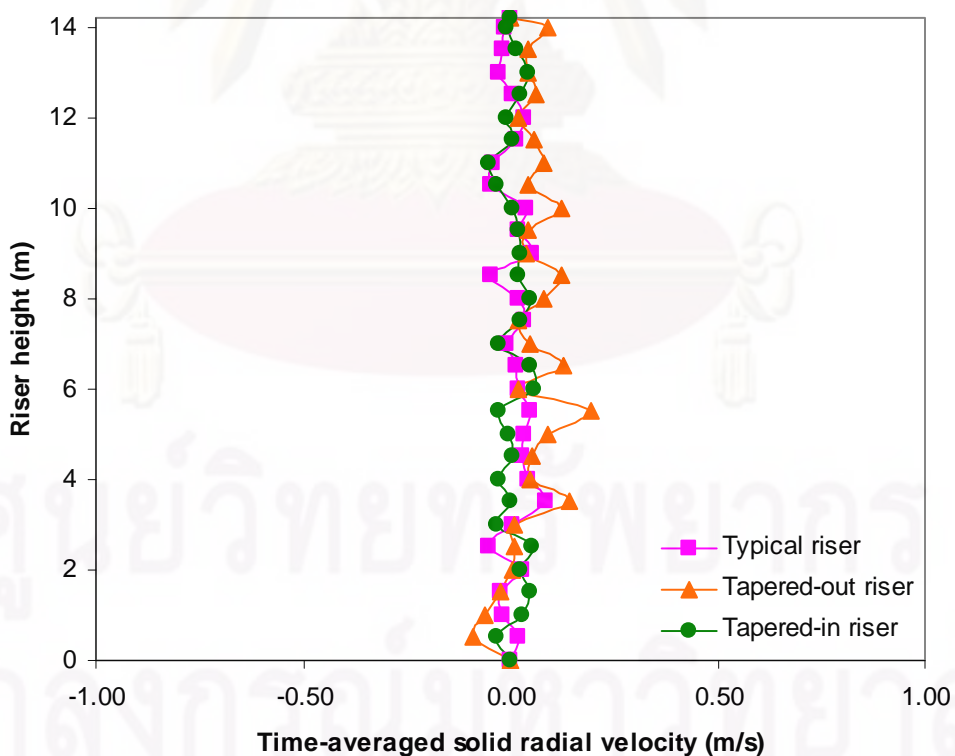
(b)

Figure 6.26 Computed time- and area- averaged solid (a) axial and (b) radial velocity

profiles in the riser with three different riser geometries.
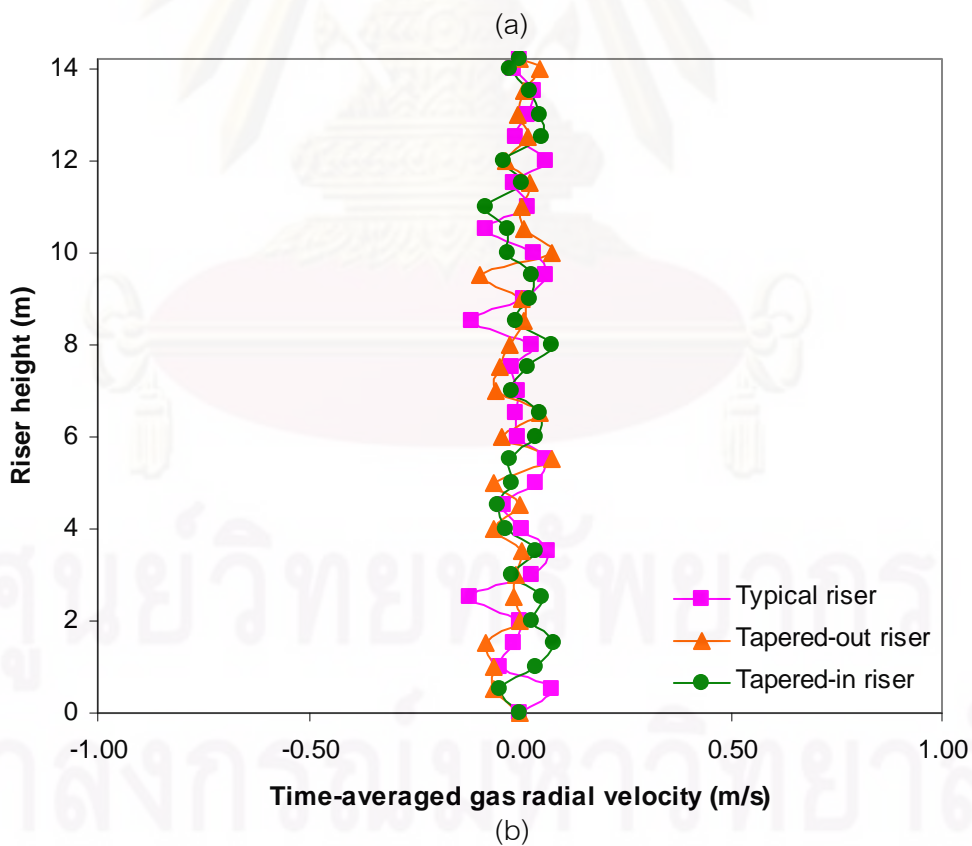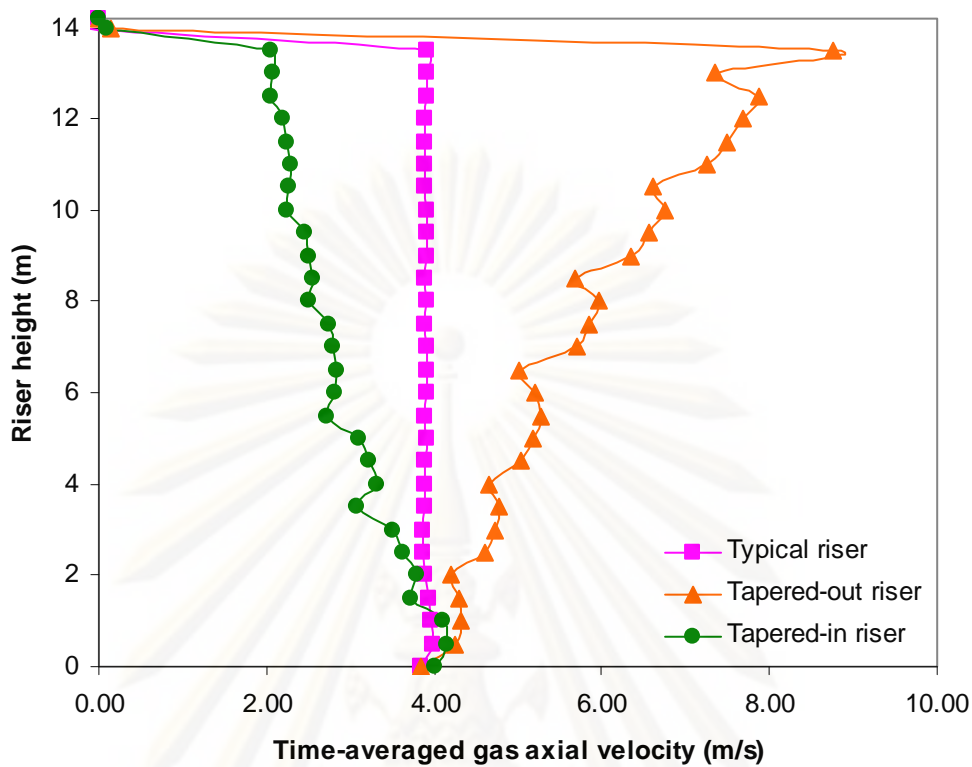
Figure 6.27 Computed time- and area- averaged gas (a) axial and (b) radial velocity

profiles in the riser with three different riser geometries.
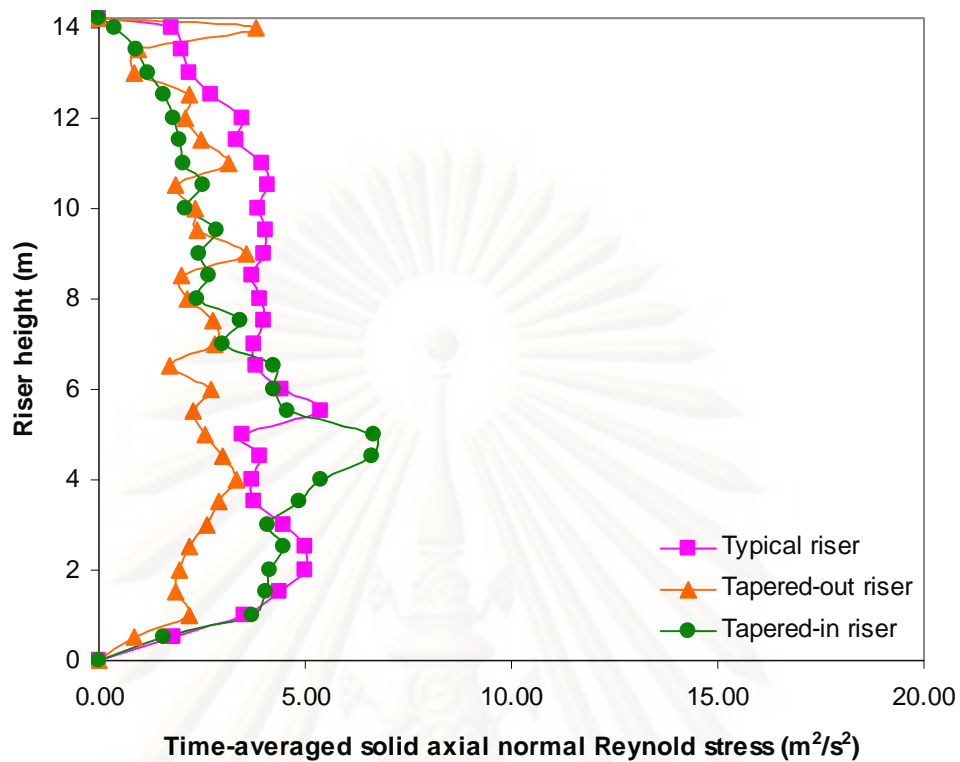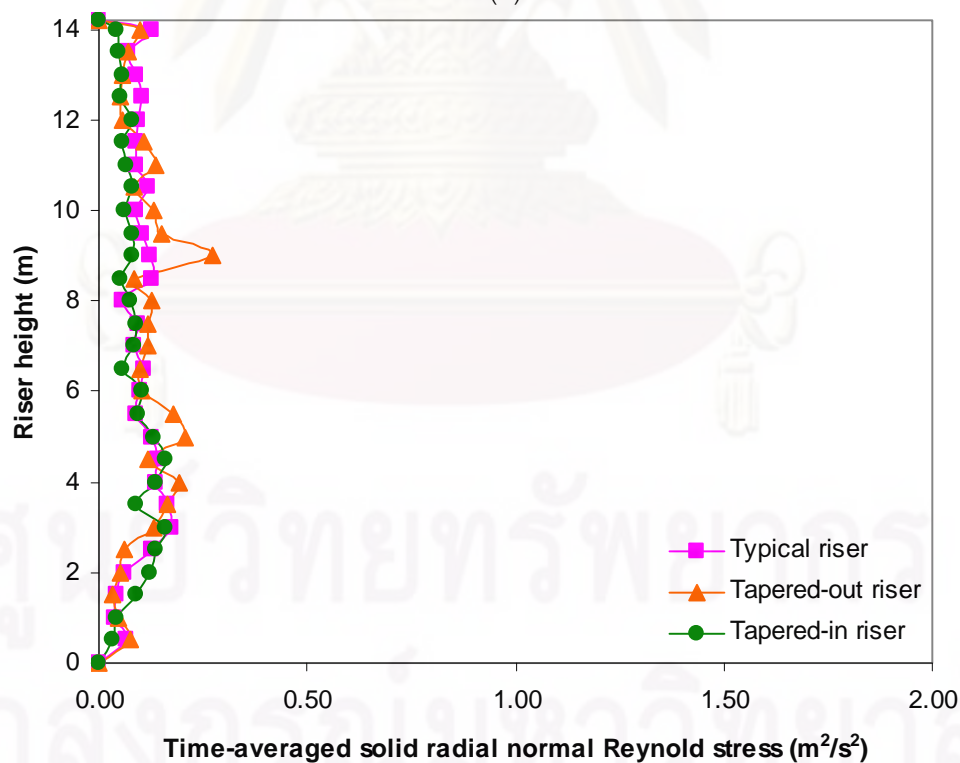
Figure 6.28 Axial distributions of computed time- and area- averaged solid (a) axial and

(b) radial normal Reynolds stresses with three different riser geometries.
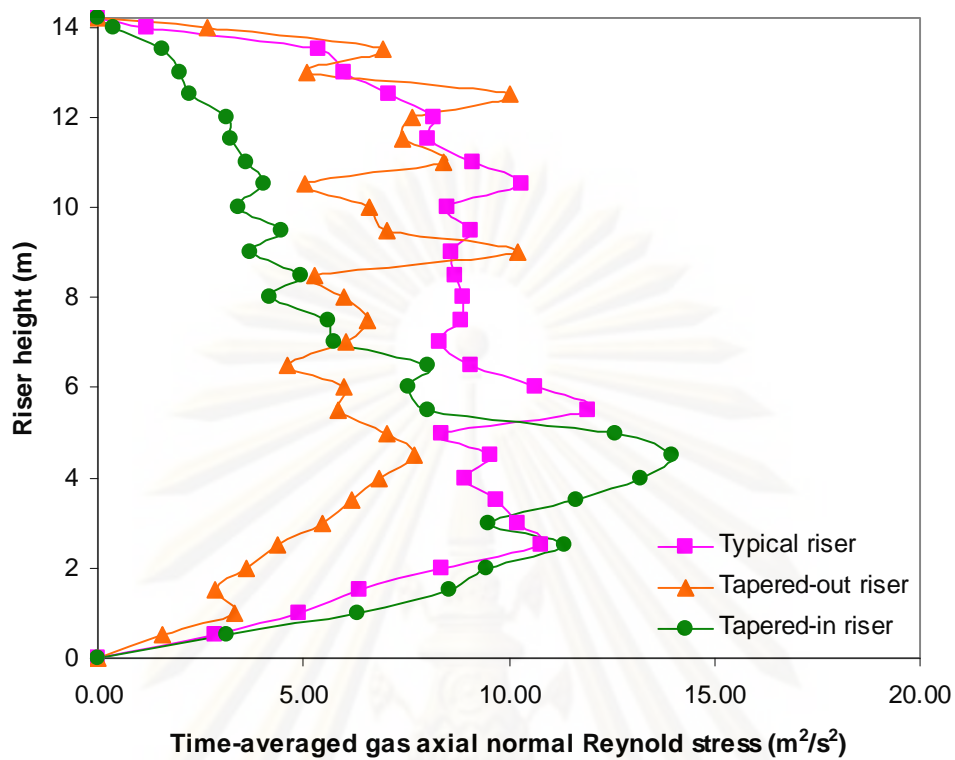
(a)
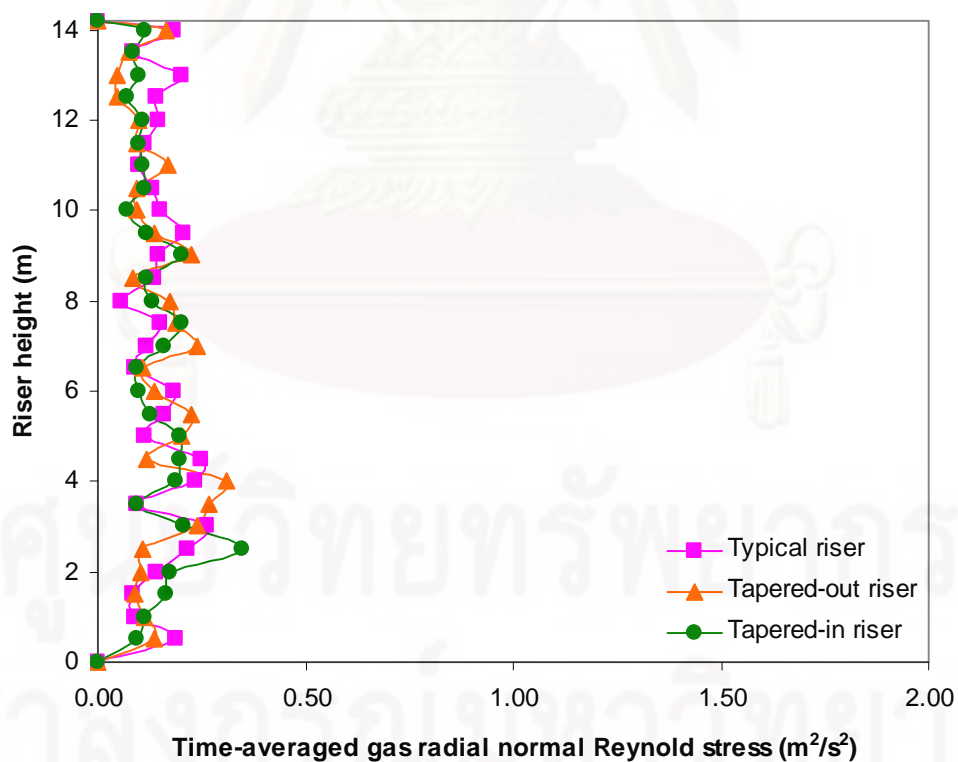
(b)

Figure 6.29 Axial distributions of computed time- and area- averaged gas (a) axial and

(b) radial normal Reynolds stresses with three different riser geometries.
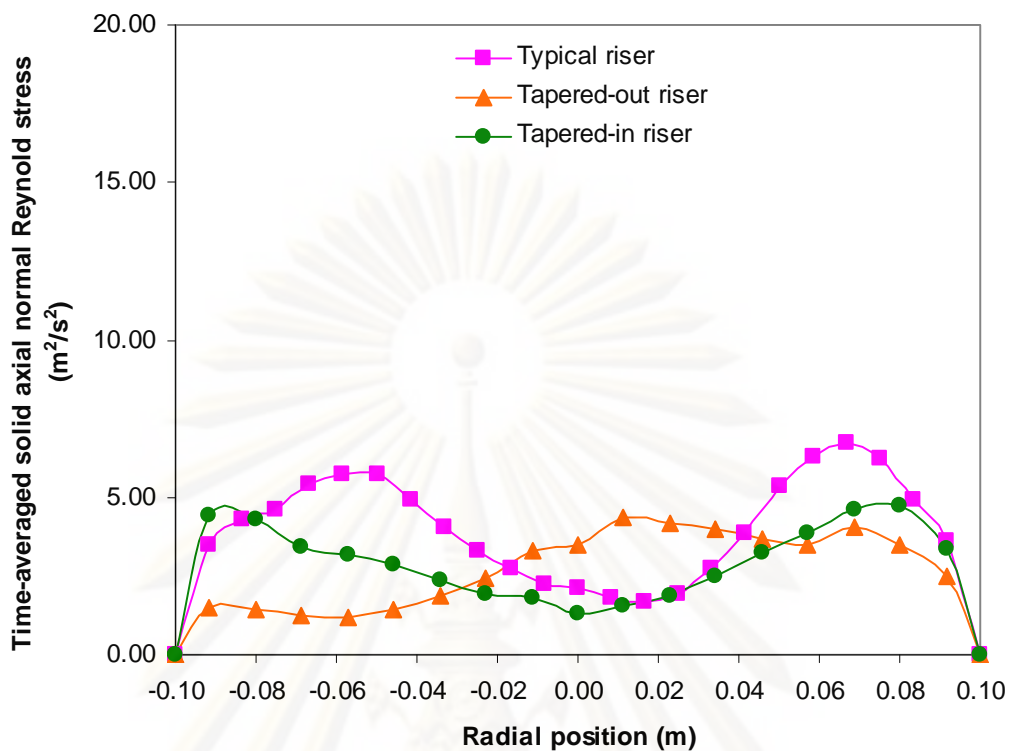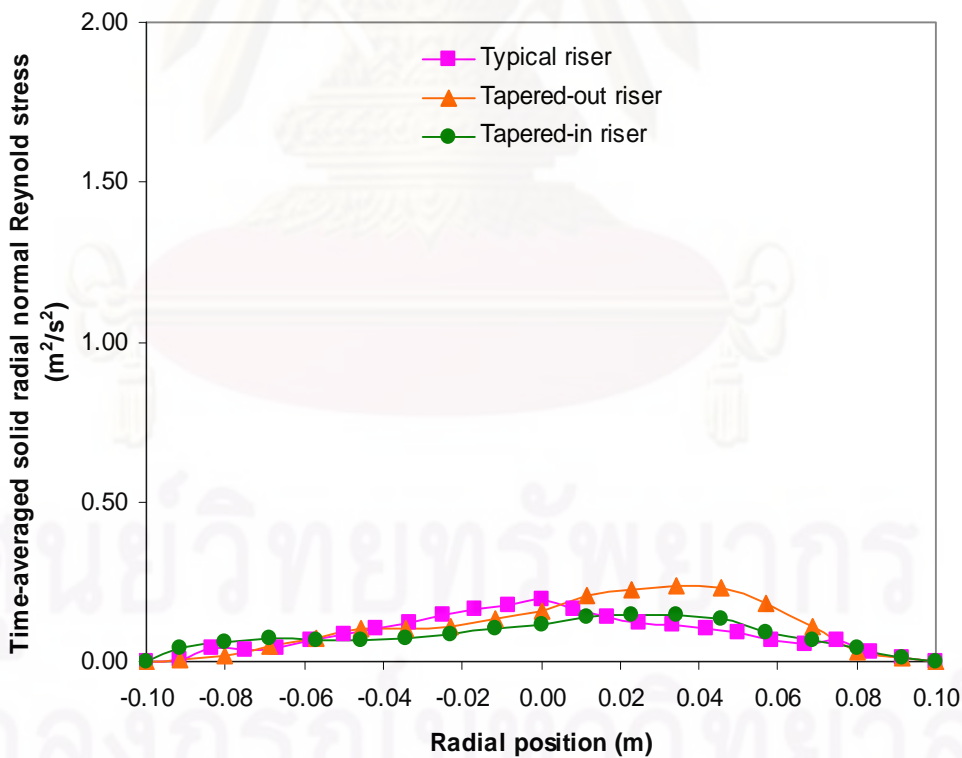
Figure 6.30 Radial distributions at h = 7.0 m of computed time-averaged solid (a) axial

and (b) radial normal Reynolds stresses with three different riser geometries.
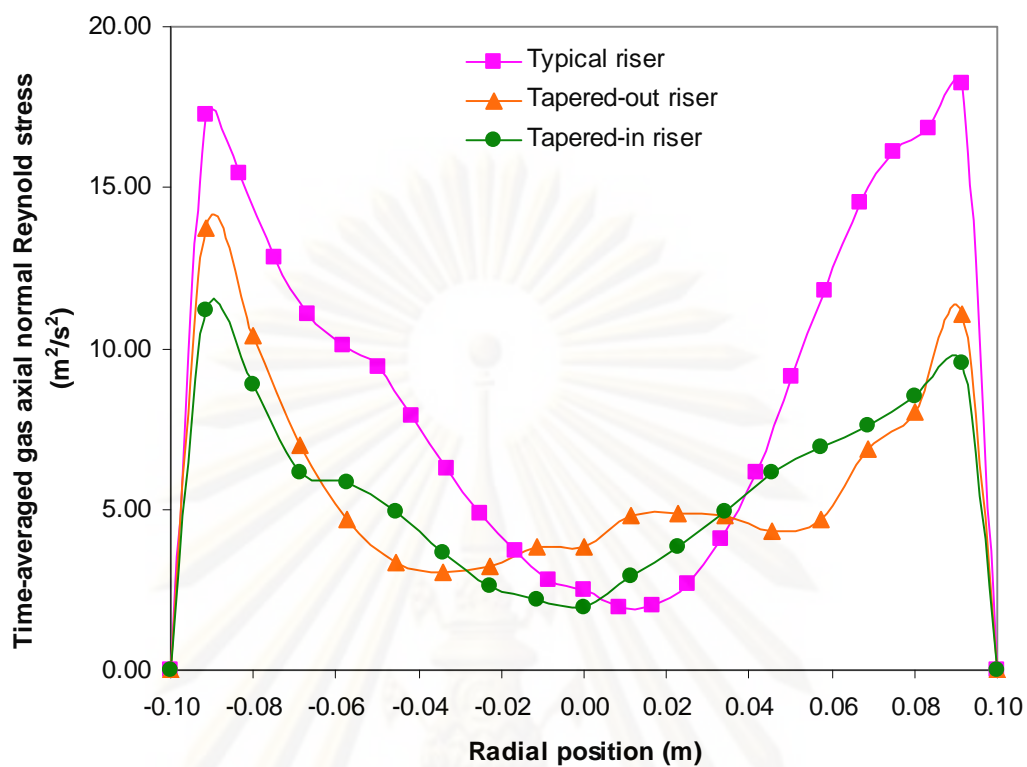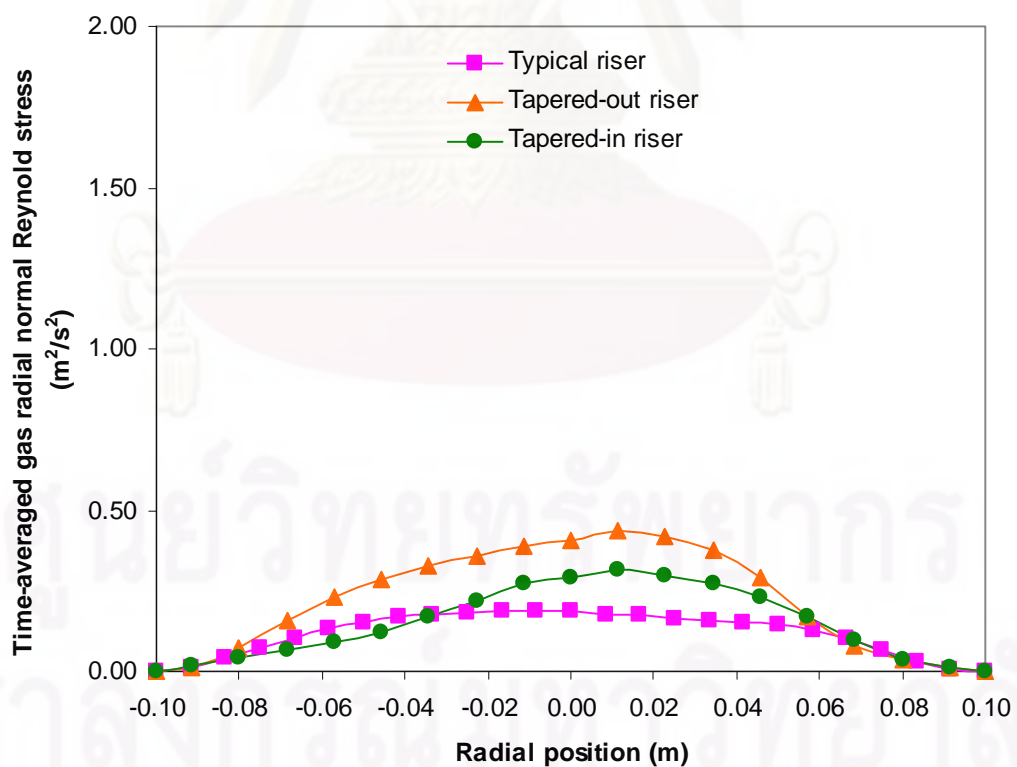
Figure 6.31 Radial distributions at h = 7.0 m of computed time-averaged gas (a) axial

and (b) radial normal Reynolds stresses with three different riser geometries.
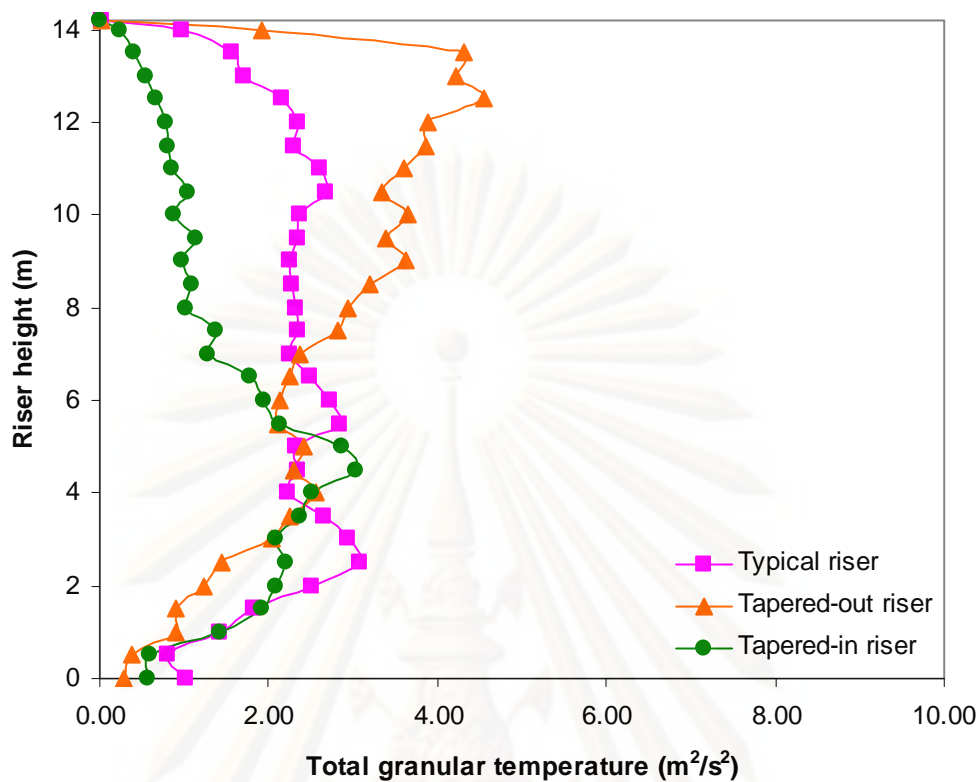
Figure 6.32 Axial distributions of computed total granular temperature with three different riser geometries.
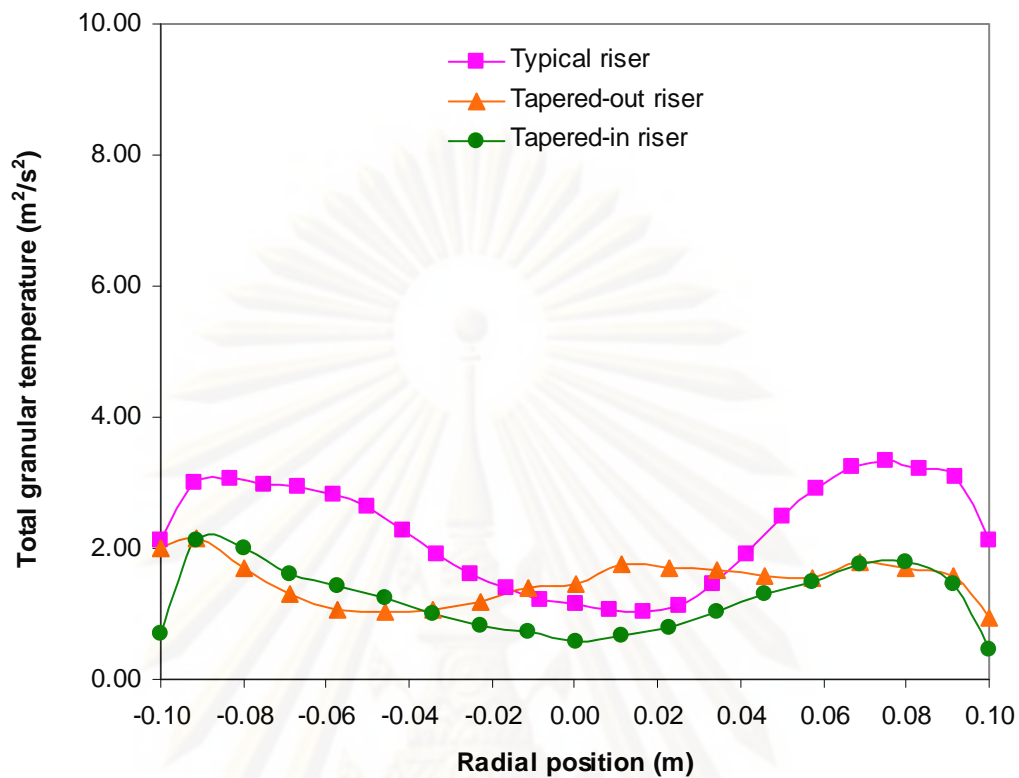
Figure 6.33 Radial distributions at h = 7.0 m of computed total granular temperature with three different riser geometries.
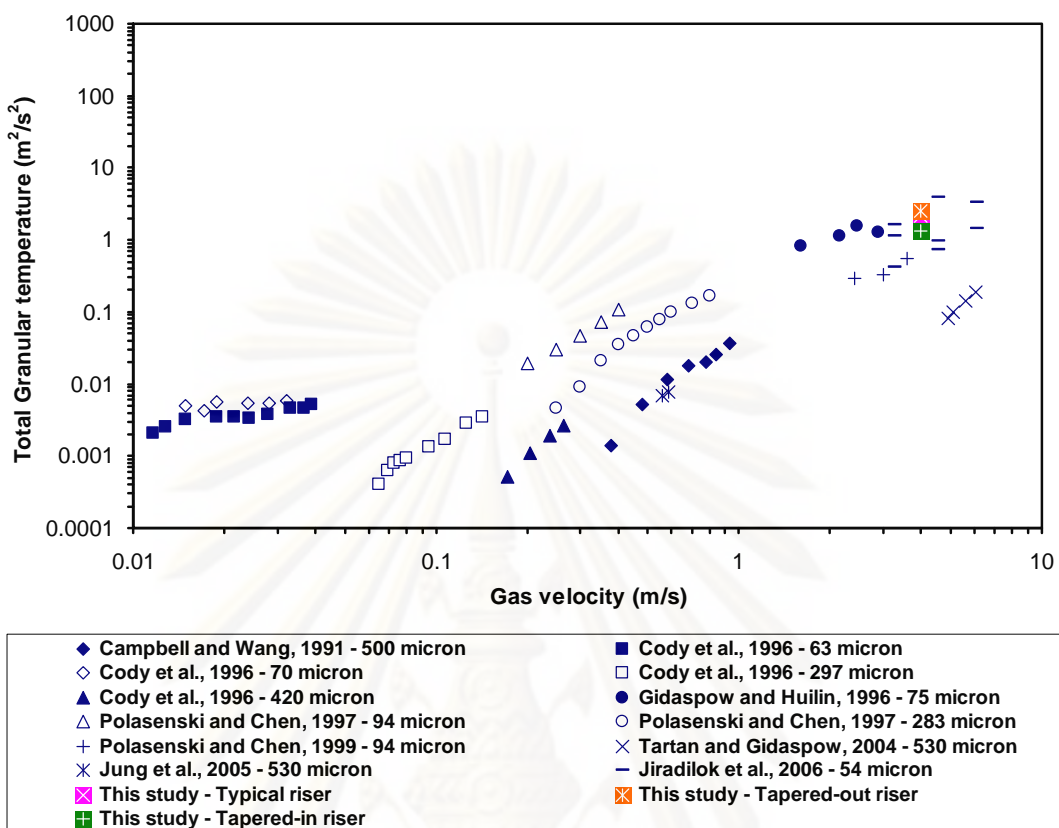
Figure 6.34 Comparison of total granular temperatures with the literature values.
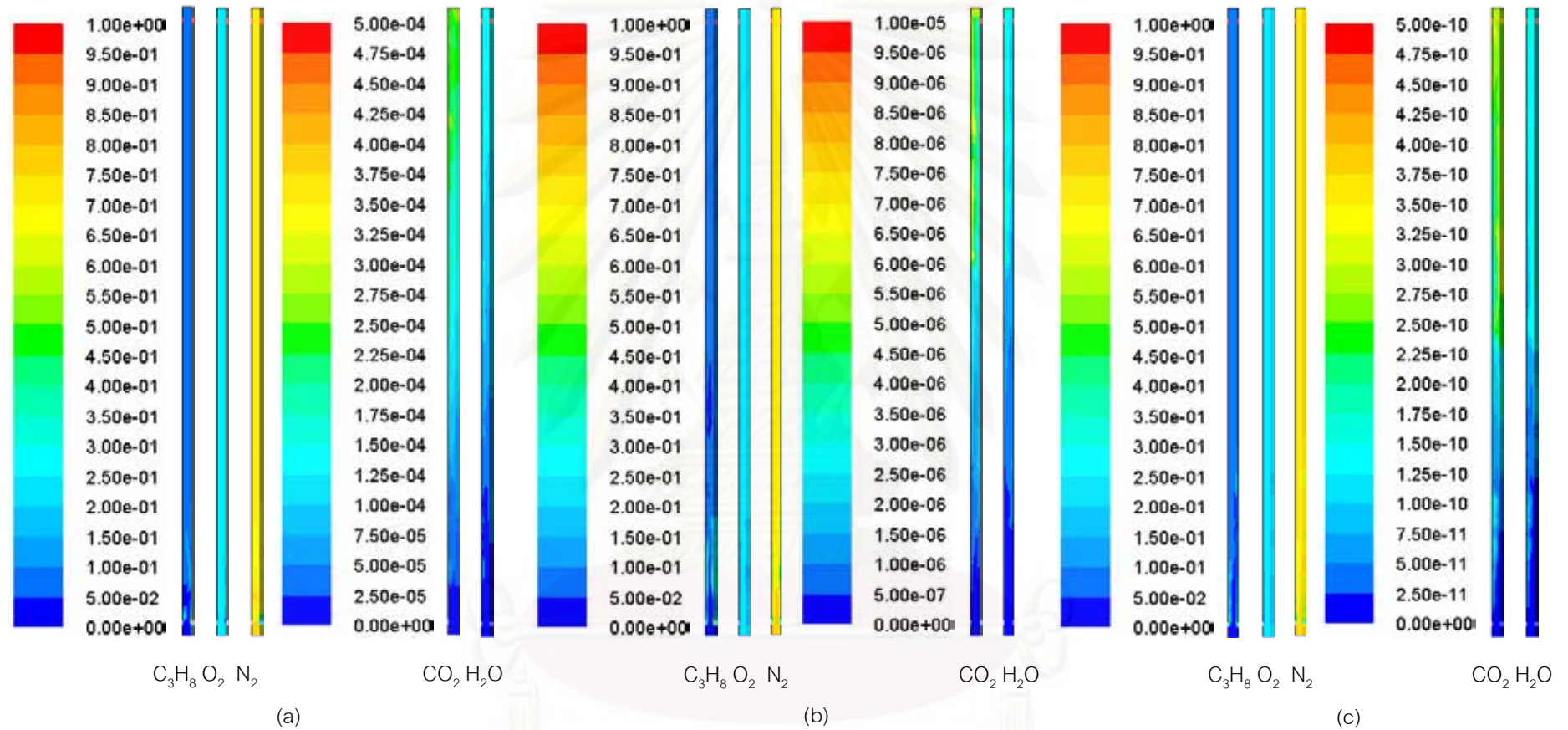
Figure 6.35 Contour of mass fraction distributions of gas compositions in the typical riser with (a) faster reaction rate, (b) medium reaction rate and (c) slower reaction rate.
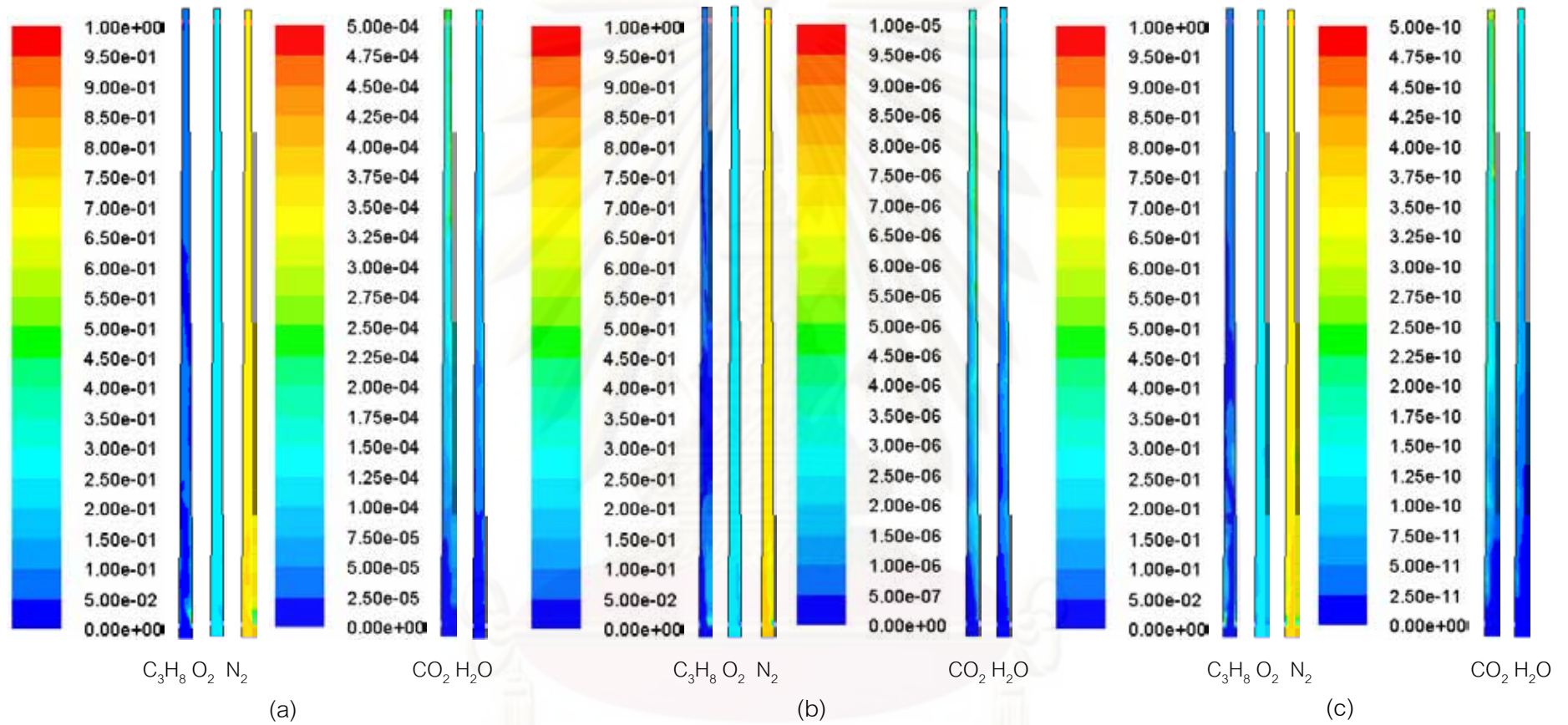
Figure 6.36 Contour of mass fraction distributions of gas compositions in the tapered-out riser with (a) faster reaction rate, (b) medium reaction rate and (c) slower reaction rate.

$C_3H_8 \ O_2 \ N_2$ $CO_2 \ H_2O$ $C_3H_8 \ O_2 \ N_2$ $CO_2 \ H_2O$ $C_3H_8 \ O_2 \ N_2$ $CO_2 \ H_2O$

(a)   (b)   (c)
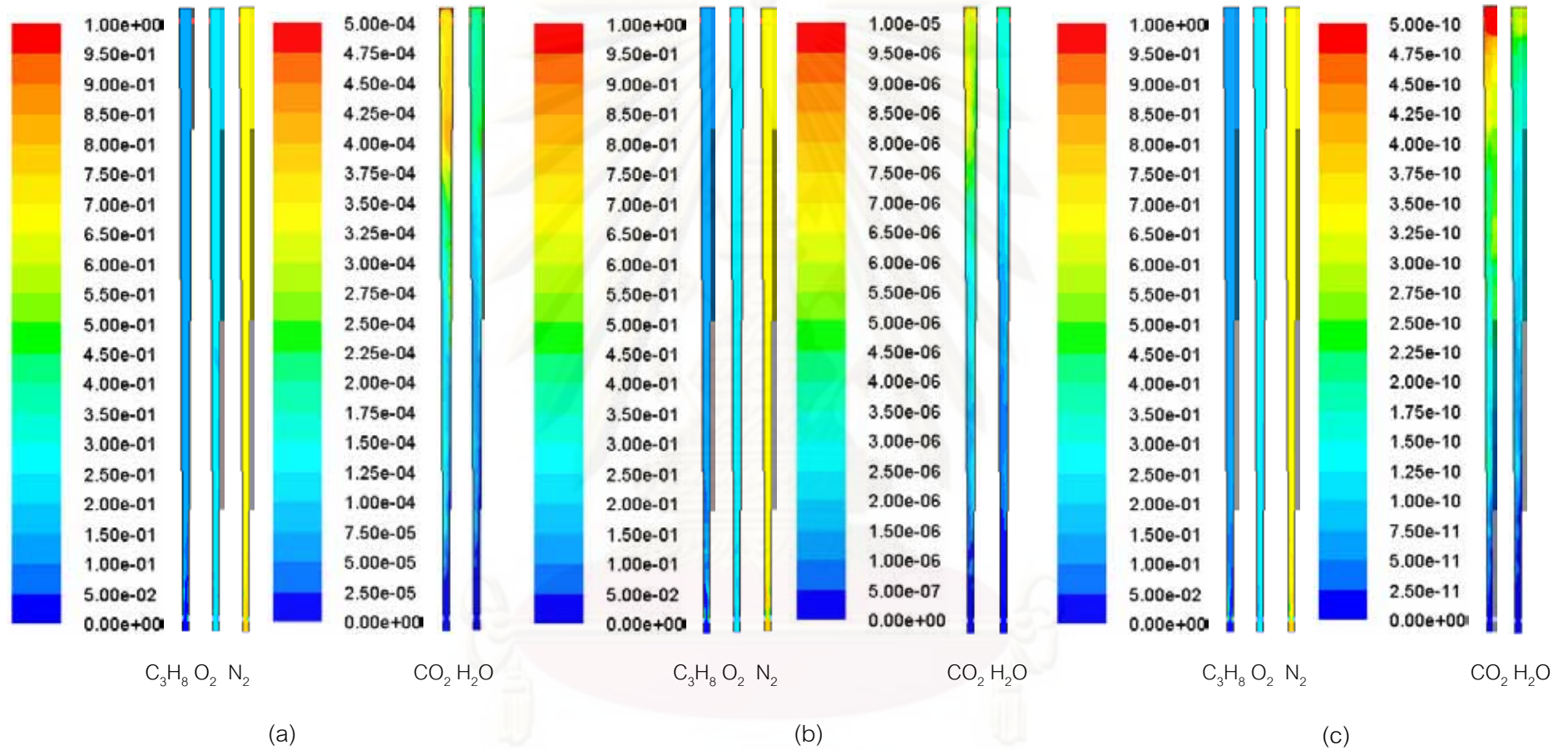
Figure 6.37 Contour of mass fraction distributions of gas compositions in the tapered-in riser with (a) faster reaction rate, (b) medium reaction rate

and (c) slower reaction rate.
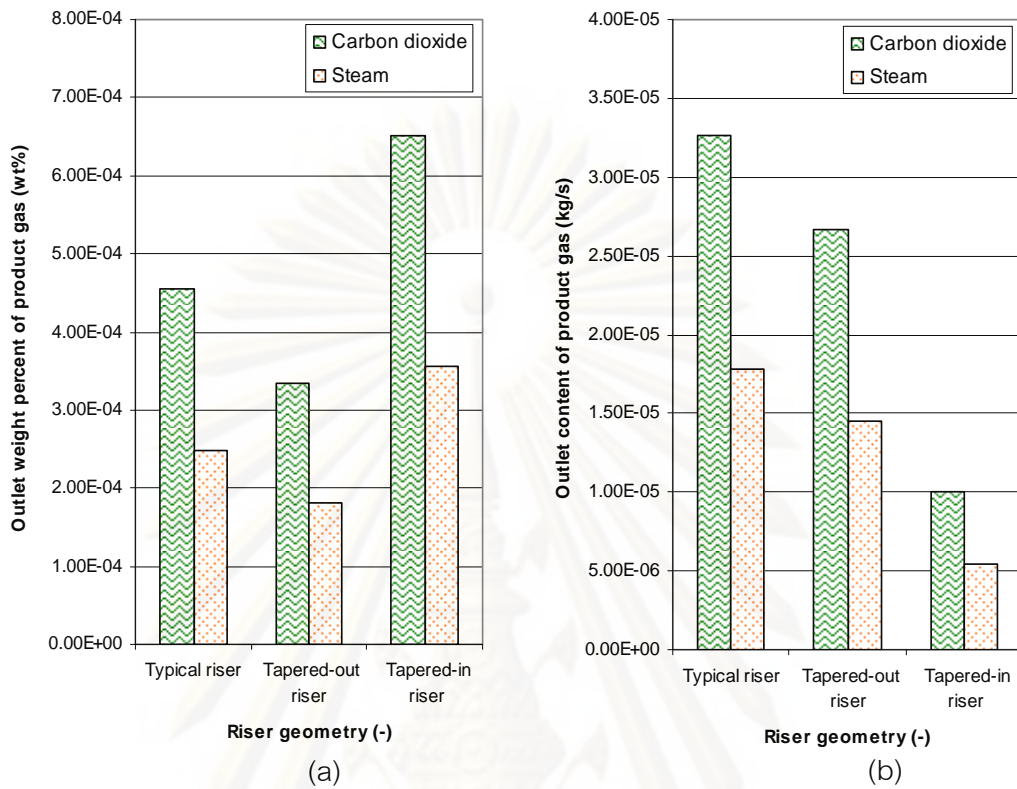
Figure 6.38 (a) The outlet weight percent and (b) the outlet content of product gases in three different riser geometries with medium reaction rate.
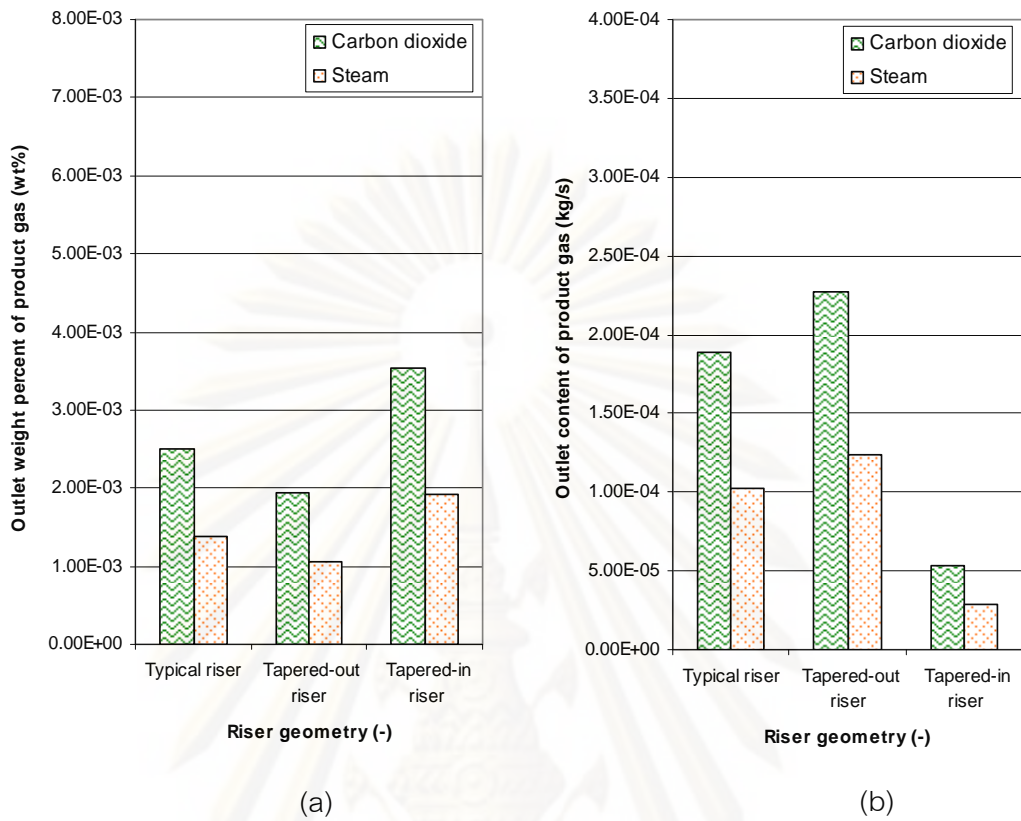
Figure 6.39 (a) The outlet weight percent and (b) the outlet content of product gases in three different riser geometries with fast reaction rate.
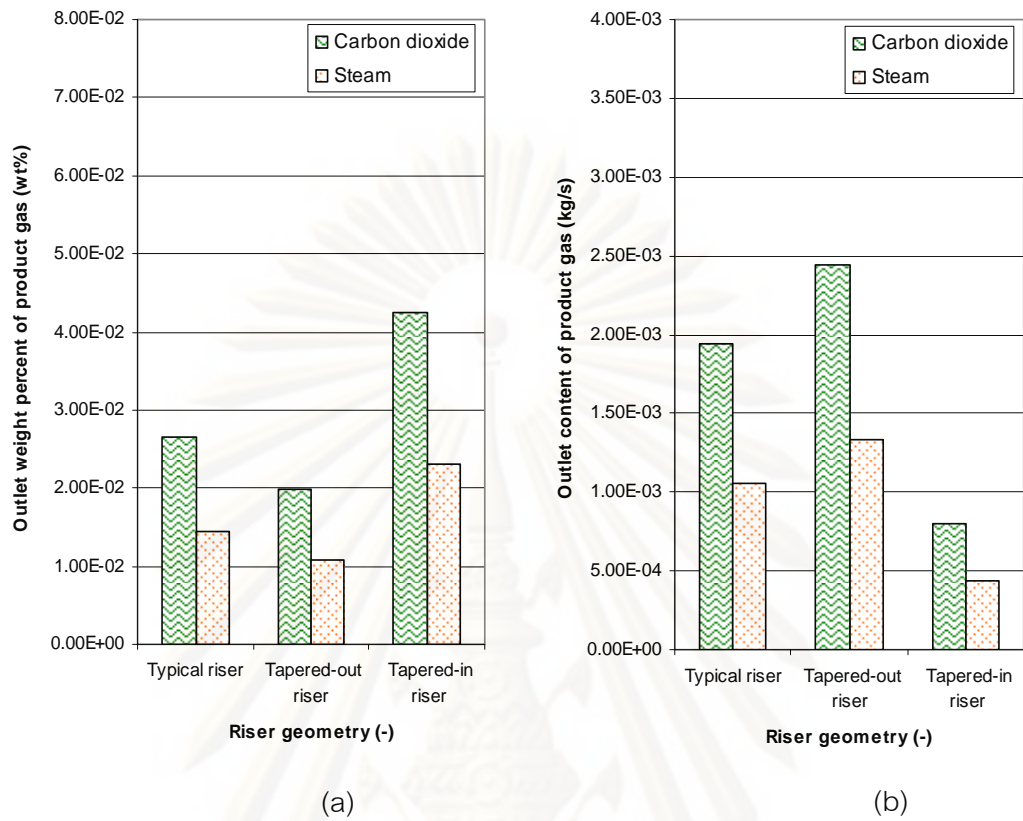
Figure 6.40 (a) The outlet weight percent and (b) the outlet content of product gases in three different riser geometries with faster reaction rate.
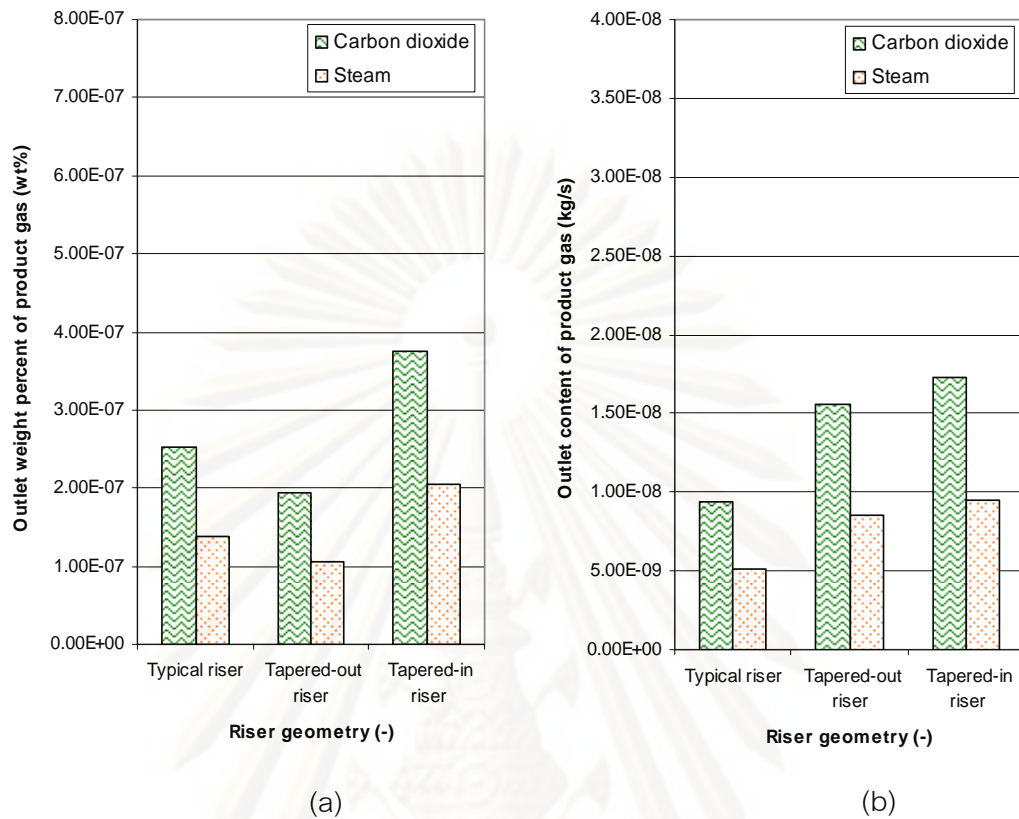
Figure 6.41 (a) The outlet weight percent and (b) the outlet content of product gases in three different riser geometries with slow reaction rate.
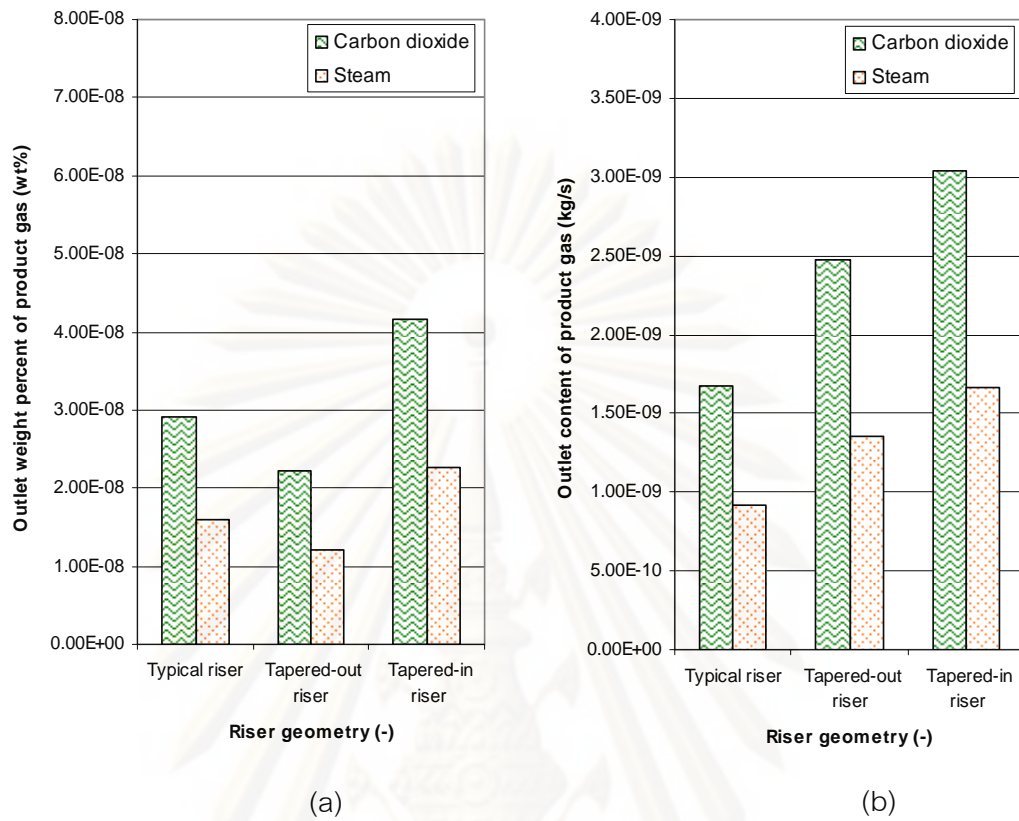
Figure 6.42 (a) The outlet weight percent and (b) the outlet content of product gases in three different riser geometries with slower reaction rate.

CHAPTER VII

MEASUREMENT OF TURBULENCE AND LOW DISPERSION
AT THE WALL REGION IN A CIRCULATING FLUIDIZED BED RISER

7.1. Introduction

Quantitative understanding of the hydrodynamic based transport relationship for mass transfer and heat transfer, by analogy, is required for the design and scale-up of a circulating fluidized bed (CFB) riser as stated by Breault (2006) and Jiradilok et al. (2007). Particle dispersion coefficient is one of the key parameters for measuring the quality of mass transfer. It can be viewed from two perspectives, macroscopically and microscopically. In the macroscopic view, a tracer is used to determine the degree of system non-ideal mixing behavior. In the microscopic view, the dispersion arises from the local turbulence. Considering on the latter point of view, the main characteristics of system turbulence are the production of additional stresses and the random oscillation of solid particles, called granular temperature. Breault et al. (2005, 2008) conducted an experiment with Laser Doppler Velocimetry (LDV) method and obtained granular temperatures and axial dispersions from time dependent particle velocities. The radial dispersions, which are more important mixing direction, were not considered because of their technique limitation. If the particles are not fully mixed laterally, the chemical reaction conversion will decrease. However, Jiradilok et al. (2006, 2008) showed that similar technique could be used to obtain both the axial and radial dispersion coefficients with computational fluid dynamics data.

Due to the wall effect, particle velocity decreases at the wall region in a CFB riser. This situation may result in an internal circulating hydrodynamics or flow induced by the phase velocity gradient. A detail study of this region therefore may help the understanding of physical system and the improvement. In this study, an alternative method, named particle image velocimetry (PIV), was used to determine both axial and radial dispersion coefficients at the wall region from particle velocity data. The

computed dispersions were then compared with the literature data and were employed to explain the system behaviors.

7.2. Experimental

7.2.1. Circulating fluidized bed riser

Experimental data were taken from the acrylic section of the National Energy Technology Laboratory CFB riser at Department of Energy, Morgantown, USA. Figure 7.1 shows the schematic drawing of the CFB system. The diameter and height of the riser were 0.30 and 15.79 m, respectively. Solid particles entered the riser from a 0.23 m diameter side port at 0.33 m above the gas distributor. Solid particles exited the riser through a 0.20 m diameter bend port at 0.33 m below the top of the riser. The riser was connected to a cyclone and downcomer through a 0.23 m diameter and 1.52 m length L-valve. The diameter and height of the downcomer were 0.25 and 12.63 m, respectively. In this study, the particle velocity data were measured at a height of 7.00 m above the gas distributor. The experiments were carried out at ambient temperature and pressure. The system relative humidity was controlled to minimize the effect of static charge building up on the solid particles.

The used solid particles were 750 μm polyethylene beads, having a density of 863 kg/m^3. Experiments were performed at two different operating conditions referred as dilute and dense conditions. For both conditions, the superficial gas velocity was remained constant at 7.57 m/s. The solid mass fluxes for dilute and dense conditions were 19.39 and 39.08 kg/m^{2}s, respectively.

7.2.2. Particle image velocimetry (PIV)

Figure 7.2 (a) displays the PIV measurement system. The system basically consists of a charge coupled device (CCD, Sony DVC-151A) camera, a fiber optic light, a small motor with a rotating transparent sheet and a computer with image processing software of Image-Pro Plus^{TM}. The PIV method is capable of measuring instantaneous particle velocities as non-intrusive measurement using a CCD camera.

The principle is that particles scatter light into a photographic zoom lens. Images are formed on a video array detector and transferred to a computer. A micro-imaging board is used for capturing and digitizing the images. The instantaneous particle velocities are then analyzed by using Image-Pro Plus^{TM}. The particle velocity is the length of the observed streak line or the space traveled by the particles divided by the exposure time which in this study is 1/250 s. For the current system configuration, it can only measure the two velocity components in the plane normal to the camera which are axial (y-direction) and radial (x-direction) velocities. The third or in-plane radial velocity component (z-direction) can be easily obtained in the image at the position normal to the first plane or it can be simultaneously obtained by using the two CCD cameras PIV measurement system. However, the technique to compute the turbulence and dispersion will be exactly the same. For a clearly visualization of streak line, the system must have the correct position of light. The transparent sheet is used to consider the flow direction of the particles which can be considered by the arrangement of streak line colors. The example of streak line distribution generated on the computer screen is depicted in Figure 7.2 (b).

7.3. Results and discussion

7.3.1. Particle velocities

Instantaneous particle velocities (c_i) at the wall region were measured using PIV method. In this system, the number of streak lines per frame was approximately between 2 and 10 and the CCD camera captured pictures at the rate of 30 frames/s. The raw data from PIV method were the time dependent instantaneous particle velocities. The time-averaged results were computed using 10 s range after the system reached steady state. The total number of streak lines or particles observed in this study was about 1000. This large number of data is sufficient to use as a representative of the system population. Also, the small frame area for averaging of the point variable is large enough to contain the information of particles while still possessing small dimensions compared with the actual system dimensions.

Figures 7.3 (a) and 7.3 (b) illustrate the histograms of measured axial (c_y) and radial (c_x) instantaneous particle velocities, respectively. Both the dense and dilute conditions results are shown in the same figures. From the axial instantaneous particle velocity results, the axial particle flow at the wall region was divided into two groups, upward and downward. However, the normal distributions of axial instantaneous particle velocity were observed in each group. These particles hovered upward but there were periods of downward flow as well. The situations were consistent with the experimental observation from the literature. For the radial instantaneous particle velocity, the results were also had normal distribution with the mean of about zero. The radial velocities were much smaller than the axial ones. The radial particle flow at the wall region thus was restrictive. This infers that the particles not have any changed in the lateral position or the flow is fully developed. Comparing between dense and dilute conditions, the instantaneous particle velocities in dilute condition were higher and widely distributed than dense condition which can be explained by the system available area.

Besides the instantaneous particle velocities, the hydrodynamic particle velocities (v_i) were computed. The hydrodynamic particle velocity is the average of the instantaneous particle velocities in each frame. It can be used as a cluster of solid particles velocity representative defined as:

$$v_i(t) = \frac{1}{b} \sum_1^b c_i(t)$$
(7.1)

where i is system directions, t is time and b is the number of solid particles per unit area in each frame. The histograms of computed axial (v_y) and radial (v_x) hydrodynamic particle velocities for both system operating conditions, dense and dilute, are shown in Figures 7.3 (c) and 7.3 (d), respectively. The trends of hydrodynamic particle velocity result were consistent with the instantaneous particle velocity. The individual particle and the cluster of solid particles hence established similar flow structure at this position.

7.3.2. Particle normal stresses and normal Reynolds stresses

As mentioned in the previous chapter, one characteristics of system turbulence is the production of additional stresses, called particle normal stresses ($\langle C_i C_i \rangle(t)$) and normal Reynolds stresses ($\overline{v_i' v_i'}(t)$). The particle normal stresses and the particle normal Reynolds stresses are computed using instantaneous and hydrodynamic particle velocities, respectively. The methodology to calculate particle normal Reynolds stresses is proposed in Chapter IV. Here, the methodology to calculate particle normal stresses is defined:

$$\langle C_i C_i \rangle(t) = \frac{1}{b} \sum_1^b \left(c_i(t) - v_i(t) \right)\left(c_i(t) - v_i(t) \right) \qquad (7.2)$$

Table 7.1 summarizes the computed particle normal stresses and normal Reynolds stresses at the wall region with dilute and dense conditions. In the table, the stresses are shown both in the axial and radial directions. The particle normal stress and normal Reynolds stress trends were similar with each others. However, the particle normal stresses were slightly higher than the particle normal Reynolds stresses. The high particle normal stresses imply that system mixing occurs due to individual particle similar to molecular diffusion of gases. For both the particle normal stresses and normal Reynolds stresses, the anisotropic characteristics of the velocity fluctuations could be clearly observed. At this position, the velocity fluctuations in the axial direction were higher than in the radial direction. The variances of fluctuating velocity in the axial direction or the direction of flow were approximately one order of magnitude higher than those in the radial direction. This is due to the high gradient of axial particle velocities. In developed flow, the radial particle velocities are quite small and, hence, their gradients are small, as well. From the table, it could also be seen that the stresses in dense condition were lower than in dilute condition. As discussed, the explanation is owing to the system vacant area. These results were consistent with the experimental results conducted by Jung et al. (2005). In their study, the velocity fluctuation decreased with the increasing of solid concentration or volume fraction. Moreover, the total particle

normal stresses in each direction can be obtained by adding together the particle normal stresses and normal Reynolds stresses.

7.3.3. Granular temperatures

The other characteristic of system turbulent is the particle random oscillations or granular temperatures which can be characterized into two kinds: due to individual particle called "laminar granular temperature (θ_l)" and due to cluster of solid particles called "turbulent granular temperature (θ_t)". For the computation of turbulent granular temperature, the method is already described in the previous chapters. For the computation of laminar granular temperature, the method is shown below:

$$\theta_l(t) \cong \frac{2}{3}\langle C_x C_x \rangle(t) + \frac{1}{3}\langle C_y C_y \rangle(t) \qquad (7.3)$$

Figure 7.4 (a) displays a time series of the computed laminar and turbulent granular temperatures with two different system operating conditions. These granular temperatures oscillated with time. They have very large values because of much higher oscillations at the times of less solids in the system. The computed time-averaged laminar, turbulent and total granular temperatures with dilute and dense conditions are shown in Table 7.2. At this system position, the computed laminar and turbulent granular temperatures were close to each others. However, the laminar granular temperatures were slightly higher than the turbulent granular temperatures. This confirms the stress results that the system is dominated by individual particle. The computed total granular temperature in dense condition was lower than in dilute condition and consistent with the time dependent results in Figure 7.4 (a). The system with high oscillation has high energy content. As a consequence, the dilute condition will have larger force to support the weight of solids as can be seen from the particle velocity data. Figure 7.4 (b) compares the computed time-averaged total granular temperatures with dilute and dense conditions to the experimental literature data. This study values were lower than the literature values at the same range of gas velocity. The reason is due to the measurement position. In the literature, the measured values were not mainly considered the values at the wall or annulus region. This result verified the

analytical solution by Tartan and Gidaspow (2004) that the oscillations in the wall region were smaller than in the center region.

7.3.4. Particle dispersion coefficients

A measure of the quality of system mixing is the dispersion coefficient. In this study, axial ($D_{y,l}$) and radial ($D_{x,l}$) laminar dispersion coefficients were determined as a function of particle normal stress while axial ($D_{y,t}$) and radial ($D_{x,t}$) turbulent dispersion coefficients were obtained as a function of particle normal Reynolds stress. The methods to calculate turbulent dispersion coefficients are already shown in the previous chapters while the methods to calculate laminar dispersion coefficients are expressed below:

$$D_{y,l} = \langle C_y C_y \rangle T_L \text{ and } D_{x,l} = \langle C_x C_x \rangle T_L \tag{7.4}$$

where T_L is Lagrangian integral time scale.

The computed time-averaged, axial and radial, laminar and turbulent dispersion coefficients with dilute and dense conditions are summarized in Table 7.3. Both system operating conditions showed similar trends of the result. The axial dispersions were higher than the radial dispersions owing to the direction of flow. The laminar dispersions were higher than the turbulent dispersions. This also confirms more importance of individual particle oscillations. About the effect of system operating condition, the dilute condition had higher axial and radial dispersions than the dense condition. The axial dispersion trend was similar to Breault et al. (2006). The axial dispersion decreased with the increasing of solid volume fraction. In this study, the trend of radial dispersion was observed. The radial dispersion also decreased with the increasing of solid volume fraction or mass flux. The comparisons between the computed time-averaged laminar and turbulent dispersion coefficients with two different system operating conditions and the literature for axial and radial directions are plotted in Figures 7.5 (a) and 7.5 (b), respectively. The results showed that the computed dispersion coefficients were significantly lower than the literature. Since the methods

and technique used in the literature were different from this study, some assumptions were included. Like granular temperatures, the literature values were not considered at the wall region. The low axial and high radial dispersions imply that the solids have well mixed which then increase the system reaction conversion. The computed values thus demonstrate that the system radial mixing is worse than expected and the system improvement is needed. The reason for this low dispersions is due to the high solid volume fraction when comparing to the center region. Baffle addition at this position may be one of the solutions to increase the system radial mixing as employed in the heat transfer case.

7.4. Conclusion

1. The particle velocity data obtained by PIV method was successfully used to compute the turbulence and dispersion for polyethylene beads at the wall region in a CFB riser. This study presented a method to determine particle velocities and its derivation which were stresses, granular temperatures and dispersions. All the values were computed both in the axial and radial directions and classified into two types based on the solid particle characteristic which were individual particle and cluster of solid particles.

2. In this study, the turbulence and dispersion at the wall region were lower than the literature dataset. It demonstrates that the system radial mixing at this region is worse and an improvement is required. Considering on system operating condition, the axial and radial dispersions increased with decrease of solid volume fraction. This is attributed to the reduced ability of solids to move in a dense condition. The axial dispersions were higher than the radial ones which are due to the direction of flow. Also, this study showed a greater importance of individual particles than clusters of solid particles on system flow behavior.

Table 7.1 A comparison of the axial and radial particle normal stresses and normal Reynolds stresses at the wall region with dilute and dense conditions.

Run	Particle normal stress (m^2/s^2)		Particle normal Reynolds stress (m^2/s^2)	
	Axial	Radial	Axial	Radial
Dilute condition	0.3063	0.0731	0.2658	0.0334
Dense condition	0.1196	0.0319	0.1119	0.0209

Table 7.2 A comparison of the laminar, turbulent and total granular temperatures at the wall region with dilute and dense conditions.

Run	Granular temperature (m^2/s^2)		
	Laminar	Turbulent	Total
Dilute condition	0.1509	0.1109	0.2617
Dense condition	0.0612	0.0512	0.1124

Table 7.3 A comparison of the axial and radial laminar and turbulent dispersion coefficients at the wall region with dilute and dense conditions.

Run	Laminar dispersion coefficient (m^2/s)		Turbulent dispersion coefficient (m^2/s)	
	Axial	Radial	Axial	Radial
Dilute condition	0.0036	0.0016	0.0031	0.0007
Dense condition	0.0013	0.0007	0.0013	0.0005
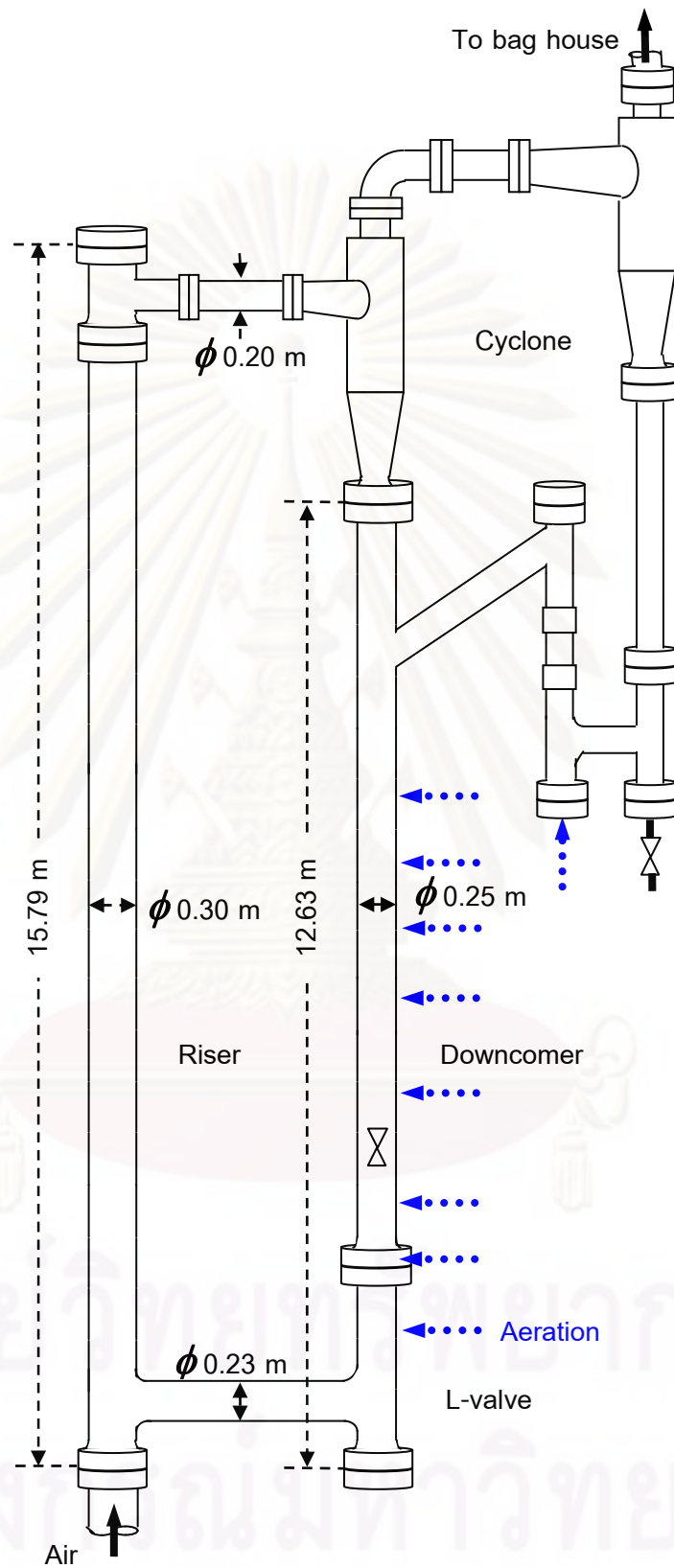
Figure 7.1 Schematic drawing of National Energy Technology Laboratory CFB system.

(a)
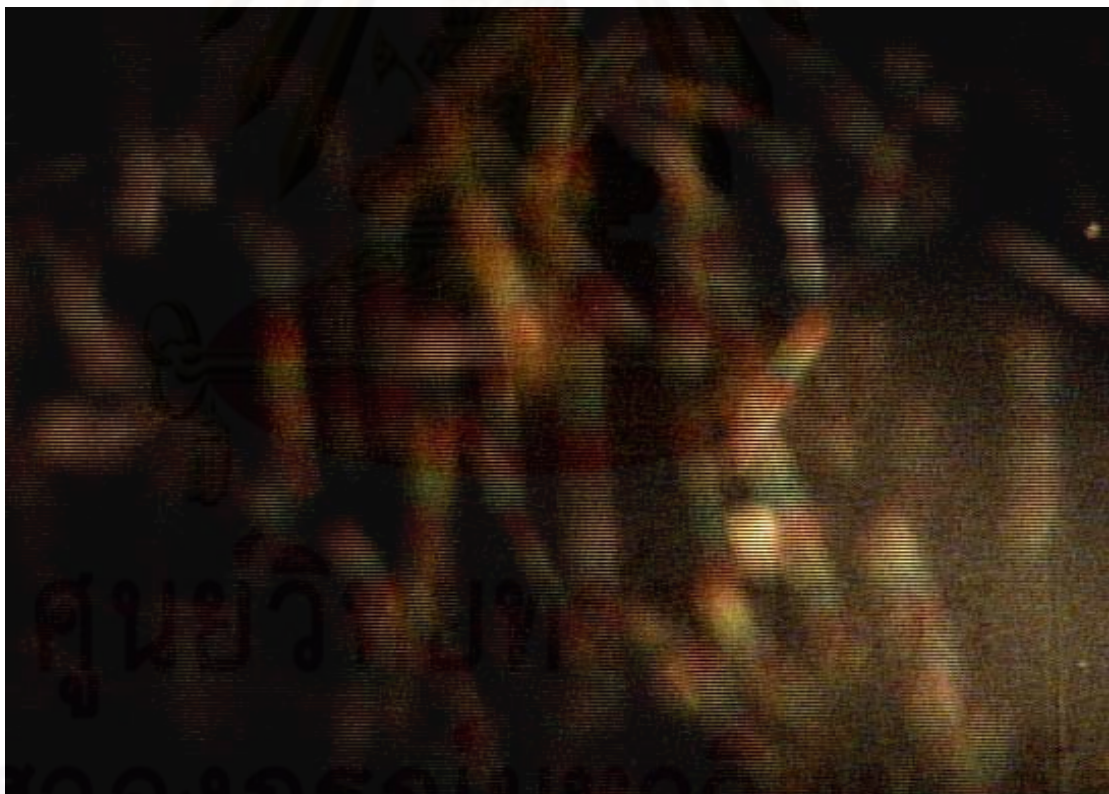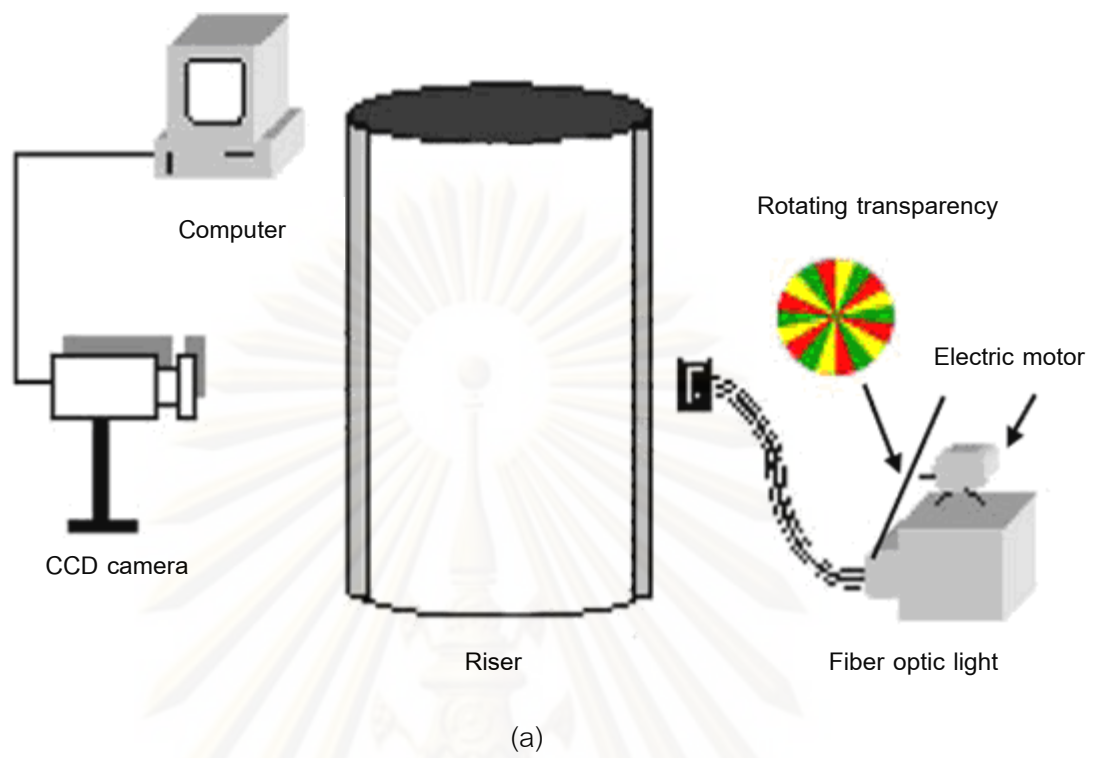
(b)

Figure 7.2 (a) Particle image velocimetry measurement system and (b) typical streak line

distribution generated on the computer screen.
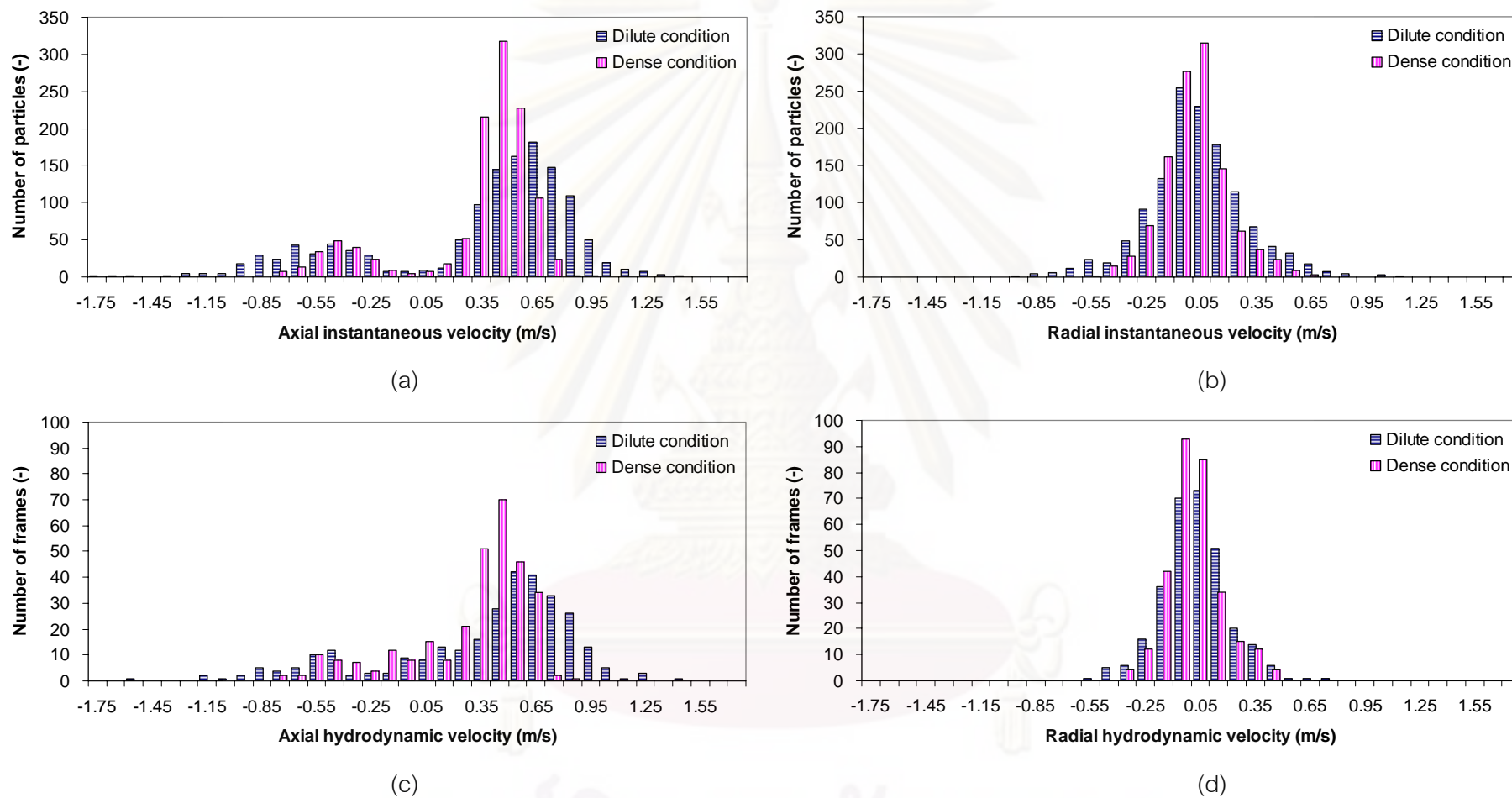
Figure 7.3 The histograms of (a) axial instantaneous, (b) radial instantaneous, (c) axial hydrodynamic and (d) radial hydrodynamic particle velocities at the wall region with two different system operating conditions.

Figure 7.4 (a) A time series of the laminar and turbulent granular temperatures at the
wall region with two different system operating conditions and (b) a comparison
between the total granular temperatures at the wall region with dilute and dense
conditions and the experimental literature data.
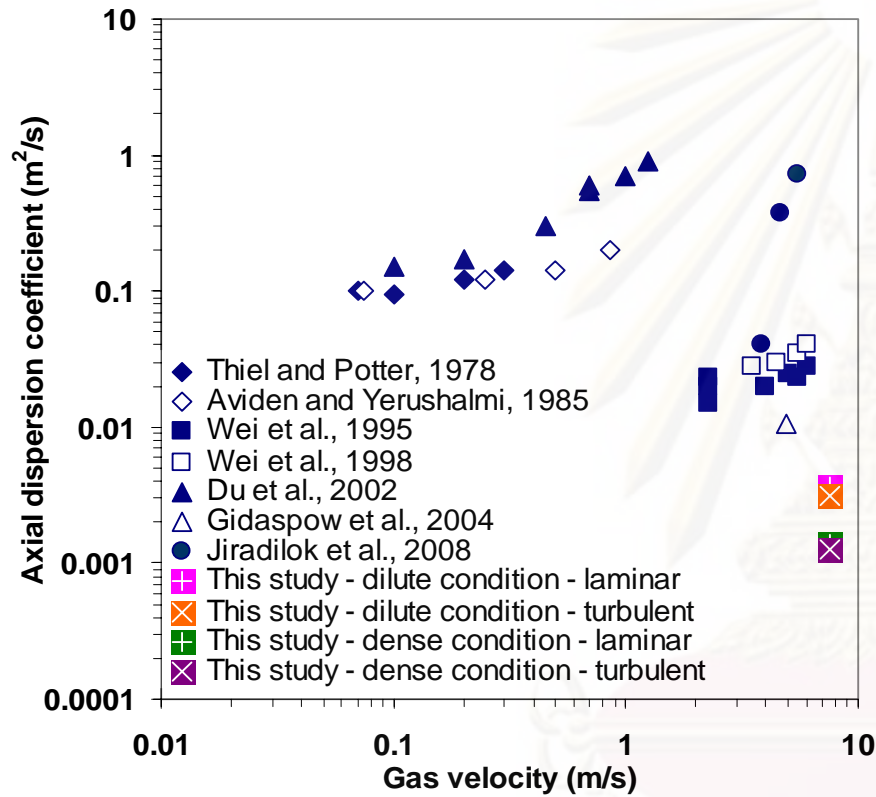
(a)
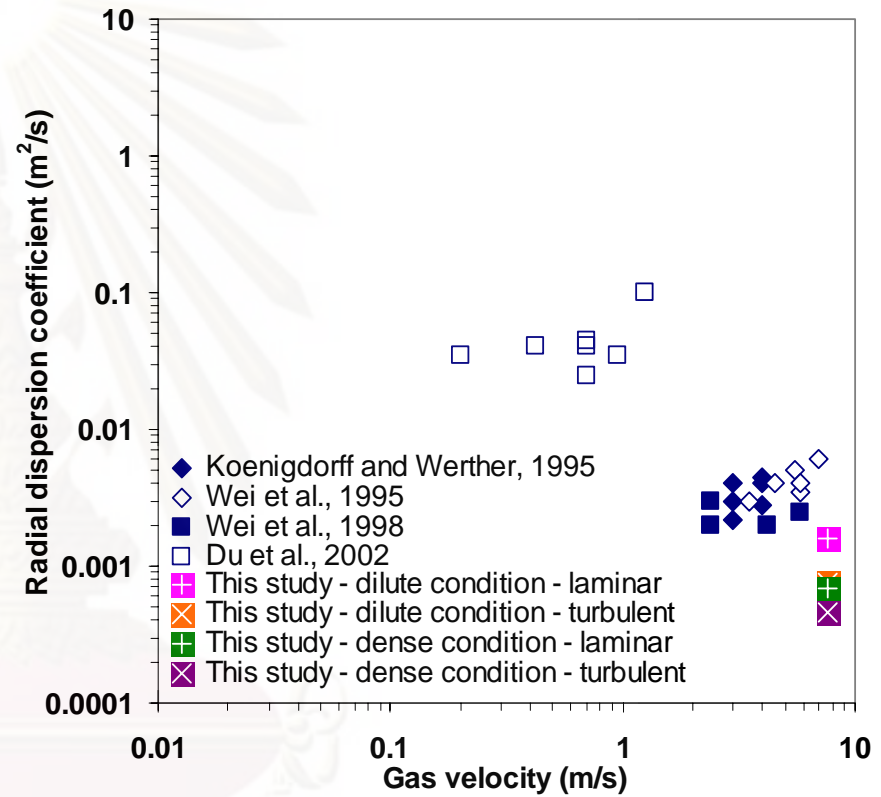
(b)

Figure 7.5 The comparisons between the laminar and turbulent dispersion coefficients at the wall region with two different system operating

conditions and the literature for (a) axial and (b) radial directions.

CHAPTER VIII

CONCLUSIONS AND RECOMMENDATIONS

8.1. Conclusions

In these research studies, the kinetic theory based computational fluid dynamics model was used to resolve the hydrodynamics and mass transfer issues in fluidized beds. Although there are a number of studies in fluidized bed systems, most of them are focused on the macroscopic behavior, such as the alteration of flow structure with various operating conditions. However, studies from a microscopic viewpoint are lacking in the literature that is the understanding of the in-depth parameters describing the hydrodynamics and the complex mass transfer. This knowledge will enable scientists and engineers to design better, more efficient, reactors that may effectively deal with the current problem and expand the range of fluidized bed reactor applications.

In all the chapters, we have shown that the kinetic theory based computational fluid dynamics commercial code, FLUENT 6.2.16, can accurately calculate:

1.   Dispersion coefficients and

2.   Mass transfer coefficients

Therefore, the general kinetic theory based computational fluid dynamics codes can be used for fluidized bed reactor design without any additional modeling input variables.

For Chapter IV, Kinetic theory based computation of fast fluidization regime in PSRI riser: Part I – Estimation of mass transfer coefficient with particle cluster concept, the results can be summarized as follows:

1.   The PSRI challenge problem I data for flow of FCC particles in a riser with a high solids flux and low gas velocity was modeled

using the kinetic theory of granular flow with the non-modified and modified interface exchange coefficient models. In the dense regime, the modified interface exchange coefficient model or the EMMS drag law gives a closer comparison of the computed solid mass flux, solid density and pressure drop than the standard drag law.

2. The computer model was also used to calculate axial and radial normal Reynolds stresses, energy spectra, power spectra, granular temperature, the FCC viscosity, and axial and radial dispersion coefficients, accurately.

3. Particle cluster sizes were computed from the radial dispersion coefficient divided by the radial oscillating velocity. The particle cluster diameters agree with published empirical correlations.

4. From the cluster diameter, the computed Sherwood number is of the order of 10^{-2} and the mass transfer coefficient is of the order of 10^{-3} m/s, in agreement with the experimental data for fluidization of fine particles.

In Chapter V, Kinetic theory based computation of fast fluidization regime in PSRI riser: Part II – Computation of mass transfer coefficient with chemical reaction concept, the results can be concluded as follows:

1. From additive diffusional and chemical resistance concept, the computed Sherwood number is of the order of 4×10^{-3} and the mass transfer coefficient is of the order of 2×10^{-3} m/s, in agreement with measured literature experimental data for fluidization of small particles.

2. The Sherwood number or mass transfer coefficient is high near the inlet section, and decreases to a constant value with the

height of the riser. This is similar to the normal behavior of the Sherwood number in convective mass transfer process (Kato et al., 1970).

3. The Sherwood number or mass transfer coefficient varies slightly with reaction rate constant. For the higher reaction rate constant case, the ozone reactant is almost used up which makes the rate of reaction to be slower. Therefore, the computed values of Sherwood numbers and mass transfer coefficients increase with the increasing reaction rate constant.

4. In this study, two explanations are possible for the low Sherwood numbers measured in the fluidization of fine particles. One explanation is due to the particle cluster formation studied in the previous chapter. The second explanation is that the conventional method of computing the mass transfer coefficients does not measure the diffusional resistance to the particles implied by the conventional Sherwood number representation. However, it shows the effect of concentration mal-distribution.

From Chapter VI, Effect of circulating fluidized bed reactor riser geometries on chemical reaction rates by using CFD simulations, the results can be summarized as follows:

1. The novel designs of the riser geometries have been studied by computer simulation using a two dimensional transient Eulerian model combined with kinetic theory of granular flow.

2. In the first section, the concept of the new designs is proposed on the improvement of the factors that have effects on the chemical reaction via the hydrodynamics inside the riser. It is found that different types of particles (Geldart group A and B) do

not affect the simulation result. The tapered-out riser could improve the turbulence or mixing in the system. On the other hands, the tapered-in riser could enhance the particle residence time and give uniform temperature distribution in the system. This result leads to the criteria for choosing riser geometry with different reaction characteristics. The tapered-out riser will suit the reactions with fast reaction rate, while the tapered-in riser will fit to the reactions with slow reaction rate.

3.   In the second section, the proposed model was used for predicting in-depth hydrodynamics responses and computing system turbulent properties in the typical and tapered-riser geometries. The tapered-in riser enhances the solid particle residence time and gives uniform temperature distribution in the system. The explanation is due to this riser geometry not having enough force to support the weight of solid particles as justified by the normal Reynolds stresses and the granular temperatures. The tapered-out riser improves the turbulence or mixing in the system which can be clarified by the dispersion coefficients. In addition, the chemical reaction responses were directly modeled and used to prove the proposed criteria. These modeling results prove the criteria for choosing riser geometry with reaction characteristics. It can be used as alternatives in the designing stage of the CFBR system.

From Chapter VII, Measurement of turbulence and low dispersion at the wall region in a circulating fluidized bed riser, the results can be concluded as follows:

1.   The particle velocity data obtained by PIV method was successfully used to compute the turbulence and dispersion for polyethylene beads at the wall region in a CFB riser. This study

presented a method to determine particle velocities and its derivation which were stresses, granular temperatures and dispersions. All the values were computed both in the axial and radial directions and classified into two types based on the solid particle characteristic which were individual particle and cluster of solid particles.

2.   In this study, the turbulence and dispersion at the wall region were lower than the literature dataset. It demonstrates that the system radial mixing at this region is worse and an improvement is required. Considering on system operating condition, the axial and radial dispersions increased with decrease of solid volume fraction. This is attributed to the reduced ability of solids to move in a dense condition. The axial dispersions were higher than the radial ones which are due to the direction of flow. Also, this study showed a greater importance of individual particles than clusters of solid particles on system flow behavior.

8.2. Recommendations

These research studies demonstrate the power of the computational fluid dynamics simulations. However, the computer program speed is the major limiting factor for simulating a complex system. In addition to improvements in the speed of the Navier-Stokes equation solvers, some further studies are suggested below:

In Chapter IV, the methodologies have already been developed for the computation of hydrodynamics and mass transfer in circulating fluidized bed reactor risers. These methodologies should then be applied to the other similar kinds of systems, such as the circulating fluidized bed reactor downer. This will allow us to compare the chemical reaction or process efficiency of the two different systems. Also, the particle cluster properties in the circulating fluidized bed reactor downer are not available in the literature.

In Chapter V, the method to compute mass transfer coefficient from chemical reaction concept was proposed. In order to solve the species conservation equation, this method was simplified by some additional assumptions and it was only developed for the first order ozone decomposition reaction. The method thus should be extended to be more complex behavior to be valid for any higher order chemical reaction. Also, the proposed computation method should be tested, experimentally.

In Chapter VI, adequate experimental results will be needed to confirm the observed hydrodynamics and chemical reaction responses in different circulating fluidized bed reactor riser geometries to verify the proposed criteria for choosing the circulating fluidized bed reactor riser geometries with different chemical reaction characteristics. In addition, the computational fluid dynamics simulation with gas-solid heterogeneous reaction such as air-coal or air-biomass combustion may be performed to ensure the proposed criteria.

In Chapter VII, two experimental operating conditions were performed. More operating parameters should be studied, such as temperature, relative humidity and material properties, to explore their effects on turbulence and dispersion at the near wall region. The current PIV measurement system can only measure the two velocity components in the plane normal to the camera. To obtain more precise results, the third or in-plane velocity component should be obtained. This PIV measurement system however is difficult to use in the dense system.

REFERENCES

Almuttahar, A., and Taghipour, F. Computational fluid dynamics of a circulating fluidized bed under various fluidization conditions. <u>Chemical Engineering Science</u> 63 (2008a): 1696-1709.

Almuttahar, A., and Taghipour, F. Computational fluid dynamics of high density circulating fluidized bed riser: Study of modeling parameters. <u>Powder Technology</u> 185 (2008b): 11-23.

Amos, G., Rhodes, M. J., and Mineo, H. Gas mixing in gas-solids risers. <u>Chemical Engineering Science</u> 48 (1993): 943-949.

Andreux, R., Petit, G., Hemati, M., and Simonin, O. Hydrodynamic and solid residence time distribution in a circulating fluidized bed: Experimental and 3D computational study. <u>Chemical Engineering and Processing: Process Intensification</u> 47 (2007): 463-473.

Andrews, A. T.IV, and Sundaresan, S. Coarse-graining of two-fluid models for fluidized gas-particle suspensions. <u>AIChE Annual Meeting</u>, Cincinnati, October 30-November 4, 2005.

Avidan, A. A. Fluid catalytic cracking. In J. R. Grace, A. A. Avidan, and T. M. Knowlton (eds.), <u>Circulating Fluidized Beds</u>, pp.466-488. London: Blackie Academic & Professional, 1997.

Avidan, A. A., and Shinnar, R. Development of catalytic cracking technology. A lesson in chemical reactor design. <u>Industrial and Engineering Chemistry Research</u> 29 (1990): 931-942.

Avidan, A. A., and Yerushalmi, J. Bed expansion in high velocity fluidization. <u>Powder Technology</u> 32 (1982): 223-232.

Avidan, A. A., and Yerushalmi, J. Solid mixing in an expanded top fluid bed. AIChE Journal 31 (1985): 835-841.

Bajura, R. New coal technologies: opportunities for West Virginia. West Virginia Energy Roadmap Workshop on National Coal, United States, November 10, 2004.

Balasubramanian, N., Srinivasakannan, C., and Ahmed Basha, C. Transition velocities in the riser of a circulating fluidized bed. Advanced Powder Technology 16 (2005): 247-260.

Barthod, D., Del Pozo, M., and Mirgain, C. CFD-aided design improves FCC performance. Oil and Gas Journal 97 (1999): 66-69.

Basu, P. Combustion and Gasification in Fluidized Beds. Boca Raton: CRC Press, 2006.

Basu, P., and Fraser, S. A. Circulating Fluidized Bed Boilers. Stoneham: Butterworth-Heinemann, 1991.

Benyahia, S., Arastoopour, H., Knowlton, T.M., and Massah, H. Simulation of particles and gas flow behavior in the riser section of a circulating fluidized bed using the kinetic theory approach for the particulate phase. Powder Technology 112 (2000): 24-33.

Benyahia, S., Arastoopour, H., and Knowlton, T.M. Two dimensional transient numerical simulation of solids and gas flow in the riser section of a circulating fluidized bed. Chemical Engineering Communications 189 (2002): 510-527.

Berruti, F., Chaouki, J., Godfroy, L., Pugsley, T. S., and Patience, G. S. Hydrodynamics of circulating fluidized bed risers: A review. Canadian Journal of Chemical Engineering 73 (1995): 579-602.

Bi, H. T., and Fan, L.-S. Regime transitions in gas-solid circulating fluidized beds. AIChE Annual Meeting, Los Angeles, November 17-22, 1991.

Bi, H. T., and Grace, J. R. Effect of measurement method on the velocities used to demarcate the onset of turbulent fluidization. The Chemical Engineering Journal and the Biochemical Engineering Journal 57 (1995): 261-271.

Bi, H. T., Grace, J. R., and Zhu, J. X. On types of choking in pneumatic systems. International Journal of Multiphase flow 19 (1993): 1077-1092.

Bi, H. T., Grace, J. R., and Zhu, J. X. Regime transitions affecting gas-solids suspensions and fluidized beds. Transactions Institute of Chemical Engineers 73 (1995): 154-161.

Bird, R. B., Stewart, W. E., and Lightfoot, E. N. Transport Phenomena. New York: John Wiley & Sons, 2002.

Bolland, O. Describing mass transfer in circulating fluidized beds by ozone decomposition. NTNU Report Number 1998:02, 1998.

Bolland, O., and Nicolai, R. Describing mass transfer in circulating fluidized beds by ozone decomposition. Chemical Engineering Communications 187 (2001): 1-21.

Breault, R.W. A review of gas-solid dispersion and mass transfer coefficient correlations in circulating fluidized beds. Powder Technology 163 (2006): 9-17.

Breault, R.W., and Guenther, C. P. Mass transfer in the core-annular and fast fluidization flow regimes of a CFB. Powder Technology 190 (2009): 385-389.

Breault, R. W., Guenther, C. P., and Shadle, L. J. Velocity fluctuation interpretation in the near wall region of a dense riser. Powder Technology 182 (2008): 137-145.

Breault, R. W., Ludlow, C. J., and Yue, P. C. Cluster particle number and granular temperature for cork particles at the wall in the riser of a CFB. Powder Technology 149 (2005): 68-77.

Cabezas-Gómez, L., and Milioli, F. E. Numerical study on the influence of various physical parameters over the gas-solid two-phase flow in the 2D riser of a circulating fluidized bed. <u>Powder Technology</u> 132 (2003): 216-225.

Cabezas-Gómez, L., da Silva, R. C., Navarro, H. A., and Milioli, F. E. Cluster identification and characterization in the riser of a circulating fluidized bed from numerical simulation results. <u>Applied Mathematical Modelling</u> 32 (2008): 327-340.

Campbell, C. S., and Brennen, C. E. Computer simulations of granular shear flows. <u>Journal of Fluid Mechanics</u> 151 (1985): 167-188.

Campbell, C., and Wang, D. Particle pressures in gas-fluidized beds. <u>Journal of Fluid Mechanics</u> 227 (1991): 495-508.

Chapman, S., and Cowling, T. G. <u>The Mathematical Theory of Non-Uniform Gases</u>. New York: Cambridge University Press, 1970.

Chen, J. C. Experiments that address phenomenological issues of fast fluidization. <u>Chemical Engineering Science</u> 54 (1999): 5529-5539.

Chen, R. Y., Chiou, H. C., and Sun, D. Deposition of particles in a convergent channel. <u>Powder Technology</u> 87 (1996): 83-86.

Cheng, Y., Wei, F., Yang, G., and Jin, Y. Inlet and outlet effects on flow patterns in gas-solid risers. <u>Powder Technology</u> 98 (1998): 151-156.

Christou, C., Hadjipaschalis, I., and Poullikkas, A. Assessment of integrated gasification combined cycle technology competitiveness. <u>Renewable and Sustainable Energy Reviews</u> 12 (2008): 2459-2471.

Chu, J. C., Kalil, J., and Wetteroth, W. A. Mass transfer in a fluidized bed. <u>Chemical Engineering Progress</u> 49 (1953): 141-149.

Cody, G., Goldfarb, D., Storch, G., and Norris, A. Particle granular temperature in gas-fluidized beds. Powder Technology 87 (1996): 211-232.

Crowe, C., Sommerfeld, M., and Tsuji, M. Multiphase Flows with Droplets and Particles. Boca Raton: CRC Press, 1997.

Cundall, P. A., and Strack, O. D. L. A discrete numerical model for granular assemblies. Geotechnique 29 (1979): 47-65.

Das, M., Bandyopadhyay, A., Meikap, B. C., and Saha, R. K. Axial voidage profiles and identification of flow regimes in the riser of a circulating fluidized bed. Chemical Engineering Journal 145 (2008): 249-258.

Deen, N. G., van sint Annaland, M., van der Hoef, M. A., and Kuipers, J. A. M. Review of discrete particle modeling of fluidized beds. Chemical Engineering Science 62 (2007): 28-44.

Ding, J., and Gidaspow, D. A bubbling fluidization model using kinetic theory of granular flow. AIChE Journal 36 (1990): 523-538.

Dry, R. J., and White, C. C. Gas residence-time characteristics in a high-velocity circulating fluidized bed of FCC catalyst. Powder Technology 58 (1989): 17-23.

Du, B., Fan, L.-S., Wei, F., and Warsito, W. Gas and solids mixing in a turbulent fluidized bed. AIChE Journal 48 (2002): 1896-1909.

Du, B., Warsito, W., and Fan, L.-S. Nonhomogeneity in turbulent gas–solid fluidization. AIChE Journal 49 (2003): 1109-1126.

Ergun, S. Fluid flow through packed columns. Chemical Engineering Progress 48 (1952): 89-94.

Fang, Y., Huang, J., Wang, Y., and Zhang, B. Experiment and mathematical modeling of a bench-scale circulating fluidized bed gasifier. Fuel Processing Technology 69 (2001): 29-44.

Fletcher, D. F., Haynes, B. S., Chen, J., and Joseph, S. D. Computational fluid dynamics modelling of an entrained flow biomass gasifier. Applied Mathematical Modelling 22 (1998): 747-757.

Fletcher, D. F., Haynes, B. S., Christo, F. C., and Joseph, S. D. A CFD based combustion model of an entrained flow biomass gasifier. Applied Mathematical Modelling 24 (2000): 165-182.

Fluent Inc. GAMBIT 2.2 Modeling Guide Volume 1. Lebanon: Fluent Inc., 2004a.

Fluent Inc. GAMBIT 2.2 Modeling Guide Volume 2. Lebanon: Fluent Inc., 2004b.

Fluent Inc. Fluent 6.2 User's Guide. Lebanon: Fluent Inc., 2005a.

Fluent Inc. Fluent 6.2 UDF Manual. Lebanon: Fluent Inc., 2005b.

Fogler, H.S. Elements of Chemical Reaction Engineering. New Jersey: Prentice Hall, 1999.

Fryer, C., and Potter, O. E. Experimental investigation of models for fluidized bed catalytic reactors. AIChE Journal 22 (1976): 38-47.

Gamwo, I. K., Gidaspow, D., and Jung, J. Optimum catalyst size for slurry bubble column reactors. Industrial and Engineering Chemistry Research 44 (2005): 6393-6402.

Gayan, P., de Diego, L.F., and Adanez, J. Radial gas mixing in fast fluidized bed. Powder Technology 94 (1997): 163-171.

Geldart, D., and Abrahamsen, A. R. Homogeneous fluidization of fine powders using various gases and pressures. Powder Technology 19 (1978): 133-136.

Gelderbloom, S. J., Gidaspow, D., and Lyczkowski, R. W. CFD simulations of bubbling/collapsing fluidized beds for three Geldart groups. AIChE Journal 49 (2003): 844-858.

Gentric, C., Mignon, D., Bousquet, J., and Tanguy, P. A. Comparison of mixing in two industrial gas-liquid reactors using CFD simulations. Chemical Engineering Science 60 (2005): 2253-2272.

Gidaspow, D. Multiphase Flow and Fluidization: Continuum and Kinetic Theory Description. Boston: Academic Press, 1994.

Gidaspow, D., and Huilin, L. Collisional viscosity of FCC particles in a CFB. AIChE Journal 42 (1996): 2503-2510.

Gidaspow, D., and Huilin, L. A comparison of gas-solid and liquid-solid fluidization using kinetic theory and statistical mechanics. In L.-S. Fan, and T. M. Knowlton (eds.), Fluidization Volume IX, p.661. New York: Engineering Foundation, 1998a.

Gidaspow, D., and Huilin, L. Equation of state and radial distribution functions of FCC particles in a CFB. AIChE Journal 44 (1998b): 279-293.

Gidaspow, D., Huilin, L., and Mostofi, R. Large scale oscillations or gravity waves in a riser and bubbling beds. In M. Kwauk, J. Li, and W. C. Yang (eds.), Fluidization Volume X, p.317. New York: Engineering Foundation, 2001.

Gidaspow, D., and Jiradilok, V. Nanoparticle gasifier fuel cell for sustainable energy future. Journal of Power Sources 166 (2007): 400-410.

Gidaspow, D., and Jiradilok, V. Computational Techniques: The Multiphase CFD Approach to Fluidization and Green Energy Technologies (Energy Science, Engineering and Technology Series). New York: Nova Science Publishers Inc., 2009.

Gidaspow, D., Jung, J., and Singh, R.K. Hydrodynamics of fluidization using kinetic theory: An emerging paradigm: 2002 Flour-Daniel lecture. Powder Technology 148 (2004): 123-141.

Gidaspow, D., Tsuo, Y.P., and Luo, K.M. Computed and experimental cluster formation and velocity profiles in circulating fluidized beds. In J. R. Grace, L. W. Shemilt, and M. A. Bergougnou (eds.), Fluidization Volume IV, p.81. Alberta: Engineering Foundation, 1989.

Goldschmidt, M. J. V., Kuipers, J. A. M., and van Swaaij, W. P. M. Hydrodynamic modeling of dense gas-fluidized beds using the kinetic theory of granular flow: Effect of coefficient of restitution on bed dynamics. Chemical Engineering Science 56 (2001): 571-578.

Grace, J. R. Fluidized-bed hydrodynamics. In G. Hestroni (ed.), Handbook of Multiphase Systems, pp.5-64. Washington: Hemisphere, 1982.

Grace, J. R., Avidan, A. A., and Knowlton, T. M. Circulating Fluidized Beds. London: Blackie Academic & Professional, 1997.

Gu, W.K., and Chen, J.C. A model for solid concentration in circulating fluidized beds. In L.-S. Fan, and T. M. Knowlton (eds.), Fluidization Volume IX, p.501. New York: Engineering Foundation, 1998.

Gunn, D.J. Transfer of heat or mass to particles in fixed and fluidized beds. International Journal of Heat and Mass Transfer 21 (1978): 467-476.

Gupta, S. K., and Berruti, F. Evaluation of the gas-solid suspension density in CFB risers with exit effects. Powder Technology 108 (2000): 21-31.

Hansen, K.G., Solberg, T., and Hjertager, B.H. A three-dimensional simulation of gas/particle flow and ozone decomposition in the riser of a circulating fluidized bed. Chemical Engineering Science 59 (2004): 5217-5224.

Harris, A.T., Davidson, J.F., and Thorpe, R.B. The prediction of particle cluster properties in the near wall region of a vertical riser (200157). Powder Technology 127 (2002): 128-143.

Harris, A. T., Davidson, J. F., and Thorpe, R. B. The influence of the riser exit on the particle residence time distribution in a circulating fluidized bed riser. <u>Chemical Engineering Science</u> 58 (2003): 3669-3680.

Hinze, H.O. <u>Turbulence</u>. New York: McGraw-Hill, 1959.

Horio, M., and Kuroki, H. Three-dimensional flow visualization of dilutely dispersed solids in bubbling and circulating fluidized beds. <u>Chemical Engineering Science</u> 49 (1994): 2413-2421.

Hu, N., Zhang, H., Yang, H., Yang, S., Yue, G., Lu, J., and Liu, Q. Effects of riser height and total solids inventory on the gas-solids in an ultra-tall CFB riser. <u>Powder Technology</u> 196 (2009): 8-13.

Huilin, L., and Gidaspow, D. Hydrodynamic simulations of gas–solid flow in a riser. <u>Industrial and Engineering Chemistry Research</u> 42 (2003): 2390-2398.

Huilin, L., Gidaspow, D., Bouillard, J., and Wentie, L. Hydrodynamic simulation of gas-solid flow in a riser using kinetic theory of granular flow. <u>Chemical Engineering Journal</u> 95 (2003): 1-13.

Huilin, L., Qiaoqun, S., Yurong, H., Yongli, S., Ding, J., and Xiang, L. Numerical study of particle cluster flow in risers with cluster-based approach. <u>Chemical Engineering Science</u> 60 (2005): 6757-6767.

Huilin, L., Yunhua, Z., Zhiheng, S., Ding, J., and Jiying, J. Numerical simulations of gas-solid flow in tapered risers. <u>Powder Technology</u> 169 (2006): 89-98.

Hunt, J.C.R., and Vassilicos, J.C. <u>Turbulence Structure and Vortex Dynamics</u>. Cambridge: Cambridge University Press, 2000.

Hurt, R., Sun, J., and Lunden, M. A kinetic model of carbon burnout in pulverized coal combustion. <u>Combustion and Flame</u> 113 (1998): 181-197.

Issangya, A. S., Bai, D., Bi, H. T., Lim, K. S., Zhu, J., and Grace, J. R. Suspension densities in a high-density circulating fluidized bed riser. <u>Chemical Engineering Science</u> 54 (1999): 5451-5460.

Jiang, P., Bi, H., Jean, R., and Fan, L. Baffle effects on performance of catalytic circulating fluidized bed reactor. <u>AIChE Journal</u> 37 (1991): 1392-1400.

Jianzhi, W., Bingyan, X., Zhenfang, L., and Xiguang, Z. Performance analysis of a biomass circulating fluidized bed gasifier. <u>Biomass and Bioenergy</u> 3 (1992): 105-110.

Jiradilok, V., Gidaspow, D., and Breault, R.W. Computation of gas and solid dispersion coefficients in turbulent risers and bubbling beds. <u>Chemical Engineering Science</u> 62 (2007): 3397-3409.

Jiradilok, V., Gidaspow, D., Breault, R. W., Shadle, L. J., Guenther, C., and Shi, S. Computation of turbulence and dispersion of cork in the NETL riser. <u>Chemical Engineering Science</u> 63 (2008): 2135-2148.

Jiradilok, V., Gidaspow, D., Damronglerd, S., Koves, W.J., and Mostofi, R. Kinetic theory based CFD simulation of turbulent fluidization of FCC particles in a riser. <u>Chemical Engineering Science</u> 61 (2006): 5544-5559.

Johnson, P.C., and Jackson, R. Frictional-collisional constitutive relations for granular materials, with application to plane shearing. <u>Journal of Fluid Mechanics</u> 176 (1987): 67-93.

Jung, J., Gidaspow, D., and Gamwo, I.K. Measurement of two kinds of granular temperatures, stresses, and dispersion in bubbling beds. <u>Industrial and Engineering Chemistry Research</u> 44 (2005): 1329-1341.

Kaneko, Y., Shiojima, T. and Horio, M. DEM simulation of fluidized beds for gas-phase olefin polymerization. <u>Chemical Engineering Science</u> 54 (1999): 5809-5821.

Kato, K., Kubota, H., and Wen, C.Y. Mass transfer in fixed and fluidized beds. Chemical Engineering Progress Symposium Series 105 (1970): 87-99.

Kersten, R. A., Prins, W., van der Drift, B., and van Swaaij, W. P. M. Principles of a novel multistage circulating fluidized bed reactor for bimass gasification. Chemical Engineering Science 58 (2003): 725-731.

Kim, J., Moin, P., and Moser, R. Turbulent statistics in fully developed channel flow at low Reynolds number. Journal of Fluid Mechanics 177 (1987): 133-166.

Kim, S.D., and Namkung, W. Gas backmixing in a circulating fluidized bed. Powder Technology 99 (1998): 70-78.

Kim, J. S., Tachino, R., and Tsutsumi, A. Effects of solids feeder and riser exit configuration on establishing high density circulating fluidized beds. Powder Technology 187 (2008): 37-45.

Klinzing, G. E. Gas-Solid Transport. New York: McGraw-Hill, 1981.

Knowlton, T., Geldart, D., Masten, J., and King, D. Comparison of CFB hydrodynamic models, PSRI Challenge Problem. The Eighth International Fluidization Conference, France, May 14-19, 1995.

Koenigsdorff, R., and Werther, J. Gas and solids mixing and flow structure modeling of the upper dilute zone of a circulating fluidized bed. Powder Technology 82 (1995): 317-329.

Kulacki, F.A., and Gidaspow, D. Convective diffusion in a parallel plate duct with one catalytic wall - laminar flow - first order reaction Part II - Experimental. Canadian Journal of Chemical Engineering 45 (1967): 72-78.

Kunii, D., and Levenspiel, O. Fluidization Engineering. Boston: Butterworth-Heinemann, 1991.

Kuwagi, K., Mikami, T., and Horio, M. Numerical simulation of metallic solid bridging particles in a fluidized bed at high temperature. Powder Technology 109 (2000): 27-40.

Leung, L. S. Vertical pneumatic conveying: A flow regime diagram and a review of choking versus non-choking systems. Powder Technology 25 (1980): 185-190.

Levenspiel, O. Chemical Reaction Engineering. New York: John Wiley & Sons, 1999.

Lewis, W. K., and Gilliland, E. R. Conversion of Hydrocarbons with Suspended Catalyst. US Patent Number 2498088, 1950.

Li, J. and Weinstein, H. An experimental comparison of gas backmixing in fluidized beds across the regime spectrum. Chemical Engineering Science 44 (1989): 1697-1705.

Lim, K. S., Zhu, J. X., and Grace, J. R. Hydrodynamics of gas-sold fluidization. International Journal of Multiphase flow 21 (1995): 141-193.

Limtrakul, S., Chalermwattanatai, A., Unggurawirote, K., Tsuji, Y., Kawaguchi, T., and Tanthapanichakoon, W. Discrete particle simulation of solids motion in a gas-solid fluidized bed. Chemical Engineering Science 58 (2003): 915-921.

Liu, H., Ni, W., Li, Z., and Ma, L. Strategic thinking on IGCC development in China. Energy Policy 36 (2008): 1-11.

Lun, C. K. K., Savage, S. B., Jeffrey, D. J., and Chepurniy, N. Kinetic theories for granular flow: Inelastic particles in couette flow and slightly inelastic particles in a general flow field. Journal of Fluid Mechanics 140 (1984): 223-256.

Mathiesen, V., Solverg, T., and Hjertager, B. H. An experimental and computational study of multiphase flow behavior in a circulating fluidized bed. International Journal of Multiphase flow 26 (2000): 387-419.

Mathieu, J., and Scott, J. An Introduction to Turbulent Flow. Cambridge: Cambridge University Press, 2000.

Matonis, D., Gidaspow, D., and Bahary, M. CFD simulation of flow and turbulence in a slurry bubble column. AIChE Journal 48 (2002): 1413-1429.

Maurstad, O. An Overview of Coal Based Integrated Gasification Combined Cycle (IGCC) Technology. MIT Publication Number LFEE 2005-002 WP, 2005.

McComb, W.D. The Physics of Fluid Turbulence. Oxford: Clarendon Press, 1990.

van der Meer, E. H., Thorpe, R. B., and Davidson, J. F. Flow patterns in the square cross-section riser of a circulating fluidized bed and the effect of riser exit design. Chemical Engineering Science 55 (2000): 4079-4099.

Miller, A., and Gidaspow, D. Dense, vertical gas-solids flow in a pipe. AIChE Journal 38 (1992): 1801-1813.

Monazam, E. R., Shadle, L. J., Mei, J. S., and Spenik, J. Identification and characteristics of different flow regimes in a circulating fluidized bed. Powder Technology 155 (2005): 17-25.

Nakajima, M., Harada, M., Asai, M., Yamazaki, R., and Jimbo, G. Bubble fraction and voidage in an emulsion phase in the transition to a turbulent fluidized bed. In P. Basu, M. Hasatani, and M. Horio (eds.), Circulating Fluidized Bed Technology III, pp.79-85. Oxford: Pergamon Press, 1991.

Namkung, W., and Kim, S.D. Gas backmixing in the dense region of a circulating fluidized bed. Korean Journal of Chemical Engineering 16 (1999): 456-461.

Naren, P. R., Lali, A. M., and Ranade, V. V. Evaluating EMMS model for simulating high solid flux risers. Chemical Engineering Research and Design 85 (2007): 1188-1202.

Neri, A., and Gidaspow, D.   Riser hydrodynamics: simulation using kinetic theory. <u>AIChE Journal</u> 46 (2000): 52-67.

Ng, W. K., and Tan, R. B. H.   Case study: Optimization of an industrial fluidized bed drying process for large Geldart Type D nylon particles.   <u>Powder Technology</u> 180 (2008): 289-295.

Ouyang, S., Lin, J., and Potter, O.E.   Ozone decomposition in a 0.254m diameter circulating fluidized bed reactor.   <u>Powder Technology</u> 75 (1993): 73-78.

Ouyang, S., Lin, J., and Potter, O.E.   Circulating fluidized bed as a catalytic reactor: Experimental study. <u>AIChE Journal</u> 41 (1995): 1534-1542.

Pagliolico, S., Tiprigan, M., Rovero, G., and Gianetto, A.   Pseudo-homogeneous approach to CFB reactor design.   <u>Chemical Engineering Science</u> 47 (1992): 2269-2274.

Pan, Y., Dudukovic, M.P., and Chang, M. Dynamic simulation of bubbly flow in bubble columns. <u>Chemical Engineering Science</u> 54 (1999): 2481-2489.

Perez-Fortes, M., Bojarski, A. D., Velo, E., Nougues, J. M., and Puigjaner, L. Conceptual model and evaluation of generated power and emissions in an IGCC plant. <u>Energy</u> 34 (2009): 1721-1732.

Polashenski, W., and Chen, J.   Normal solid stress in fluidized beds.   <u>Powder Technology</u> 90 (1997): 13-23.

Polashenski, W., and Chen, J. Measurement of particle stresses in fast fluidized beds. <u>Industrial and Engineering Chemistry Research</u> 38 (1999): 705-713.

Pope, S.B. <u>Turbulent Flows</u>. Cambridge: Cambridge University Press, 2000.

Ranade, V. V. <u>Computational Flow Modeling for Chemical Reactor Engineering</u>. New York: Academic Press, 2002.

Raynal, L., Ben Rayana, F., and Royon-Lobeaud, A. Use of CFD for CO_2 absorbers optimum design: Form local scale to large industrial scale. Energy Procedia 1 (2009): 917-924.

Resnick, W. E., and White, R. R. Mass transfer in systems of gas and fluidized solids. Chemical Engineering Progress 45 (1949): 377-390.

Rhodes, M. What is turbulent fluidization?. Powder Technology 88 (1996): 3-14.

Rhodes, M.J., Wang, X.S., Nguyen, M., Stewart, P., and Liffman, K. Use of discrete element method simulation in studying fluidization characteristics: Influence of interparticle force. Chemical Engineering Science 56 (2001): 69-76.

Samuelsberg, A., and Hjertager, B.H. Simulation of two-phase gas/particle flow and ozone decompositions in a 0.25m I.D. riser. In A. Serizawa, T. Fukano, and J. Batalille (eds.), Advances in Multiphase Flow, p.679. Amsterdam: Elsevier Science B.V., 1995.

Schoenfelder, H., Kruse, M., and Werther, J. Two-dimensional model for circulating fluidized bed reactors. AIChE Journal 42 (1996): 1875-1888.

Seader, J. D., and Henley, E. J. Separation Process Principles. New York: John Wiley & Sons, 1998.

Sharma, A., Tuzla, K., Matsen, J., and Chen, J. Parametric effects of particle size and gas velocity on cluster characteristics in fast fluidized beds. Powder Technology 111 (2000): 114-122.

Shuyan, W., Lijie, Y., Huilin, L., Long, Y., Bouillard, J., and Zhenhua, H. Numerical analysis of interphase heat and mass transfer of cluster in a circulating fluidized bed. Powder Technology 189 (2009): 87-96.

Sinclair, J.L., and Jackson, R. Gas-particle flow in a vertical pipe with particle-particle interaction. AIChE Journal 35 (1989): 1473-1486.

Smolders, K., and Baeyens, J. Gas fluidized beds operating at high velocities: A critical review of occurring regimes. Powder Technology 119 (2001): 269-291.

Solbrig, C.W., and Gidaspow, D. Convective diffusion in a parallel plate duct with one catalytic wall - laminar flow - first order reaction Part I - Analytical. Canadian Journal of Chemical Engineering 45 (1967): 35-39.

Soong, C., Tuzla, K., and Chen, J. Identification of particle clusters in circulating fluidized bed. In A. A. Avidan (ed.), Circulating Fluidized Bed Technology Volume IV, pp.615-620. New York: Engineering Foundation, 1995.

Sparrow, E. M., and Ruiz, R. Experiments on natural convection in divergent vertical channels and correlation of divergent, convergent, and parallel-channel Nusselt numbers. International Journal of Heat and Mass Transfer 31 (1988): 2197-2205.

Sparrow, E. M., Ruiz, R., and Azevedo, L. F. A. Experimental and numerical investigation of natural convection in convergent vertical channels. International Journal of Heat and Mass Transfer 31 (1988): 907-915.

Sterneus, J., Johnsson, F., and Leckner, B. Gas mixing in circulating fluidized-bed risers. Chemical Engineering Science 55 (2000): 129-148.

Sterneus, J., Johnsson, F., and Leckner, B. Characteristics of gas mixing in a circulating fluidized bed. Powder Technology 126 (2002): 28-41.

Stopford, P. J. Recent applications of CFD modeling in the power generation and combustion industries. Applied Mathematical Modelling 26 (2002): 351-374.

Subbarao, D., and Gambhir, S. Gas to particle mass transfer in risers. The Seventh International Conference on Circulating Fluidized Beds, Canada, May 5-8, 2002.

Sun, B., and Gidaspow, D. Computation of circulating fluidized-bed riser flow for the Fluidization VIII benchmark test. Industrial and Engineering Chemistry Research 38 (1999): 787-792.

Syamlal, M., and O'Brien, T. J. Computer simulation of bubbles in a fluidized bed. AIChE Symposium Series 85 (1989): 22-31.

Syamlal, M., and O'Brien, T. J. Fluid dynamic simulation of O_3 decomposition in a bubbling fluidized bed. AIChE Journal 49 (2003): 2793-2801.

Takeuchi, H., Hirama, T., Chiba, T., Biswas, J., and Leung, L. S. A quantitative definition and flow regime diagram for fast fluidization. Powder Technology 47 (1986): 195-199.

Tartan, M., and Gidaspow, D. Measurement of granular temperature and stresses in risers. AIChE Journal 50 (2004): 1760-1775.

Tennekes, H., and Lumley, J.L. A First Course in Turbulence. Cambridge: MIT Press, 1972.

Therdthianwong, A., Pantaraks, P., and Therdthainwong, S. Modeling and simulation of circulating fluidized bed reactor with catalytic ozone decomposition reaction. Powder Technology 133 (2003): 1-14.

Thiel, W. J., and Potter, O. E. The mixing of solids in slugging gas fluidized beds. AIChE Journal 24 (1978): 561-569.

Tsuji, Y., Kawaguchi, T., and Tanaka, T. Discrete particle simulation of two-dimensional fluidized bed. Powder Technology 77 (1993): 79-87.

Tsukada, M., Nakanishi, D., and Horio, M. The effect of pressure on the phase transition from bubbling to turbulent fluidization. International Journal of Multiphase flow 19 (1993): 27-34.

Tsuo, Y.P., and Gidaspow, D. Computation of flow patterns in circulating fluidized beds. AIChE Journal 36 (1990): 885-896.

Turton, R., and Levenspiel, O. An experiment investigation of gas-particle heat transfer coefficients in fluidized beds of fine particles. In J. R. Grace, L. W. Schemildt,

and M. A. Bergougnou (eds.), Fluidization Volume VI, p.669. Alberta: Engineering Foundation, 1989.

Venderborsch, R. H., Prins, W., and van Swaaij, W. P. M. Mass transfer and influence of the local catalyst activity on the conversion in a riser reactor. Canadian Journal of Chemical Engineering 77 (1999): 262-274.

van Wachem, B. G. M., Schouten, J. C., and van der Bleek, C. M. Comparative analysis of CFD models of dense gas-solid systems. AIChE Journal 47 (2001): 1035-1051.

Wang, C., Lu, Z., and Li, D. Experimental study of the effect of internals on optimizing gas-solid flow in a circulating fluidized bed. Powder Technology 184 (2008): 267-274.

Wang, Y., and Mason, M. T. Two-dimensional rigid-body collisions with friction. Journal of Applied Mechanics 59 (1992): 635-642.

Wang, X.S., and Rhodes, M.J. Determination of particle residence time at the walls of gas fluidized beds by discrete element method simulation. Chemical Engineering Science 58 (2003): 387-395.

Wang, X. S., Rhodes, M. J., and Gibbs, B. M. Influence of temperature on solids flux distribution in a CFB riser. Chemical Engineering Science 50 (1995): 2441-2447.

Wei, F., Cheng, Y., Jin, Y., and Yu, Z. Axial and lateral dispersion of fine particles in a binary-solid riser. Canadian Journal of Chemical Engineering 76 (1998): 19-26.

Wei, F., Jin, Y., Yu, Z., Chen, W., and Mori, S. Lateral and axial mixing of the dispersed particles in CFB. Journal of Chemical Engineering of Japan 28 (1995): 506-510.

Welty, J.R., Wicks, C.E., Wilson, R.E., and Rorrer, G. Fundamentals of Momentum, Heat and Mass Transfer. New York: John Wiley & Sons, 2001.

Wen, C.-Y., and Yu, Y. H. Mechanics of fluidization. <u>Chemical Engineering Progress Symposium Series</u> 62 (1966): 100-111.

Werther, J., Hartge, E.-U., and Kruse, M. Radial gas mixing in the upper dilute core of a circulating fluidized bed. <u>Powder Technology</u> 70 (1992) 293-301.

Williams, M. C., Strakey, J. P., and Surdoval, W. A. U.S. DOE fossil energy fuel cells program. <u>Journal of Power Sources</u> 159 (2006): 1241-1247.

Winkler, F. <u>Verfahren zum Herstellen von Wassergas</u>. German Patent Number 437970, 1922.

Xu, G., Nomura, K., Nakagawa, N., and Kato, K. Hydrodynamic dependence on riser diameter for different particles in circulating fluidized beds. <u>Powder Technology</u> 113 (2000): 80-87.

Yang, Y., Jia, X., Wei, F., and Jin, Y. Hydrodynamics and lateral gas dispersion in a high density circulating fluidized bed reactor with bluff internals. <u>Chinese Journal of Chemical Engineering</u> 9 (2001): 291-296.

Yang, N., Wang, W., Ge, W., and Li, J. CFD simulation of concurrent-up gas-solid flow in circulating fluidized beds with structure-dependent drag coefficient. <u>Chemical Engineering Journal</u> 96 (2003): 71-80.

Yang, N., Wang, W., Ge, W., Wang, L., and Li, J. Simulation of heterogeneous structure in a circulating fluidized-bed riser by combining the two-fluid model with the EMMS approach. <u>Industrial and Engineering Chemistry Research</u> 43 (2004) 5548-5561.

Ye, M., van der Hoef, M. A., and Kuipers, J. A. M. The effects of particle and gas properties on the fluidization of Geldart A particles. <u>Chemical Engineering Science</u> 60 (2005): 4567-4580.

Yerushalmi, J., and Cankurt, N. T. Further studies of the regimes of fluidization. Powder Technology 24 (1979): 187-205.

Yerushalmi, J., Cankurt, N.T., Geldart, D., and Liss, B. Flow regimes in vertical gas-solid contact systems. AIChE Symposium Series 74 (1976a): 1-13.

Yerushalmi, J., Turner, D. H., and Squires, A. M. The fast fluidized bed. Industrial and Engineering Chemistry Process Design and Development 15 (1976b): 47-51.

Yin, X., Wu, C. Z., Zheng, S. P., and Chen, Y. Design and operation of a CFB gasification and power generation system for rice husk. Biomass and Bioenergy 23 (2002): 181-187.

Yoon, H., Wei, J., and Denn, M.M. A model for moving-bed coal gasification reactors. AIChE Journal 24 (1987): 885-903.

Yunhau, Z., Huilin, L., Yurong, H., Ding, J., and Lijie, Y. Numerical prediction of combustion of carbon particle clusters in a circulating fluidized bed riser. Chemical Engineering Journal 118 (2006): 1-10.

Zabrodsky, S. S. Hydrodynamics and Heat Transfer in Fluidized Beds. Cambridge: MIT Press, 1966.

Zevenhoven, R., and Järvinen, M. CFB combustion, particle slip velocity and particle/turbulence interactions. The Seventh International Conference on Circulating Fluidized Beds, Canada, May 5-8, 2002.

Zhang, Y., Lu, C., and Shi, M. Evaluating solids dispersion in fluidized beds of fine particles by gas backmixing experiments. Chemical Engineering Research and Design 87 (2009): 1400-1408.

Zhu, H., and Zhu, J. Gas-solids flow structures in a novel circulating turbulent fluidized bed. AIChE Journal 54 (2008): 1213-1223.

APPENDICES

Appendix A

The principle of GAMBIT program

A.1. Introduction

The GAMBIT computer software is a geometric modeling and grid generation tool for computational fluid dynamics and other scientific applications. The program helps designers to build the system geometry or even import system geometry from other computer-aided design (CAD) computer software. Then, it can manually or automatically grid the system areas or surfaces (for two-dimensional system) or volumes (for three-dimensional system). The grid, also called a mesh, is discrete elements located throughout the computational domain and fits with the system geometry. The conservation equations will solve in each of these elements. For manual grid operation, the program allows designers to control the grid through the use of sizing functions. For automatic grid operation, the program constructs the grid with the possible smallest sizes. If the overall grid is too coarse, the resulting computation may be inaccurate. If the overall grid is too fine, the computational cost may become restrictive. For any given computational domain, the program default defines the outer sides of the system geometry as walls and the space between these sides as interior which can either be a fluid or solid. The boundary conditions and continuums, therefore, should be specified according to the real system specifications after geometry and mesh generation. About the program operation, it receives designer input by means of its graphical user interface (GUI) which makes the basic steps of building and meshing a system geometry model easy and simple.

In the following topic, the GAMBIT program modeling steps and the detailed information of each steps are fully discussed. The purpose is to categorize and describe the main operations that are available in the program. The explanations are mainly emphasized on two-dimensional system as employed in this study. In addition, the GAMBIT program system geometries as used in Chapters IV to VI are summarized.

A.2. The GAMBIT program modeling steps

After starting the GAMBIT program, it creates a modeling session. An example picture of the GAMBIT computer software is illustrated in Figure A.1. As already stated, the program lets designer to build and mesh system geometry model by means of its graphical user interface which consists of eight components. Each of which serves a separate purpose with respect to the creating and meshing of a model. The eight graphical user interface components are as follows:

- Main menu bar: It contains the four menu items which are file, edit, solver and help. Each of the items is associated with its own menu of program operation commands.

- Graphics window: It consists of one to maximum of four separate areas which can be displayed simultaneously. In these areas, the system geometry model is displayed.

- Description window: It displays messages describing the various graphical user interface components at the current mouse pointer position, including fields, windows and command buttons.

- Transcript window: It illustrates a log of commands executed and messages displayed by the program during the current modeling session.

- Command text box: It is used to perform modeling and meshing operations using the keyboard input, rather than using the mouse operations on the graphical user interface.

- Operation toolpad: It consists of a field of command buttons. Each of which performs a specific function associated with the process of creating and meshing the system geometry model.

- Form field: It allows designer to specify parameters related to modeling and meshing operations and to assign the boundary condition and continuum types.

- Global control toolpad: It is used to control the layout and operation of the graphics window, specify the appearance of the model and undo operations.

The general GAMBIT program modeling can be divided into three main steps as summarized below. After all of these steps are completed, the system geometry model is ready to export to use in other computational fluid dynamics programs such as MIXSIM or FLUENT 6.2.16. The specific modeling steps are not discussed in this appendix. However, the information can be found easily in the GAMBIT program manual or open source literature elsewhere (Fluent Inc., 2004a, 2004b).

- Creation of geometry.

- Generation of a mesh.

- Assignment of boundary condition and continuum types.

A.2.1. Creation of geometry

For two-dimensional system as in this study, the geometry can be built by using edge (or line) and face (or area) buttons on geometry operation toolpad. Several edges can be connected to be a two-dimensional face.

A.2.1.1. Edge

In the GAMBIT program, the edges can be created using various methodologies. Three main methodologies are:

- Vertices edge: It builds one or more edges between any two or more existing vertices or points.

- Circular or spiral arc edge: It creates an edge in the shape of a circular arc with the specification of the arc radius, angle and center.

- Full cycle edge: It constructs an edge in the shape of a full cycle with the specification of the center and two points that lie on the circle.

A.2.1.2. Face

In the program, the faces also can be created using various techniques. The five major techniques are:

- Wireframe face: It builds a face from a set of existing edges (called as a wireframe).

- Polygon face: It creates a planar polygonal face which defined by a set of at least three existing points.

- Rectangular face: It constructs a planar face in the shape of a rectangular with the specification of the width and height.

- Circular face: It generates a planar face in the shape of a circle with the specification of the radius.

- Elliptical face: It produces a planar face in the shape of an ellipse with the specification of two radiuses. The two radiuses represent the lengths of the major and minor ellipse axes.

Besides the above operations, the GAMBIT program provides the assistant functions for designers to create edges and faces of the complex system geometry. Those functions are connect/disconnect, unite/subtract/intersect (for face only), move/copy/align, spilt/merge, collapse/simplify (for face only), smooth/convert, heal (for face only) and delete.

A.2.2. Generation of a mesh

Similar to the creation of geometry step, the generation of a mesh step can be done by using edge and face buttons on mesh operation toolpad.

A.2.2.1. Edge

The mesh edge is used to grid any or all edges in the system geometry model. When meshing an edge, the GAMBIT program creates mesh nodes according to the specifications. To perform a mesh edge operation, the grading scheme and mesh node spacing must be specified. For grading scheme, the program provides both symmetrical and non-symmetrical schemes. Generally, the mesh should be sufficiently fine at the region where there is much system variation. For mesh node spacing, the program offers three different ways to define the number of interval which are interval count (the number of mesh intervals on an edge), interval size (the interval length) and shortest edge percent (the interval size value expressed as a percentage of edge length). Also, this mesh edge can be used as an initial mesh for mesh face operation.

A.2.2.2. Face

The mesh face is used to create the mesh for one or more faces in the system geometry model. When meshing a face, the GAMBIT program generates mesh nodes on the face according to the currently specified meshing parameters. To mesh a face, designer must provide meshing scheme and mesh node spacing. For meshing scheme, the program gives three options which are quadrilateral, triangular and quadrilateral/triangular meshes. Figure A.2 illustrates the (a) quadrilateral and (b) triangular two-dimensional meshing elements. Quadrilateral and triangular meshes are usually used in simple and difficult (irregular) system geometry, respectively. For mesh node spacing, the program offers three different ways similar to mesh edge operation.

The assistant functions are also provided for designers to grid edges and faces. They are link/unlink, move/modify (for face only), spilt, smooth (for face only) and delete.

A.2.3. Assignment of boundary condition and continuum types

Boundary condition and continuum type specifications define the physical and operational characteristics of the system geometry model.

A.2.3.1. Boundary condition types

Boundary condition type specifications define the physical and operational characteristics at the sections that represent model external and internal boundaries. Each computational solver is associated with a unique set of allowable boundary condition types. For FLUENT 6.2.16 program, the boundary conditions that can be selected are axis, exhaust fan, inlet vent, intake fan, interior, mass flow inlet, outflow, outlet vent, pressure inlet, pressure outlet, symmetry, velocity inlet and wall.

A.2.3.2. Continuum types

Continuum type specifications define the physical characteristics of the system geometry model within specified regions of its domain. If a fluid continuum type is used, the model is defined such that conservation equations of mass, momentum, energy and species transport apply at mesh nodes or cells that exist within the volume. Conversely, if a solid continuum type is assigned, only the energy and species transport conservation equations apply at mesh nodes or cells that exist within the volume.

A.3. The used GAMBIT program system geometries

Figure A.3 illustrates the computational domain with their boundary condition and continuum specifications of this study (a) typical, (b) tapered-out and (c) tapered-in risers. The system geometry for typical riser was created from rectangular face operation while the system geometries for the other two risers were constructed from wireframe face operation (with vertices edge). Then, all the risers were meshed using non-symmetrical meshes in horizontal or x- direction and symmetrical meshes in vertical or y- direction (mesh edge) and quadrilateral meshes (mesh face). Finally, the boundary condition and continuum types are addressed as shown in Figure A.3.
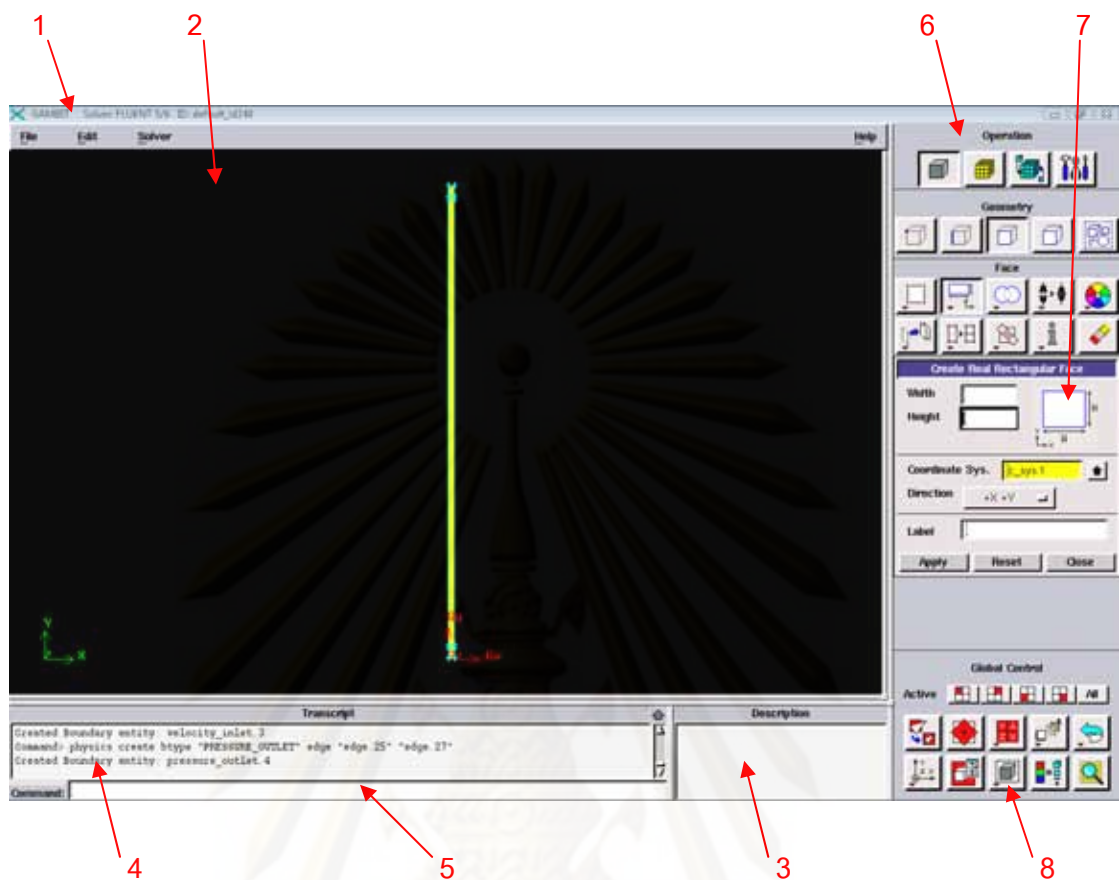
Figure A.1 An example picture of the GAMBIT computer software (where 1 is main menu bar, 2 is graphics window, 3 is description window, 4 is transcript window, 5 is command text box, 6 is operation toolpad, 7 is form field and 8 is global control toolpad).
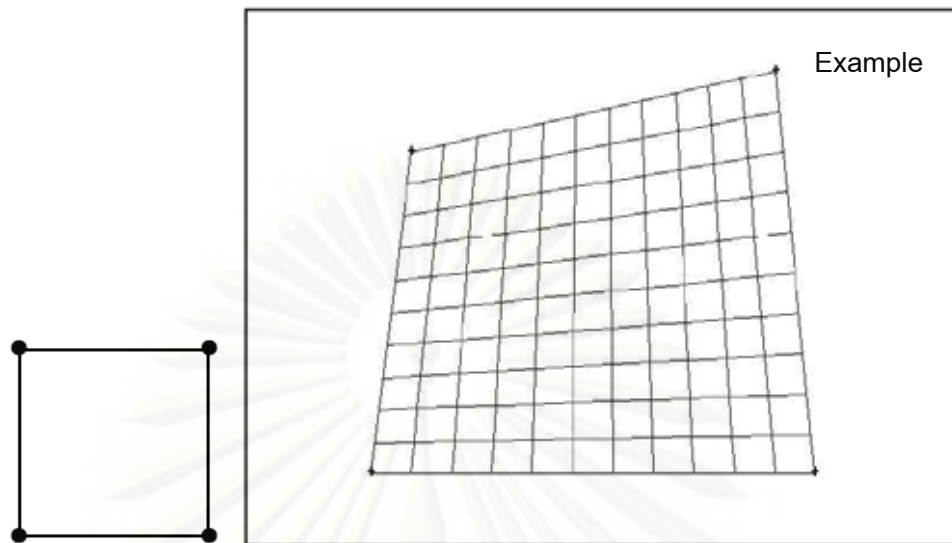
(a) Quadrilateral meshing element
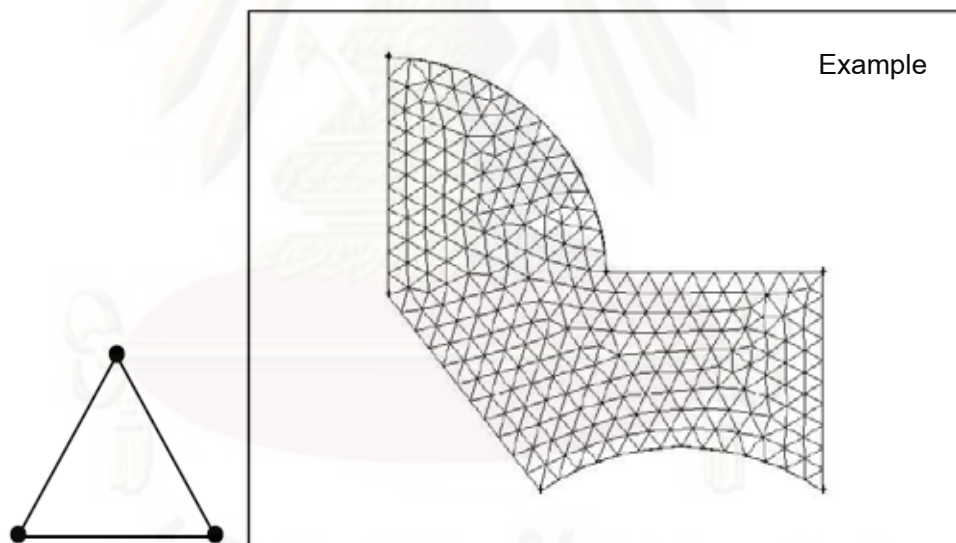
(b) Triangular meshing element

Figure A.2 The (a) quadrilateral and (b) triangular two-dimensional meshing elements.
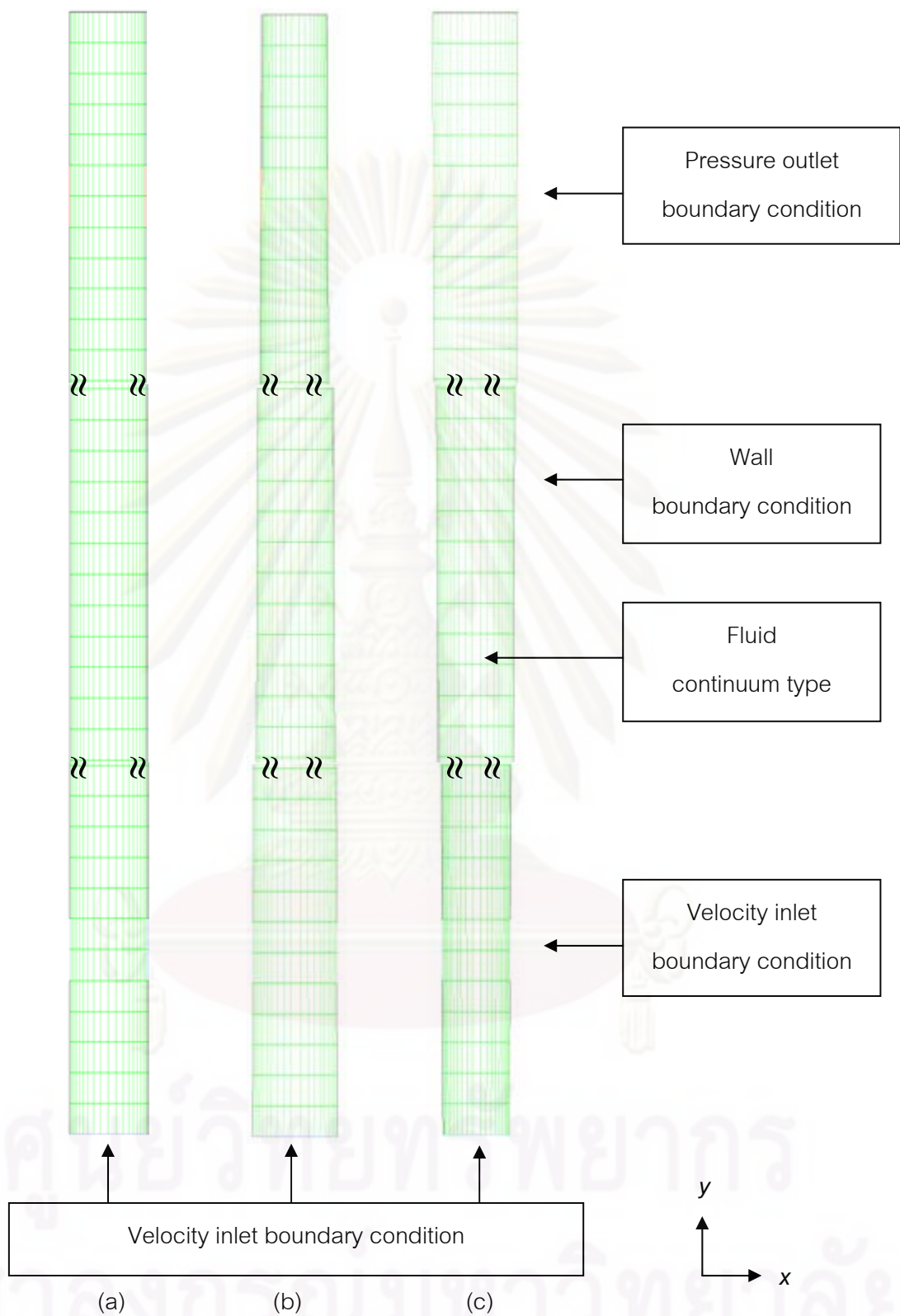
Figure A.3 The computational domain with their boundary condition and continuum specifications of this study (a) typical, (b) tapered-out and (c) tapered-in risers.

Appendix B

The principle of FLUENT 6.2.16 program

B.1. Introduction

The FLUENT 6.2.16 computer software is a general purpose computational fluid dynamics code based on the finite volume method on a collocated grid. The program contains a broad physical and chemical modeling capabilities which can use to model fluid flow, turbulence, heat transfer, multiphase and chemical reaction. Once the mesh file is imported into the program, the program checks the grids. If there are no errors, several modeling and controlled options can be set to solve each specific system. User modeling and controlled options are numerical solvers, physical models, material properties, operating conditions, boundary conditions and initial conditions. The program then applies a set of equations to the system geometry model in order to predict system behavior. The finite volume method converts the governing or conservation partial differential equations into algebraic form. Subsequently, the algebraic equations are solved in an iterative process until the solution has converged (for all time steps). Convergence is a point when the solution is no longer changing with successive iterations. In addition, the grid independence study should be considered to obtain correct computation results. The grid should be changed until the solution does not change with the grid, otherwise, the process of refining the grids continues. The results of the modeling can be presented and interpreted in both graphical and numerical formats. Similar to the GAMBIT program, the FLUENT 6.2.16 program receives designer input by means of its graphical user interface (GUI).

In the following topic, the basic FLUENT 6.2.16 program modeling steps and the detailed information of each steps are discussed. The meanings of some important modeling and controlled options are defined. As already declared, the program supplies various available modeling and controlled options, of which only few relevant to this study will be mentioned. Finally, the FLUENT 6.2.16 program modeling and controlled options selected to use in Chapters IV to VI of this study are reviewed.

B.2. The FLUENT 6.2.16 program modeling steps

Figure B.1 displays an example picture of the FLUENT 6.2.16 computer software. The program consists of four main graphical user interface components which are a console window, dialog boxes, control panels and graphical windows. The four graphical user interface components are described below.

- Console window: It is the main window that controls the execution of the program. In this console window, designer can also interact with the program via text user interface (TUI).

- Dialog boxes: They are used to perform simple input/output tasks, such as selecting reading or writing files, issuing warning or error messages and asking a yes/no question.

- Control panels: They are used to perform more complicated input tasks. Each panel employs various types of input controls that make up the form such as selecting display information and identify boundary condition values.

- Graphical windows: They are separate windows that display the graphical output results.

Before simulating the system geometry model using the FLUENT 6.2.16 or other computational fluid dynamics program, careful consideration of each modeling steps will contribute significantly to the success of simulation results. The understanding of the modeling and controlled options will help the designer to model the system, efficiently. The following are three basic modeling steps in FLUENT 6.2.16 program:

- Setup the modeling and controlled options (Pre-processor).

- Compute the solutions (Solver).

- Display the output results (Post-processor).

B.2.1. Setup the modeling and controlled options

B.2.1.1. Numerical solvers

- Discretization method -> finite volume method

Discretization is the process of converting the governing partial differential equations into algebraic equations that can be solved numerically. There are three distinct streams of the discretization process. The finite difference method converts partial differential equations using Taylor series expansion at each grid point. The finite volume method evaluates partial differential equations using divergence theorem for the small volume surrounding each node point on a mesh. The finite element method approximates partial differential equations using simple approximate functions valid on elements to describe the local variations of unknown flow variable.

The program solves the governing partial differential equations for mass, momentum, energy, species transport and other scalars using finite volume method. In this method, the governing equations are first integrated about each control volume (with divergence theorem). This is illustrated in Equation (B.1), which shows the integration of the generic governing equation of a scalar φ over an arbitrary control volume (V).

$$\int_V \frac{\partial \rho \varphi}{\partial t} dV + \oint \rho \varphi \vec{v} \cdot d\vec{A} = \oint \Gamma_\varphi \nabla \varphi \cdot d\vec{A} + \int_V S_\varphi dV \qquad (B.1)$$

where $\vec{v}$ is the velocity vector, $\vec{A}$ is the surface area vector, Γ_φ is the diffusion coefficient of φ, $\nabla \varphi$ is the gradient of φ and S_φ is the source term of φ. The Equation (B.1) is applied to each control volume in the computational domain. The integral form is then discretized to an algebraic form using various schemes. Depending on each scheme, the discretized equations will contain the unknown variable φ at the cell center and the neighbor faces or cells. The equations will, in general, be non linear with respect to these variables. Therefore, the final step is to linearize the discretized equations. This will give the system of linear equations which is prepared for the iteration using automatic program algorithm such as Gauss-Seidel.

Here, the schemes to convert the governing equation from integral form to discretized form are discussed. By the FLUENT 6.2.16 program default, all variable values are calculated and stored at the cell center. However, as already mentioned, the discretization of the governing equation for φ may require the value of φ at the face of the cell. An upwind scheme thus is provided to use for predicting the value of φ at the faces, based on the cell center values. The program allows designers to choose several upwind schemes which, the two main schemes, are first order and second order.

The first order upwind scheme assumes that the value of a variable at the cell center represents an average value of the variable throughout the cell. Hence, the value of a variable at the center of the cell just upstream of the face is approximated as the value of the variable at the face.

The second order upwind scheme computes the quantities at cell faces using a multidimensional linear reconstruction approach. In this approach, the Taylor series expansion is applied at cell face. Therefore, the face value is computed from the cell-centered value and its gradient (cell to face centroids) in the upstream cell.

About the comparison between these two schemes, the first order upwind scheme generally yields better convergence and stability than the second order upwind scheme. On the other hand, the second order upwind scheme normally gives more accurate results than the first order upwind scheme, especially for complex flow system geometry.

- Under-relaxation factor

As the governing equations being solved are fundamentally non linear, huge fluctuations in the calculated value of the variables are thus occurred. To reduce the fluctuations, the change of the variables is controlled by an under-relaxation factor (ranges from 0 to 1). The new value of the variable φ depends upon the old value (φ_{old}), the computed change in φ ($\Delta\varphi$) and the under-relaxation factor (α) as follows:

$$\varphi = \varphi_{old} + \alpha\Delta\varphi \qquad\qquad (B.2)$$

- Linearization approaches -> implicit/explicit approaches

The manner in which the governing equations are linearized may take implicit or explicit approaches with respect to the dependent variable. For implicit approach, the unknown value in each cell is computed using a relation that includes both existing and unknown values from neighboring cells. Each unknown will appear in more than one equation. Thus, these equations must be solved simultaneously to give the unknown quantities. For explicit approach, the unknown value in each cell is computed using a relation that includes only existing values. Therefore, each unknown will appear in only one equation and the equations for the unknown value in each cell can be solved one at a time to give the unknown quantities. These linearization approaches should be selected according to the employed solver approaches (below).

- Solver approaches -> segregated/coupled approaches

About the approaches how to solve the governing equations, segregated and coupled approaches are available. Both approaches employ a similar finite volume discretization method, but the techniques used to solve the equations are different.

For the segregated approach (suitable with implicit linearization), the governing equations are solved sequentially. Because the governing equations are non linear, several iterations must be performed before a converged solution is obtained as illustrated in Figure B.2 (a). First, the properties are calculated based on the current solution. For the first time step, the properties are calculated based on the initial values. Then, the components of the momentum equations are solved to obtain a new velocity field using the current values of pressure and mass flux. Since the obtained velocity may not satisfy the continuity equation, a pressure correction equation is used to correct the pressure and the mass flux. This pressure correction equation is derived from the continuity and the momentum equations. Then, equations for energy, species transport and other scalars are solved using the corrected values. Finally, the solution is checked for convergence. The sequence will repeat until the convergence criteria are obtained. This segregated approach is suitable for incompressible and mildly compressible flows.

For coupled approach (suitable with implicit and explicit linearizations), the governing equations for mass, momentum, energy and species transport are solved simultaneously while the governing equations for additional scalars are solved sequentially. Also, several iterations of the solution loop must be performed as shown in Figure B.2 (b). Initially, the properties are calculated based on the current solution. If the calculation has just started, the properties will be calculated based on the initialized condition. Then, the mass momentum, energy and species transport equations are solved simultaneously. After that, the equations for other scalars are computed using the updated variable values. Finally, a check for convergence is made. This sequence will continue until the convergence criteria are met. This coupled scheme is designed for high speed compressible flows.

- Pressure-velocity coupling algorithm -> phase coupled SIMPLE

As described above, the mass and momentum equations for segregated approach are solved separately in a sequential manner. The velocities obtained from solving the momentum equations may not necessarily satisfy the continuity equation. The pressure-velocity coupling algorithm or pressure correction equation is then used to compute the pressure and mass flux corrections. A brief description of the available pressure-velocity coupling algorithm, named phase coupled SIMPLE, is given below:

The phase coupled SIMPLE (semi-implicit method for pressure linked equations) algorithm uses a relationship between velocity and pressure to enforce mass conservation. Firstly, the momentum equations are solved with an initial pressure field to obtain the velocity components. The velocities are solved coupled by phases. If the resulting velocities do not satisfy the total mass continuity, the pressure and velocities correction terms are added. The correct variables or correction equations are the summation between initial variable and correction term. Then, the algorithm substitutes the correction equations into the continuity equation to obtain an equation for the pressure correction. Once a solution is obtained, the pressure and the mass flux are updated. A full detail of this algorithm can be found in fundamental numerical textbooks.

- Time-advancement schemes -> iterative/non-iterative schemes

There are two schemes in which the solutions are advanced to the next time step (time-advancement). They are iterative and non-iterative time-advancement schemes.

In the iterative time-advancement scheme, all the equations are solved iteratively, for a given time step, until the convergence criteria are met. Advancing the solutions by one time step normally requires a number of iterations. Thus, the iterative time-advancement scheme requires a considerable amount of computational effort due to a large number of iterations performed for each time step. For the non-iterative time-advancement scheme, in order to preserve overall time accuracy, the error in each steps is not really needed to reduce to zero but only decreases to the same order as the truncation error. The non-iterative time-advancement scheme thus performs only a single iteration per time step, which significantly speeds up transient simulations.

B.2.1.2. Physical models

There are several physical models that can be selected in the FLUENT 6.2.16 program. Here, two important physical models are explained.

-    Energy model: It is used to calculate the thermal energy flow by three mechanisms: conduction, convection and radiation.

-    Multiphase model: It is used to model a system with includes a mixture of phases: gas, solid and liquid. A full discussion about the multiphase model is already given in Chapter III.

B.2.1.3. Material properties

The FLUENT 6.2.16 program allows designers to define three main types of material which are fluids, solids and mixtures. In the program, a material database along with their properties, such as density, molecular weight and viscosity, is provided for the well-known substances. Also, designers can create own material property using

user-defined function code. The properties of fluids and solids are associated with the selected or created substances. The property of mixtures is depended on the properties of constituent substances in species transport or chemical reaction modeling problem.

B.2.1.4. Operating conditions

The important operating condition parameters needed to be input are operating pressure, operating temperature and gravitational acceleration. The operating pressure and temperature are the reference system conditions for further setting the boundary conditions. The gravitational acceleration is the attraction force between two masses (usually between the earth and the mass near its surface).

B.2.1.5. Boundary conditions

Boundary conditions specify the flow and thermal variables on the boundaries of the system geometry model. They should be selected according to the known system information. In the program, the accessible boundary condition types are classified as follows:

- Flow inlet and outlet boundaries: inlet vent, intake fan, mass flow inlet, pressure inlet, velocity inlet, exhaust fan, outflow, outlet vent and pressure outlet.

- Wall, repeating and pole boundaries: axis, symmetry and wall.

- Internal face boundaries: interior and wall.

B.2.1.6. Initial conditions

Similar to boundary conditions, initial conditions give the flow and thermal variables of the system geometry model. The difference is that the initial condition variables are set at the time equals to zero. These values then provide the starting points for the mathematical calculation. For general single phase flow system without energy model, the initial conditions that are required to input are system pressure and velocities.

B.2.2. Compute the solutions

After the modeling and controlled options are setup, the system of discretized conservation equations are solved iteratively with the specifying time step. A number of iterations are usually required to reach a converged solution. Convergence is reached when there is no change in solution variables between iterations. During the computation process, the convergence can dynamically be monitored by checking the conservation equation imbalances or residuals. At the end of each iterations, the residual summation for each of the conserved variables is calculated. On a computer with infinite precision, these residuals will go to zero as the solution converges. On an actual computer, the residuals decay to some small value and then stop changing. The convergence criteria thus are needed.

B.2.3. Display the output results

The FLUENT 6.2.16 program allows designers to display or process the information contained in computational fluid dynamics output results in various ways. They are:

- Grid: Outline of all or part of the system geometry model.

- Contour: Area of constant magnitude for a selected variable.

- Vector: Arrow representing velocity magnitude and direction.

- XY Plots: Line chart, symbol chart or numeric table of data.

B.3. The used FLUENT 6.2.16 program modeling and controlled options

The commercial FLUENT 6.2.16 program was used in this study simulation. As already stated, the program solves the governing partial differential equations using finite volume discretization method. In this topic, the setup of modeling and controlled options for this study is reviewed. Table B.1 summarizes the used FLUENT 6.2.16 program modeling and controlled options.

Table B.1 The used FLUENT 6.2.16 program modeling and controlled options.

No.	Modeling and controlled options	Used options
1	Discretization method	Finite volume method
2	Discretization scheme	Second order upwind scheme
3	Under-relaxation factor	
	- pressure, momentum, volume fraction and granular temperature	0.2
	- density, energy and species	1.0
4	Linearization approach	Implicit approach
5	Solver approach	Segregated approach
6	Pressure-velocity coupling algorithm	Phase coupled SIMPLE algorithm
7	Time-advancement scheme	Iterative scheme
8	Physical model	
	- Energy model (Hot flow model)	✓
	- Multiphase model	✓
9	Material property	As in chapter
10	Operating condition	
	- Operating pressure	101325 Pa
	- Operating temperature (Hot flow model)	As in chapter
	- Gravitational acceleration	9.81 m/s^2
11	Boundary condition	
	- Velocity inlet	As in chapter
	- Pressure outlet	As in chapter
	- Wall	As in chapter
12	Initial condition	As in chapter
13	Time step	0.001 s
14	Convergence criteria	0.001
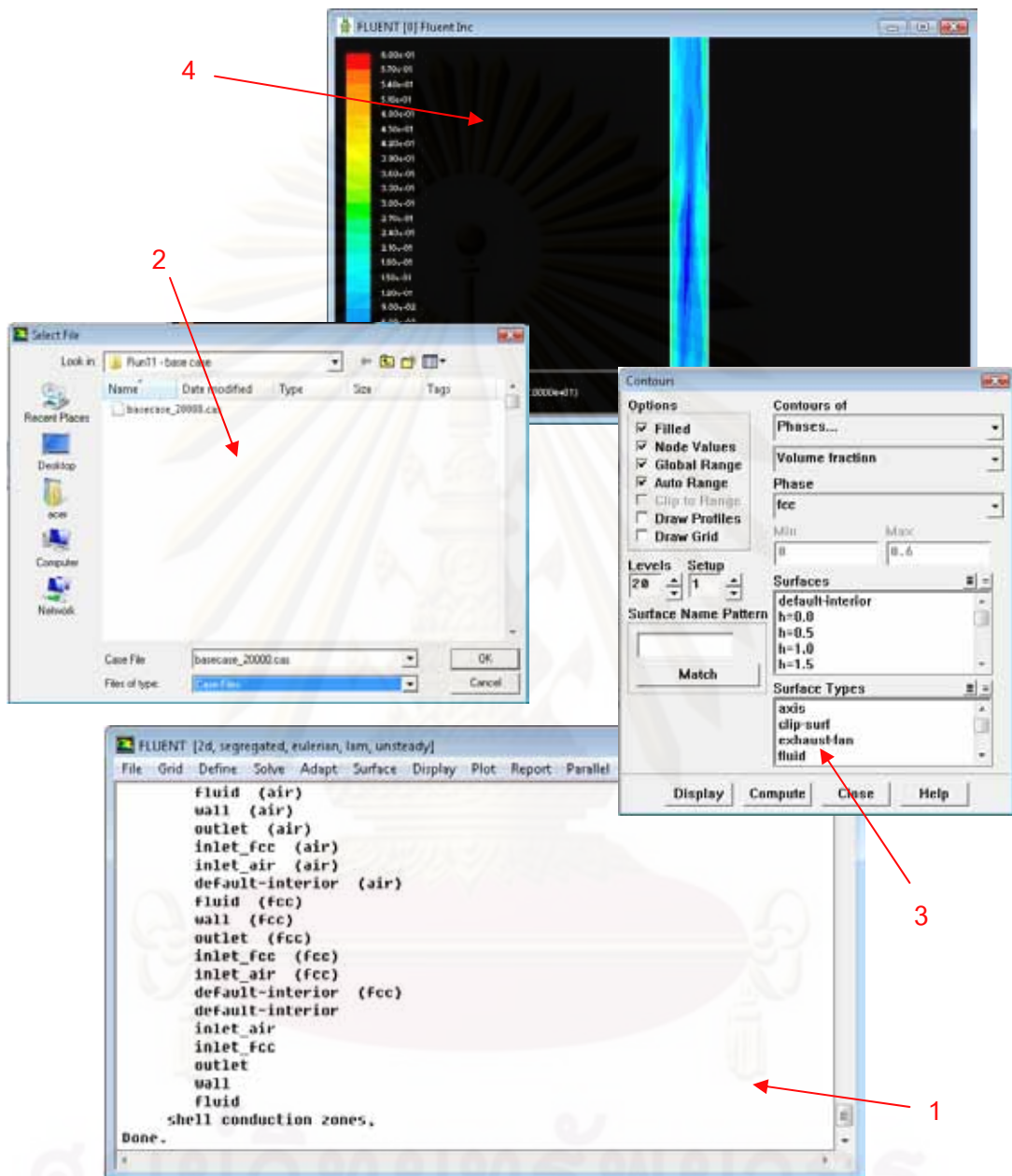
Figure B.1 An example picture of the FLUENT 6.2.16 computer software (where 1 is

console window, 2 is dialog box, 3 is control panel and 4 is graphical window).
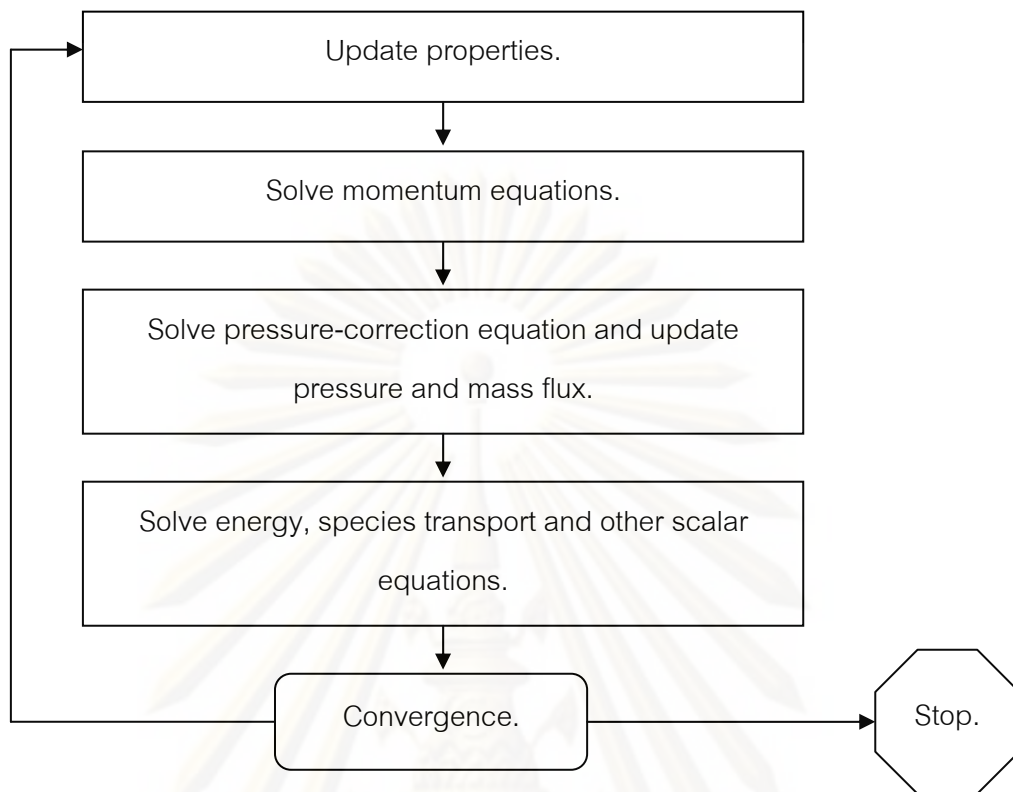
(a) The segregated solver approach
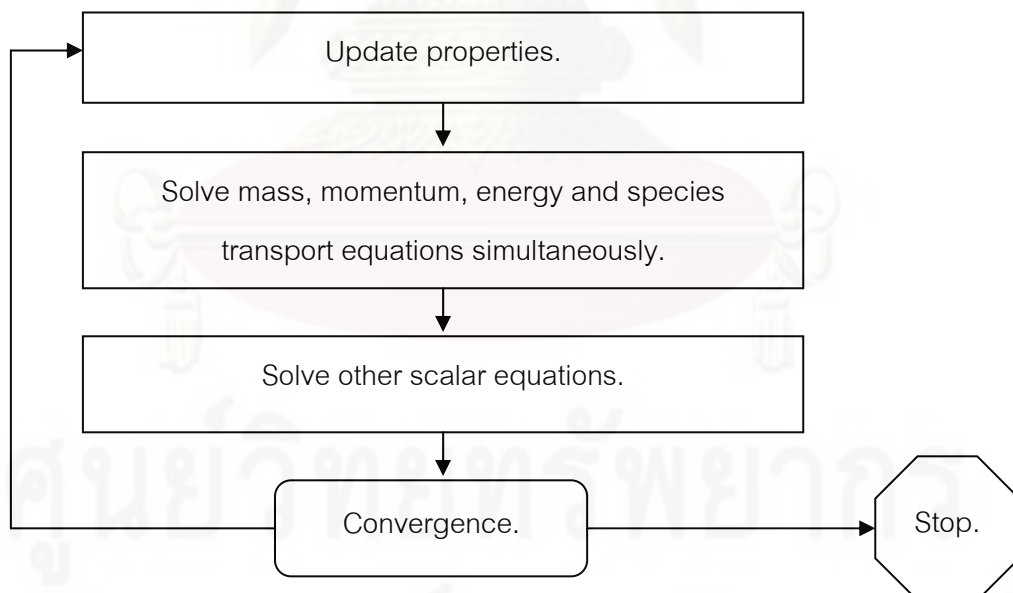
(b) The coupled solver approach

Figure B.2 Overview of (a) the segregated and (b) the coupled solver approaches.

Appendix C

The FLUENT program additional user-defined function

C.1. Introduction

A user-defined function (UDF) is a manual function or code that can be simultaneously loaded with the FLUENT program solver to enhance the capabilities of the standard FLUENT program. User-defined functions are written in the C programming language using any text editor such as WordPad or Microsoft Visual C++. However, the code file must be saved with a .c file extension. User-defined functions are defined using DEFINE macros that are supplied by the main Fluent program. Every user-defined function contains the udf.h file inclusion directive (#include "udf.h") at the beginning of the code file, which allows definitions for DEFINE macros and other provided macros and functions to be included during the compilation process. Then, user-defined functions are either interpreted or compiled and are hooked to the FLUENT program solver using a graphical user interface panel. For interpreted user-defined functions, the code files are interpreted and loaded directly at runtime, in a single-step process. For compiled user-defined functions, the process involves two separate steps. A shared object code library is first built and then it is loaded into the main FLUENT program. For a user-defined function that is called on a per-cell basis in every iteration as in this study simulation, the complied user-defined function is recommended. Once compiled, user-defined functions will become visible and selectable in FLUENT program graphics panels, and can be hooked to a solver by choosing the function name in the appropriate panel. Values that are passed to a solver by a user-defined function or returned by the solver to a user-defined function are specified in SI units.

In this study, the user-defined function for the interphase exchange coefficient model (the energy minimization multi-scale or EMMS drag model) was written using DEFINE_EXCHANGE_PROPERTY macro. In the following topics, a detail of macro description, variable description, user-defined function code and hooking methodology are provided for this DEFINE_EXCHANGE_PROPERTY macro.

C.2. DEFINE_EXCHANGE_PROPERTY

C.2.1. Macro description

The DEFINE_EXCHANGE_PROPERTY macro can be used to specify user-defined functions for various phase interaction variables in multiphase flow models. The multiphase application that can be used this DEFINE_EXCHANGE_PROPERTY macro are net heat transfer rates between phases, lift coefficient and drag coefficient functions. The program statement to use the DEFINE_EXCHANGE_PROPERTY macro is as shown below:

DEFINE_EXCHANGE_PROPERTY(name, cellind, mixture_thread, secnd phase ind, first phase index)

C.2.2. Variable description

Variable type	Description
char (character) name	User-defined function name.
cell_t (cell identifier) cellind	Cell index.
Thread *mixture_thread	Pointer to the mixture-level thread (a group of cells for mixture of phases).
int (integer) secnd phase ind	Identifier that corresponds to the pair of phases in the multiphase flow model. These identifiers should resemble with the selected phases in the Phase Interaction panel from the graphical user interface. An index of 0 is equated to the primary phase and is incremented by one for each secondary phase.
int (integer) first phase ind	See int (integer) secod phase ind.

There are five important variables in DEFINE_EXCHANGE_PROPERTY macro: name, cellind, mixture_thread, secnd phase ind and first phase ind. The name of the user-defined function is needed to be supplied. The other variables, which are cellind, mixture_thread, secnd phase ind and first phase ind are variables that are passed by the FLUENT program solver to user-defined function. The user-defined function will return the real value of the heat transfer, lift coefficient and drag coefficient to the FLUENT program solver.

C.2.3. User-define function code

The following user-defined function, named custom_drag, can be used to customize the default interphase exchange coefficient or drag model in the main FLUENT program. As already stated, the energy minimization multi-scale or EMMS interphase exchange coefficient model is developed using Microsoft Visual C++ text editor. Figure C.1 illustrates an example picture of the Microsoft Visual C++ program with new written custom_drag user-defined function code. The full information about this interphase exchange coefficient model is already discussed in Chapter III (3.3.2. Constitutive equations).

```
/*****************************************************************************************
                User-defined function for EMMS drag model in FLUENT program
*****************************************************************************************/
#include "udf.h"
#define diam 76.e-6
DEFINE_EXCHANGE_PROPERTY(custom_drag, cellind, mix_thread, gas, solid)
{
        /* define the additional sub threads */

        Thread          *thread_g, *thread_s;
```

```
/* define the additional variables as real variable type*/

real            x_vel_g, x_vel_s, y_vel_g, y_vel_s, slip_x, slip_y, abs_v,

                rho_g, mu_g, void_g, void_s, reyno, afac, bfac, cfac, dfac, k_g_s;

/* find the sub thread for the gas (primary phase) */

thread_g = THREAD_SUB_THREAD(mix_thread, gas);          /* gas phase */

/* find the sub thread for the solid (secondary phase) */

thread_s = THREAD_SUB_THREAD(mix_thread, solid);        /* solid phase */

/* find phase velocities */

x_vel_g = C_U(cellind, thread_g);                       /* radial gas */

y_vel_g = C_V(cellind, thread_g);                       /* axial gas */

x_vel_s = C_U(cellind, thread_s);                       /* radial solid */

y_vel_s = C_V(cellind, thread_s);                       /* axial solid */

slip_x = x_vel_g - x_vel_s;

slip_y = y_vel_g - y_vel_s;

/* compute absolute slip velocity */

abs_v = sqrt(slip_x*slip_x + slip_y*slip_y);

/* find phase properties */

rho_g = C_R(cellind, thread_g);                         /* gas density */

mu_g = C_MU_L(cellind, thread_g);                       /* gas viscosity */

void_g = C_VOF(cellind, thread_g);                      /* gas fraction */

void_s = 1-void_g;                                      /* solid fraction */

/* compute Reynolds number */

reyno = void_g*rho_g *abs_v*diam/mu_g;
```

```
/* compute drag and return drag coefficient (k_g_s) */

if (void_g<0.74)

{

        afac = ((150.00*void_s*void_s*mu_g)/(void_g*diam*diam));

        bfac = ((1.75*void_s *rho_g*abs_v)/(diam));

        k_g_s = afac+bfac;

}

else

{

        if (reyno<1000.00)

                cfac = (24.00)*(1+(0.15*pow(reyno, 0.687)));

        else

                cfac = 0.44*reyno;

        if (void_g>0.97)

                dfac = -31.8295+(32.8295*void_g);

        else if (void_g>0.82)

                dfac = -0.0101+(0.0038/((4.00*(void_g-0.7789)*(void_g-
                0.7789))+0.0040));

        else

                dfac = -0.5760+(0.0214/((4.00*(void_g-0.7463)*(void_g-
                0.7463))+0.0044));

        k_g_s = (3.00/(4.00*diam*diam))*void_s*cfac*mu_g*dfac;

}

return k_g_s;

}
```

C.2.4. Hooking methodology

After the above user-defined function code is compiled using Complied UDFs panel (Figure C.2) and Select File panel (Figure C.3), the supplied user-defined function name in the DEFINE_EXCHANGE_PROPERTY macro statement (custom_drag) will become visible and selectable in the Phase Interaction panel in the main FLUENT program. About the general information on compilation steps, it can be found in the open literature elsewhere (Fluent Inc., 2005b).

To hook the written user-defined function into the FLUENT program, the Phase Interaction panel as shown in Figure C.4 needs to be opened first by clicking on the Interactions button in the Phases panel. Then, click on the Drag Coefficient tab in the Phase Interaction panel and choose user-defined in the drop-down list for the corresponding exchange property. This will open the User-Defined Functions panel as illustrated in Figure C.5. Finally, choose the user-defined function name from the list of available user-defined functions and click on the OK button. The supplied user-defined function name will then be presented under the user-defined function box for Drag Coefficient tab in the Phase Interaction panel. When the computational fluid dynamics model is simulated, the drag or interphase exchange coefficient model will be computed using the additional custom_drag user-defined function code.

Figure C.1 An example picture of the Microsoft Visual C++ program with new written

custom_drag user-defined function code.
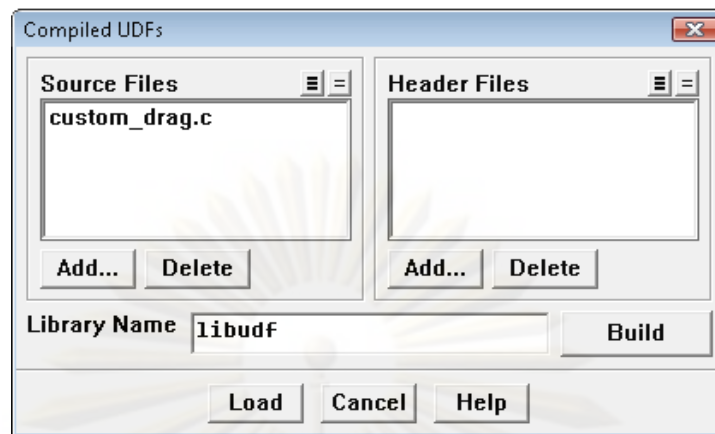
Figure C.2 The Complied UDFs panel.
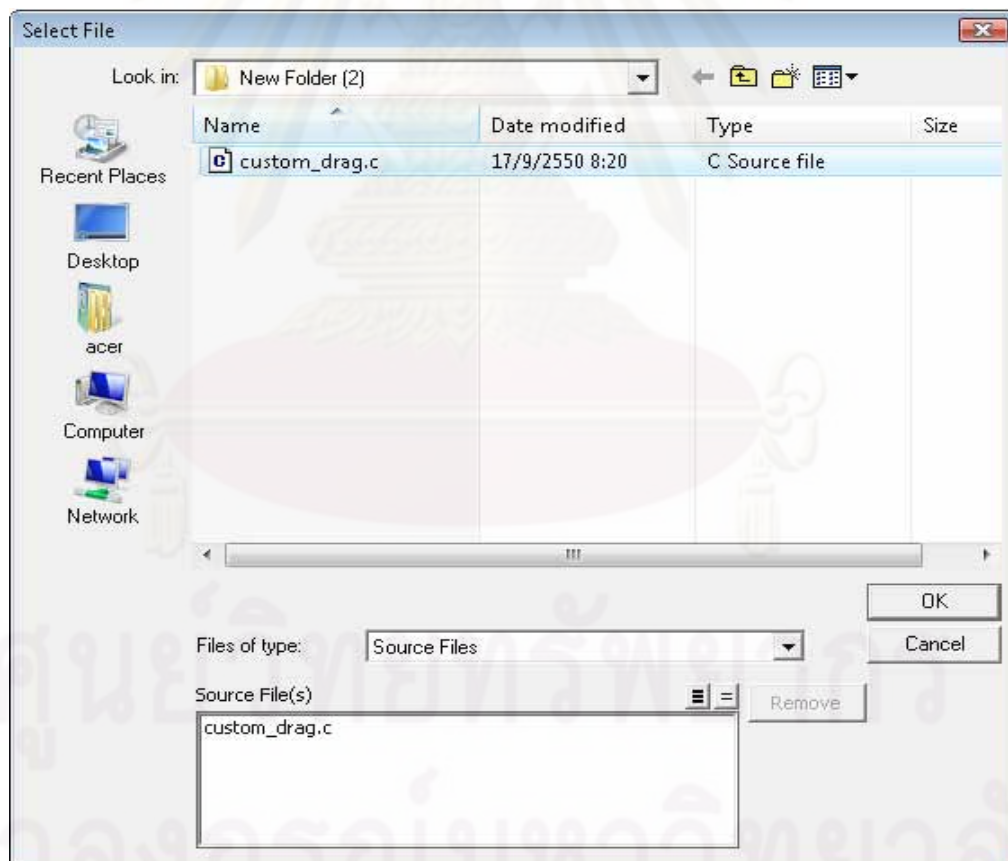
Figure C.3 The Select File panel.
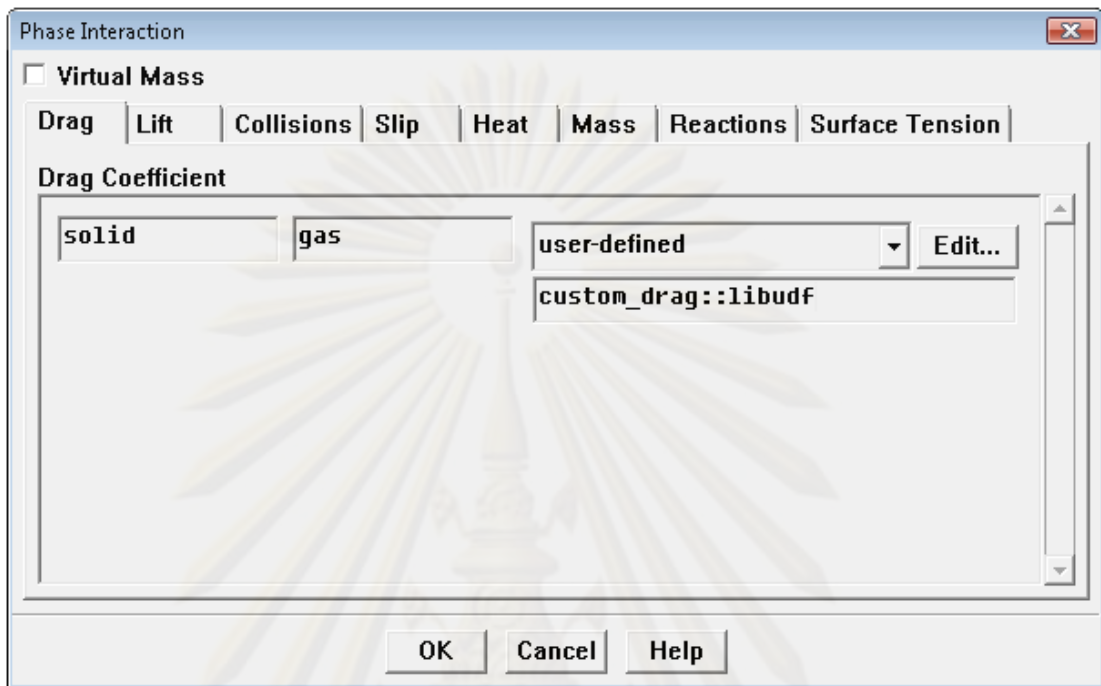
Figure C.4 The Phase Interaction panel.

Figure C.5 The User-Defined Functions panel.

Appendix D

The principle of particle image velocimetry technique

D.1. Introduction

Particle image velocimetry (PIV) is an optical technique for measuring instantaneous velocity field in a considering plane. The fluid or gas stream is seeded with tracer or solid light reflecting particles which are assumed to follow the system flow dynamics. The motion of these seeding particles is then used to compute velocity information of the flow being studied. The other techniques used to obtain flow visualization are Laser doppler velocimetry (LDV), Laser doppler anemometry (LDA) and Hot-wire anemometry. The major difference between particle image velocimetry and those techniques is that particle image velocimetry produces two-dimensional instantaneous vector field, while the other techniques measure the velocity at a specific point. Besides, the particle image velocimetry technique has the other advantage features as summarized below:

- This technique is large degree non-intrusive or no probe is disturbing the flows.

- This technique is capable to measure the flow dynamics of both single and multi- phase systems. For single phase system, the tracers are assumed to have negligible influence on the fluid flow.

- This technique is applicable for the system with instantaneous velocity range from zero to supersonic.

All of these features have made particle image velocimetry as a very useful technique. In the following topics, equipments and principle of particle image velocimetry technique are fully discussed. At the end of this appendix, the raw particle image velocimetry data obtained for both dilute and dense experimental conditions in Chapter VII are given.

D.2. Equipments of particle image velocimetry technique

A typical particle image velocimetry system consists of three standard components. They are:

D.2.1. Light source

The light source is used to illuminate the considering plane where the measurement is going to be taken. In common particle image velocimetry system, the fiber optic or laser is employed. Figure D.1 illustrates an example picture of fiber optic light source.

D.2.2. Camera

To perform particle image velocimetry technique on the flow, two exposures of light source are required upon the camera. Generally, both exposures are captured on the same frame. This single frame is then used to measure the system flow dynamics. With the new technology of camera to capture multiple frames at high speeds, it can capture two frames within a small time difference between them. However, the restriction is that this fast speed is limited to a pair of frames. This is because each pair of frames must be transferred to the computer before another pair of frames can be taken. Nowadays, the CCD (charge coupled device) camera is one of the selected cameras to use for this particle image velocimetry technique due to its high sensitivity to the incoming light source. An example picture of charge coupled device camera is displayed in Figure D.2.

D.2.3. Computer software

Once the frame is captured, the computer software is used to store and extract the obtained instantaneous velocity information. The frames can be analyzed using various commercial softwares, such as MATLAB and Image-Pro Plus^{TM}, or other available non-commercial softwares in the open source community. Figure D.3 depicts an example picture of the Image-Pro Plus^{TM} computer software.

D.3. Principle of particle image velocimetry technique

The working principle of a particle image velocimetry technique is quite simple. Particle image velocimetry technique is based on determining the movement of a group of particles seeded into the flow. The instantaneous velocity is determined from the basic properties which is the displacement of imaged tracer or solid particles divided by the time separation for that displacement. An example configuration of the particle image velocimetry system is already shown in Chapter VII (Figure 7.2 (a)). Firstly, the light source is flashed into two-dimensional considering plane and area. The measurement plane is cut in the system flow by a light source and the measurement area in this plane is restricted by the field of camera view. The light then illuminates fine seeding tracer (for single phase flow) or solid (for multiphase flow) particles following the system flow dynamics. The tracer or solid particles scatter that light into a camera photographic zoom lens. Simultaneously, image is formed on a video array detector and transferred to a connecting computer. A micro-imaging board is used for capturing and digitalizing the image frame. About the time separation between the two frames, it is set by the user and known with high accuracy. Ordinarily, the time interval between the frames is in the unit of microseconds. Finally, the instantaneous velocities are analyzed by using the computer software as already stated in the previous topic. In general particle image velocimetry system, only the in-plane velocity components can be obtained. The out-of-plane velocity component is superimposed on the in-plane velocity components. Using two-camera particle image velocimetry technique, the out-of-plane velocity component can also be obtained.

To employ this particle image velocimetry technique, three major considerations are needed to consider as follow:

- Image acquisition

- Image interrogation

- Post processing

D.3.1. Image acquisition

Various parameters have to be optimized for a good image acquisition. They are considering plane, time separation, interrogation window, light source power and camera aperture. Typically, the considering plane should be chosen dependent on the flow velocity normal to the considering plane. The time separation must be long enough to be able to determine the displacement and short enough to avoid particles leaving the considering plane. The tracer or solid particles must stay inside the small chosen area. About the light source intensity, it should be as uniform as possible. This can be obtained by finding a balance between light source power and camera aperture opening. In addition, the seeding is very important parameter for both image quality and accuracy in the velocity measurement.

D.3.2. Image interrogation

The main objective of the image interrogation is to determine the particle displacement with high precision. For evaluation, the image frame is captured as a small area called interrogation window. The interrogation window should be small to resolve small structure properties but it has to be enough particles in the window to make an accurate velocity estimation. If both exposures are recorded on a single frame, this leads to a directional ambiguity. The motor with rotating transparent sheet may be used to work out this problem. On the other hand, if both exposures are recorded on separate frames, it is difficult to identify and match particle pairs clearly. Therefore, it is more convenient to describe the particles by measuring the average displacement of local groups of particles.

D.3.3. Post processing

Post processing consists of data validation, removal of incorrect data and replacement of removed data. As already discussed above, it is important to reduce the error during image acquisition as much as possible. However, all the steps for detecting, recording, digitizing and storing of particle image velocimetry technique are contributed

error to the data. Generally, random error does not result severe alteration of the velocity information. But real system flow dynamics is not perfectly random which leads to erroneous velocity vectors. From the old rule of thumb, incorrect or bad data can best be replaced by interpolating from the valid neighbors.

D.4. Raw particle image velocimetry data

In this topic, the raw particle image velocimetry data obtained for both dilute and dense experimental conditions in Chapter VII are provided. For both experimental conditions, the superficial gas velocity was set at 7.57 m/s. The solid mass fluxes were 19.39 and 39.08 kg/m^{2}s for dilute and dense experimental conditions, respectively. Besides, the example pictures obtained from particle image velocimetry technique for both experimental conditions are shown.

Figures D.4 and D.5 display the example pictures obtained from particle image velocimetry technique for dilute and dense experimental conditions, respectively.

Tables D.1 and D.2 summarize the raw data obtained from particle image velocimetry technique for dilute and dense experimental conditions, respectively. The raw data are lengths and angles of the particle displacement streak line. These angles are based on the vertical axis of image frame.

Tables D.1 The raw data obtained from particle image velocimetry technique

for dilute experimental condition.

Frame	Length	Angle	Frame	Length	Angle	Frame	Length	Angle	Frame	Length	Angle
(-)	(cm)	(°)	(-)	(cm)	(°)	(-)	(cm)	(°)	(-)	(cm)	(°)
0	0.21	20.32	8	0.30	132.04	17	0.20	17.47	25	0.28	6.58
0	0.31	331.97	8	0.18	59.42	17	0.16	41.42	25	0.26	22.68
0	0.20	329.22	9	0.33	358.15	17	0.13	228.37	25	0.29	15.95
0	0.23	2.64	9	0.27	172.30	17	0.20	308.33	25	0.17	24.94
0	0.32	329.15	10	0.39	7.91	18	0.27	39.51	25	0.20	357.92
1	0.38	9.82	10	0.35	8.38	18	0.25	14.04	26	0.37	351.00
1	0.45	186.49	10	0.36	6.91	18	0.32	28.61	26	0.27	6.84
2	0.20	81.57	11	0.22	6.44	19	0.27	7.80	26	0.30	354.49
2	0.20	66.67	11	0.22	33.69	19	0.20	352.88	26	0.29	0.00
2	0.32	85.50	11	0.24	17.61	19	0.29	359.30	27	0.15	20.22
2	0.23	240.26	11	0.21	0.00	19	0.27	2.29	27	0.12	25.77
2	0.19	350.18	12	0.33	10.81	19	0.29	344.05	27	0.29	13.86
3	0.35	359.41	12	0.27	6.17	19	0.26	1.59	27	0.26	19.92
3	0.35	354.11	12	0.27	357.71	20	0.29	0.00	28	0.31	33.14
3	0.32	4.50	12	0.35	0.00	20	0.36	356.00	28	0.20	18.10
3	0.31	354.62	12	0.33	2.52	20	0.20	353.77	28	0.17	57.34
4	0.31	347.91	13	0.34	167.28	21	0.37	354.40	28	0.18	52.91
4	0.35	347.99	13	0.26	196.70	21	0.36	352.59	29	0.23	346.40
4	0.31	347.76	13	0.19	151.99	21	0.32	0.65	29	0.18	347.35
4	0.29	2.12	13	0.21	148.71	21	0.29	355.76	29	0.23	20.14
5	0.32	354.23	13	0.23	203.32	22	0.20	1.04	30	0.17	151.29
5	0.32	350.33	14	0.32	189.67	22	0.18	353.29	30	0.27	158.91
5	0.33	343.36	14	0.21	163.11	22	0.24	353.95	30	0.37	160.87
5	0.30	349.76	14	0.15	171.87	22	0.19	1.08	30	0.26	153.43
5	0.27	352.30	14	0.21	185.91	22	0.21	356.05	30	0.25	186.52
6	0.23	7.13	14	0.24	182.53	22	0.26	335.96	30	0.29	193.86
6	0.23	26.57	15	0.23	10.62	22	0.16	0.00	31	0.25	345.17
6	0.22	15.17	15	0.23	21.30	23	0.30	1.38	31	0.21	353.99
6	0.17	8.65	15	0.20	9.29	23	0.22	345.50	31	0.16	357.46
6	0.27	14.78	15	0.26	22.38	23	0.24	358.32	31	0.21	351.33
6	0.16	14.35	16	0.25	353.39	23	0.27	350.67	31	0.18	356.50
7	0.42	15.21	16	0.29	347.86	24	0.24	116.95	31	0.18	351.87
7	0.37	13.90	16	0.33	356.86	24	0.14	141.12	32	0.28	8.75
7	0.34	8.56	16	0.23	343.30	24	0.16	324.16	32	0.33	8.65
8	0.32	285.77	16	0.26	355.24	24	0.14	90.00	32	0.28	2.17
8	0.24	359.16	16	0.23	343.56	24	0.23	110.97	32	0.26	10.38
8	0.33	62.33	17	0.16	221.42	24	0.18	111.37	32	0.28	10.44

Frame (-)	Length (cm)	Angle (°)	Frame (-)	Length (cm)	Angle (°)	Frame (-)	Length (cm)	Angle (°)	Frame (-)	Length (cm)	Angle (°)
32	0.25	0.00	44	0.23	10.62	54	0.12	358.32	65	0.21	343.78
33	0.14	52.25	44	0.33	6.82	54	0.12	358.21	66	0.23	1.79
33	0.16	38.66	44	0.26	355.30	54	0.10	1.97	66	0.22	359.06
33	0.22	289.03	44	0.26	340.82	54	0.13	23.81	66	0.24	3.47
33	0.15	180.00	45	0.27	357.74	54	0.15	2.79	66	0.20	4.16
34	0.14	331.39	45	0.38	1.08	55	0.23	355.60	67	0.29	359.29
34	0.22	218.37	46	0.27	160.60	55	0.22	353.45	67	0.28	4.46
34	0.15	123.31	46	0.32	166.91	55	0.23	347.07	67	0.30	6.95
34	0.15	105.02	46	0.19	155.38	55	0.16	354.92	68	0.24	13.19
35	0.22	332.15	46	0.22	160.67	56	0.16	215.10	68	0.26	345.77
35	0.25	352.67	46	0.24	158.84	56	0.18	173.29	68	0.20	344.20
35	0.20	19.09	46	0.25	167.56	56	0.20	327.45	68	0.24	18.71
35	0.26	3.18	46	0.26	183.97	56	0.19	151.05	68	0.29	11.45
36	0.35	352.29	47	0.32	162.80	57	0.17	350.13	69	0.34	331.00
36	0.31	2.66	47	0.30	169.76	57	0.16	3.99	69	0.34	350.84
36	0.38	357.84	47	0.44	195.05	58	0.22	355.39	69	0.26	358.41
37	0.33	246.55	48	0.35	223.76	58	0.18	0.00	69	0.25	45.00
37	0.29	357.14	48	0.24	195.95	58	0.20	358.96	69	0.32	0.00
37	0.28	233.86	48	0.19	225.00	59	0.18	339.44	70	0.17	129.81
37	0.27	12.94	48	0.18	197.02	59	0.28	357.10	70	0.17	11.07
38	0.29	357.88	48	0.27	187.59	59	0.22	2.86	71	0.35	355.83
38	0.28	352.60	48	0.32	185.84	59	0.21	342.82	71	0.34	355.19
38	0.26	4.03	49	0.29	355.00	59	0.21	8.67	72	0.32	9.57
38	0.25	355.10	49	0.38	185.39	60	0.33	9.46	72	0.29	10.75
38	0.29	357.17	49	0.40	185.19	60	0.30	11.04	72	0.22	22.83
39	0.26	348.85	50	0.29	9.34	61	0.14	220.76	72	0.27	343.01
39	0.29	347.01	50	0.28	12.04	61	0.19	48.81	72	0.28	19.36
39	0.30	5.51	50	0.26	15.40	62	0.25	9.06	72	0.32	1.29
39	0.28	2.97	51	0.28	354.87	62	0.19	0.00	72	0.30	24.39
40	0.25	353.39	51	0.19	166.76	62	0.24	5.12	73	0.32	32.28
40	0.24	0.00	51	0.17	315.88	62	0.25	15.61	73	0.17	141.15
40	0.26	0.81	51	0.14	321.12	62	0.27	14.04	73	0.24	114.30
40	0.25	6.71	52	0.23	324.04	63	0.18	245.46	73	0.30	28.72
41	0.37	6.22	52	0.24	338.04	63	0.20	287.78	73	0.14	73.86
41	0.34	12.40	52	0.20	343.50	63	0.20	41.38	74	0.20	129.81
42	0.18	0.00	52	0.26	342.07	64	0.28	0.00	74	0.21	336.54
42	0.25	339.73	52	0.22	333.43	64	0.25	0.00	74	0.18	107.35
43	0.33	355.03	53	0.23	48.81	64	0.26	358.43	75	0.30	162.44
43	0.29	343.16	53	0.25	11.63	64	0.23	3.63	75	0.29	183.58
44	0.20	302.01	53	0.18	15.15	64	0.26	3.22	76	0.28	165.96
44	0.22	359.08	53	0.27	1.55	65	0.33	6.97	76	0.33	179.38
44	0.21	5.01	53	0.24	24.66	65	0.22	2.82	76	0.32	184.45

Frame	Length	Angle	Frame	Length	Angle	Frame	Length	Angle	Frame	Length	Angle
(-)	(cm)	(°)	(-)	(cm)	(°)	(-)	(cm)	(°)	(-)	(cm)	(°)
77	0.38	193.77	86	0.27	188.46	97	0.21	0.00	105	0.30	21.29
77	0.38	183.78	86	0.29	196.43	98	0.27	167.64	105	0.32	15.77
78	0.15	35.54	87	0.12	227.39	98	0.24	167.85	106	0.27	15.52
78	0.13	25.11	87	0.16	40.31	98	0.39	163.25	106	0.34	12.72
78	0.25	17.90	87	0.14	35.71	98	0.33	154.00	106	0.23	10.06
78	0.16	45.94	88	0.25	16.39	98	0.21	168.11	106	0.25	5.04
78	0.32	65.77	88	0.16	27.70	98	0.18	161.57	106	0.25	14.24
79	0.34	347.28	88	0.20	17.10	98	0.29	123.29	106	0.16	2.54
79	0.35	347.54	88	0.18	8.13	99	0.22	54.46	107	0.27	63.43
80	0.22	327.89	89	0.19	0.00	99	0.15	54.46	107	0.23	42.51
80	0.19	327.53	89	0.17	3.73	99	0.24	237.72	107	0.19	17.74
80	0.25	326.77	89	0.18	338.63	99	0.25	54.46	107	0.24	28.47
80	0.23	298.97	89	0.19	6.46	100	0.31	186.04	107	0.22	56.58
80	0.16	334.59	90	0.36	343.58	100	0.35	190.73	108	0.32	187.05
80	0.21	305.88	90	0.33	343.54	100	0.33	145.97	108	0.33	23.77
81	0.30	5.51	91	0.22	182.86	100	0.25	153.07	108	0.23	54.36
81	0.31	8.80	91	0.22	184.69	100	0.40	200.74	108	0.23	12.93
81	0.28	359.27	91	0.17	192.01	100	0.38	355.68	109	0.52	352.48
82	0.27	357.74	91	0.28	197.05	101	0.10	173.88	109	0.31	336.37
82	0.25	344.74	91	0.23	177.36	101	0.18	152.93	109	0.34	6.60
82	0.24	0.00	92	0.16	2.60	101	0.28	204.93	109	0.31	217.00
82	0.27	20.11	92	0.12	334.18	101	0.13	204.44	109	0.37	8.37
82	0.23	3.63	92	0.13	341.57	101	0.22	138.99	110	0.36	13.21
82	0.24	2.53	92	0.17	357.56	101	0.30	134.51	110	0.22	11.13
82	0.24	343.71	93	0.14	157.38	101	0.24	133.19	110	0.21	0.99
83	0.24	199.54	93	0.19	160.87	102	0.46	208.79	110	0.26	13.84
83	0.14	201.80	94	0.20	326.02	102	0.19	19.44	111	0.17	12.26
84	0.29	353.50	94	0.15	325.56	102	0.18	156.50	111	0.21	359.01
84	0.28	0.00	94	0.15	343.30	102	0.26	228.96	111	0.18	12.41
84	0.20	5.19	94	0.14	337.93	102	0.29	203.75	111	0.24	15.71
84	0.20	29.74	95	0.26	22.68	102	0.33	188.04	111	0.24	26.18
84	0.16	26.00	95	0.18	25.51	103	0.38	167.29	111	0.25	351.87
84	0.24	17.35	95	0.22	25.30	103	0.57	163.96	111	0.30	7.64
84	0.30	16.70	95	0.20	24.27	104	0.37	359.45	111	0.18	10.62
85	0.31	272.66	95	0.19	38.16	104	0.40	2.06	112	0.28	330.16
85	0.24	306.53	95	0.22	32.11	105	0.33	9.36	112	0.45	115.74
85	0.23	312.51	96	0.27	359.25	105	0.21	313.60	112	0.45	111.80
86	0.14	191.89	96	0.23	9.02	105	0.28	40.28	112	0.49	112.20
86	0.29	203.39	96	0.25	357.51	105	0.22	14.04	112	0.34	110.34
86	0.22	176.19	96	0.21	358.06	105	0.25	8.25	113	0.25	46.15
86	0.32	175.45	97	0.13	12.88	105	0.25	6.61	113	0.26	17.93
86	0.20	193.78	97	0.11	20.14	105	0.30	30.26	113	0.38	9.28

Frame	Length	Angle	Frame	Length	Angle	Frame	Length	Angle	Frame	Length	Angle
(-)	(cm)	(°)	(-)	(cm)	(°)	(-)	(cm)	(°)	(-)	(cm)	(°)
113	0.40	17.78	120	0.30	1.40	129	0.20	42.14	137	0.25	34.59
113	0.27	92.29	121	0.26	6.34	129	0.27	346.15	137	0.25	10.01
113	0.24	40.70	121	0.38	5.98	129	0.30	346.80	137	0.22	359.05
113	0.31	9.89	121	0.35	180.59	129	0.22	316.97	138	0.41	21.43
114	0.35	102.01	122	0.22	5.53	129	0.28	20.98	138	0.25	11.80
114	0.23	110.14	122	0.21	353.00	130	0.27	12.20	138	0.21	346.43
114	0.32	90.00	122	0.18	357.66	130	0.35	12.46	138	0.19	51.17
114	0.19	79.32	122	0.18	337.56	130	0.37	8.29	138	0.26	354.45
114	0.12	21.80	122	0.23	356.37	131	0.30	18.43	138	0.22	311.71
114	0.16	313.15	122	0.20	346.22	131	0.15	16.70	139	0.24	356.53
114	0.18	129.37	122	0.30	3.45	131	0.23	335.85	139	0.30	353.74
115	0.37	359.45	123	0.40	355.84	131	0.17	21.80	139	0.32	3.81
115	0.36	357.11	123	0.30	157.17	131	0.25	58.61	139	0.39	350.54
115	0.32	355.45	123	0.17	32.38	131	0.25	133.23	139	0.35	352.29
115	0.43	358.56	123	0.40	356.88	132	0.18	164.54	140	0.27	351.43
116	0.27	355.43	124	0.17	340.43	132	0.30	170.19	140	0.36	345.55
116	0.17	357.61	124	0.12	332.65	132	0.32	170.96	140	0.26	352.09
116	0.24	354.04	124	0.11	316.33	132	0.39	187.91	141	0.35	351.62
116	0.24	350.39	124	0.19	135.78	132	0.24	13.83	141	0.32	357.46
116	0.24	358.32	124	0.27	202.09	133	0.29	356.47	141	0.22	328.09
116	0.29	7.21	125	0.32	166.91	133	0.36	348.58	141	0.25	323.30
117	0.24	237.99	125	0.35	196.19	133	0.29	0.72	141	0.28	333.77
117	0.15	57.09	125	0.30	184.76	133	0.54	359.62	141	0.18	1.15
117	0.19	315.00	125	0.37	176.15	133	0.43	8.60	142	0.35	14.74
117	0.19	331.99	125	0.24	186.91	134	0.23	0.88	142	0.48	11.31
117	0.26	272.35	125	0.19	6.58	134	0.24	69.94	142	0.35	16.76
117	0.21	305.07	126	0.33	3.11	134	0.25	338.66	142	0.48	13.09
118	0.32	40.05	126	0.43	352.28	134	0.20	312.14	142	0.27	4.64
118	0.27	286.99	126	0.49	0.42	134	0.21	6.01	143	0.46	353.26
118	0.22	45.00	126	0.45	359.54	135	0.24	327.26	143	0.40	349.51
118	0.29	198.89	126	0.30	22.19	135	0.29	330.88	144	0.32	292.28
118	0.22	241.31	126	0.30	356.59	135	0.25	340.79	144	0.19	314.22
118	0.25	243.80	127	0.28	2.97	136	0.26	344.60	144	0.24	327.72
118	0.23	195.57	127	0.34	353.40	136	0.27	3.81	145	0.27	291.09
119	0.25	173.48	127	0.33	8.75	136	0.20	2.08	145	0.26	328.76
119	0.17	175.14	128	0.28	62.76	136	0.23	8.00	145	0.22	333.85
119	0.29	350.77	128	0.18	55.01	136	0.24	200.35	145	0.18	314.17
119	0.27	357.71	128	0.17	324.61	136	0.23	23.78	146	0.59	2.08
119	0.29	351.47	128	0.12	15.26	136	0.22	320.31	146	0.42	1.48
120	0.39	355.72	128	0.12	5.36	137	0.24	59.62	147	0.30	227.96
120	0.30	1.38	129	0.27	347.80	137	0.19	352.33	147	0.19	137.29
120	0.29	357.17	129	0.23	335.85	137	0.21	20.90	147	0.23	128.66

Frame (-)	Length (cm)	Angle (°)	Frame (-)	Length (cm)	Angle (°)	Frame (-)	Length (cm)	Angle (°)	Frame (-)	Length (cm)	Angle (°)
147	0.25	50.30	155	0.14	150.07	166	0.23	180.00	178	0.20	30.26
147	0.26	92.35	156	0.27	181.53	166	0.40	187.84	179	0.28	20.05
147	0.29	62.80	156	0.18	173.16	166	0.26	170.41	179	0.24	359.16
148	0.28	19.60	157	0.29	134.49	166	0.39	176.29	179	0.21	353.23
148	0.27	19.40	157	0.31	149.60	166	0.34	186.01	180	0.26	21.95
148	0.22	357.18	157	0.16	144.16	167	0.49	4.21	180	0.14	324.29
148	0.28	20.05	157	0.18	222.58	167	0.36	5.14	181	0.18	12.65
148	0.20	9.46	158	0.19	171.25	168	0.36	11.53	181	0.22	0.00
149	0.24	71.29	158	0.26	194.23	168	0.24	16.53	182	0.31	337.33
149	0.15	29.05	158	0.44	184.72	169	0.26	241.65	182	0.41	345.36
149	0.21	92.96	158	0.45	183.18	169	0.20	0.00	183	0.32	7.77
150	0.30	239.15	158	0.37	164.74	169	0.26	13.65	183	0.44	357.63
150	0.19	10.89	158	0.59	146.41	169	0.36	17.53	183	0.35	9.46
150	0.30	22.31	159	0.23	2.73	169	0.26	242.39	183	0.31	358.65
151	0.20	302.01	159	0.26	358.41	170	0.31	9.35	184	0.25	333.80
151	0.30	238.80	159	0.21	337.46	170	0.29	1.41	184	0.26	4.76
151	0.09	182.20	159	0.20	345.47	170	0.26	350.41	184	0.25	45.59
151	0.20	203.33	160	0.33	355.03	170	0.23	350.25	184	0.33	0.00
151	0.10	16.50	160	0.33	345.35	170	0.50	7.02	184	0.26	237.41
151	0.08	347.20	160	0.28	355.66	171	0.33	8.65	184	0.25	292.43
152	0.27	9.33	160	0.33	354.41	171	0.30	9.12	185	0.61	10.91
152	0.19	358.94	160	0.26	6.43	171	0.37	12.83	185	0.54	9.15
152	0.20	356.88	161	0.36	178.26	172	0.32	1.95	186	0.38	17.58
152	0.25	356.73	161	0.25	179.17	172	0.36	352.52	186	0.36	347.78
152	0.16	352.06	161	0.27	9.96	172	0.32	3.18	186	0.28	11.16
152	0.20	357.92	162	0.50	11.31	173	0.44	239.44	187	0.21	149.89
152	0.30	3.41	162	0.41	8.13	173	0.56	169.99	187	0.27	196.48
153	0.33	339.96	163	0.30	16.23	173	0.38	143.46	187	0.25	126.87
153	0.31	54.31	163	0.19	14.57	173	0.38	243.19	187	0.22	128.37
153	0.36	354.86	163	0.31	12.60	174	0.38	143.89	188	0.48	25.22
153	0.32	346.91	164	0.48	13.93	174	0.37	240.95	188	0.46	23.37
153	0.24	346.17	164	0.36	13.76	175	0.50	1.66	188	0.23	352.00
153	0.37	295.05	164	0.27	9.33	175	0.35	182.39	188	0.54	27.08
153	0.32	356.78	164	0.34	5.41	176	0.49	6.76	189	0.46	20.56
154	0.36	348.47	164	0.31	2.63	176	0.35	8.88	189	0.30	54.38
154	0.46	347.91	164	0.35	8.88	176	0.37	3.85	189	0.33	35.25
155	0.33	181.87	165	0.37	185.55	177	0.40	12.53	189	0.36	36.53
155	0.27	133.92	165	0.31	166.45	177	0.44	10.39	189	0.23	41.27
155	0.28	188.86	165	0.45	188.64	178	0.27	6.01	189	0.34	62.61
155	0.27	244.47	165	0.36	178.28	178	0.24	16.78	190	0.37	117.81
155	0.15	194.04	165	0.29	331.50	178	0.24	15.71	190	0.47	120.13
155	0.20	128.50	165	0.52	172.83	178	0.24	36.03	190	0.30	138.37

Frame	Length	Angle	Frame	Length	Angle	Frame	Length	Angle	Frame	Length	Angle
(-)	(cm)	(°)	(-)	(cm)	(°)	(-)	(cm)	(°)	(-)	(cm)	(°)
190	0.41	152.31	200	0.34	358.17	208	0.24	246.47	219	0.30	352.45
190	0.32	156.89	200	0.31	355.35	209	0.44	348.60	220	0.39	5.87
190	0.31	128.87	200	0.48	4.73	209	0.39	4.72	220	0.32	8.31
191	0.48	154.98	200	0.32	1.30	209	0.28	351.25	221	0.23	356.48
191	0.39	163.05	201	0.36	31.46	209	0.35	9.46	221	0.19	25.14
191	0.34	161.95	201	0.36	347.22	209	0.33	17.24	221	0.20	39.94
191	0.36	174.81	201	0.37	336.95	210	0.25	9.87	221	0.21	19.98
191	0.29	139.01	201	0.21	329.89	210	0.29	26.25	221	0.21	36.47
192	0.63	176.40	201	0.40	4.09	211	0.26	56.75	221	0.26	0.78
192	0.67	180.62	201	0.21	321.95	211	0.27	40.19	222	0.24	14.66
192	0.50	177.55	202	0.34	340.59	212	0.22	25.74	222	0.24	351.38
193	0.33	6.89	202	0.21	333.87	212	0.17	163.89	222	0.27	13.85
193	0.38	341.57	202	0.15	242.82	212	0.18	177.75	222	0.21	13.57
193	0.33	334.56	202	0.31	266.01	212	0.19	335.82	223	0.26	356.03
193	0.22	324.25	203	0.50	4.09	212	0.19	30.02	223	0.23	353.66
193	0.31	12.75	203	0.48	5.19	212	0.30	89.31	223	0.31	352.06
193	0.34	348.45	204	0.26	166.53	213	0.29	347.86	223	0.25	26.20
194	0.22	37.79	204	0.33	151.49	213	0.33	346.12	223	0.30	2.05
194	0.25	8.37	204	0.26	162.32	213	0.30	349.76	224	0.22	157.67
194	0.23	16.44	204	0.37	206.82	214	0.32	350.33	224	0.18	201.37
195	0.29	7.83	204	0.24	328.45	214	0.29	357.88	224	0.29	224.50
195	0.48	308.33	205	0.38	202.41	215	0.21	59.04	224	0.27	231.58
195	0.28	333.76	205	0.28	32.08	215	0.23	33.94	224	0.30	192.53
195	0.39	353.20	205	0.22	40.29	215	0.23	7.13	225	0.27	20.65
195	0.33	339.59	206	0.50	21.80	215	0.21	41.55	225	0.24	96.91
195	0.33	353.73	206	0.26	169.62	215	0.31	58.35	225	0.24	25.43
196	0.28	351.97	206	0.34	160.99	216	0.34	250.99	225	0.32	350.86
196	0.35	355.91	206	0.26	185.63	216	0.32	232.24	225	0.24	10.46
196	0.33	340.18	206	0.23	315.63	216	0.24	185.96	225	0.19	354.51
196	0.19	352.48	207	0.26	6.25	216	0.19	77.01	225	0.20	7.13
196	0.38	322.27	207	0.39	355.24	216	0.25	206.20	226	0.22	344.58
197	0.28	335.07	207	0.20	350.71	216	0.26	242.02	226	0.26	340.08
197	0.37	357.75	207	0.29	343.16	217	0.28	2.94	226	0.18	319.14
197	0.37	334.92	207	0.27	3.76	217	0.22	338.90	226	0.19	317.29
197	0.35	345.11	207	0.26	3.14	217	0.36	349.03	226	0.19	320.33
198	0.56	355.57	207	0.20	10.12	217	0.29	0.00	227	0.22	318.99
198	0.41	349.88	207	0.30	6.87	217	0.30	2.07	227	0.17	24.44
199	0.26	306.71	207	0.21	27.01	217	0.21	4.93	227	0.26	60.95
199	0.32	302.42	208	0.29	30.36	218	0.12	352.88	227	0.30	14.53
199	0.21	349.08	208	0.28	28.55	218	0.20	349.88	227	0.23	17.88
199	0.34	342.90	208	0.28	26.23	219	0.33	3.77	228	0.13	356.73
199	0.30	338.96	208	0.16	161.57	219	0.28	0.73	228	0.23	2.68

Frame	Length	Angle	Frame	Length	Angle	Frame	Length	Angle	Frame	Length	Angle
(-)	(cm)	(°)	(-)	(cm)	(°)	(-)	(cm)	(°)	(-)	(cm)	(°)
228	0.19	342.58	241	0.35	5.25	251	0.35	354.75	260	0.41	191.21
228	0.18	10.62	241	0.35	358.82	251	0.22	59.20	261	0.34	165.82
228	0.34	33.02	242	0.36	2.83	251	0.22	353.56	261	0.37	8.37
229	0.12	347.66	242	0.41	358.99	251	0.25	2.49	261	0.28	184.34
229	0.21	340.62	243	0.40	4.09	251	0.23	10.62	261	0.40	183.58
229	0.14	343.01	243	0.36	8.62	252	0.27	5.33	261	0.32	179.36
230	0.16	160.77	243	0.28	1.45	252	0.22	1.88	262	0.18	227.49
230	0.21	172.01	244	0.37	8.91	252	0.38	358.91	262	0.21	249.10
230	0.23	210.19	244	0.30	11.71	252	0.26	359.20	263	0.14	349.29
230	0.23	149.81	244	0.27	14.78	252	0.23	0.88	263	0.28	351.76
230	0.35	177.61	244	0.32	14.81	252	0.23	355.53	263	0.31	333.14
231	0.20	4.16	244	0.33	14.04	253	0.32	344.41	263	0.27	335.17
231	0.24	5.12	245	0.40	18.76	253	0.30	18.00	263	0.25	341.05
232	0.33	340.97	245	0.31	18.23	253	0.24	345.34	263	0.14	343.44
232	0.43	348.41	245	0.36	38.57	253	0.23	324.04	263	0.16	329.47
233	0.25	349.99	245	0.33	356.86	254	0.33	359.38	263	0.25	353.48
233	0.26	358.39	245	0.27	357.68	254	0.32	7.85	263	0.27	335.81
234	0.19	41.19	245	0.27	22.09	254	0.31	9.25	264	0.31	6.71
234	0.29	41.93	245	0.36	22.97	255	0.36	6.91	264	0.32	3.25
234	0.19	28.01	246	0.25	17.90	255	0.30	6.79	264	0.31	358.03
234	0.31	44.05	246	0.37	3.89	256	0.35	34.51	264	0.31	7.29
234	0.28	59.42	247	0.25	326.53	256	0.13	339.08	265	0.76	198.26
234	0.29	41.99	247	0.32	347.82	256	0.26	12.70	265	0.36	187.48
235	0.20	192.31	247	0.35	355.83	256	0.25	12.62	265	0.45	196.57
235	0.24	349.54	247	0.38	358.36	256	0.40	15.30	265	0.34	197.28
235	0.16	134.09	247	0.39	358.41	256	0.29	14.56	266	0.18	338.63
236	0.19	343.61	247	0.36	338.63	256	0.32	48.15	266	0.28	322.39
236	0.22	351.47	248	0.39	0.53	256	0.26	340.29	266	0.20	351.87
237	0.25	14.04	248	0.44	356.72	257	0.29	73.16	266	0.17	346.26
237	0.24	18.43	248	0.35	354.70	257	0.20	332.05	266	0.15	349.22
237	0.20	21.41	249	0.32	18.64	257	0.23	328.57	267	0.34	10.47
237	0.22	5.53	249	0.19	358.90	257	0.23	34.70	267	0.38	4.90
237	0.26	17.68	249	0.23	357.36	257	0.16	118.93	268	0.21	352.01
238	0.31	348.04	249	0.41	15.39	258	0.52	191.93	268	0.22	5.62
238	0.30	348.96	249	0.33	9.36	258	0.32	168.31	268	0.18	10.41
239	0.29	355.00	249	0.21	24.36	258	0.28	173.25	268	0.15	358.60
239	0.33	357.54	250	0.35	4.09	258	0.25	184.09	268	0.16	15.95
240	0.18	310.86	250	0.34	0.00	258	0.26	166.53	269	0.31	169.22
240	0.28	292.91	250	0.31	359.33	259	0.36	178.28	269	0.35	161.38
240	0.27	252.05	250	0.26	353.75	259	0.34	183.61	269	0.21	153.43
240	0.30	288.00	251	0.21	337.83	260	0.37	182.20	269	0.24	180.00
240	0.26	172.97	251	0.18	336.95	260	0.46	176.45	270	0.31	354.62

Frame	Length	Angle	Frame	Length	Angle	Frame	Length	Angle	Frame	Length	Angle
(-)	(cm)	(°)	(-)	(cm)	(°)	(-)	(cm)	(°)	(-)	(cm)	(°)
270	0.29	337.54	279	0.28	21.25	289	0.24	14.88	299	0.33	358.77
271	0.20	349.70	280	0.35	180.00	290	0.32	41.79	299	0.36	0.57
271	0.15	348.69	280	0.15	132.09	290	0.34	59.35	299	0.39	359.47
271	0.31	354.69	280	0.16	189.25	290	0.15	48.81	299	0.35	355.83
271	0.24	358.29	280	0.24	148.74	290	0.19	133.45	300	0.45	11.13
272	0.28	55.30	280	0.30	120.26	291	0.35	357.02	300	0.24	30.07
272	0.21	42.88	281	0.48	37.73	291	0.40	4.16	300	0.38	0.00
272	0.25	87.51	281	0.32	219.97	292	0.30	351.77	300	0.40	28.16
272	0.27	201.52	281	0.24	246.91	292	0.37	346.92	300	0.27	2.32
272	0.26	35.45	281	0.21	243.43	292	0.26	356.08	300	0.30	137.41
273	0.13	329.30	281	0.30	29.66	292	0.26	352.97			
273	0.14	335.43	282	0.32	359.35	292	0.24	28.89			
273	0.12	340.46	282	0.33	7.59	293	0.22	24.90			
273	0.19	344.36	283	0.24	347.20	293	0.28	22.22			
274	0.33	24.60	283	0.22	347.77	293	0.26	39.40			
274	0.24	3.47	283	0.22	342.76	293	0.26	32.35			
275	0.30	351.67	283	0.26	353.57	293	0.24	1.68			
275	0.19	6.58	284	0.28	2.17	294	0.36	25.54			
275	0.34	6.67	285	0.32	0.64	294	0.28	18.67			
275	0.25	355.10	285	0.37	353.84	294	0.28	31.22			
275	0.20	352.75	285	0.33	356.92	294	0.26	344.81			
275	0.19	8.58	286	0.27	339.89	294	0.22	23.68			
275	0.27	6.09	286	0.26	336.28	294	0.15	27.76			
276	0.28	60.16	286	0.22	343.03	295	0.25	306.87			
276	0.20	47.17	286	0.32	348.44	295	0.17	321.91			
276	0.26	53.29	287	0.35	337.65	295	0.19	319.64			
276	0.14	18.43	287	0.21	5.01	295	0.27	296.57			
276	0.23	29.74	287	0.22	2.82	295	0.24	322.96			
277	0.16	230.53	287	0.21	317.07	295	0.21	311.47			
277	0.13	60.64	287	0.20	4.09	296	0.31	9.46			
277	0.13	14.04	287	0.19	326.61	296	0.29	7.21			
277	0.17	125.68	287	0.13	18.43	296	0.25	354.29			
277	0.23	295.35	287	0.17	16.46	296	0.26	7.03			
277	0.12	293.43	288	0.29	0.00	296	0.29	7.73			
278	0.16	336.30	288	0.16	345.32	297	0.25	345.76			
278	0.21	2.91	288	0.13	352.09	297	0.15	353.21			
278	0.20	0.00	288	0.20	335.73	297	0.29	357.85			
279	0.19	65.38	288	0.19	2.12	297	0.31	5.38			
279	0.28	71.80	289	0.24	18.71	297	0.26	7.03			
279	0.30	47.91	289	0.23	13.39	297	0.24	6.05			
279	0.30	49.84	289	0.14	7.13	298	0.33	356.89			
279	0.17	355.24	289	0.20	0.00	298	0.31	353.96			

Tables D.2 The raw data obtained from particle image velocimetry technique
for dense experimental condition.

Frame (-)	Length (cm)	Angle (°)	Frame (-)	Length (cm)	Angle (°)	Frame (-)	Length (cm)	Angle (°)	Frame (-)	Length (cm)	Angle (°)	Frame (-)	Length (cm)	Angle (°)
0	0.20	184.97	9	0.17	339.27	19	0.19	10.78	27	0.13	14.04			
0	0.20	173.80	9	0.21	120.76	20	0.19	9.25	28	0.20	3.81			
0	0.25	6.12	9	0.24	133.49	20	0.18	337.17	28	0.16	1.55			
1	0.22	355.52	9	0.19	336.45	20	0.22	7.97	28	0.23	8.75			
1	0.22	353.16	9	0.17	346.33	20	0.22	14.04	28	0.15	349.99			
1	0.21	3.58	10	0.24	15.07	20	0.15	358.32	28	0.18	15.75			
2	0.39	359.36	10	0.21	178.78	20	0.26	17.53	29	0.23	352.33			
2	0.32	355.30	10	0.20	195.26	21	0.15	0.00	29	0.27	357.23			
2	0.32	5.55	11	0.21	7.13	21	0.14	14.93	29	0.30	352.46			
2	0.29	353.95	11	0.23	23.20	21	0.11	0.00	29	0.27	338.03			
3	0.21	23.84	11	0.17	7.31	22	0.15	326.77	30	0.19	15.95			
3	0.23	4.40	11	0.14	14.04	22	0.16	352.30	30	0.22	15.95			
3	0.18	18.43	11	0.17	354.14	22	0.18	299.74	30	0.20	355.03			
3	0.22	9.09	12	0.16	352.09	23	0.20	8.84	30	0.19	7.77			
3	0.22	20.96	12	0.16	344.48	23	0.18	355.71	30	0.16	353.83			
3	0.27	5.62	12	0.16	4.64	23	0.15	341.57	30	0.15	3.47			
4	0.18	7.13	12	0.19	353.37	23	0.15	335.70	31	0.11	175.60			
4	0.15	33.23	12	0.19	350.75	23	0.19	354.69	31	0.14	174.64			
4	0.17	12.20	13	0.16	4.76	23	0.16	345.96	31	0.12	169.88			
5	0.20	31.61	13	0.19	1.33	23	0.21	355.14	32	0.28	352.76			
5	0.17	16.99	13	0.19	353.21	24	0.18	15.38	32	0.24	341.57			
5	0.18	2.73	14	0.21	342.72	24	0.19	28.30	33	0.21	82.87			
5	0.19	10.78	14	0.18	195.75	24	0.23	96.46	33	0.23	115.08			
5	0.15	3.27	14	0.19	2.60	25	0.29	26.18	33	0.15	353.09			
6	0.25	357.99	15	0.19	187.94	25	0.25	3.07	34	0.24	11.51			
6	0.22	2.25	15	0.17	332.78	25	0.23	14.30	34	0.25	2.01			
6	0.24	5.19	15	0.18	208.39	25	0.25	13.30	34	0.26	8.82			
6	0.21	12.26	16	0.24	11.73	26	0.22	11.53	34	0.26	188.67			
6	0.24	3.12	16	0.21	8.47	26	0.15	10.30	35	0.25	353.88			
7	0.20	347.20	17	0.26	2.86	26	0.17	4.51	35	0.16	350.79			
7	0.15	351.63	17	0.17	11.59	26	0.24	15.07	35	0.16	8.13			
7	0.15	3.27	18	0.19	143.67	26	0.20	9.87	35	0.16	339.62			
8	0.22	349.59	18	0.16	129.40	26	0.20	7.59	35	0.18	0.00			
8	0.17	348.41	18	0.20	168.69	26	0.20	9.04	35	0.19	0.00			
8	0.22	349.59	18	0.16	154.80	26	0.18	1.36	36	0.20	200.85			
8	0.20	358.75	19	0.20	344.41	26	0.19	9.46	36	0.20	148.39			
9	0.16	305.91	19	0.16	164.48	27	0.15	3.37	36	0.22	138.27			

Frame (-)	Length (cm)	Angle (°)	Frame (-)	Length (cm)	Angle (°)	Frame (-)	Length (cm)	Angle (°)	Frame (-)	Length (cm)	Angle (°)	Frame (-)	Length (cm)	Angle (°)
36	0.20	114.34	48	0.21	242.90	57	0.23	321.17	67	0.15	356.63			
37	0.15	184.90	48	0.12	34.29	57	0.24	311.28	68	0.19	14.35			
37	0.22	178.88	48	0.14	5.53	57	0.23	349.99	68	0.18	0.00			
37	0.13	25.71	49	0.13	5.91	58	0.25	189.95	68	0.16	49.40			
37	0.12	27.47	49	0.14	333.43	58	0.19	198.43	68	0.18	15.38			
38	0.26	21.45	50	0.19	0.00	58	0.21	214.70	69	0.21	62.35			
38	0.25	51.34	50	0.16	3.18	59	0.28	349.22	69	0.12	66.25			
38	0.19	22.52	50	0.17	355.60	59	0.24	4.16	69	0.18	58.30			
38	0.21	21.12	50	0.22	5.60	59	0.22	350.91	69	0.21	45.00			
38	0.19	17.59	50	0.14	14.04	59	0.23	7.82	69	0.16	51.58			
39	0.17	68.20	50	0.21	358.83	60	0.20	348.44	70	0.23	28.52			
39	0.11	239.42	50	0.19	353.52	60	0.23	337.80	70	0.14	323.84			
40	0.23	353.42	50	0.22	358.88	60	0.22	342.98	71	0.17	333.43			
40	0.18	0.00	51	0.27	352.65	60	0.18	4.29	71	0.19	271.30			
40	0.21	356.42	51	0.22	10.20	61	0.17	17.97	71	0.13	160.97			
40	0.20	19.23	51	0.22	357.71	61	0.18	11.04	71	0.13	164.58			
40	0.19	349.46	51	0.22	356.63	61	0.15	0.00	71	0.14	302.20			
41	0.24	2.12	51	0.20	351.16	61	0.15	3.47	72	0.21	172.88			
41	0.23	0.00	51	0.20	354.92	61	0.12	8.13	72	0.24	161.57			
41	0.26	0.95	52	0.24	353.66	62	0.28	349.05	73	0.20	0.00			
41	0.22	356.57	52	0.18	12.99	62	0.29	359.13	73	0.21	358.78			
42	0.13	350.54	52	0.19	1.30	62	0.25	346.70	73	0.18	1.40			
42	0.21	10.84	52	0.18	0.00	63	0.22	348.69	73	0.21	1.19			
42	0.19	9.25	52	0.22	3.37	63	0.26	353.35	73	0.28	0.90			
43	0.26	346.43	53	0.18	1.40	63	0.27	359.06	73	0.19	357.34			
43	0.26	344.05	53	0.23	2.16	63	0.27	0.94	74	0.16	345.58			
44	0.17	6.01	53	0.20	13.74	64	0.17	329.53	74	0.15	3.47			
44	0.17	213.27	53	0.20	5.08	64	0.16	22.38	74	0.14	8.88			
45	0.17	343.44	54	0.31	350.13	64	0.15	55.41	74	0.17	4.40			
45	0.16	350.27	54	0.28	351.87	65	0.18	9.69	75	0.20	198.82			
45	0.19	357.34	54	0.24	345.96	65	0.17	222.88	75	0.17	191.59			
45	0.16	356.91	54	0.28	354.56	65	0.17	217.48	75	0.19	187.94			
45	0.15	345.17	54	0.29	350.39	65	0.18	203.39	75	0.17	196.14			
46	0.26	358.06	55	0.18	164.25	66	0.23	171.25	75	0.19	180.00			
46	0.19	6.48	55	0.13	344.05	66	0.16	170.79	76	0.16	332.02			
46	0.20	14.04	55	0.19	112.52	66	0.21	156.16	76	0.11	331.39			
46	0.21	19.57	55	0.12	124.82	66	0.25	174.99	76	0.17	345.26			
47	0.14	147.80	56	0.20	19.23	67	0.18	1.36	76	0.17	171.03			
47	0.14	165.53	56	0.21	16.11	67	0.15	358.32	77	0.18	326.69			
47	0.19	296.57	56	0.22	28.07	67	0.14	352.65	77	0.17	238.78			
47	0.14	159.86	56	0.23	26.57	67	0.15	346.76	78	0.18	168.69			
48	0.19	230.71	56	0.24	12.53	67	0.15	356.73	78	0.22	183.37			

Frame	Length	Angle	Frame	Length	Angle	Frame	Length	Angle	Frame	Length	Angle
(-)	(cm)	(°)	(-)	(cm)	(°)	(-)	(cm)	(°)	(-)	(cm)	(°)
78	0.17	169.56	89	0.17	11.59	100	0.18	28.39	109	0.23	348.06
79	0.17	222.88	89	0.16	32.35	100	0.19	37.41	109	0.15	341.03
79	0.14	232.43	90	0.24	13.54	100	0.18	49.84	109	0.20	350.96
79	0.14	231.34	90	0.21	15.78	100	0.20	40.46	109	0.18	6.95
80	0.21	338.20	90	0.22	12.41	100	0.19	58.82	110	0.16	114.44
80	0.18	326.69	90	0.29	3.52	100	0.26	53.90	110	0.21	118.14
80	0.15	326.77	90	0.20	23.20	100	0.19	29.58	111	0.21	339.30
80	0.19	338.20	91	0.17	311.88	101	0.24	356.88	111	0.14	331.82
80	0.21	302.01	91	0.12	322.31	101	0.20	357.46	111	0.18	322.85
81	0.26	338.20	91	0.10	0.00	101	0.18	347.62	111	0.17	1.47
81	0.24	349.32	91	0.17	1.51	101	0.24	354.71	111	0.16	9.73
82	0.18	344.62	92	0.16	164.05	101	0.24	346.46	112	0.20	10.08
82	0.15	214.59	92	0.16	25.87	101	0.21	346.83	112	0.19	3.99
83	0.16	355.36	92	0.19	330.42	101	0.23	352.48	112	0.23	6.58
83	0.17	337.38	92	0.17	348.11	102	0.23	215.54	112	0.22	356.57
83	0.20	319.40	93	0.24	3.18	102	0.22	210.17	112	0.19	12.09
83	0.16	326.31	93	0.29	355.67	102	0.30	190.15	113	0.20	7.43
83	0.21	332.90	94	0.25	356.99	102	0.19	219.47	113	0.19	17.59
83	0.17	319.24	94	0.18	2.73	102	0.20	195.26	113	0.18	12.38
83	0.18	336.61	94	0.23	0.00	103	0.31	186.43	113	0.18	12.68
84	0.18	175.71	94	0.21	0.00	103	0.31	186.52	113	0.24	3.12
84	0.19	18.85	94	0.18	2.73	104	0.26	184.84	114	0.15	6.91
84	0.19	189.46	94	0.18	350.07	104	0.19	155.22	114	0.14	8.88
85	0.19	27.15	94	0.21	4.76	105	0.24	175.84	115	0.25	2.05
85	0.20	19.23	95	0.28	1.82	105	0.22	156.95	115	0.18	353.05
85	0.20	30.53	95	0.30	2.49	105	0.17	157.38	115	0.20	335.14
85	0.24	22.38	95	0.24	8.28	106	0.20	347.47	115	0.20	350.96
85	0.22	34.33	96	0.18	295.94	106	0.23	349.11	116	0.28	341.00
86	0.16	171.87	96	0.13	354.09	107	0.15	300.38	116	0.31	341.82
86	0.22	210.58	97	0.21	319.14	107	0.18	36.87	117	0.29	63.05
86	0.15	211.83	97	0.19	323.39	107	0.17	67.38	117	0.25	159.33
87	0.26	6.77	97	0.21	332.35	108	0.24	9.46	117	0.28	171.87
87	0.24	358.96	97	0.18	321.77	108	0.19	10.78	118	0.26	358.09
87	0.23	188.91	98	0.21	175.14	108	0.20	352.41	118	0.25	354.99
87	0.25	346.70	98	0.22	194.86	108	0.17	0.00	118	0.23	347.01
88	0.26	9.78	99	0.15	11.98	108	0.25	340.28	119	0.24	351.57
88	0.28	10.06	99	0.17	352.50	108	0.23	9.82	119	0.27	356.31
88	0.26	12.43	99	0.16	1.59	109	0.19	350.54	120	0.18	351.47
88	0.25	10.12	99	0.16	12.53	109	0.18	325.92	120	0.17	146.73
88	0.21	9.46	99	0.14	24.15	109	0.23	1.08	120	0.21	349.16
89	0.17	35.36	99	0.14	17.88	109	0.17	352.50	120	0.23	194.30
89	0.18	14.04	100	0.20	29.43	109	0.18	335.90	121	0.15	13.24

Frame	Length	Angle	Frame	Length	Angle	Frame	Length	Angle	Frame	Length	Angle
(-)	(cm)	(°)	(-)	(cm)	(°)	(-)	(cm)	(°)	(-)	(cm)	(°)
121	0.14	1.74	131	0.21	8.47	144	0.18	355.91	156	0.18	345.96
121	0.12	18.43	131	0.17	1.47	144	0.23	356.70	157	0.15	349.99
121	0.22	23.50	131	0.24	3.12	144	0.18	2.79	157	0.19	348.18
122	0.14	337.52	132	0.17	185.86	144	0.23	10.01	157	0.14	7.13
122	0.16	350.79	132	0.21	180.00	145	0.19	127.41	158	0.20	345.07
122	0.15	342.65	133	0.15	348.37	145	0.16	148.50	158	0.19	349.46
123	0.18	355.71	133	0.14	0.00	145	0.19	115.41	158	0.14	19.54
123	0.17	345.26	133	0.14	356.31	146	0.16	7.70	159	0.24	350.54
123	0.21	353.93	134	0.19	5.31	146	0.18	358.64	159	0.27	12.23
123	0.16	341.08	134	0.20	0.00	146	0.17	1.47	160	0.24	17.10
123	0.19	351.87	134	0.24	37.50	146	0.20	1.27	160	0.23	24.08
123	0.20	0.00	134	0.17	2.94	146	0.19	3.99	160	0.23	13.50
124	0.16	9.21	134	0.18	351.67	147	0.31	154.89	161	0.20	348.69
124	0.21	55.98	135	0.31	7.43	147	0.28	164.43	161	0.19	16.31
125	0.23	13.50	135	0.22	14.04	147	0.29	146.79	161	0.16	1.55
125	0.23	21.19	135	0.21	14.32	148	0.26	354.19	161	0.23	17.74
125	0.23	23.63	135	0.23	14.30	148	0.30	358.34	162	0.24	17.78
126	0.22	11.31	135	0.21	14.62	148	0.27	4.69	162	0.27	14.93
126	0.19	6.63	136	0.13	22.17	149	0.14	217.57	163	0.14	32.20
126	0.16	3.18	136	0.15	0.00	149	0.18	36.87	163	0.17	40.76
126	0.21	14.32	137	0.23	10.89	150	0.24	12.53	164	0.16	353.66
126	0.21	14.62	137	0.23	8.91	150	0.16	4.76	164	0.21	355.24
126	0.22	355.52	137	0.27	16.34	150	0.12	351.87	164	0.19	1.30
127	0.23	358.90	137	0.27	0.00	151	0.21	202.25	164	0.18	9.69
127	0.19	1.33	137	0.26	8.82	151	0.19	190.54	164	0.18	355.82
127	0.19	347.91	138	0.18	325.92	151	0.22	194.86	165	0.19	19.29
127	0.23	3.30	138	0.17	328.78	151	0.26	195.95	165	0.23	183.30
128	0.21	358.81	138	0.18	350.31	152	0.21	0.00	166	0.19	9.46
128	0.16	1.59	139	0.17	343.86	152	0.17	1.47	166	0.21	63.97
128	0.21	3.65	139	0.18	351.67	152	0.23	15.64	167	0.23	126.43
128	0.19	7.77	139	0.16	349.00	152	0.22	12.91	167	0.25	132.83
129	0.24	349.32	140	0.20	61.19	152	0.24	3.12	167	0.21	130.86
129	0.25	327.14	140	0.17	210.47	153	0.18	21.54	167	0.24	116.10
129	0.29	353.85	141	0.24	13.78	153	0.22	11.53	167	0.22	32.74
129	0.21	344.54	141	0.21	168.93	153	0.18	11.04	168	0.18	350.31
129	0.30	338.36	141	0.22	187.97	153	0.16	11.00	168	0.19	353.52
130	0.20	12.53	142	0.19	191.82	154	0.13	58.39	168	0.24	5.19
130	0.21	5.95	142	0.21	193.45	154	0.14	29.74	169	0.16	345.96
130	0.20	5.08	142	0.22	196.59	155	0.15	337.89	169	0.14	356.31
130	0.23	11.94	143	0.16	345.96	155	0.14	351.12	169	0.16	0.00
130	0.24	12.76	143	0.17	4.40	156	0.30	10.82	169	0.18	0.00
131	0.20	339.15	144	0.17	0.00	156	0.19	3.90	169	0.21	7.28

Frame	Length	Angle	Frame	Length	Angle	Frame	Length	Angle	Frame	Length	Angle
(-)	(cm)	(°)	(-)	(cm)	(°)	(-)	(cm)	(°)	(-)	(cm)	(°)
170	0.22	353.02	182	0.21	327.62	194	0.29	0.00	206	0.21	338.20
170	0.21	193.45	182	0.16	327.17	194	0.27	3.69	206	0.20	337.29
171	0.12	320.71	182	0.18	292.31	194	0.24	348.49	206	0.21	338.88
171	0.14	345.96	183	0.21	3.58	194	0.25	4.09	207	0.25	86.99
171	0.16	345.58	183	0.17	20.73	194	0.19	358.70	207	0.21	14.32
171	0.12	344.93	183	0.17	19.86	195	0.19	13.39	208	0.23	3.30
172	0.23	11.94	183	0.15	3.27	195	0.19	9.46	208	0.21	193.17
172	0.25	10.12	184	0.25	1.02	195	0.22	16.26	208	0.18	327.09
172	0.24	14.04	184	0.25	4.01	195	0.20	14.04	208	0.16	30.14
172	0.19	11.82	185	0.19	7.94	195	0.20	24.86	209	0.18	213.31
173	0.29	359.12	185	0.19	353.52	196	0.25	347.69	209	0.23	305.54
173	0.22	352.03	185	0.22	346.24	196	0.27	352.53	209	0.17	49.24
174	0.19	346.61	186	0.27	193.13	197	0.22	342.65	209	0.19	267.40
174	0.19	10.54	186	0.23	147.20	197	0.17	346.33	209	0.19	347.91
174	0.22	346.24	186	0.23	172.48	197	0.18	341.11	210	0.15	336.37
174	0.22	348.47	186	0.20	161.18	197	0.19	354.81	210	0.15	358.32
174	0.16	9.21	186	0.22	192.41	198	0.12	109.80	210	0.15	335.70
175	0.17	46.04	187	0.22	22.44	198	0.13	323.13	210	0.20	352.57
175	0.19	7.94	187	0.27	30.32	199	0.19	353.52	210	0.18	345.62
175	0.21	237.62	187	0.23	18.78	199	0.17	132.95	211	0.17	309.61
176	0.19	15.95	187	0.22	18.43	199	0.20	1.25	211	0.14	248.20
176	0.19	20.10	187	0.22	31.76	199	0.20	327.72	211	0.18	175.82
176	0.15	6.52	187	0.23	25.60	200	0.25	13.30	211	0.13	172.41
176	0.16	12.88	188	0.29	8.75	200	0.26	9.78	212	0.22	3.43
177	0.23	355.68	188	0.25	7.99	201	0.26	164.58	212	0.20	348.69
177	0.23	355.68	188	0.25	7.00	201	0.26	344.32	212	0.26	346.43
177	0.23	353.29	189	0.18	133.03	201	0.22	184.57	212	0.20	343.18
177	0.23	351.09	189	0.18	4.18	201	0.26	352.15	212	0.21	349.38
177	0.17	2.94	189	0.19	328.13	202	0.19	358.70	212	0.21	352.88
177	0.21	358.83	189	0.19	322.59	202	0.24	10.68	212	0.23	345.43
178	0.17	4.51	190	0.24	174.71	203	0.16	16.39	213	0.25	327.68
178	0.13	7.59	190	0.17	343.44	203	0.16	355.36	213	0.23	329.98
178	0.15	324.46	190	0.16	191.31	203	0.14	0.00	213	0.27	311.10
179	0.12	338.20	191	0.24	116.57	203	0.17	353.99	213	0.24	320.19
179	0.16	61.39	191	0.21	124.99	204	0.29	9.46	213	0.24	323.97
179	0.17	293.20	192	0.15	342.65	204	0.22	14.86	213	0.22	330.83
180	0.15	332.70	192	0.17	334.72	205	0.27	58.09	214	0.15	199.98
180	0.19	111.80	192	0.16	345.58	205	0.23	71.92	214	0.18	191.31
180	0.20	212.28	192	0.13	178.03	205	0.16	48.37	215	0.19	9.46
181	0.18	9.69	193	0.26	16.61	205	0.16	29.36	215	0.15	13.24
181	0.18	0.00	193	0.20	23.70	206	0.22	347.59	215	0.17	16.99
181	0.17	7.31	193	0.21	353.93	206	0.20	340.77	215	0.21	6.07

Frame	Length	Angle	Frame	Length	Angle	Frame	Length	Angle	Frame	Length	Angle
(-)	(cm)	(°)	(-)	(cm)	(°)	(-)	(cm)	(°)	(-)	(cm)	(°)
216	0.24	22.38	226	0.16	349.00	238	0.19	76.29	249	0.21	201.80
216	0.20	256.26	227	0.16	61.39	238	0.13	103.57	249	0.13	1.97
216	0.21	61.29	227	0.26	55.49	239	0.15	348.02	250	0.19	3.90
217	0.18	342.90	227	0.18	48.95	239	0.16	0.00	250	0.21	8.30
217	0.17	331.50	227	0.14	48.81	239	0.17	358.49	250	0.21	2.39
217	0.23	304.29	228	0.19	310.31	239	0.18	0.00	250	0.22	2.34
218	0.17	7.31	228	0.16	11.31	239	0.21	3.65	250	0.23	352.18
218	0.14	14.47	229	0.16	70.56	240	0.15	1.68	251	0.30	354.12
218	0.15	11.98	229	0.18	81.67	240	0.22	358.88	251	0.29	349.54
218	0.16	7.70	229	0.18	4.18	240	0.25	343.50	251	0.27	8.39
219	0.19	347.91	230	0.24	351.57	241	0.16	352.30	252	0.18	334.06
219	0.22	341.20	230	0.24	355.76	241	0.17	318.12	252	0.15	337.89
219	0.23	151.48	230	0.22	351.87	241	0.17	346.68	252	0.16	343.61
219	0.18	170.07	230	0.25	358.98	241	0.16	4.76	252	0.15	355.10
220	0.20	352.57	230	0.25	0.99	241	0.20	1.27	252	0.18	332.82
220	0.21	356.35	230	0.25	354.99	242	0.20	3.73	252	0.19	353.37
220	0.17	355.60	230	0.20	349.92	242	0.17	10.71	252	0.21	314.17
220	0.22	355.33	230	0.24	342.22	242	0.17	40.76	253	0.21	335.06
220	0.20	3.73	231	0.31	350.27	242	0.17	21.80	253	0.16	348.69
220	0.22	353.02	231	0.25	341.88	242	0.20	314.09	253	0.13	352.41
221	0.12	45.00	231	0.29	339.34	243	0.20	353.80	253	0.17	357.06
221	0.12	19.80	232	0.26	348.31	243	0.19	346.61	253	0.20	0.00
221	0.18	340.25	232	0.21	347.74	243	0.21	349.16	253	0.18	17.10
221	0.18	347.01	232	0.28	354.56	243	0.20	355.03	253	0.24	347.24
221	0.16	347.47	232	0.27	351.47	243	0.18	352.88	254	0.22	343.74
221	0.23	358.90	233	0.15	353.48	244	0.19	7.94	254	0.14	24.90
221	0.19	358.70	233	0.14	358.26	244	0.19	25.97	254	0.20	354.92
221	0.16	358.41	233	0.15	358.32	245	0.25	153.89	254	0.22	9.09
222	0.18	34.08	233	0.19	351.87	245	0.29	140.53	255	0.19	316.85
222	0.18	90.00	233	0.20	349.92	246	0.24	94.16	255	0.17	345.26
222	0.19	58.57	233	0.23	350.18	246	0.16	49.57	255	0.25	356.99
223	0.15	1.64	234	0.20	341.18	246	0.14	0.00	255	0.24	340.91
223	0.16	356.82	234	0.15	355.10	246	0.22	17.02	256	0.24	8.28
223	0.15	10.30	234	0.22	2.25	246	0.25	1.02	256	0.26	6.65
224	0.25	351.03	234	0.18	4.09	247	0.22	6.84	257	0.21	26.03
224	0.19	5.31	235	0.19	291.80	247	0.20	15.26	257	0.25	48.53
224	0.24	351.57	235	0.17	55.49	247	0.22	4.67	257	0.20	11.56
224	0.21	343.89	235	0.16	284.42	248	0.16	221.63	258	0.24	24.18
225	0.16	341.08	236	0.21	217.35	248	0.21	173.93	258	0.25	18.76
225	0.15	337.89	236	0.20	180.00	248	0.16	175.36	258	0.25	17.47
226	0.18	66.61	237	0.21	350.54	248	0.19	154.59	259	0.17	219.81
226	0.18	317.91	237	0.17	348.11	248	0.23	201.60	259	0.12	171.57

Frame (-)	Length (cm)	Angle (°)	Frame (-)	Length (cm)	Angle (°)	Frame (-)	Length (cm)	Angle (°)	Frame (-)	Length (cm)	Angle (°)
259	0.13	191.69	270	0.15	16.86	281	0.24	342.22	292	0.19	189.46
260	0.22	330.40	271	0.23	177.80	281	0.20	1.27	292	0.13	15.42
260	0.17	338.20	271	0.24	225.74	281	0.19	345.65	292	0.13	25.71
260	0.25	333.43	272	0.25	171.03	282	0.18	212.15	293	0.16	0.00
260	0.16	332.74	272	0.26	179.03	282	0.14	203.43	293	0.19	7.94
261	0.24	350.71	272	0.28	349.94	282	0.15	162.65	293	0.18	27.82
261	0.26	348.50	273	0.19	41.19	282	0.14	165.53	294	0.27	341.27
261	0.22	5.83	273	0.15	115.02	283	0.30	168.86	294	0.19	336.45
262	0.14	3.58	273	0.18	9.69	283	0.31	179.18	294	0.18	342.00
262	0.14	358.15	274	0.16	334.89	284	0.25	181.02	294	0.18	342.00
262	0.18	22.07	274	0.17	349.29	284	0.29	180.00	294	0.20	322.13
262	0.14	65.85	274	0.15	11.63	285	0.14	18.43	294	0.22	338.63
262	0.23	357.84	274	0.16	352.09	285	0.15	11.98	295	0.12	347.47
263	0.18	343.30	274	0.18	12.99	285	0.17	127.48	295	0.14	347.66
263	0.20	1.27	275	0.25	346.70	285	0.16	22.99	295	0.12	10.49
263	0.15	348.37	275	0.24	23.33	286	0.22	357.66	295	0.15	10.30
263	0.14	14.04	275	0.25	5.10	286	0.20	356.19	296	0.14	331.82
263	0.19	340.71	275	0.22	5.83	286	0.19	346.61	296	0.14	315.00
264	0.27	351.47	275	0.24	349.51	286	0.19	344.05	296	0.16	312.80
264	0.25	352.88	276	0.26	10.56	286	0.21	1.17	296	0.21	317.49
264	0.23	354.51	276	0.26	10.56	286	0.22	357.71	297	0.16	85.24
264	0.27	342.15	277	0.23	21.19	287	0.15	336.37	297	0.17	11.89
265	0.24	11.51	277	0.19	10.54	287	0.18	355.91	298	0.12	4.24
265	0.27	7.59	277	0.18	25.35	287	0.16	355.36	298	0.14	3.69
265	0.24	8.58	277	0.19	33.69	287	0.19	344.05	298	0.16	57.17
265	0.23	9.82	277	0.18	351.47	287	0.22	343.74	299	0.20	10.08
266	0.21	1.17	277	0.16	342.55	288	0.15	168.37	299	0.17	14.74
266	0.17	37.48	278	0.28	7.13	288	0.15	327.26	299	0.21	13.17
266	0.22	344.85	278	0.27	7.47	289	0.16	14.04	299	0.22	9.27
267	0.17	5.86	279	0.22	32.74	289	0.20	19.65	299	0.17	0.00
267	0.17	0.00	279	0.20	4.97	289	0.17	19.86	300	0.24	351.57
267	0.19	12.09	279	0.20	18.03	290	0.14	349.05	300	0.26	355.24
267	0.20	345.96	279	0.25	12.31	290	0.18	4.29			
267	0.17	336.80	279	0.19	10.78	290	0.20	26.00			
268	0.26	3.81	279	0.16	25.11	290	0.17	339.27			
268	0.23	5.49	279	0.22	4.67	290	0.15	342.65			
268	0.25	348.69	279	0.21	2.44	290	0.19	351.87			
269	0.14	14.93	280	0.17	346.68	290	0.13	7.85			
269	0.15	230.83	280	0.24	299.36	291	0.17	336.04			
269	0.15	242.70	280	0.18	354.29	291	0.15	34.16			
269	0.14	322.77	280	0.12	342.26	292	0.20	194.04			
270	0.18	153.43	281	0.25	335.22	292	0.21	0.00			

Figure D.1 An example picture of fiber optic light source.

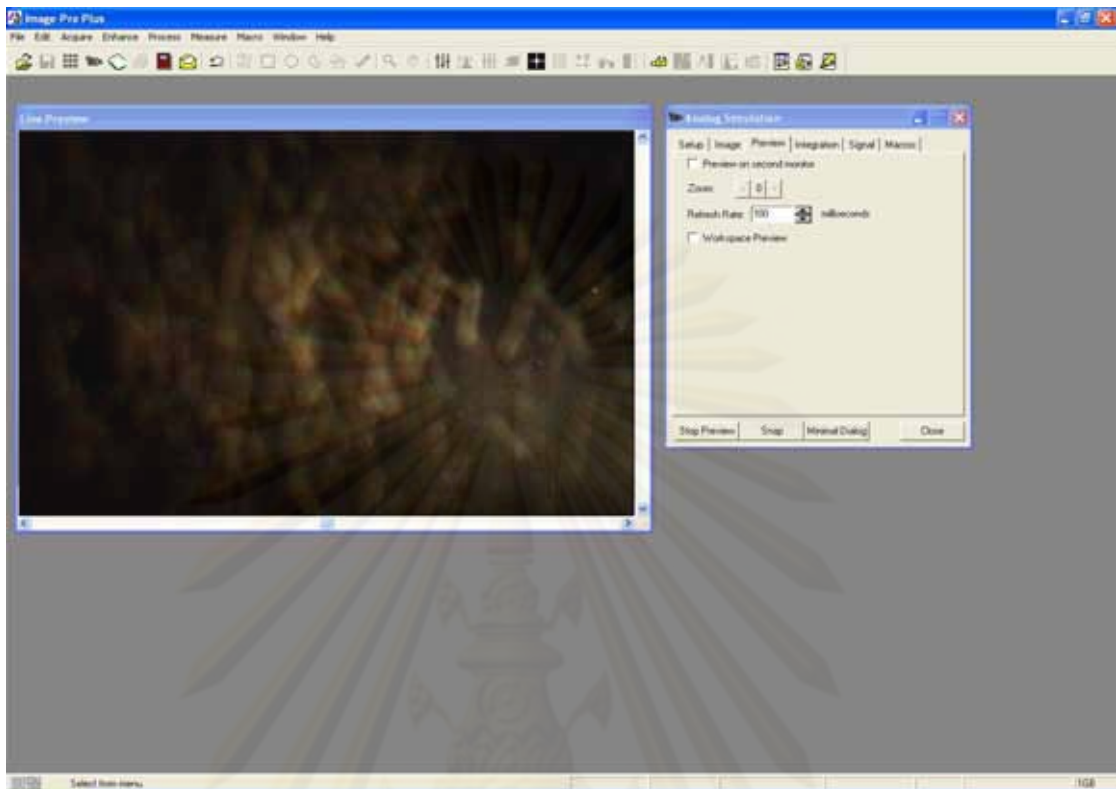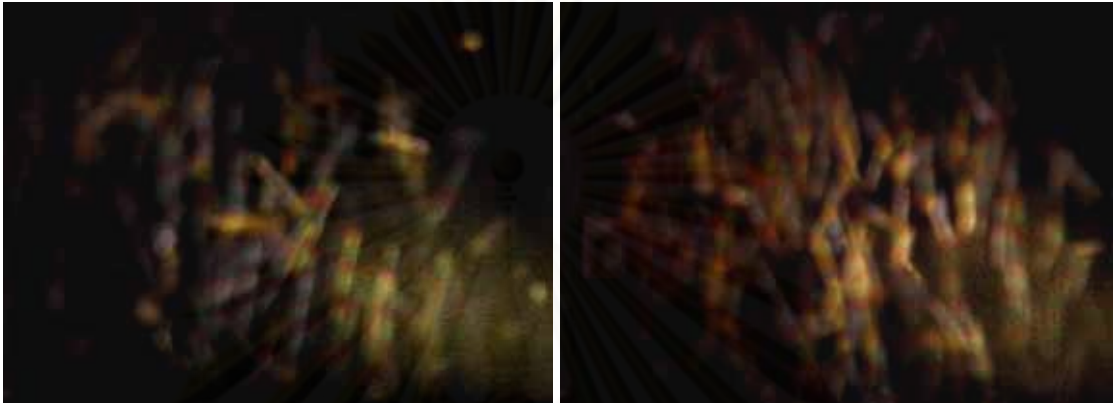Figure D.2 An example picture of charge coupled device camera.

Figure D.3 An example picture of the Image-Pro Plus^{TM} computer software.

Figures D.4 The example pictures obtained from particle image velocimetry technique
for dilute experimental condition.

Figures D.5 The example pictures obtained from particle image velocimetry technique
for dense experimental condition.

BIOGRAPHY

Mr. Benjapon Chalermsinsuwan was born on May 28, 1983 in Bangkok, Thailand. He graduated with a Bachelor's degree of Science from Department of Chemical Technology, Faculty of Science, Chulalongkorn University in 2005. He has continued his study in Ph.D. program at the same Department of Chemical Technology, Faculty of Science, Chulalongkorn University since 2005 and finished his study in 2009. During 2007-2008, he spent his research studies at Department of Chemical and Biological Engineering, Armour College of Engineering, Illinois Institute of Technology in Chicago, USA.

The journal publications involving his research studies are the following:

Chalermsinsuwan, B., Kuchonthara, P., and Piumsomboon, P. Effect of circulating fluidized bed reactor riser geometries on chemical reaction rates by using CFD simulations. Chemical Engineering and Processing: Process Intensification 48 (2009): 165-177.

Chalermsinsuwan, B., Piumsomboon, P., and Gidaspow, D. Kinetic theory based computation of PSRI riser: Part I - Estimate of mass transfer coefficient. Chemical Engineering Science 64 (2009): 1195-1211.

Chalermsinsuwan, B., Piumsomboon, P., and Gidaspow, D. Kinetic theory based computation of PSRI riser: Part II - Computation of mass transfer coefficient with chemical reaction. Chemical Engineering Science 64 (2009):1212-1222.